PREFACE

The enclosed report is the work of Mr. Tao-Ming Chang the graduate student working under this research project. The report is entitled *Evaluation of surface-wave waveform modeling for lithosphere velocity structure*. The text is the draft of a Ph. D. Dissertation.

This report is the culmination of efforts to implement and compare broadband waveform modeling techniques to constrain crustal velocity models. The impetus for this effort lies in the need of CTBT monitoring for accurate event location and confident identification from sparse data. The velocity models obtained by analyzing large seismic events may provide the necessary regional constraints required for the small events of interest to the CTBT.

This report implements and compares techniques for one well recorded North American earthquake rather than looking at a lot of earthquakes. There is enough variability in wave propagation in North America to test a method. The single event is understood well enough that the effects of the source on the waveform is constrained.

This effort is just the beginning of a long effort of algorithm testing and improvement.

EVALUATION OF SURFACE-WAVE WAVEFORM MODELING FOR LITHOSPHERE VELOCITY STRUCTURE

Tao-Ming Chang

Saint Louis University
1997

TABLE OF CONTENTS

LIST OF FIGURES

LIST OF TABLES

CHAPTER 1
INTRODUCTION

1.1 The Problem

To verify seismological inferences about the Earth, matching observed seismograms an ultimate task for modern seismology. After the success in modeling long-period seismograms and routinely estimating earthquake mechanisms in the early 80s, seismologists are now challenged to model entire regional seismograms at the high frequencies. In this study, two different methods will be used to model the surface-wave waveform. One of the proposed algorithms uses the gradient information from the hypersurface of the misfit function to formulate the inversion algorithm, the other is based on a global search technique. The advantages and weaknesses of each proposed algorithm will be examined in terms of robustness and uniqueness of the resultant model. The ultimate purpose of this type of research is to quantify the limitations of one-dimensional earth models as an initial step in approximating 3-D structures.

1.2 Review of Related Literature

Since the birth of quantitative seismology, seismologists have shared the same goal: that one day we can use all geophysical knowledge to design an intelligent system which can routinely analyze all near real-time earthquake data, predict future earthquakes, and systematically update our knowledge about the Earth. To reach this goal, there are several important tasks to accomplish: collecting earthquake

data, developing more sophisticated computational techniques, and finding a better way to interpret data systematically.

For the past half century, seismological research into Earth structure can be roughly divided into three scales: planetary scale (global seismology), regional scale (regional seismology; a few hundred kilometers), and small scale (exploration seismology; a few tens of kilometers). The development for these three scales has not been uniform. Global and exploration seismology were developed more systematically than regional seismology. The reasons for this phenomenon are differences in interests of science and industry, in data coverages, and in the theoretical computational methods in seismology. In this review, historical developments will be briefly described, possible future developing directions will be outlined, and the emphasis of this study will be addressed.

1.2.1 Development Of Global Seismology

Although earthquakes happen in the world everyday, the currently available data are very limited in both spatial and temporal distribution. Confined by the dataset, only the low-wavenumber (harmonic) global structural features could be estimated. In fact, even though research in global seismology has been boosted by specific scientific interests, the global earth structures determined is not unique. However, global seismology developed very systematically. For example, scientists inferred earth structure using different types of data (free oscillations, surface waves, and body wave travel times) and reference models have been established (e.g. Dziewonski and Anderson 1981). Based on the reference models, routine analysis of seismic sources for large earthquakes became possible (Dziewonski, Chou, and Woodhouse, 1981; Dziewonski and Woodhouse, 1983; Sipkin, 1986). On the other hand, global heterogeneity (obtained using tomographic techniques) have been well studied using different data such as phase

and group velocities of long-period surface waves (Nakanishi and Anderson, 1983, 1984; Nataf, Nakanishi, and Anderson, 1986), long-period waveforms (Woodhouse and Dziewonski, 1984), P-velocities from teleseismic events (Dziewonski, 1984), and normal modes (Masters *et al.*, 1982). In these studies, the horizontal resolution is greater than 1000 km (Zhang and Tanimoto, 1992), and many significant features, such as mid-ocean ridges, require better resolution.

There are several ways to increase the resolving power of seismological techniques. The first way is to use more data in inversion. Although the number of global seismic stations are increasing, the earthquake dataset is increasing steadily but slowly. A few decades may be needed to meet the required size for studying detailed features. Under such a limitation, seismologists have to find better ways to increase the usable data which means to efficiently use the current dataset. One possibility is to use waveforms data directly and another possibility is to use shorter period data from smaller earthquakes. A difficulty associated with using waveforms is the availability of accurate source mechanism of smaller regional earthquakes. The second way to increase resolution is reducing some uncertainties caused by the inaccurate shallow structure. Mooney *et al.* (1996) show improvement of the resolving power in global structure when using an improved global crustal model for station corrections. The third way for increasing resolution is to find new ways to interpret data. Two experiments have been reported. One uses body wave travel-time residuals (Su and Dziewonski, 1992), the other uses differential travel times (Woodward and Masters, 1991). The typical horizontal resolving length for such experiments is 550 km (Su *et al.* 1992).

It is clear that the current effort on global seismology is directed toward increasing resolution. To achieve this, more knowledge is required about the regional structure. More complicated techniques to invert different types of data simultaneously must also be developed and proven.

1.2.2 Development Of Exploration Seismology

The purpose of exploration seismology is search for resources by obtaining a high-resolution image of underground structure. To do this, artificial sources and dense receiver coverage are necessary instead of relying on natural earthquakes and sparse seismic stations. Huge exploration seismic datasets enable seismologists to investigate the heterogeneity of shallow structure, even only travel time data are used. In the early stages of exploration seismology, it was natural to use the first arrival data (refraction signal) to infer layer structures. But the problem of non-uniqueness of solutions has pushed the joint use both refraction and wide-angle reflection data. The use of both refraction and reflection data to invert 1-D (e.g. Braile, 1973), and 2-D structure (e.g. Zelt and Smith, 1992) is well reported.

However, as pointed out by many researchers (e.g. Huang *et al.* 1986), the precise identification of refraction and reflection signals (triplication) is crucial for the success of such inversion schemes. During data processing steps like picking phases, artifacts can be introduced. Sometimes it is worse when it is necessary to interpolate travel time data in order to avoid several problems associated with data sparseness. All these procedures will introduce uncertainties and errors in inversion results. Another imperfection about this inversion algorithm is that it can not retrieve the shear velocity information. Even though a system of signal enhancement techniques such as CDP stacking and migration were developed in oil industry, oil companies still need new techniques to improve the image of the subsurface structure. All these factors challenge seismologists to find a better way solving problems.

Waveform inversion seems to be a way to avoid introducing artificial effects and to use more information than travel times. Unfortunately seismologists find it very difficult to directly invert the wide-band seismic waveform, and a two-step approach is often used

(Nowack and Braile, 1993). Therefore in the exploration seismology, there are two different problems regarding waveform inversion: the first is how to retrieve the background velocity (to match the low-frequency part waveform), and the other is how to match the entire waveform once the background velocity is available. Much research is reported on fitting the entire waveform when a good starting model is available (e.g. Mora, 1987; Pan and Phinney, 1989; and Crase *et al.* 1990). Although the assumption of availability of a good starting model seems suitable because of standard velocity analysis procedures widely-used in oil industry, there has been no progress in retrieving background velocities using waveform inversion technique because of its fully nonlinear character.

Recently, there are two good experiments in retrieving background velocity were performed by Koren *et al.* (1991) and Bunks *et al.* (1995). Koren *et al.* (1991) try to find the possible velocity model using a Simulated Annealing algorithm. In their experiment, they found the existence of local minima on the hypersurface of the misfit function is caused by a cycle-skipping effect, and *a posteriori* probability density can be computed by using simulated annealing algorithm. As outlined previously, seismologists know, from experience, it is not a simple task to match the entire waveform. It seems that at least two-step approach is needed. Based on this idea, Bunks *et al.* (1995) try to use different low-pass filtered waveform in inversion. They first inverted for a simple 1-D model from the low-frequency signal (0-7 Hz), then inverted for a gross 2-D model using middle-frequency waveform (0-10 Hz), and finally obtained a detail structure from inverting high-frequency waveform (0-15 Hz). The results of the Monte Carlo search and multiscale inversion are encouraging. These experiments show the good resolution can we expect when we have enough data coverage. As commented by Nowack and Braile (1993), the current state of wavefield inversion in exploration seismology is to find a best inversion procedure.

1.2.3 The Possible Future Direction Of Development

We can see that global seismology is currently trying to improve the resolution of the tomographic image and determination of focal mechanism of smaller events by extending Harvard CMT method (Ekstrom, 1996). In exploration seismology, high resolution images of subsurface structure can be obtained, but only for shallow depths. So there is an existing gap between this two scales. From the development of both global seismology and exploration seismology, we believe the future attention will focus on systematically studying the regional structures.

Theoretically, we should directly model the waveform for 3-D structures, but practically, it is impossible because of our current limited knowledge about the complicated structures and our sparse data coverage. So far, there is no report on successful modeling waveform for 3-D, even 2-D structure. The attempt, such as Vidale and Helmberger (1992), for matching the complicated waveform using 2-D finite-difference method is not successful. Due to the limited computing ability of synthetic seismograms in a realistic earth, two directions should be considered for separated source inversion and structure inversion regarding extracting more information in a simplified 1-D model. The first is inversion using broadband waveform data. The second is inversion using as many different types data as possible. The reason for this is that while broadband waveform data place better constraints than any single data type, additional constraints can be obtained from other data such as $pP - P$ providing constraints on source depth. Once seismologists develop all these tools, the final stage is to build a system which will automatically locate earthquakes, analyze source mechanisms, and indicate the "anomalous" earthquakes for further study. All of these will greatly contribute to other branch of geoscience researches such as delineating the tectonic processes, and even monitoring the failure stress change in a fault system (Stein *et al.* 1992). In

the meantime, seismologists should continuously develop forward and inverse algorithms for 2-D and 3-D structures, and a further experiment regarding the iterative source and structure inversion could be tested.

Recently, there has been much research in focal mechanism analysis using regional broadband waveform. This work using different subsets data such as surface-wave (Thio and Kanamori, 1995), body-wave waveform (Dreger and Helmberger, 1993), full waveform (Mao, Panza, and Suhadolc, 1994), and even one single station (Fan and Wallace, 1991). Zhou *et al.* (1994) and Zhu *et al.* (1996) showed one interesting method which uses both high-frequency body-wave waveform and low-frequency full waveform in searching for the best focal mechanism. In this study, we will concentrate on the regional structure inversion problem since earth structure is fundamental to source parameter estimation.

1.2.4 Emphasis Of This Study

To model regional broadband waveforms, there are two different approaches. The first approach is to match different phases of body-wave such as P_{nl} and S_{nl}. Zhao and Helmberger (1991) proposed one strategy to model the waveform. First, they model long-period data (P_n and S_n) assuming a single crustal layer model and get the average crustal and upper mantle P, S velocities, and crustal thickness. Next, they model the fundamental mode Rayleigh wave by adding some layers in the crust to the previous simple model. Third, they model those short-period waveforms riding on P_n and S_n by adding some layers in upper mantle structure. Finally, they do the final adjustments by trial and error. This is a great strategy which utilizes many body-wave phases with clear physical meanings, but it requires an experienced seismologist. The second approach requires matching the surface-wave waveform. One example for this approach is linear inversion

method shown by Gomberg and Masters (1988). They use modal superposition to create synthetic seismograms and perturb them with respect to layer parameters (such as S-velocity). Using these partial derivatives, they formulate a linear inverse problem for the differential seismogram between observed and synthetic. In this study, we will develop other inversion methods for surface-waveform because this approach has the potential to be a fully automatic process. In most regions, the sparse data coverage does not support directly modeling waveform in 2-D, or 3-D structures. Therefore, the synthetic seismograms used in this study will be generated for a 1-D model using mode summation method (Wang, 1981).

Using a cross-correlation technique, Lerner-Lam and Jordan (1983) formulated an inversion algorithm to obtain earth structure from long-period teleseismic surface-wave waveforms. A successful application was presented by the same group (Lerner-Lam and Jordan 1987) on investigating the continental thickness of Eurasia. Similar to this idea, Cara and Leveque (1987) showed a slightly different way to extract the "secondary observations" and formulated an algorithm to invert these "secondary observations". They used teleseismic seismograms which have well separated fundamental mode and higher modes to ensure their success. However, seismograms show more complicated mode interference effects on the regional scale.

Gee and Jordan (1992) introduced Generalized Seismological Data Functionals theory (GSDF) to deal with surface-wave modal interference effects. In this study, an algorithm based on the GSDF theory is proposed and will be tested using an earthquake that occurred in the west Texas and was well recorded throughout North America. The comparison between GSDF and linear inversion (Gomberg and Masters 1988) will also be addressed.

Using linear inversion theory, a good starting model is necessary to guarantee the success of final convergence. It is necessary to use a global search method to ease the dependence on *apriori* information.

A second algorithm is considered. To use Genetic Algorithms (GA) in searching models which produce good surface-wave waveform fit. Hopefully, these two algorithms will provide more insight in how to build a more intelligent and robust inversion algorithm.

CHAPTER 2

DATA SET USED FOR COMPARISON

In this study, the different algorithms will be tested using the April 14, 1995 western Texas earthquake data. This earthquake is well recorded by broadband seismometers in the northern America. The currently data set is collected from IRIS (Incorporated Research Institutions for Seismology), CNSN (Canadian National Seismological Network), USGS (United States Geological Survey), UNAM, and PASSCAL experiments. The station distribution map is shown as Figure2.1, and the station information is listed on Table 2.1. In Table 2.1, the information of each station's location, azimuth, hypocenter distance, P wave first arrival polarity, takeoff angle, and whether the dispersion data used in searching Rayleigh or Love wave radiation pattern are shown.

Using these data, the different algorithms for modeling surface-waveform will be tested. Before this stage, the source parameters will be reestimated, i.e. source depth and focal mechanism. Table 2.2 lists three different source parameters which include Harvard CMT solution, USGS Sipkin's solution, and the reestimated source parameters used in this study.

Comparing USGS and Harvard CMT solution, they both have good agreement in hypocenter location and origin time. However, the focal mechanism is very different from these two solutions. From experiences, the published source depth for shallow events usually have huge uncertainty. Therefore, we simply use USGS's hypocenter location and origin time and will reestimate the focal mechanism and depth.

Table 2.1 The station informations

STA	LON	LAT	AZ	DIST	P	R	L	IH-P
ALE	-62.3500	82.5033	6.0800	6036.3398	-1	0	0	29.5
ANMO	-106.4567	34.9462	331.3424	596.7890	-3	1	1	71.0
ARC	-124.0750	40.8770	307.8156	2210.4399	0	1	0	47.6
BAR	-116.6720	32.6800	285.3669	1295.2960	0	0	1	65.2
BBB	-128.1133	52.1847	327.2636	3169.0320	0	1	1	37.0
BINY	-75.9861	42.1993	53.9871	2774.6509	0	1	1	39.9
BKS	-122.2350	37.8770	300.9237	1934.0950	-3	1	0	57.4
BMN	-117.2218	40.4315	315.6311	1689.8090	-1	1	1	60.6
CAIG	-100.2680	17.0480	167.3191	1496.1100	0	1	1	62.2
CALB	-118.6270	34.1430	290.0596	1503.6780	-5	1	0	62.1
CBKS	-99.7374	38.8140	18.1580	1004.1560	0	1	0	69.0
CCM	-91.2446	38.0557	48.9178	1408.1630	0	1	1	63.3
CEH	-79.0928	35.8908	68.1402	2340.4871	-3	0	0	43.7
CMB	-120.3850	38.0350	303.3337	1789.8700	-1	1	1	60.0
COL	-147.7933	64.9000	334.6238	4911.2661	-1	0	0	32.8
COR	-123.3032	45.5857	317.7288	2365.8679	0	1	1	42.0
CUIG	-99.1780	19.3290	159.9880	1281.2321	0	1	1	65.5
CYF	-109.8660	37.5542	324.9922	1009.3980	-1	1	1	69.0
DAWY	-139.4320	64.0530	336.5904	4525.5771	0	0	0	33.7
DGR	-117.0090	33.6500	289.7421	1345.7460	3	1	1	64.3
DLBC	-130.0272	58.4372	334.7115	3733.0969	0	1	1	35.6
DRLN	-57.5042	49.2560	47.8932	4368.4370	0	0	0	34.0
DUG	-112.8133	40.1950	324.5603	1398.2980	0	1	1	63.4
EDM	-113.3500	53.2220	345.1403	2677.0239	-1	1	1	40.3
EYMN	-91.4950	47.9460	23.9364	2208.1650	-1	1	1	47.6
FCC	-94.0870	58.7620	9.8789	3244.3350	-1	1	1	36.7
FFC	-101.9783	54.7350	1.8890	2719.7180	-1	0	0	40.1
FRB	-68.5470	63.7470	23.2040	4453.6089	-1	0	0	33.8
GAC	-75.4783	45.7033	46.8810	2962.3689	0	1	0	38.6
GAR	-114.1020	38.8808	316.9895	1373.5229	-1	1	1	63.8
GOL	-105.3711	39.7003	350.4675	1063.6190	-5	0	0	68.6
GSC	-116.8083	35.3028	297.4232	1397.5800	0	1	1	63.7
HOPS	-123.0723	38.9935	303.5273	2047.1680	0	0	0	53.9
HRV	-71.5580	42.5060	55.5348	3132.9500	0	1	1	37.3
INK	-133.5200	68.3070	343.7640	4662.9888	-1	0	0	33.4
ISA	-118.4733	35.6633	296.9282	1535.3850	0	0	0	61.8
JFWS	-90.2488	42.9149	36.0724	1823.3640	0	1	1	59.6
JRSC	-122.2376	37.4038	299.4258	1916.7350	0	0	0	57.8
LBNH	-71.9259	44.2401	51.8728	3160.6780	0	1	1	37.1
LMN	-64.8060	45.8520	51.6319	3749.1060	0	1	1	35.5
LMP	-111.1960	37.9783	321.8398	1121.4580	-1	1	1	67.9
LMQ	-70.3267	47.5483	46.3837	3406.0991	0	1	1	36.6
LSCT	-73.2244	41.6784	56.5500	2975.6770	0	1	1	38.5
MBC	-119.3600	76.2420	354.7885	5187.3291	0	0	0	32.0
MDW	-112.3570	38.8927	321.6075	1264.8280	-3	1	1	65.8
MHC	-121.6420	37.3420	299.7602	1864.6530	-1	0	0	58.9
MIAR	-93.5730	34.5457	60.0795	1032.6490	5	1	0	68.8
MIN	-121.6050	40.3450	308.9899	1997.3640	-1	1	0	55.5
MLAC	-118.8340	37.6310	303.8644	1647.0140	-3	1	1	60.9
MLC	-116.7680	38.9883	311.8189	1564.3490	-1	1	1	61.5
MNV	-118.1530	38.4328	307.6257	1634.5140	-1	0	0	61.0
NEE	-114.5960	34.8230	298.4929	1172.2111	0	1	1	67.3
NEW	-117.1200	48.2630	333.4136	2318.1299	-1	1	1	44.2
NWC	-113.5566	37.6332	313.6112	1248.7170	0	0	0	66.0
ORV	-121.5000	39.5560	306.8155	1949.1410	-1	1	1	57.0
OXIG	-96.7230	17.0820	153.8263	1606.6180	0	0	0	61.2
PAS	-118.1717	34.1483	190.9800	1462.8500	0	1	1	62.6

PFO	-116.4553	33.6092	290.0471	1294.6429	0	0	0	65.2
PGC	-123.4508	48.6500	325.7721	2660.2791	0	1	1	40.4
PH2	-114.9839	37.6645	310.4570	1352.8110	-3	1	1	64.2
PKD1	-120.4249	35.8892	295.8760	1711.1760	-1	1	0	60.5
PLIG	-99.5010	18.3890	162.7272	1370.8290	1	1	1	63.9
PMB	-123.0765	50.5188	329.3981	2786.8779	-1	1	1	39.8
PNIG	-98.1270	16.3950	159.8122	1624.5060	0	1	1	61.0
PNT	-119.6200	49.3200	331.5872	2522.8210	0	1	0	40.9
RCC	-110.5850	40.5163	331.9426	1313.9041	-1	1	1	64.8
RES	-94.9000	74.6870	317.4068	4965.4668	-1	0	0	32.6
RPV	-118.4035	33.7438	289.0763	1474.4340	-3	1	1	62.4
RTS	-115.7900	39.6681	315.9504	1541.3740	-3	1	0	61.7
SADO	-79.1417	44.7694	46.0372	2659.1970	-1	1	1	40.4
SAO	-121.4450	36.7650	298.0289	1827.4780	-3	0	0	59.5
SCHQ	-66.8336	54.8319	36.0646	3975.2800	-3	1	1	34.7
SMTC	-115.7200	32.9490	287.4082	1212.3929	0	1	0	66.7
SRS	-110.6010	38.9126	327.1899	1168.0090	-1	1	1	67.3
SSPA	-77.8914	40.6401	56.4481	2567.4299	-1	0	0	40.6
TUC	-110.7846	32.3096	289.6425	745.3420	-2	1	1	69.6
ULM	-95.8750	50.2498	13.5989	2305.5010	-2	1	1	44.6
USC	-118.2870	34.0210	290.3445	1470.1250	0	1	1	62.5
VTV	-117.3330	34.5670	293.5786	1399.8250	0	1	0	63.4
WALA	-113.9115	49.0586	339.7463	2270.9600	-1	1	1	45.5
WCP	-114.1670	40.5242	322.1671	1502.9880	-1	1	1	62.1
WDC	-122.5400	40.5800	308.5890	2079.6699	-3	1	1	52.7
WHY	-134.9906	60.6597	334.5919	4102.5229	-1	1	1	34.4
WMOK	-98.7810	34.7379	39.5295	655.0750	3	1	0	70.3
WMT	-111.8380	40.1111	327.0212	1338.3270	0	1	1	64.4
WVOR	-118.6367	42.4339	318.8431	1921.1140	-1	0	0	57.7
YBH	-122.7195	41.7318	311.4840	2154.2839	0	1	1	49.8
YKW3	-114.6050	62.5620	350.4589	3681.6750	-1	1	0	35.9
ZIIG	-101.4650	17.6070	171.9038	1414.2450	0	0	0	63.2

From stations which have source-receiver distance greater than 3600 km, it is very clear to see a general 7-9 seconds time difference between P and pP phases (Figure2.2). At such distance, the observed first arrival P is beyond the upper mantle P triplication zone which caused by upper mantle discontinuities. This means that source depth is not as shallow as suggested by Harvard and USGS solutions. For a simple crust model, such a $pP-P$ difference will correspond to an earthquake deeper than 20 kilometers.

The source mechanism used in this study is based on the grid search for Love and Rayleigh wave radiation pattern (Herrmann, 1974) using observed spectrum amplitude of fundamental mode group velocities at different frequencies. Based on the grid search for focal mechanism at different source depths, the optimum result is a point source at 23 km in depth, with strike, dip, rake as (114°, 64°, -101°), and with seismic moment 3.0E24 dyne-cm.

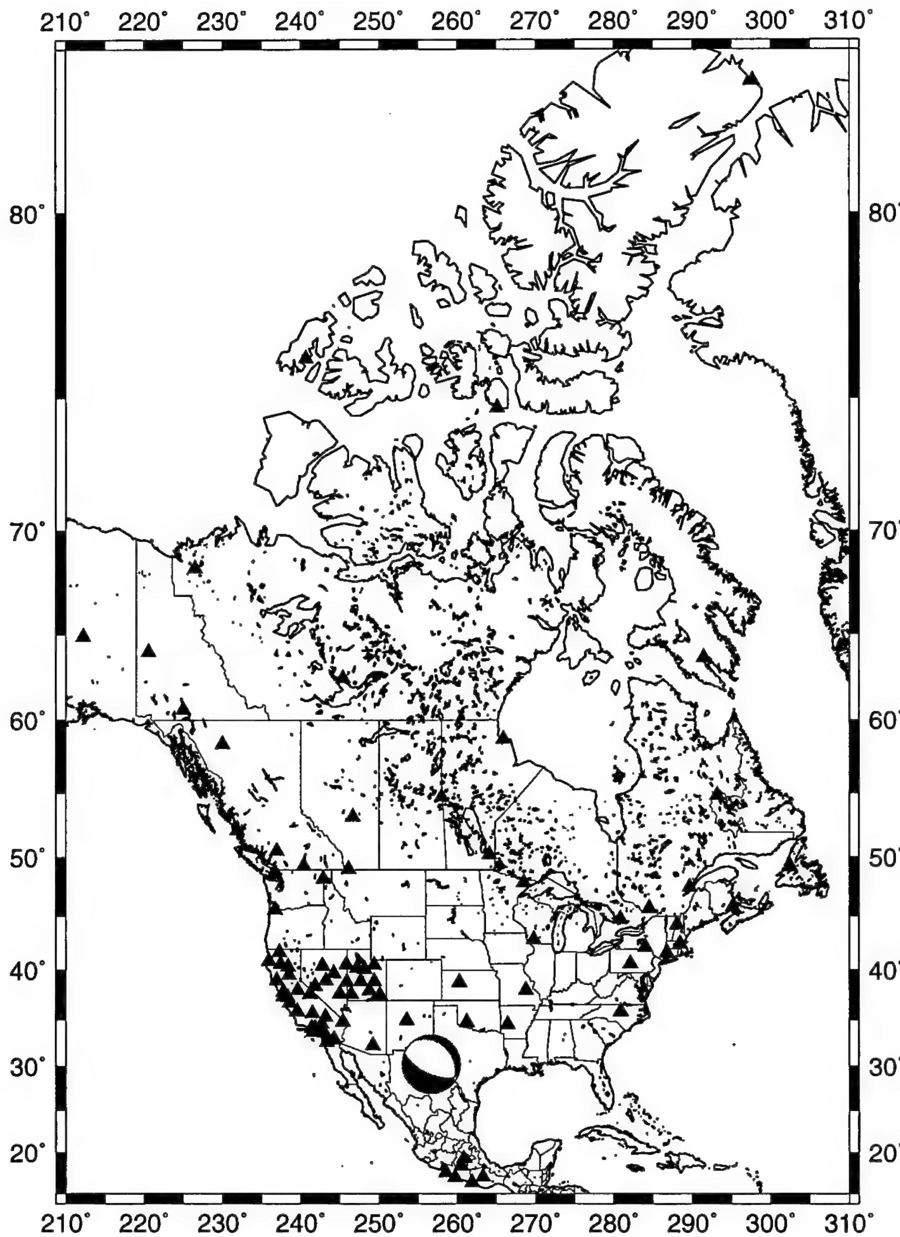

Fig. 2.1. Station distribution map. The stations are shown as triangles. The focal mechanism used in this study is shown as the beach ball. This map is generated using GMT (Wessel and Smith, 1991)

From the station distribution map (figure 2.1), we can see that most of broadband stations are in the western United States. The

Table 2.2 Source parameters for different solutions

	Lon	Lat	Depth	Origin Time	Strike	Dip	Rake	moment
HARVARD	-103.32	30.24	15.0	00:32:54.2	117	53	-87	3.82E24
USGS	-103.327	30.261	13.0	00:32:55.04	136	60	-86	4.00E24
this study	-103.327	30.261	23.0	00:32:55.04	114	64	-101	3.00E24

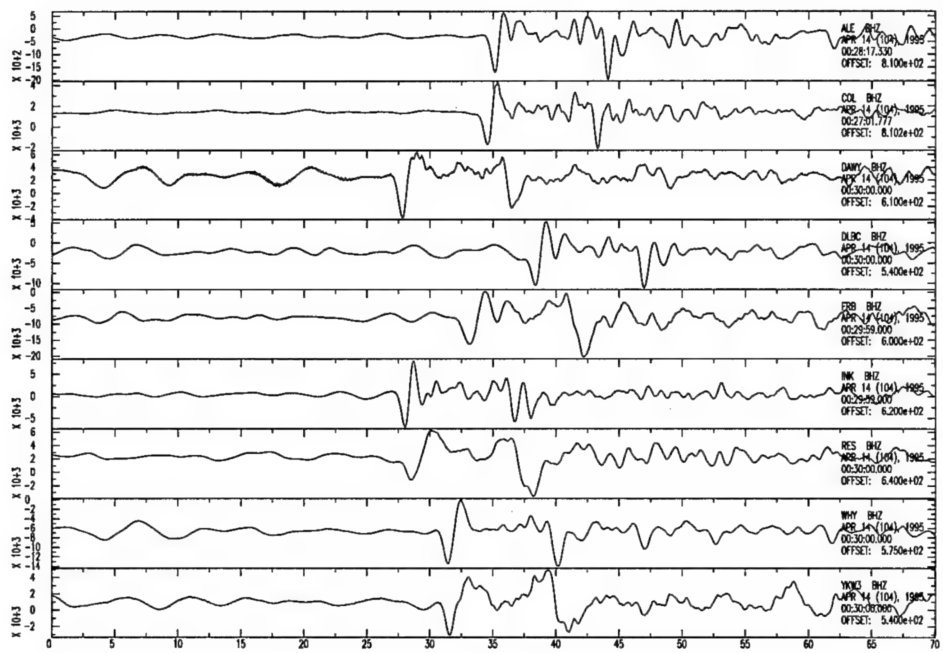

Fig. 2.2. For teleseismic records, a general 7-9 seconds travel time difference for *pP-P* is observable.

second best cover region is the northeast United States. The fundamental mode Rayleigh and Love wave spectrum amplitudes used in radiation pattern search also have more dense data points in these two regions. Looking at the observed spectrum amplitude data, it delineates a clear nodal plane for Love wave radiation pattern. All three

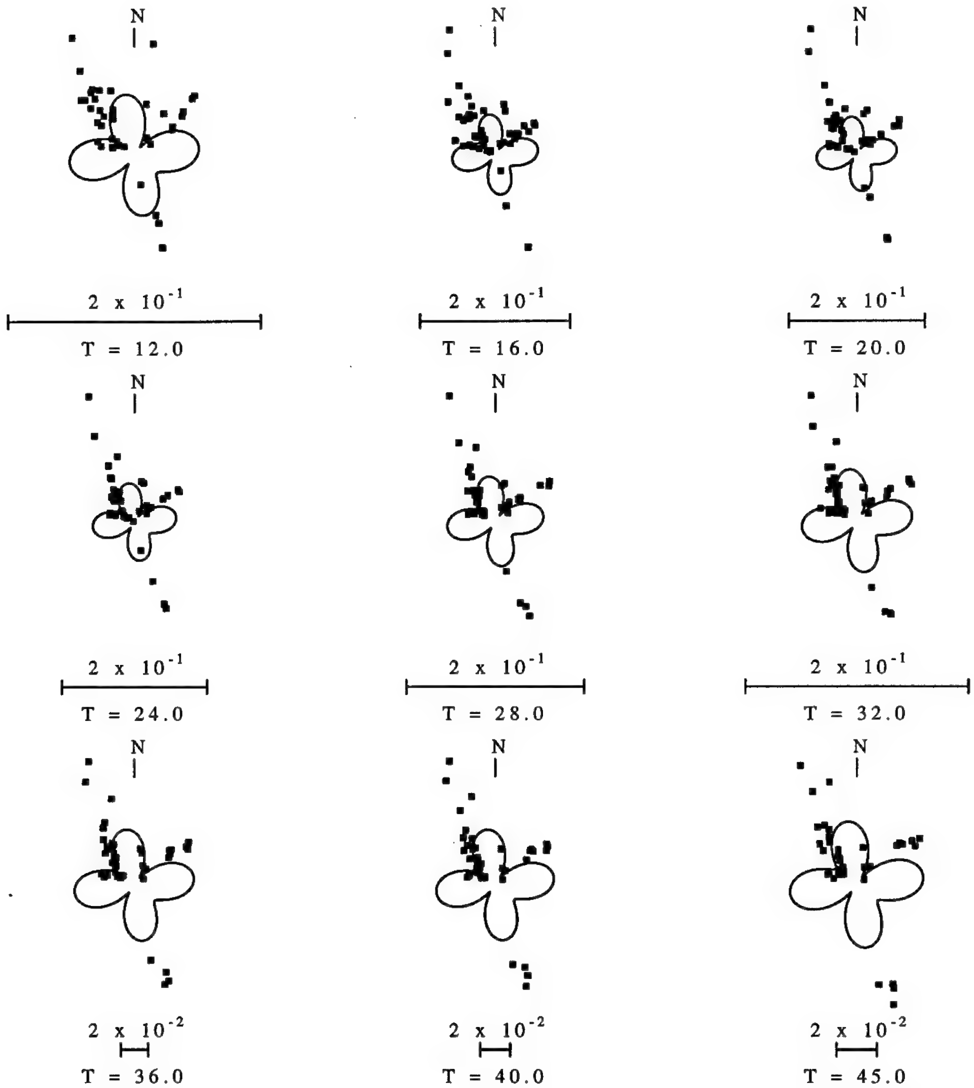

Fig. 2.3. The Love wave radiation patterns for the preferred focal mechanism at 23 km depth. The bars indicate attenuation corrected spectral amplitudes in cm-sec normalized for geometrical spreading to 1000 km.

solutions can provide good Love wave radiation pattern to match the observed data. But from Rayleigh wave radiation pattern fit, the reestimated focal mechanism is better than other solutions. For comparison, figure 2.3, 2.4, and 2.5 will show the Love wave radiation pattern at nine periods for the mechanism used in this study, Harvard CMT solution, and USGS Sipkin's solution. Similar to Love wave, Figure 2.6, 2.7, and 2.8 will display the Rayleigh wave radiation patterns.

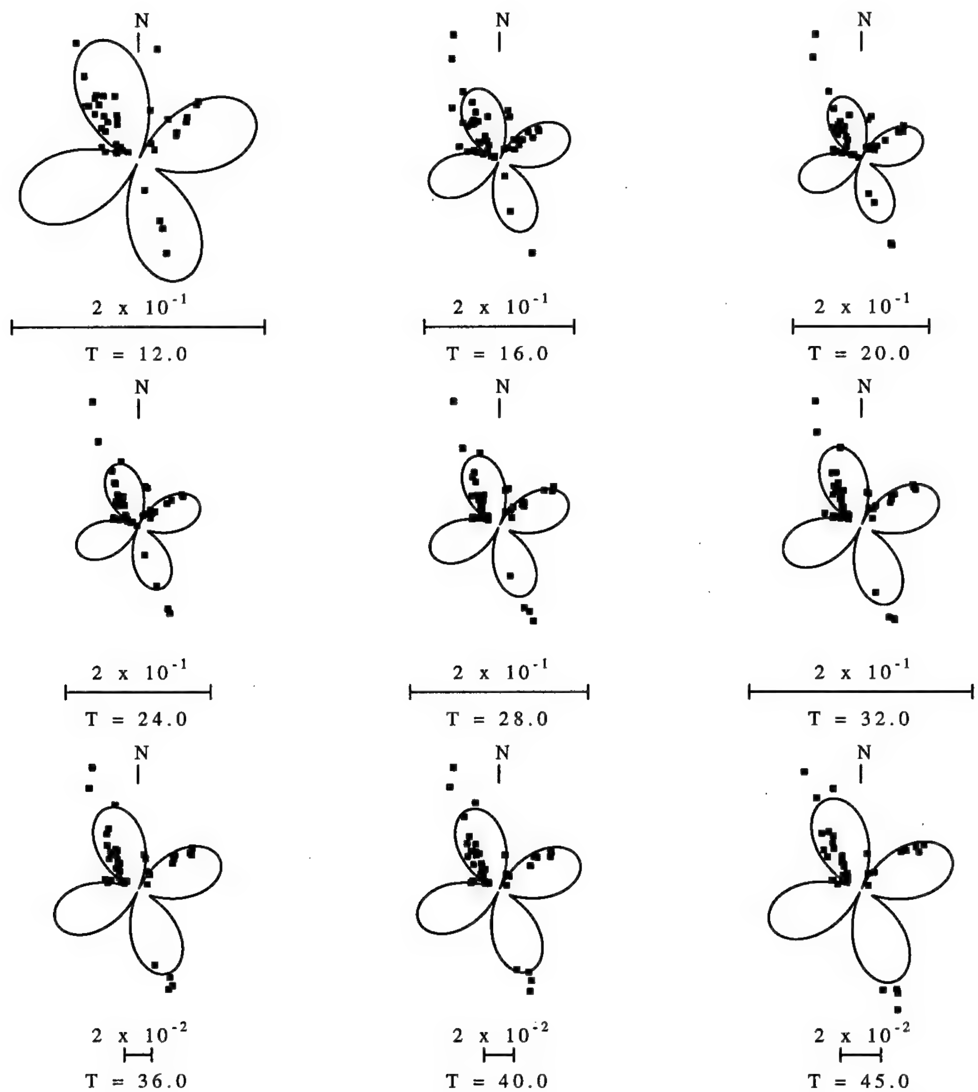

Fig. 2.4. The Love wave radiation patterns for Harvard CMT solution at 15 km depth.

P-wave polarities provide another property to check the focal mechanisms. The P-wave polarity reading is shown in table 2.1. The negative number indicates the downward movement, and the positive number indicates the upward movement. The number 1 indicates a impulsive P-wave arrival; the larger numbers indicate the emergent arrivals with less confident. The P-wave polarities for these three focal mechanisms are shown as figure 2.9, 2.10, and 2.11. In these

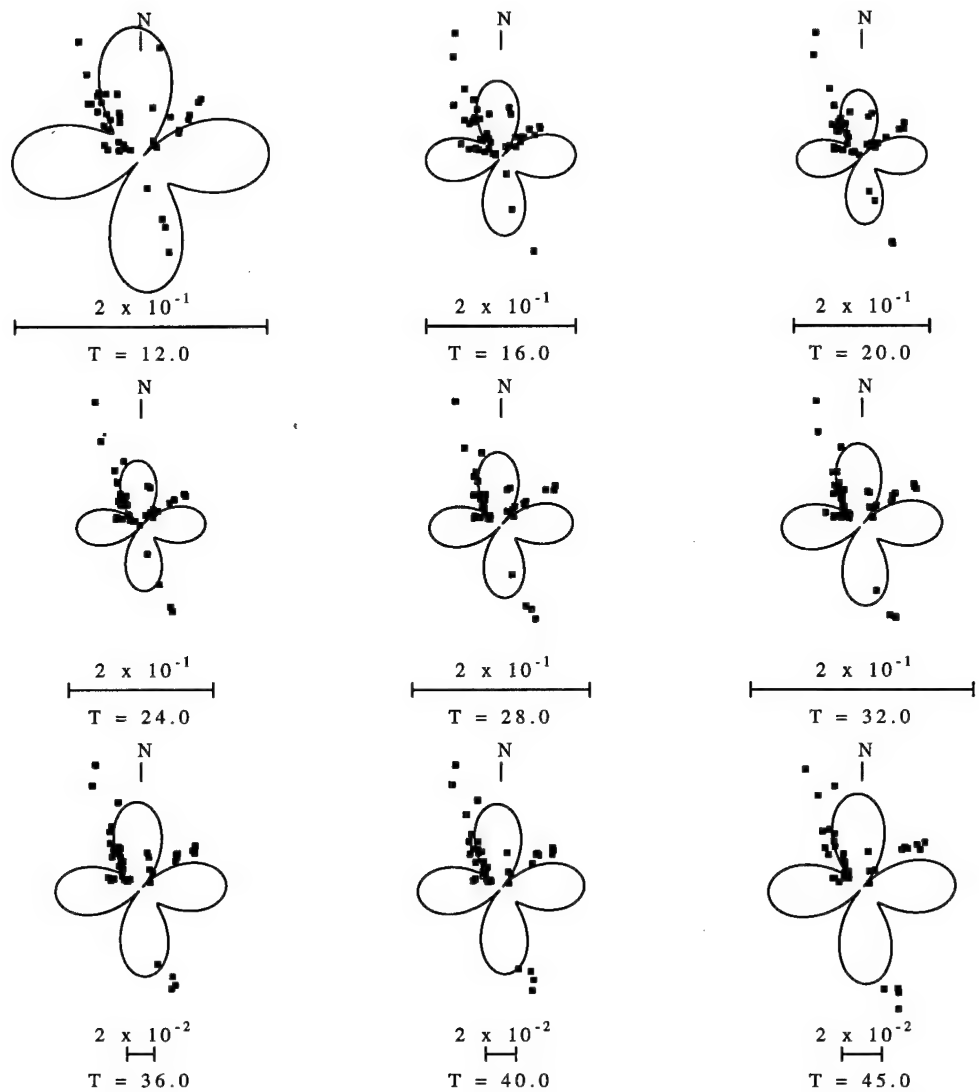

Fig. 2.5. The Love wave radiation patterns for Sipkin's USGS solution at 13 km depth.

figures, the cycles represent the impulsive upward P arrivals while the plus signs represent the emergent upward P arrivals; in the similar way, the triangle represent the impulsive downward P arrivals and the minus signs are for the emergent downward P arrivals. The reestimated focal mechanism which have only one inconsistent station is better than the other two solutions.

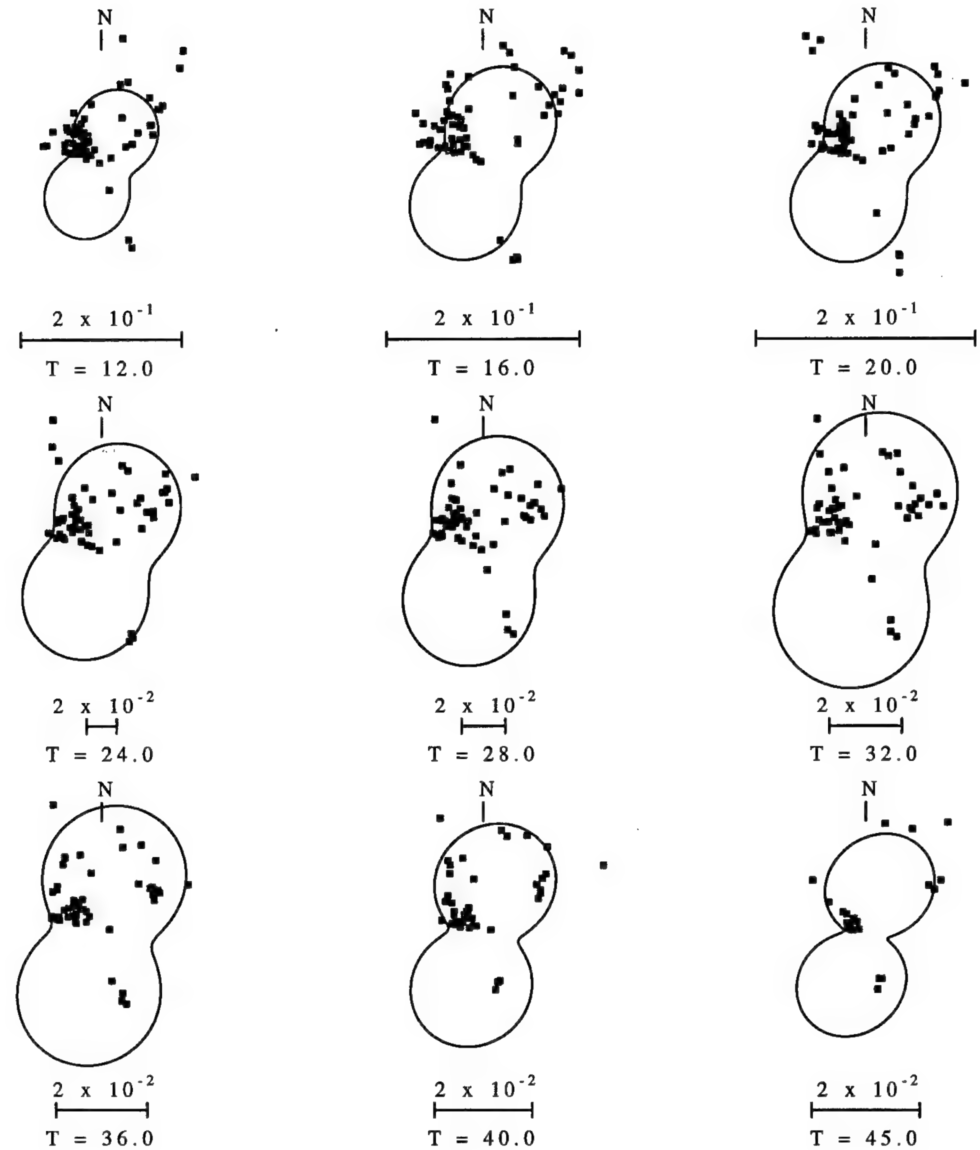

Fig. 2.6. The Rayleigh wave radiation patterns for the preferred focal mechanism at 23 km depth.

From all these comparisons, the depth phases, Rayleigh and Love wave radiation patterns, and the first arrival P wave polarities, we are sure that the reestimated focal mechanism is better than the others.

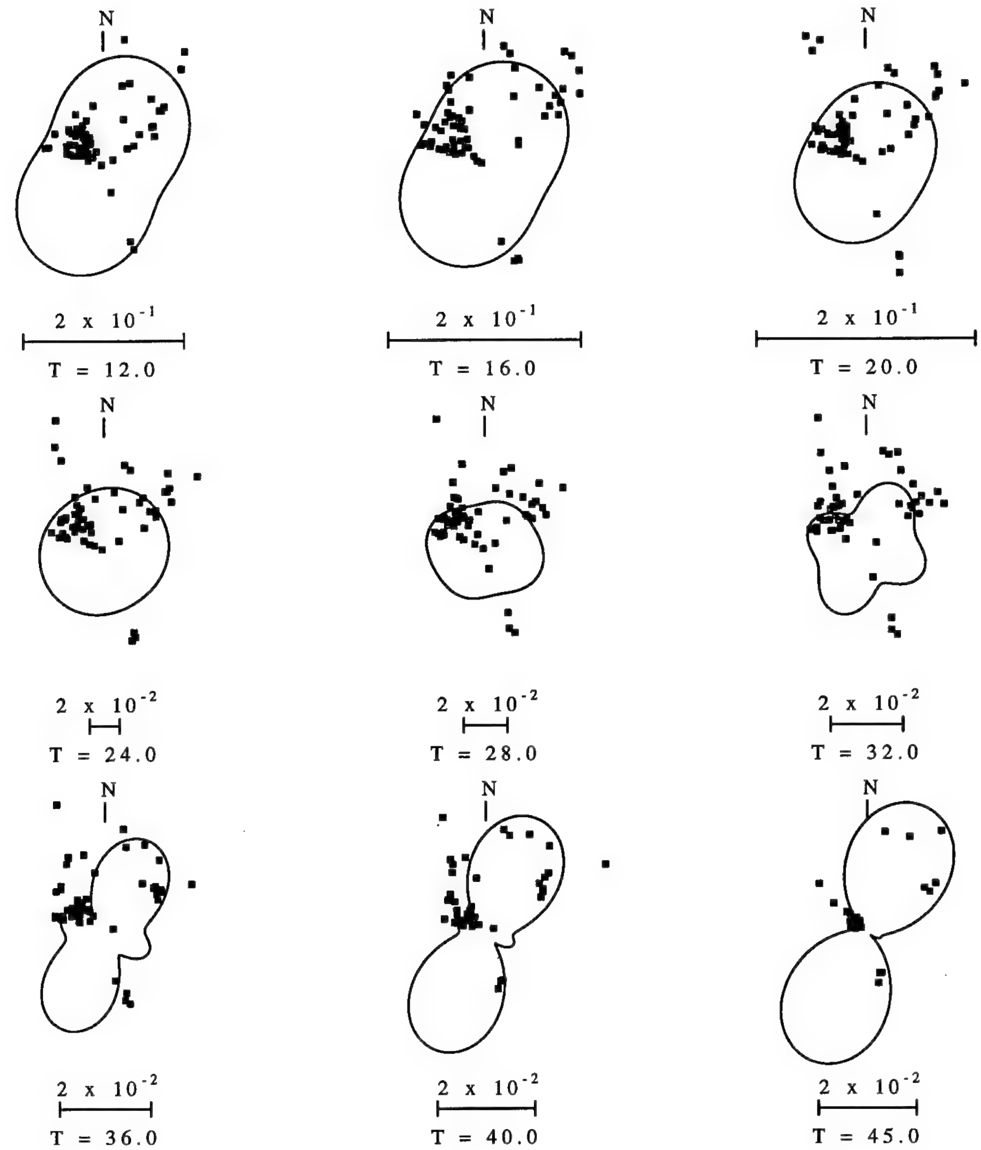

Fig. 2.7. The Rayleigh wave radiation patterns for Harvard CMT solution at 15 km depth.

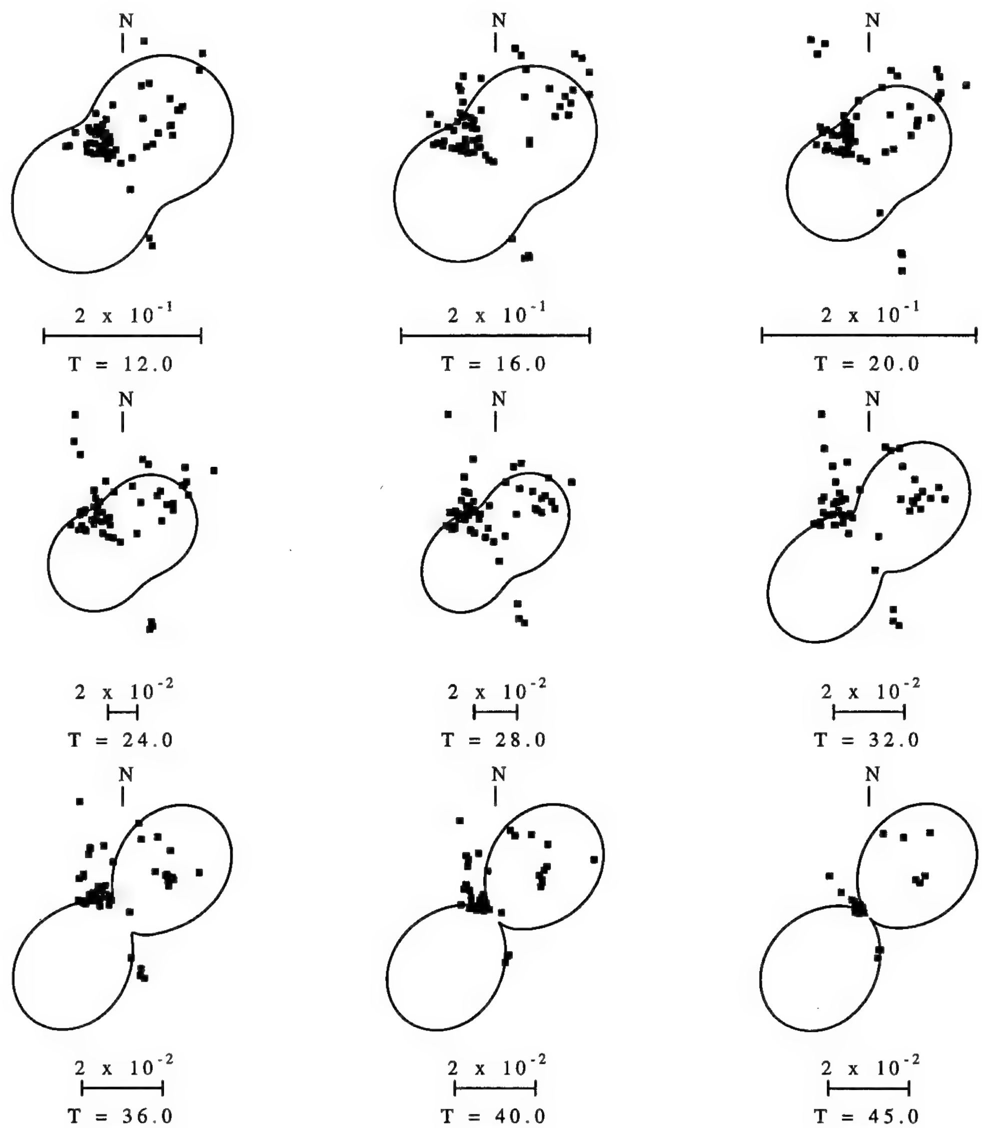

Fig. 2.8. The Rayleigh wave radiation patterns for Sipkin's USGS solution at 13 km depth.

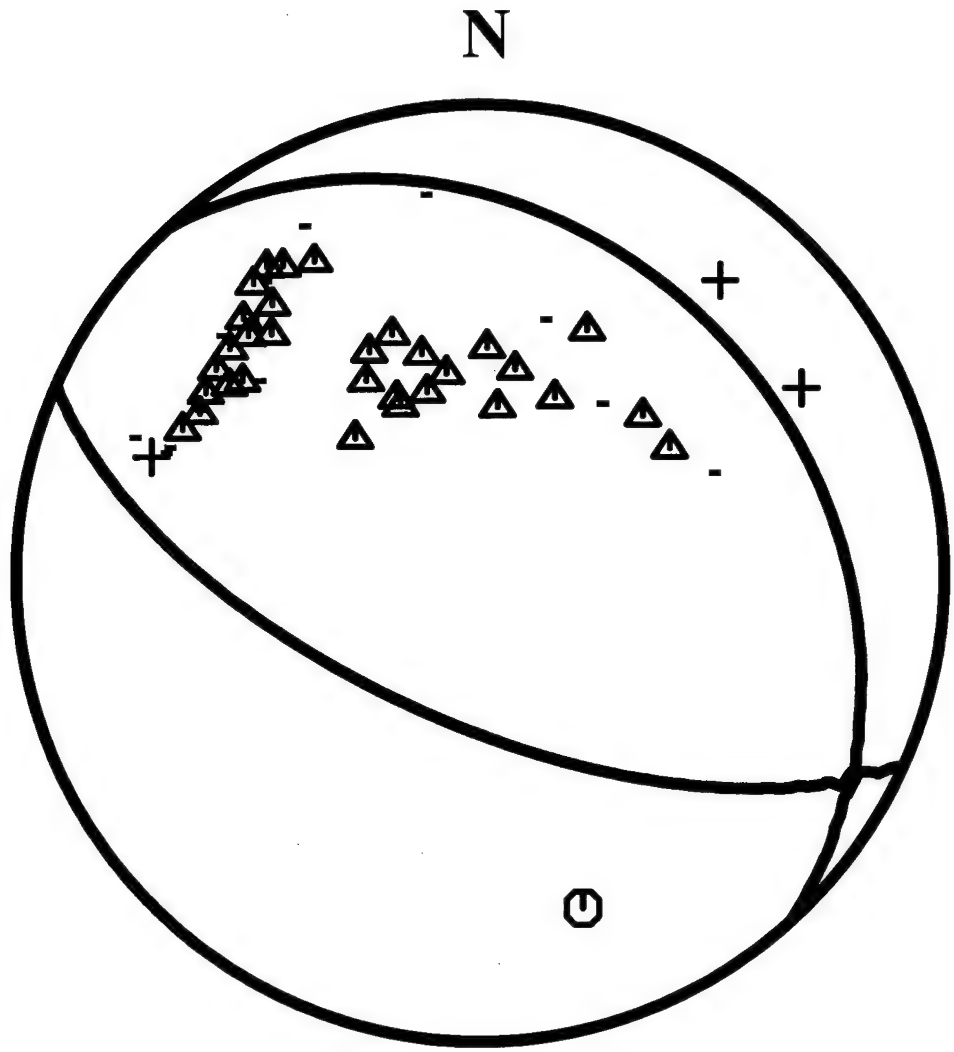

Fig. 2.9. This figure shows the observed P-wave polarities and the reestimated focal mechanism which will be used for testing several surface-waveform modeling algorithms.

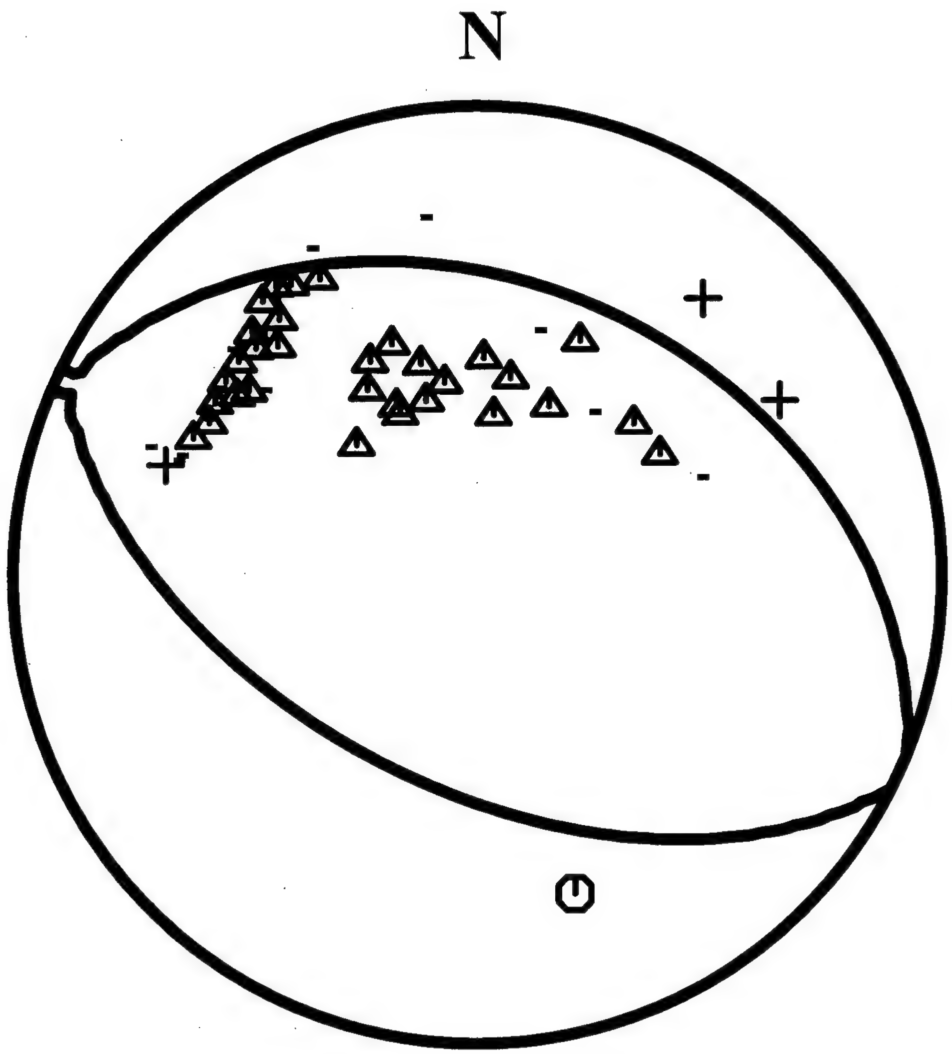

Fig. 2.10. This figure shows the focal mechanism of Harvard CMT solution and the observed P-wave polarities.

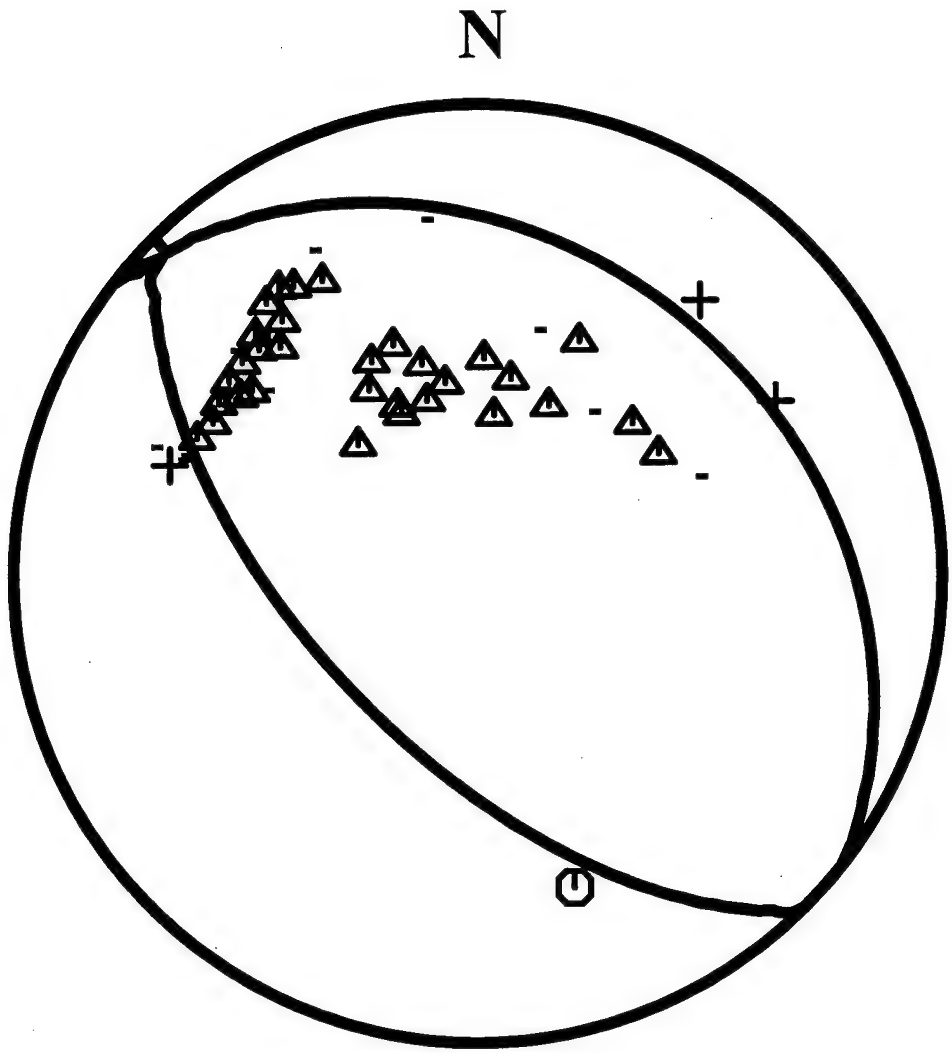

Fig. 2.11. This figure shows the focal mechanism of Sipkin's USGS solution and the observed P-wave polarities.

CHAPTER 3

REVIEW OF GSDF THEORY AND FORMULATE STRUCTURE INVERSION ALGORITHM USING GSDF

3.1 Introduction

After successful observing the apparent anisotropy of Eurasian upper mantle (Gee and Jordan, 1988), Gee and Jordan (1992) introduced the theory of Generalized Seismological Data Functionals (GSDF) which deals with the interference effects of different surface wave modes at a certain frequency. This theory allow seismologists to precisely measure the group and phase delays between observed and synthetic seismograms for different frequencies even when the modal interference effect can not be ignored. The applications have been reported by Gaherty *et al.* (1995, 1996) who use this method to invert the upper mantle velocity structure and anisotropy. In this study, we extend the Generalized Seismological Data Functionals (GSDF) theory to the inversion of broadband waveforms modeled as a superposition of surface-wave modes (Wang, 1981). We demonstrate the utility of this inversion algorithm by conducting a simple synthetic test, and then apply the algorithm to real data to see what new knowledge about earth structure can be obtained from this new inversion algorithm.

3.2 Theory of Generalized Seismological Data Functionals

To use the GSDF approach, we need to construct a synthetic seismogram ($\tilde{s}$), an isolation function ($\tilde{f}$) and single-mode seismograms.

An isolation function is a sum of single-mode seismograms which may represent the dominant part of the observed seismogram (s). Using a cross-correlation technique, we can quantify the similarity observed and synthetic seismograms. For a model which does not significantly deviate from actual earth structure, the peak of cross-correlagrams will be located near zero lag-time for all frequency bands and for all windowed segments of the seismograms. The cross-correlagrams reflect the degree that the model used to create synthetic seismogram, isolation function and single-mode seismograms is different from real earth structure. To utilize this information, we have to extract information from different frequency ranges and interpret it in term of differences in earth structure.

Gee and Jordan (1992) call the extracted information Generalized Seismological Data Functionals (GSDF). In the following, we give a brief review of how the GSDF is defined, how the GSDF is related to familiar physical quantities, and how we extend this theory to invert for Earth structure. Equations directly adapted from Gee and Jordan (1992) will be cited as (GJ.#), where # indicates the original equation number in their paper.

First, we review the definition and computation of a GSDF. We can use a Gaussian wavelet to approximate the filtered and windowed cross-correlagrams at a specified frequency. Specifically, the windowed, filtered cross-correlagram of an isolation function with a seismogram (either observed or synthetic) is modeled using a five-parameter Gaussian wavelet:

$$\mathbf{F}_i\mathbf{W}\mathbf{C}_{fs}(t) \approx g(t) \equiv A\mathrm{Ga}[\sigma_s(t-t_g)]\cos[\omega_s(t-t_p)] \tag{GJ.5}$$

$$\mathbf{F}_i\mathbf{W}\tilde{\mathbf{C}}_{fs}(t) \approx \tilde{g}(t) \equiv \tilde{A}\mathrm{Ga}[\tilde{\sigma}_s(t-\tilde{t}_g)]\cos[\tilde{\omega}_s(t-\tilde{t}_p)] \tag{GJ.8}$$

$$\mathbf{F}_i\mathbf{W}\tilde{\mathbf{C}}_{ff}(t) \equiv \mathrm{Ga}[\tilde{\sigma}_f t]\cos[\tilde{\omega}_f t]$$

where

$\mathbf{F}_i$ is a Gaussian frequency content filter with center frequency ω_i and half-bandwidth σ_i,

$\mathbf{W} = \mathrm{Ga}[\sigma_w(t - t_w)]\left\{1 + 0.01[\sigma_w(t - t_w)]^4 - \cdots\right\}$ is a temporal window with half-bandwidth $\sigma_w$and centered at t_w; usually $t_w = t_c$, where t_c is the lag-time of the peak of $\mathbf{F}_i\mathbf{W}\mathbf{C}_{ff}$,

$\mathbf{C}_{fs}(t) \equiv \tilde{f}(t) \otimes s(t)$, $\otimes$ represents cross-correlation, is the cross-correlation with the observed time history,

$\tilde{\mathbf{C}}_{fs}(t) \equiv \tilde{f}(t) \otimes \tilde{s}(t)$, is the cross-correlation with the synthetic time history,

$\mathrm{Ga}[x] \equiv \exp(-\frac{x^2}{2})$, Ga is the Gaussian function,

A is the amplitude of Gaussian envelope,

σ is the half-bandwidth of envelope spectrum,

ω is the angular frequency of oscillating wavelet,

t_g is the envelope group delay from zero lag-time,

t_p is the wavelet phase delay from zero lag-time,

the subscript s denotes observed seismogram, subscript s combined with ~ denotes synthetic seismogram, and the subscript f with ~ denotes isolation filter.

From (GJ.5) and (GJ.8), Gee and Jordan define four data functionals to characterize the agreement between observed and predicted time histories:

$$\delta t_p = t_p - \tilde{t}_p \tag{GJ.9}$$

$$\delta t_g = t_g - \tilde{t}_g \tag{GJ.10}$$

$$\delta t_q = -\frac{1}{\tilde{\omega}_s}[\ln A - \ln \tilde{A}] \tag{GJ.11}$$

$$\delta t_a = -\frac{1}{\tilde{\sigma}_s^2}[\omega_s - \tilde{\omega}_s] \tag{GJ.12}$$

These four data functionals are related to differential phase delay, differential group delay, differences in logarithmic amplitudes and the differences in center frequencies. These four data functionals are defined from two filtered, windowed cross-correlagrams, they can be transformed into the more familiar quantities such as phase velocity, group velocity, and attenuation corrections.

We will briefly describe this transformation. We note that all filtered and windowed cross-correlagrams will be normalized by scaling $\mathbf{F}_i\mathbf{W}\tilde{\mathbf{C}}_{ff}$ to unit amplitude. Also, if the observed and synthetic seismograms are composed only of a single mode, then the GSDF are easily interpreted in terms of differences in modeled and actual phase velocity, group velocity and Q. For multi-mode time histories there interpretation is much more difficult.

Before relating GSDF to physical quantities, we must know the roles these quantities play in wave propagation. For a known instrument response and source, the difference between the spectrum of isolation filter $\tilde{f}(\omega) = I(\omega)\tilde{P}(\omega)S(\omega)$ and its corresponding component of the observed seismograms $f(\omega) = I(\omega)P(\omega)S(\omega)$ is called "differential propagation". They are related by the equation

$$
\begin{aligned}
f(\omega) &= \frac{P(\omega)}{\tilde{P}(\omega)}\tilde{f}(\omega) \\
&= D(\omega)\tilde{f}(\omega) \qquad \text{(GJ.42)} \\
&= e^{i\delta k(\omega)R}\tilde{f}(\omega) = e^{i[k(\omega)-\tilde{k}(\omega)]R}\tilde{f}(\omega)
\end{aligned}
$$

where R is source-receiver distance. To a first order approximation, the differential propagation can be approximated as

$$
\begin{aligned}
D(\omega) \approx \exp\left(-\omega_j\delta\tau_q(\omega_j) - (\omega-\omega_j)\delta\tau_a(\omega_j)\right) \qquad \text{(GJ.44)} \\
+\exp\left(i\left[\omega_j\delta\tau_p(\omega_j) + (\omega-\omega_j)\delta\tau_q(\omega_j)\right]\right)
\end{aligned}
$$

The propagation effects of the isolation filter $\tilde{f}(t)$ and the

corresponding waveform $f(t)$ on the observed seismogram are defined in four equations which are described in terms of familiar physical quantities such as total phase delay, total group delay, and attenuation factor.

$$\delta\tau_p(\omega_j) \equiv \tau_p(\omega_j) - \tilde{\tau}_p(\omega_j) \tag{GJ.45}$$

$$\delta\tau_g(\omega_j) \equiv \tau_g(\omega_j) - \tilde{\tau}_g(\omega_j) \tag{GJ.46}$$

$$\delta\tau_q(\omega_j) \equiv \frac{1}{2}\,\tilde{\tau}_p(\omega_j)[Q^{-1} - \tilde{Q}^{-1}] \tag{GJ.47}$$

$$\delta\tau_a(\omega_j) \equiv \frac{1}{2}\,\tilde{\tau}_g(\omega_j)[Q^{-1} - \tilde{Q}^{-1}] \tag{GJ.48}$$

where

$\tau_p(\omega_j)$ is total phase delay of $f(t)$ at an arbitrary frequency ω_j with respect to the original time,

$\tilde{\tau}_p(\omega_j)$ is total phase delay of $\tilde{f}(t)$ at ω_j,

$\tau_g(\omega_j)$ is total group delay of $f(t)$ at ω_j,

$\tilde{\tau}_g(\omega_j)$ is total group delay of $\tilde{f}(t)$ at ω_j,

Q is attenuation factor of $f(t)$,

$\tilde{Q}^{-1}$ is attenuation factor of $\tilde{f}(t)$.

This means that whenever we are able to measure four differential quantities $\delta\tau_x$ from observed and synthetic seismograms at a certain frequency ω_j, we can approximate the true waveform spectrum behavior $f(\omega)$ at any arbitrary frequency ω to a first order precision.

The GSDF δt_x based on the filtered, windowed cross-correlation, and the $\delta\tau_x$ is related to the time domain windowing function. Their relationships are given by

$$\delta t_g \approx \delta\tau_g(\tilde{\omega}_f) + (1 - \xi_1^2)[t_c - \delta\tau_g(\tilde{\omega}_f)] \tag{GJ.56}$$

$$\delta t_p \approx \delta\tau_p(\tilde{\omega}_f) + (1 - \xi_1^2)\left(\frac{\tilde{\omega}_f - \tilde{\omega}_c}{\tilde{\omega}_f}\right)[t_c - \delta\tau_g(\tilde{\omega}_f)] \tag{GJ.57}$$

$$\delta t_a \approx \xi_1^2 \delta\tau_a(\tilde{\omega}_f) \tag{GJ.58}$$

$$\delta t_q \approx \delta\tau_q(\tilde{\omega}_f) - (1-\xi_1^2)(\frac{\tilde{\omega}_f - \tilde{\omega}_c}{\tilde{\omega}_f})\delta\tau_a(\tilde{\omega}_f) \tag{GJ.59}$$

where

$\tilde{\omega}_c$ is the frequency from $\tilde{\mathbf{C}}_{ff}$,

ξ_1 is a window width factor,

t_c is the lag-time of the peak of cross-correlagram $\mathbf{F}_i\mathbf{W}\mathbf{C}_{ff}$.

There is an additional assumption that must be stated. Due to the difficulty in relating the isolation filter's corresponding feature in observed seismogram, it is not easy to evaluate $\mathbf{F}_i\mathbf{W}\mathbf{C}_{ff}$. However, if the windowing procedure is effective in isolating $f(t)$ from other phases on the seismograms, then $\mathbf{F}_i\mathbf{W}\mathbf{C}_{fs} \approx \mathbf{F}_i\mathbf{W}\mathbf{C}_{ff}$.

We can estimate t_c from an isolated waveform. For non-isolated waveforms, the $\mathbf{C}_{ff}$ can not be simply replaced by $\mathbf{C}_{fs}$ and this is more general situation. For non-isolated waveforms, the Gaussian wavelet can be represented as a sum of interference effects of different modes.

$$\mathbf{F}_i\mathbf{W}\tilde{\mathbf{C}}_{fs}(t) = \sum_{m=1}^{N}\sum_{n=1}^{N} \mathbf{F}_i\mathbf{W}\tilde{\mathbf{C}}_{mn}(t) \tag{GJ.63}$$

$$\mathbf{F}_i\mathbf{W}\mathbf{C}_{fs}(t) = \sum_{m=1}^{N}\sum_{n=1}^{N} \mathbf{F}_i\mathbf{W}\mathbf{C}_{mn}(t)$$

where

$\mathbf{C}_{mn}(t) \equiv [mode\ m\ of\ \tilde{f}(t)] \otimes [mode\ n\ of\ f(t)]$,

$\tilde{\mathbf{C}}_{mn}(t) \equiv [mode\ m\ of\ \tilde{f}(t)] \otimes [\ mode\ n\ of\ \tilde{f}(t)]$.

We now characterize these by the relation

$$\mathbf{F}_i\mathbf{W}\tilde{\mathbf{C}}_{mn}(t) \approx \tilde{A}_{mn}\mathrm{Ga}[\tilde{\sigma}_f(t-\tilde{t}_g^{mn})]\cos[\tilde{\omega}_{mn}(t-\tilde{t}_p^{mn})] \tag{GJ.68}$$

where

$\tilde{A}_{mn} \equiv exp(-\tilde{\omega}_f \tilde{t}_q^{mn})$,

$$\tilde{\omega}_{mn} \equiv \tilde{\omega}_f - \tilde{\sigma}_f \tilde{t}_a^{mn}.$$

In this case, we need to know four time shifts that describe the deviations of $\mathbf{F}_i\mathbf{W}\tilde{\mathbf{C}}_{fs}$ from $\mathbf{F}_i\mathbf{W}\tilde{\mathbf{C}}_{ff}$. Assume that the windowing and filtering effectively suppress the bandwidth variations, so that $\tilde{\sigma}_s \approx \tilde{\sigma}_f$. The four time shifts are the phase delay $\tilde{t}_p$, a group delay $\tilde{t}_g$, and two amplitude parameters

$$\tilde{t}_q = -\frac{1}{\tilde{\omega}_f} \ln \tilde{A} \tag{GJ.60}$$

$$\tilde{t}_a = -\frac{1}{\tilde{\sigma}_f^2} [\tilde{\omega}_s - \tilde{\omega}_f] \tag{GJ.61}$$

By defining the following notation,

$$B_{mn} = \frac{1}{2\pi_{1/2}} \exp[-\tilde{\omega}_f(\tilde{t}_q^{mn} - \tilde{t}_q)] \mathrm{Ga}[\tilde{\sigma}_f(\tilde{t}_g^{mn} - \tilde{t}_g)] \tag{GJ.73}$$

$$\phi_{mn} = (\tilde{\omega}_f - \tilde{\sigma}_f^2 \tilde{t}_a^{mm})(\tilde{t}_p^{mn} - \tilde{t}_p) - \tilde{\sigma}_f^2(\tilde{t}_a^{mn} - \tilde{t}_a)(\tilde{t}_p - \tilde{t}_g) \tag{GJ.74}$$

the perturbation expansions can be simplified by using a set $N \times N$ matrices

$$(\mathbf{C})_{mn} = B_{mn} \cos \phi_{mn} \tag{GJ.75}$$

$$(\mathbf{S})_{mn} = B_{mn} \sin \phi_{mn} \tag{GJ.76}$$

$$(\mathbf{C_x})_{mn} = B_{mn} \tilde{\omega}_f (\tilde{t}_x^{mn} - \tilde{t}_x) cos \phi_{mn} \tag{GJ.77}$$

$$(\mathbf{S_x})_{mn} = B_{mn} \tilde{\omega}_f (\tilde{t}_x^{mn} - \tilde{t}_x) sin \phi_{mn} \tag{GJ.78}$$

Gee and Jordan (1992) gave the following linearized relationships between the GSDFs and computable quantities from individual mode branches.

$$\delta t_q = \mathbf{1} \cdot \mathbf{C} \cdot \delta \mathbf{t_q} + \mathbf{1} \cdot \mathbf{S} \cdot \delta \mathbf{t_p} \tag{GJ.84}$$

$$\delta t_p = -\mathbf{1} \cdot \mathbf{S} \cdot \delta \mathbf{t_q} + \mathbf{1} \cdot \mathbf{C} \cdot \delta \mathbf{t_p} \tag{GJ.85}$$

$$\delta t_a = -\mathbf{1} \cdot (\mathbf{C_a} + \mathbf{S_g}) \cdot \delta \mathbf{t_q} + \mathbf{1} \cdot (\mathbf{C_g} - \mathbf{S_a}) \cdot \delta \mathbf{t_p} \tag{GJ.86}$$

$$+\mathbf{1}\cdot\mathbf{C}\cdot\delta\mathbf{t_a}+\mathbf{1}\cdot\mathbf{S}\cdot\delta\mathbf{t_g}$$

$$\delta t_g=-\mathbf{1}\cdot(\mathbf{C_g}-\mathbf{S_a})\cdot\delta\mathbf{t_q}-\mathbf{1}\cdot(\mathbf{C_a}+\mathbf{S_g})\cdot\delta\mathbf{t_p} \tag{GJ.87}$$

$$-\mathbf{1}\cdot\mathbf{S}\cdot\delta\mathbf{t_a}+\mathbf{1}\cdot\mathbf{C}\cdot\delta\mathbf{t_g}$$

The $\mathbf{1}$ is a N-dimension vector, each element of which equals one. The $\delta\mathbf{t_x}$ is a N-vector whose n'th component is δt_x^n, the perturbation corresponding to the quantity x of n'th mode. In the following section, we will translate this $\delta\mathbf{t_x}$ into $\delta\tau_\mathbf{x}$ which directly relate to seismogram and has clear physical meaning.

3.3 Structure Inversion

To apply GSDF theory in structure inversion, we must construct the inversion kernel, $\mathbf{G}$ for our inversion. The inverse problem can be simply expressed in the form :

$$\delta\tau_\mathbf{x}=\mathbf{G_x}\cdot\delta\mathbf{m}$$

where

$\mathbf{x}$ indicates one of $\{\mathbf{p},\mathbf{g},\mathbf{q},\mathbf{a}\}$.

$\delta\tau_\mathbf{x}$ is an N-vector for corresponding to N modes,

$\mathbf{G_x}$ is an $N\times k$ Frechet kernel matrix for structural inverse problem,

$\delta\mathbf{m}$ is a model correction vector for k unknowns.

Keep in mind, that $\delta\tau_x$ is not measurable but fortunately GSDF theory provides a way to compute these nonmeasurable quantities using the mode interference relationship. Thus, in actual application of GSDF theory, we must relate $\delta\tau_\mathbf{x}$ to $\delta\mathbf{t_x}$ to create the kernel $\mathbf{G_x}$.

From (GJ.56-59), we can transform $\delta\tau_\mathbf{x}$ to $\delta\mathbf{t_x}$ as

$$\delta\mathbf{t_g}=\delta\tau_\mathbf{g}(\tilde\omega_f)+(1-\xi_1^2)[t_c\mathbf{1}-\delta\tau_\mathbf{g}(\tilde\omega_f)]$$

$$\delta \mathbf{t_p} = \delta \boldsymbol{\tau}_{\mathbf{p}}(\tilde{\omega}_f) + a[t_c \mathbf{1} - \delta \boldsymbol{\tau}_{\mathbf{g}}(\tilde{\omega}_f)]$$

$$\delta \mathbf{t_a} = \xi_1^2 \delta \boldsymbol{\tau}_{\mathbf{a}}(\tilde{\omega}_f)$$

$$\delta \mathbf{t_q} = \delta \boldsymbol{\tau}_{\mathbf{q}}(\tilde{\omega}_f) - a \delta \boldsymbol{\tau}_{\mathbf{a}}(\tilde{\omega}_f)$$

where $a = (1 - \xi_1^2)(\frac{\tilde{\omega}_f - \tilde{\omega}_c}{\tilde{\omega}_f})$. Substituting these into (GJ.84-87) gives the following equations which relate the four GSDFs to inversion kernels $\mathbf{G_x}$.

$$\delta t_p = \mathbf{1} \cdot \mathbf{C} \cdot \mathbf{1} a\, t_c + \mathbf{1} \cdot \Big[\mathbf{C}(\mathbf{G_p} - a\mathbf{G_g}) - \mathbf{S}(\mathbf{G_q} - a\mathbf{G_a}) \Big] \cdot \delta \mathbf{m}$$

$$\delta t_q = \mathbf{1} \cdot \mathbf{S} \cdot \mathbf{1} a\, t_c + \mathbf{1} \cdot \Big[\mathbf{C}(\mathbf{G_q} - a\mathbf{G_a}) + \mathbf{S}(\mathbf{G_p} - a\mathbf{G_g}) \Big] \cdot \delta \mathbf{m}$$

$$\delta t_a = \mathbf{1} \cdot (\mathbf{C_g} - \mathbf{S_a}) \cdot \mathbf{1} a\, t_c + \mathbf{1} \cdot \mathbf{S} \cdot \mathbf{1}(1 - \xi_1^2) t_c$$

$$+ \mathbf{1} \cdot \Big[-(\mathbf{C_a} + \mathbf{S_g})(\mathbf{G_q} - a\mathbf{G_a}) + (\mathbf{C_g} - \mathbf{S_a})(\mathbf{G_p} - a\mathbf{G_g}) \Big] \cdot \delta \mathbf{m}$$

$$+ \mathbf{1} \cdot \Big[\xi_1^2 \mathbf{C} \mathbf{G_a} + \xi_1^2 \mathbf{S} \mathbf{G_g} \Big] \cdot \delta \mathbf{m}$$

$$\delta t_g = -\mathbf{1} \cdot (\mathbf{C_a} + \mathbf{S_g}) \cdot \mathbf{1} a\, t_c + \mathbf{1} \cdot \mathbf{C} \cdot \mathbf{1}(1 - \xi_1^2) t_c$$

$$+ \mathbf{1} \cdot \Big[-(\mathbf{C_g} - \mathbf{S_a})(\mathbf{G_q} - a\mathbf{G_a}) - (\mathbf{C_a} + \mathbf{S_g})(\mathbf{G_p} - a\mathbf{G_g}) \Big] \cdot \delta \mathbf{m}$$

$$+ \mathbf{1} \cdot \Big[-\xi_1^2 \mathbf{S} \mathbf{G_a} + \xi_1^2 \mathbf{C} \mathbf{G_g} \Big] \cdot \delta \mathbf{m}$$

Now, we have a general form of inversion problem for earth structure in terms of the GSDF's δt_x, kernels $\mathbf{G_x}$, and the interference effects $\mathbf{C}, \mathbf{S}, \mathbf{C_x}, \mathbf{S_x}$.

At this point, it is possible to outline this structure inversion problem. At a particular frequency, according to GSDF theory, using cross-correlation technique we can obtain four measurements as our "observations" (GJ.9-12) and evaluate the mode interference, which we will use with $\mathbf{G_x}$ to form inversion kernels. Therefore, we perform this

measuring procedure at several frequencies, we then have the "data vector" and "kernel matrix" ready for inversion. In the following sections, we will show how we create the kernels ($\mathbf{G_x}$).

Kernel $\mathbf{G_p}$

Kernel $\mathbf{G_p}$ relates phase velocity changes to model perturbations.

$$\delta\tau_{\mathbf{p}} = \mathbf{G_p} \cdot \delta\mathbf{m}$$

The n'th component in the differential phase velocity vector $\delta\tau_{\mathbf{p}}$, $\delta\tau_{p_n}$ is define as

$$\begin{aligned}
\delta\tau_{p_n} &= \frac{R}{c_{n\,obs}} - \frac{R}{c_{n\,syn}} \\
&= \frac{R}{c_n + \delta c_n} - \frac{R}{c_n} = \frac{R}{c_n}\left[-1 + (\,1 - \frac{\delta c_n}{c_n} + (\frac{\delta c_n}{c_n})^2 \cdots) \right] \\
&= \frac{R}{c_n}\left[-\frac{\delta c_n}{c_n} + (\frac{\delta c_n}{c_n})^2 \cdots \right] \\
&\approx -\frac{R}{{c_n}^2}\,\delta c_n = \left[-\frac{R}{{c_n}^2}\,\frac{\partial c_n}{\partial \mathbf{m}} \right] \cdot \delta\mathbf{m}
\end{aligned}$$

where

R is source-receiver distance,

c_n is phase velocity for n'th mode of synthetic seismogram.

In the matrix form, we can exactly see the meaning of $\delta\tau_{p_1}$ as the total phase delay for *mode* 1 when model $\mathbf{m}$ changes into $\mathbf{m} + \delta\mathbf{m}$.

$$\begin{bmatrix} \delta\tau_{p_1} \\ \delta\tau_{p_2} \\ \cdot \\ \delta\tau_{p_N} \end{bmatrix}_{N\times 1} = - \begin{bmatrix} \frac{R}{c_1^2}\frac{\partial c_1}{\partial m_1} & \frac{R}{c_1^2}\frac{\partial c_1}{\partial m_2} & \frac{R}{c_1^2}\frac{\partial c_1}{\partial m_3} & \cdots & (\#1\ mode) \\ \frac{R}{c_2^2}\frac{\partial c_2}{\partial m_1} & \frac{R}{c_2^2}\frac{\partial c_2}{\partial m_2} & \frac{R}{c_2^2}\frac{\partial c_2}{\partial m_3} & \cdots & (\#2\ mode) \\ \cdots & \cdots & \cdots & \cdots & \cdots \\ \frac{R}{c_N^2}\frac{\partial c_N}{\partial m_1} & \frac{R}{c_N^2}\frac{\partial c_N}{\partial m_2} & \frac{R}{c_N^2}\frac{\partial c_N}{\partial m_3} & \cdots & (\#N\ mode) \end{bmatrix}_{N\times k} \begin{bmatrix} \delta m_1 \\ \delta m_2 \\ \delta m_3 \\ \cdot \\ \cdot \\ \delta m_k \end{bmatrix}_{k\times 1}$$

Kernel $\mathbf{G_g}$

To construct kernel $\mathbf{G_g}$ which relates group velocity variation to model perturbations,

$$\delta\tau_{\mathbf{g}} = \mathbf{G_g} \cdot \delta\mathbf{m}$$

the n'th component in differential group velocity vector $\delta\tau_{\mathbf{g}}$, $\delta\tau_{g_n}$ is defined as

$$\delta\tau_{g_n} = \frac{R}{U_{n\,obs}} - \frac{R}{U_{n\,syn}}$$

$$= \frac{R}{U_n + \delta U_n} - \frac{R}{U_n} = \frac{R}{U_n}\left[-1 + (1 - \frac{\delta U_n}{U_n} + (\frac{\delta U_n}{U_n})^2 \cdots) \right]$$

$$= \frac{R}{U_n}\left[-\frac{\delta U_n}{U_n} + (\frac{\delta U_n}{U_n})^2 \cdots \right]$$

$$\approx -\frac{R}{U_n{}^2}\delta U_n = \left[-\frac{R}{U_n{}^2}\frac{\partial U_n}{\partial \mathbf{m}} \right] \cdot \delta\mathbf{m}$$

where

U_n is group velocity of n'th mode synthetic seismogram.

In matrix form

$$\begin{bmatrix} \delta\tau_{g_1} \\ \delta\tau_{g_2} \\ \cdot \\ \delta\tau_{g_N} \end{bmatrix}_{N\times 1} = - \begin{bmatrix} \frac{R}{U_1^2}\frac{\partial U_1}{\partial m_1} & \frac{R}{U_1^2}\frac{\partial U_1}{\partial m_2} & \frac{R}{U_1^2}\frac{\partial U_1}{\partial m_3} & \cdots & (\#1\ mode) \\ \frac{R}{U_2^2}\frac{\partial U_2}{\partial m_1} & \frac{R}{U_2^2}\frac{\partial U_2}{\partial m_2} & \frac{R}{U_2^2}\frac{\partial U_2}{\partial m_3} & \cdots & (\#2\ mode) \\ \cdots & \cdots & \cdots & \cdots & \cdots \\ \frac{R}{U_N^2}\frac{\partial U_N}{\partial m_1} & \frac{R}{U_N^2}\frac{\partial U_N}{\partial m_2} & \frac{R}{U_N^2}\frac{\partial U_N}{\partial m_3} & \cdots & (\#N\ mode) \end{bmatrix}_{N\times k} \begin{bmatrix} \delta m_1 \\ \delta m_2 \\ \delta m_3 \\ \cdot \\ \cdot \\ \delta m_k \end{bmatrix}_{k\times 1}$$

Kernel $\mathbf{G_q}$

To create kernel $\mathbf{G_q}$ which relates attenuation to model perturbations,

$$\delta\tau_{\mathbf{q}} = \mathbf{G_q} \cdot \delta\mathbf{m}$$

we extend (GJ.47) into a general matrix form and reformulate the above equation to yield

$$\delta\tau_{\mathbf{q}} = \frac{1}{2}\,\tilde{\tau}_p(\omega)[Q^{-1} - \tilde{Q}^{-1}]$$

$$= \frac{1}{2}\left[\tilde{\tau}_p(\omega)\frac{\partial Q^{-1}}{\partial \mathbf{m}}\right]\delta\mathbf{m}$$

$$= \mathbf{G_q} \cdot \delta\mathbf{m}$$

Using the relationship between γ and Q, the partial derivative of γ with respect to model perturbations can be calculated.

$$\gamma_n = \frac{\omega}{2c_{0_n}} Q_n^{-1}$$

$$\frac{\partial \gamma_n}{\partial \mathbf{m}} = \frac{\omega}{2c_{0_n}}\frac{\partial Q_n^{-1}}{\partial \mathbf{m}} - Q_n^{-1}\frac{\omega}{2{c_{0_n}}^2}\frac{\partial c_{0_n}}{\partial \mathbf{m}}$$

Therefore, the partial derivative of Q_{RL}^{-1} can be rewritten as

$$\frac{\partial Q_n^{-1}}{\partial \mathbf{m}} = \left[\frac{\partial \gamma_n}{\partial \mathbf{m}} + Q_n^{-1}\frac{\omega}{2c_{0_n}}\frac{\partial c_{0_n}}{\partial \mathbf{m}}\right]\frac{2c_{0_n}}{\omega}$$

The n'th row (# n *mode*) of kernel $\mathbf{G_q}$ is

$$(\mathbf{G_q})_n = \tilde{\tau}_{p_n}(\omega)\left\{ \frac{c_{0_n}}{\omega}\frac{\partial \gamma_n}{\partial \mathbf{m}} + \frac{Q_n^{-1}}{2c_{0_n}}\frac{\partial c_{0_n}}{\partial \mathbf{m}} \right\}$$

$\mathbf{G_q}$ in matrix form is

$$\begin{bmatrix} \tilde{\tau}_{p_1}\left(\frac{c_{0_1}}{\omega}\frac{\partial \gamma_1}{\partial m_1} + \frac{Q_1^{-1}}{2c_{0_1}}\frac{\partial c_{0_1}}{\partial m_1}\right) & \tilde{\tau}_{p_1}\left(\frac{c_{0_1}}{\omega}\frac{\partial \gamma_1}{\partial m_2} + \frac{Q_1^{-1}}{2c_{0_1}}\frac{\partial c_{0_1}}{\partial m_2}\right) & \cdots & (\#1\ mode) \\ \tilde{\tau}_{p_2}\left(\frac{c_{0_2}}{\omega}\frac{\partial \gamma_2}{\partial m_1} + \frac{Q_2^{-1}}{2c_{0_2}}\frac{\partial c_{0_2}}{\partial m_1}\right) & \tilde{\tau}_{p_2}\left(\frac{c_{0_2}}{\omega}\frac{\partial \gamma_2}{\partial m_2} + \frac{Q_2^{-1}}{2c_{0_2}}\frac{\partial c_{0_2}}{\partial m_2}\right) & \cdots & (\#2\ mode) \\ \cdots & \cdots & \cdots & \cdots \\ \tilde{\tau}_{p_N}\left(\frac{c_{0_N}}{\omega}\frac{\partial \gamma_N}{\partial m_1} + \frac{Q_N^{-1}}{2c_{0_N}}\frac{\partial c_{0_N}}{\partial m_1}\right) & \tilde{\tau}_{p_N}\left(\frac{c_{0_N}}{\omega}\frac{\partial \gamma_N}{\partial m_2} + \frac{Q_N^{-1}}{2c_{0_N}}\frac{\partial c_{0_N}}{\partial m_2}\right) & \cdots & (\#N\ mode) \end{bmatrix}_{(N\times k)}$$

Kernel $\mathbf{G_a}$

The last kernel is $\mathbf{G_a}$. From (GJ.48), we have the relationship between $\mathbf{G_a}$ and Q.

$$\delta\boldsymbol{\tau}_\mathbf{a} = \frac{1}{2}\tilde{\boldsymbol{\tau}}_g(\omega)[\,Q^{-1} - \tilde{Q}^{-1}\,] = \mathbf{G_a}\cdot\delta\mathbf{m}$$

In a manner similar to deriving $\mathbf{G_q}$, we can use the Q and γ relation and the partial derivatives of γ to obtain the kernel $\mathbf{G_a}$ as

$$(\mathbf{G_a})_n = \frac{\tilde{\tau}_{g_n}(\omega)}{2}\frac{\partial Q_n^{-1}}{\partial \mathbf{m}}$$

$$= \tilde{\tau}_{g_n}(\omega)\left\{ \frac{c_{0_n}}{\omega}\frac{\partial \gamma}{\partial \mathbf{m}} + \frac{Q_n^{-1}}{2}\frac{\partial c_{0_n}}{\partial \mathbf{m}} \right\}$$

$\mathbf{G_a}$ in matrix form is

$$\begin{bmatrix} \tilde{\tau}_{g_1}\left(\frac{c_{0_1}}{\omega}\frac{\partial\gamma_1}{\partial m_1}+\frac{Q_1^{-1}}{2c_{0_1}}\frac{\partial c_{0_1}}{\partial m_1}\right) & \tilde{\tau}_{g_1}\left(\frac{c_{0_1}}{\omega}\frac{\partial\gamma_1}{\partial m_2}+\frac{Q_1^{-1}}{2c_{0_1}}\frac{\partial c_{0_1}}{\partial m_2}\right) & \cdots & (\#1\ mode) \\ \tilde{\tau}_{g_2}\left(\frac{c_{0_2}}{\omega}\frac{\partial\gamma_2}{\partial m_1}+\frac{Q_2^{-1}}{2c_{0_2}}\frac{\partial c_{0_2}}{\partial m_1}\right) & \tilde{\tau}_{g_2}\left(\frac{c_{0_2}}{\omega}\frac{\partial\gamma_2}{\partial m_2}+\frac{Q_2^{-1}}{2c_{0_2}}\frac{\partial c_{0_2}}{\partial m_2}\right) & \cdots & (\#2\ mode) \\ \cdots & \cdots & \cdots & \cdots \\ \tilde{\tau}_{g_N}\left(\frac{c_{0_N}}{\omega}\frac{\partial\gamma_N}{\partial m_1}+\frac{Q_N^{-1}}{2c_{0_N}}\frac{\partial c_{0_N}}{\partial m_1}\right) & \tilde{\tau}_{g_N}\left(\frac{c_{0_N}}{\omega}\frac{\partial\gamma_N}{\partial m_2}+\frac{Q_N^{-1}}{2c_{0_N}}\frac{\partial c_{0_N}}{\partial m_2}\right) & \cdots & (\#N\ mode) \end{bmatrix}_{(N\times k)}$$

Partial Derivatives of c, U, and γ

All four kernels $\mathbf{G_p}$ $\mathbf{G_g}$ $\mathbf{G_q}$ $\mathbf{G_a}$ are derived in terms of partial derivatives of phase velocity c, group velocity U, and attenuation γ. In this section, We will give all partial derivatives which will be used in creating kernels.

Perturbation theory is used to obtain phase velocity partials with respect to medium parameters, and a numerical method which introduced by Rodi *et al.* (1975) is used to calculate surface-wave group-velocity partial derivatives. The following equations are calculated for a single mode at a certain frequency, therefore we omit the subscript n for n'th mode. The subscript 0 is used to denote the value before introducing causal Q. The subscript v can be substituted by P-wave velocity α or S-wave velocity β. ρ is layer density. h is layer thickness. ω_r is a reference angular frequency used for introducing causal Q.

Rayleigh Wave

$$c = c_0 + \frac{1}{\pi}\ln(\frac{\omega}{\omega_r})\sum\left[\frac{\partial c_0}{\partial\beta}\beta Q_\beta^{-1} + \frac{\partial c_0}{\partial\alpha}\alpha Q_\alpha^{-1}\right]$$

$$\gamma = \frac{\omega}{2c_0^2}\sum\left[\frac{\partial c_0}{\partial\beta}\beta Q_\beta^{-1} + \frac{\partial c_0}{\partial\alpha}\alpha Q_\alpha^{-1}\right]$$

$$u = u_0\left[1 + (2 - \frac{U_0}{c_0})(\frac{c - c_0}{c_0}) + \frac{2\gamma U_0}{\pi\omega}\right]$$

$$\frac{\partial c}{\partial v} = \frac{\partial c_0}{\partial v}\left[1 + \frac{1}{\pi Q_v}\ln(\frac{\omega}{\omega_r})\right]$$

$$\frac{\partial c}{\partial \rho} = \frac{\partial c_0}{\partial \rho} + \frac{1}{\pi}\ln(\frac{\omega}{\omega_r})\left[\frac{\partial c_0}{\partial \beta}(-\frac{\beta}{2\rho})Q_\beta^{-1} + \frac{\partial c_0}{\partial \alpha}(-\frac{\alpha}{2\rho})Q_\alpha^{-1}\right]$$

$$\frac{\partial c}{\partial h} = \frac{\partial c_0}{\partial h}$$

$$\frac{\partial c}{\partial Q_v^{-1}} = \frac{1}{\pi}\ln(\frac{\omega}{\omega_r})\frac{\partial c_0}{\partial v}v$$

$$\frac{\partial \gamma}{\partial v} = \frac{\omega}{2c_0^2}\frac{\partial c_0}{\partial v}Q_v^{-1} - \frac{2\gamma}{c_0}\frac{\partial c_0}{\partial v}$$

$$\frac{\partial \gamma}{\partial \rho} = \frac{\omega}{2c_0^2}\left[\frac{\partial c_0}{\partial \beta}(-\frac{\beta}{2\rho})Q_\beta^{-1} + \frac{\partial c_0}{\partial \alpha}(-\frac{\alpha}{2\rho})Q_\alpha^{-1}\right] - \frac{2\gamma}{c_0}\frac{\partial c_0}{\partial \rho}$$

$$\frac{\partial \gamma}{\partial h} = -\frac{2\gamma}{c_0}\frac{\partial c_0}{\partial h}$$

$$\frac{\partial \gamma}{\partial Q_v^{-1}} = \frac{\omega}{2c_0^2}\frac{\partial c_0}{\partial v}v$$

$$\frac{\partial U}{\partial v} = \frac{\partial U_0}{\partial v}\left[\frac{U}{U_0} - \frac{U_0}{c_0}(\frac{c - c_0}{c_0}) + \frac{2\gamma U_0}{\pi\omega}\right] + \frac{\partial c_0}{\partial v}(\frac{U_0}{c_0})^2\left[2\frac{c}{c_0} - 2\frac{c}{U_0} - 1\right]$$

$$+ \frac{\partial c}{\partial v}\frac{U_0}{c_0}(2 - \frac{U_0}{c_0}) + \frac{\partial \gamma}{\partial v}\frac{2u_0^2}{\pi\omega}$$

$$\frac{\partial U}{\partial \rho} = \frac{\partial U_0}{\partial \rho}\left[\frac{U}{U_0} - \frac{U_0}{c_0}(\frac{c - c_0}{c_0}) + \frac{2\gamma U_0}{\pi\omega}\right] + \frac{\partial c_0}{\partial \rho}(\frac{U_0}{c_0})^2\left[2\frac{c}{c_0} - 2\frac{c}{U_0} - 1\right]$$

$$+ \frac{\partial c}{\partial \rho}\frac{U_0}{c_0}(2 - \frac{U_0}{c_0}) + \frac{\partial \gamma}{\partial \rho}\frac{2u_0^2}{\pi\omega}$$

$$\frac{\partial U}{\partial h}=\frac{\partial U_0}{\partial h}\left[\frac{U}{U_0}-\frac{U_0}{c_0}(\frac{c-c_0}{c_0})+\frac{2\gamma U_0}{\pi\omega}\right]+\frac{\partial c_0}{\partial h}(\frac{U_0}{c_0})^2\left[2\frac{c}{c_0}-2\frac{c}{U_0}-1\right]$$

$$+\frac{\partial c}{\partial h}\frac{U_0}{c_0}(2-\frac{U_0}{c_0})+\frac{\partial\gamma}{\partial h}\frac{2u_0^2}{\pi\omega}$$

$$\frac{\partial U}{\partial Q_v^{-1}}=\frac{U_0}{c_0}(2-\frac{U_0}{c_0})\frac{\partial c}{\partial Q_v^{-1}}+\frac{2u_0^2}{\pi\omega}\frac{\partial\gamma}{\partial Q_v^{-1}}$$

Love Wave

$$c=c_0+\frac{1}{\pi}\ln(\frac{\omega}{\omega_r})\sum\frac{\partial c_0}{\partial\beta}\beta Q_\beta^{-1}$$

$$\gamma=\frac{\omega}{2c_0^2}\sum\frac{\partial c_0}{\partial\beta}\beta Q_\beta^{-1}$$

$$u=u_0\left[1+(2-\frac{U_0}{c_0})(\frac{c-c_0}{c_0})+\frac{2\gamma U_0}{\pi\omega}\right]$$

$$\frac{\partial c}{\partial\beta}=\frac{\partial c_0}{\partial\beta}\left[1+\frac{1}{\pi Q_v}\ln(\frac{\omega}{\omega_r})\right]$$

$$\frac{\partial c}{\partial\rho}=\frac{\partial c_0}{\partial\rho}+\frac{1}{\pi}\ln(\frac{\omega}{\omega_r})\left[\frac{\partial c_0}{\partial\beta}(-\frac{\beta}{2\rho})Q_\beta^{-1}\right]$$

$$\frac{\partial c}{\partial h}=\frac{\partial c_0}{\partial h}$$

$$\frac{\partial c}{\partial Q_\beta}=\frac{1}{\pi}\ln(\frac{\omega}{\omega_r})\frac{\partial c_0}{\partial\beta}\beta$$

$$\frac{\partial\gamma}{\partial\beta}=\frac{\omega}{2c_0^2}\frac{\partial c_0}{\partial\beta}Q_\beta^{-1}-\frac{2\gamma}{c_0}\frac{\partial c_0}{\partial\beta}$$

$$\frac{\partial\gamma}{\partial\rho}=\frac{\omega}{2c_0^2}\left[\frac{\partial c_0}{\partial\beta}(-\frac{\beta}{2\rho})Q_\beta^{-1}-\frac{2\gamma}{c_0}\frac{\partial c_0}{\partial\rho}\right]$$

$$\frac{\partial \gamma}{\partial h} = -\frac{2\gamma}{c_0}\frac{\partial c_0}{\partial h}$$

$$\frac{\partial \gamma}{\partial Q_\beta^{-1}} = \frac{\omega}{2c_0^2}\frac{\partial c_0}{\partial \beta}\beta$$

$$\frac{\partial U}{\partial \beta} = \frac{\partial U_0}{\partial \beta}\left[\frac{U}{U_0} - \frac{U_0}{c_0}(\frac{c-c_0}{c_0}) + \frac{2\gamma U_0}{\pi\omega}\right] + \frac{\partial c_0}{\partial \beta}(\frac{U_0}{c_0})^2\left[2\frac{c}{c_0} - 2\frac{c}{U_0} - 1\right]$$

$$+\frac{\partial c}{\partial \beta}\frac{U_0}{c_0}(2-\frac{U_0}{c_0}) + \frac{\partial \gamma}{\partial \beta}\frac{2u_0^2}{\pi\omega}$$

$$\frac{\partial U}{\partial \rho} = \frac{\partial U_0}{\partial \rho}\left[\frac{U}{U_0} - \frac{U_0}{c_0}(\frac{c-c_0}{c_0}) + \frac{2\gamma U_0}{\pi\omega}\right] + \frac{\partial c_0}{\partial \rho}(\frac{U_0}{c_0})^2\left[2\frac{c}{c_0} - 2\frac{c}{U_0} - 1\right]$$

$$+\frac{\partial c}{\partial \rho}\frac{U_0}{c_0}(2-\frac{U_0}{c_0}) + \frac{\partial \gamma}{\partial \rho}\frac{2u_0^2}{\pi\omega}$$

$$\frac{\partial U}{\partial h} = \frac{\partial U_0}{\partial h}\left[\frac{U}{U_0} - \frac{U_0}{c_0}(\frac{c-c_0}{c_0}) + \frac{2\gamma U_0}{\pi\omega}\right] + \frac{\partial c_0}{\partial h}(\frac{U_0}{c_0})^2\left[2\frac{c}{c_0} - 2\frac{c}{U_0} - 1\right]$$

$$+\frac{\partial c}{\partial h}\frac{U_0}{c_0}(2-\frac{U_0}{c_0}) + \frac{\partial \gamma}{\partial h}\frac{2u_0^2}{\pi\omega}$$

$$\frac{\partial U}{\partial Q_\beta^{-1}} = \frac{U_0}{c_0}(2-\frac{U_0}{c_0})\frac{\partial c}{\partial Q_\beta^{-1}} + \frac{2u_0^2}{\pi\omega}\frac{\partial \gamma}{\partial Q_\beta^{-1}}$$

3.4 Forming Inversion Kernel

As shown above, we calculate partial derivatives with respect to all parameters (α, β, ρ, Q_α, Q_β, h) instead of computing partial derivatives for shear velocity only. The intention is that we try to provide all the possible tools to interpret the seismograms as completely as possible, and as automatically as possible. Therefore, it is the users' responsibility to choose those model parameters they want to invert; and only the chosen part will be used to assemble the inversion kernel.

To stabilize the inversion, all information for different frequencies inside the inversion kernel are weighted according to their frequency amplitudes. This weighting procedure greatly improves the inversion stability.

When inverting teleseismic surface-waveforms, sometimes the body waves (e.g. *SS*, *SSS*) or some unwanted surface-waves due to improper rotation will have bad influence on the cross-correlation between the isolation function and the observed seismogram, and cause signal misalignment. To avoid this problem, a window is applied on the seismograms before doing cross-correlation, and this may successfully isolate the surface wave wavetrain from those body waves outside the surface wave wavetrain. Although prewindowing procedure is applied, the same trouble still may happen occasionally. In such a situation, the information at that frequency must be rejected from forming inversion kernel, otherwise it will plague the inversion for its strong misaligned "phase delay" or "group delay". Figure 3.1 shows an example of this problem. Due to improper rotation, the unwanted Love-wave waveform appears on the radial component seismogram prior to the Rayleigh wave wavetrain. This unwanted Love wave signal causes two kind mistakes, wrong identification of a Gaussian wavelet (Figure 3.1a) and signal misalignment (Figure 3.1b), which can not be incorporated in inversion.

We have mentioned that users have the power to decide what parameters will be inverted for during the inversion. An aspect which strongly related to this decision is the phrase "using what kind information ?". During each iteration in the inversion, we have calculated partial derivatives with respect to parameters for each layer at several appointed frequencies, and all this information is rearranged to form four kind delays at each frequency. After manually rejecting miscalculated cross-correlations at some frequencies, users have to decide which combinations of δt_p, δt_g, δt_a, δt_q they will use to invert for a particular combination of model parameters (α, β, ρ, Q_α, Q_β, h). From

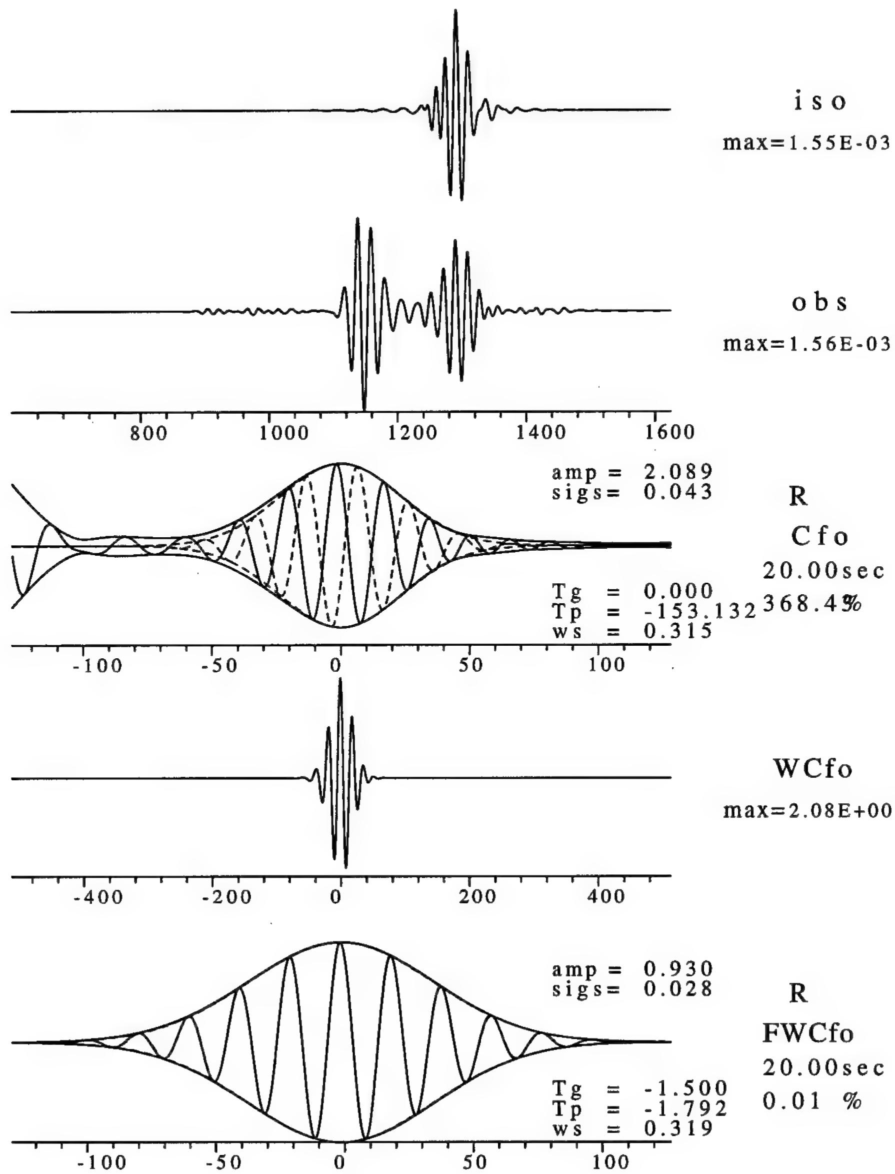

Fig. 3.1a. This is an example showning how unexpected signal interference affects the extracting procedure in GSDF theory. There are five traces presented to show the different processing stages. The top two traces are the prefiltered isolation filter and observed seismogram, respectively, The third trace shows the Gaussian filtered cross-correlation at a target period of 20.0 seconds. The five extracted parameters are shown. The dashed curves inside the envelope are from the synthetics and the solid curve are from the observed data. The fourth trace is the windowed cross-correlagram shown in the third trace. The bottom trace is the filtered windowed cross-correlagram and its five Gaussian wavelet parameters which are to be used in further processing. Due to improper rotation, the Love wave appears on radial component before the Rayleigh wave arrival. The Love wave wavetrain may causes two kind troubles like (a) wrong determination of Gaussian wavelet parameters, and

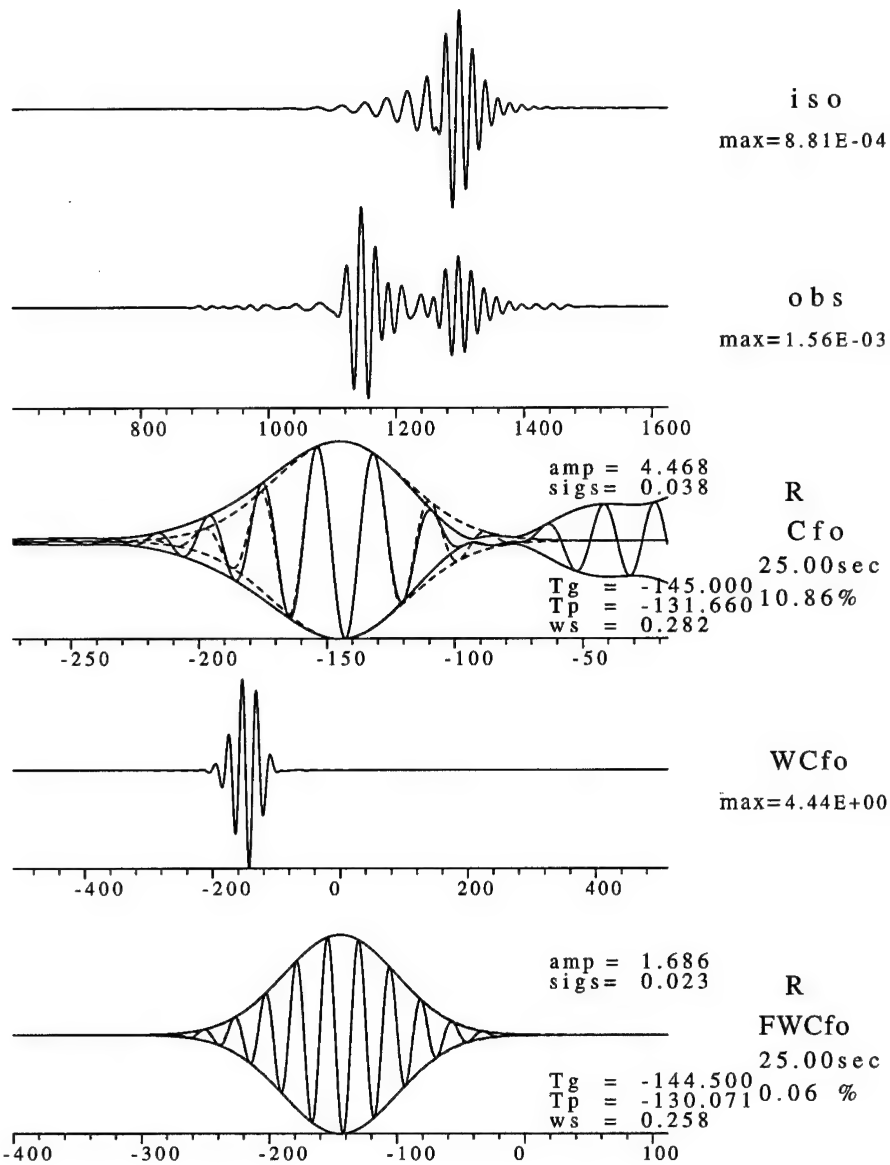

Fig. 3.1b. (cont'd). (b) Misalignment of signals which produces significant bias phase and group delay. This arises because a period of 25 seconds is considered compared to 20 seconds in Fig. 3.1a.

our experience, we found that when we invert for velocity structure the phase delay (δt_p) and the group delay (δt_g) play the major roles in inversion, and the other two delays (δt_a, δt_q) are better in inverting for attenuation factors. We also found that when the initial model is far from the final result, using group delay information in inversion can

easily pull the model close enough to the final model so that phase delays can be used. It only at the final stage when the synthetic is very close to the observed seismograms that the phase delay information can be used at a powerful fine tuning of the model since there is no "cycle skipping" problem.

3.5 Synthetic Test

A simple source with strike, dip, rake angles of 45°, 45°, 45°, respectively, in 20 km deep was used in this synthetic test. Receiver is located at 1000 km away along 10° in azimuth. The "observed" seismograms were created for a two layered crust with an upper mantle deviating slightly from the PREM model (Figure 3.2). Here, we only try to invert for shear velocity structure, so all the other parameters related to the source and earth model are assumed known. The starting model is a two-layered crust model with the PREM model beneath 40 km depth. It is clearly seen, in Figure 3.3 that the starting synthetic seismograms are very far away "observed" seismograms.

After 12 iterations, the synthetic seismograms are almost the same as "observed" seismograms (Figure 3.4). Checking the model differences between the "true" model and the final model (Figure 3.5), we can see the crust structure is almost matches the "true" model, except in the upper mantle where the surface wave doesn't provide enough resolving power the inverted structure causing the "zig-zag" pattern. The differences in Q models are not significant at these frequencies and this distance.

3.6 Real Data Test

After the successful synthetic test, we wish to test this technique on real data. The April 14, 1995 Texas earthquake is the one chosen.

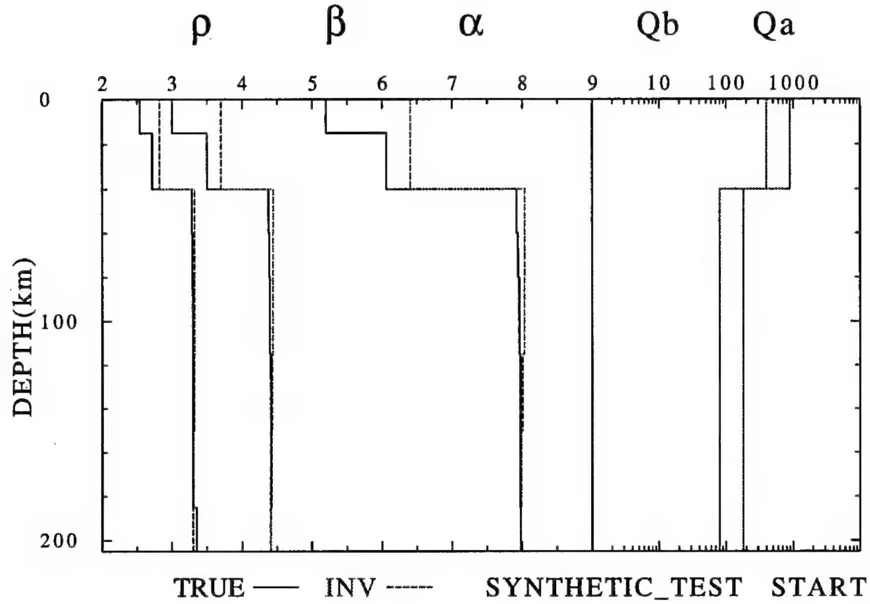

Fig. 3.2. The starting model (dashed line) used in synthetic test of GSDF inversion algorithm and the

According to Sipkin's USGS solution, the epicenter of the Texas earthquake is at 30.261°N 103.33°W and origin time is 00:32:55UT. The current collected data set consists of 89 broadband stations from IRIS, Canadian National Seismological Center (CNSDC), USGS, UNAM, and PASSCAL experiment (Figure 2.1).

Some source parameters were reestimated on the basis of fitting surface wave amplitude spectra (Table 2.2). The redetermined source depth is 23 km deep, with strike, dip, rake angles of 114°, 64°, -101°, respectively with $\mathbf{M}_w = 5.6$.

3.7 Inversion Procedure

We have tried three different inversion runs, the first two exhibit some significant difficulties in matching the waveform or in reasonableness of the resulting model, so the third one has been adapted for inverting structure. In performing the inversions, we use an earth

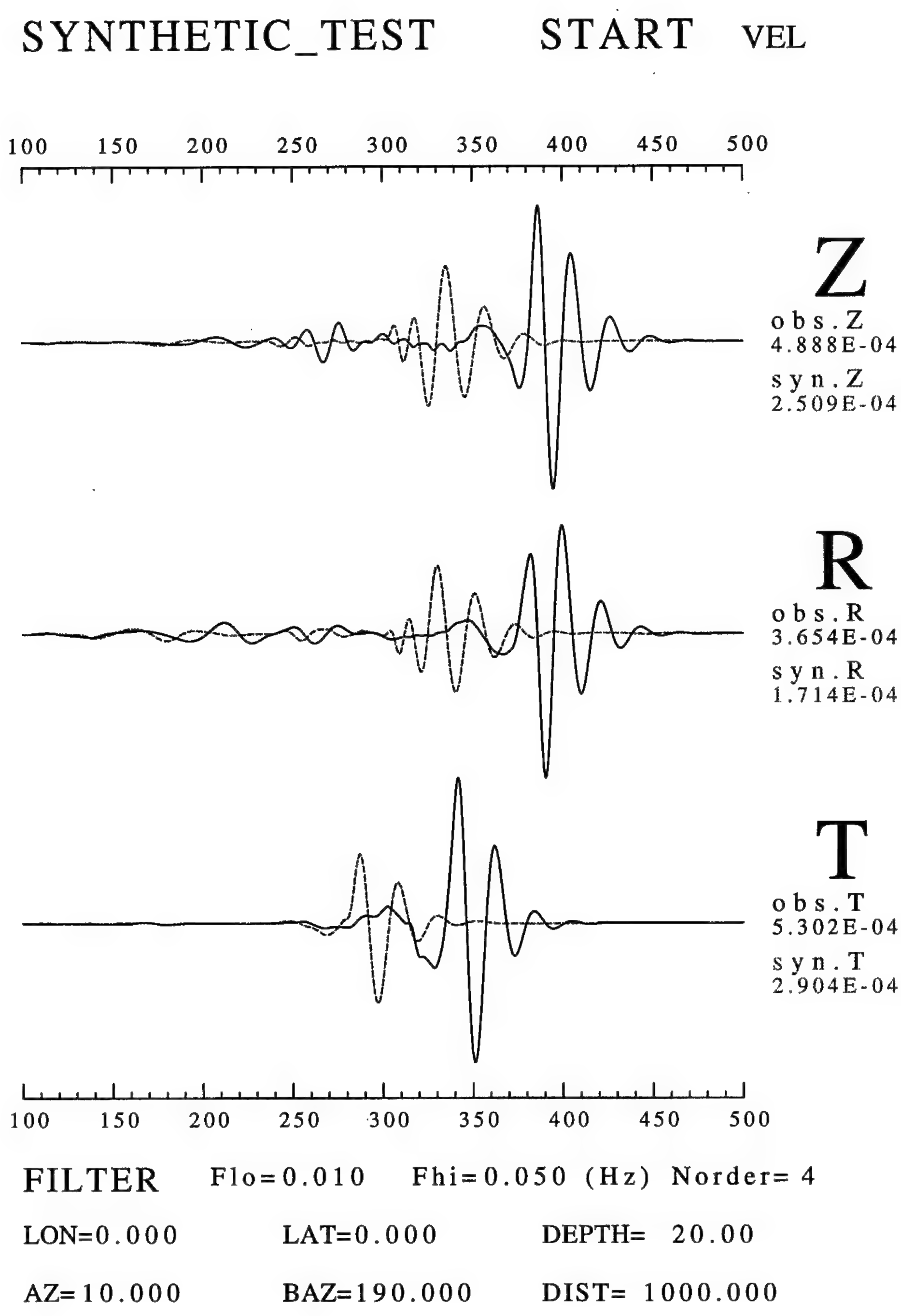

Fig. 3.3. The velocity time histories of 'observed seismograms' (solid line) and the those from the starting model (dashed line) are both filtered in the frequency band 0.01-0.05 Hz by using a Butterworth filter with four poles. The plotted seismograms are normalized according the maximum amplitude of each component in current frequency band. It is clear to see that the starting model is not close to the 'true' model and this may demonstrate the ability of the inversion programs to resolve structure.

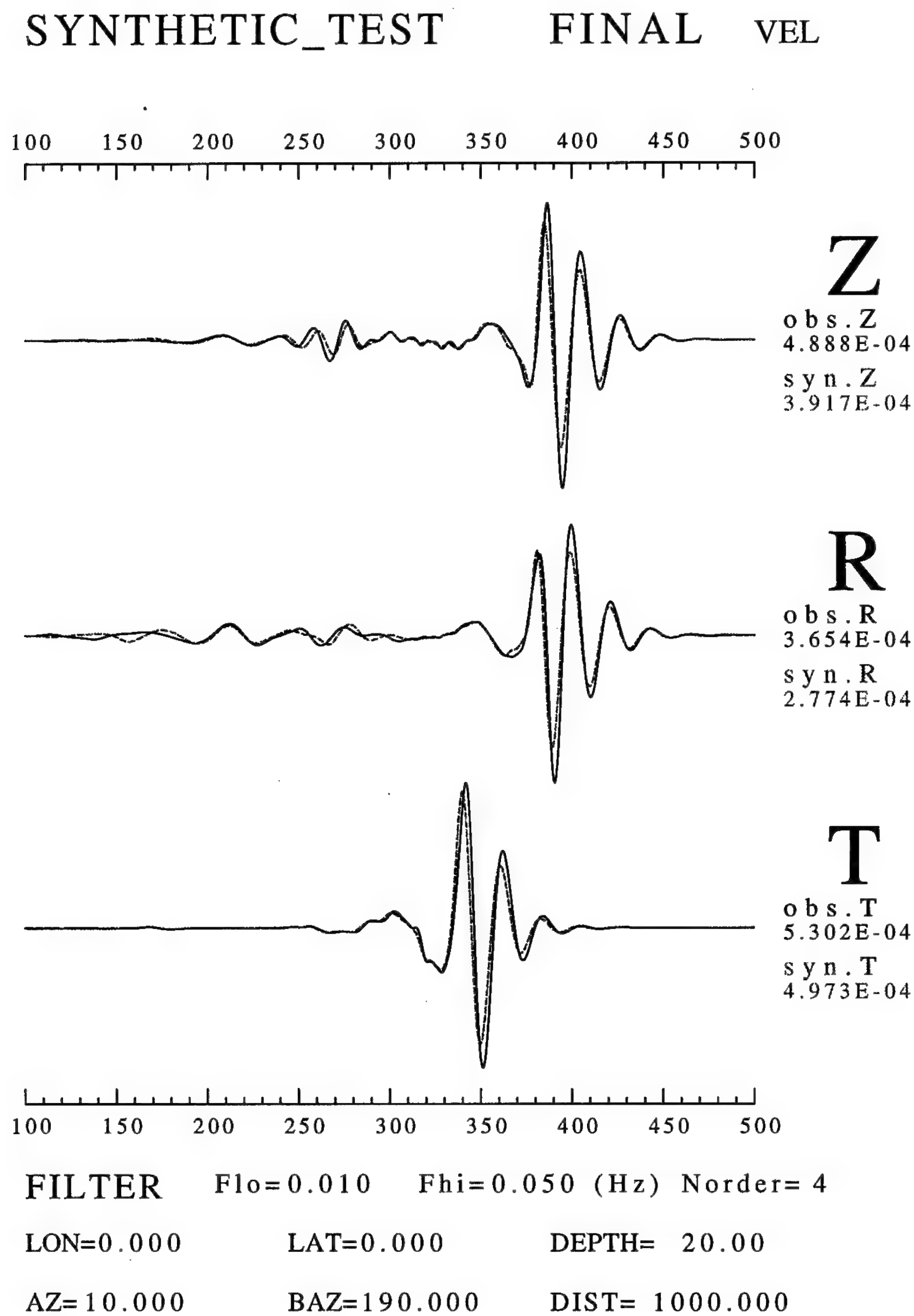

Fig. 3.4. After 12 iterations, the final inversion result show an predicted waveforms almost identical to the 'observed seismograms'.

flattening approximation to use plane-layered surface-wave theory to generate synthetics.

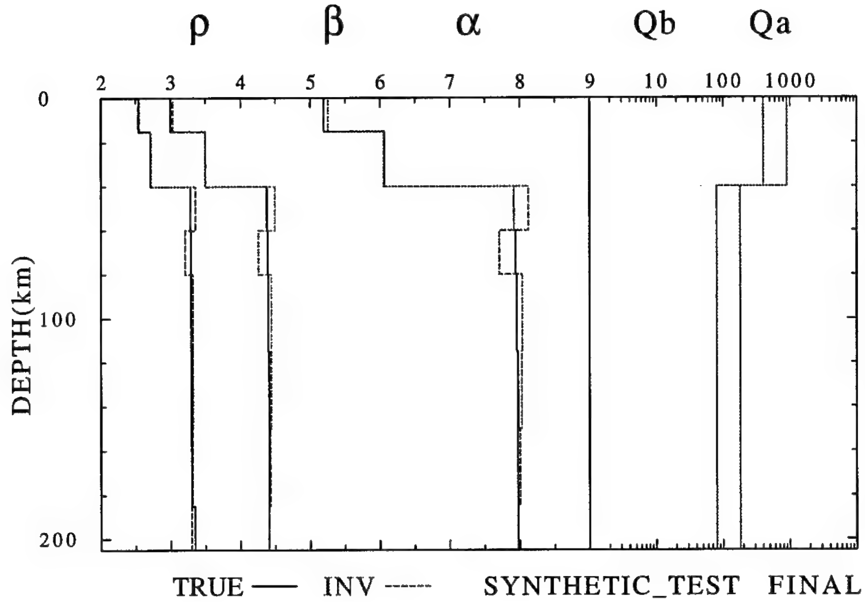

Fig. 3.5. The comparison between the final model and the 'true model'. We can see that the 2-layer crust is very close to the 'true' model, but that in the upper mantle the model shows some 'zig-zag' pattern.

The first run consisted of a joint inversion of both Rayleigh and Love wave seismograms for shear velocity structure. The result was that that the synthetic seismograms tended to fit the largest surface wave amplitude, and ignored the small amplitude wavefields. This arose because of the amplitude level weighting used to stabilize the inversion. Therefore, separate inversions for Rayleigh wave and Love wave were necessary.

The second sequence consisted of inverting for the shear velocity structure from the Love wave, and then using this structure as an *a priori* shear velocity structure so the the Rayleigh wave provided information on the compressional velocity structure. This procedure can match both Rayleigh wave and Love wave waveforms very well, but we found it is impossible to find a reasonable explanation for the anomalous Poisson's ratios in the inverted model. It is well known that the surface wave are insensitive to compressional wave velocity structure, so the only conclusion for this is that the shear velocity structure

inverted from Love wave is not adequate for Rayleigh wave. An unaccounted anisotropy effect may cause the overcorrection in compression velocity structure. Figure 3.6 compares waveforms and Figure 3.7 shows the model resulting from the second inversion procedure. Although the synthetic waveform does not perfectly fit the Rayleigh wave (Figure 3.6), we can see the general features are matched using a single model for both Love and Rayleigh waves. In Figure 3.7 we see that the P-wave velocity structure has lower values to compensate for the high shear velocity, and vice versa. The result are some unexplainable Poisson's ratios such as 0.135 for the middle crust and 0.328 for the lower crust.

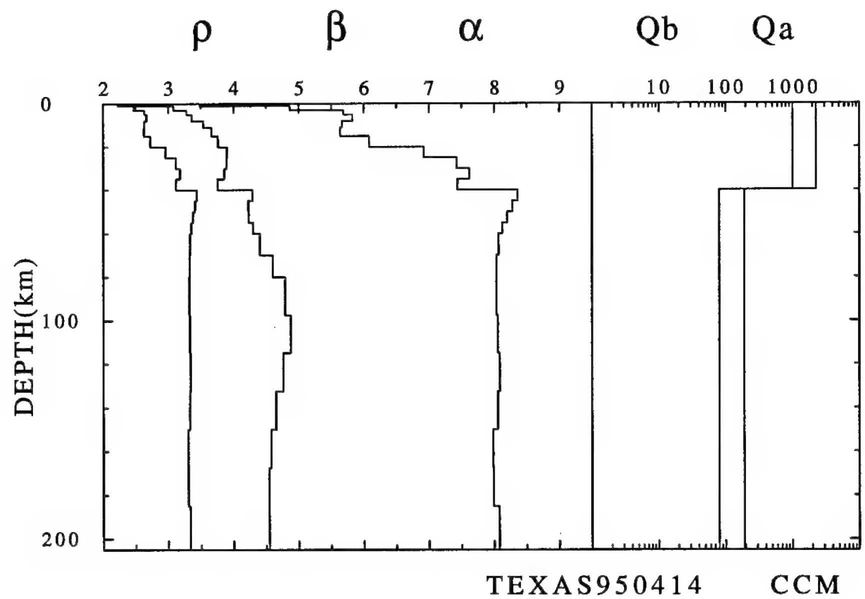

Fig. 3.7. The model inverted by the second inversion procedure.

Since our forward synthetic seismogram algorithm does not include anisotropy effect, we modify our inversion procedure as as follows: we invert V_{β_SH} from Love wave, and another separate inversion of V_{β_PSV} from Rayleigh wave on the vertical component. We fixed the Poisson's ratio when we invert V_{β_PSV} from Rayleigh wave. The fixed Poisson's ratios are kept the same as the original input model. In this

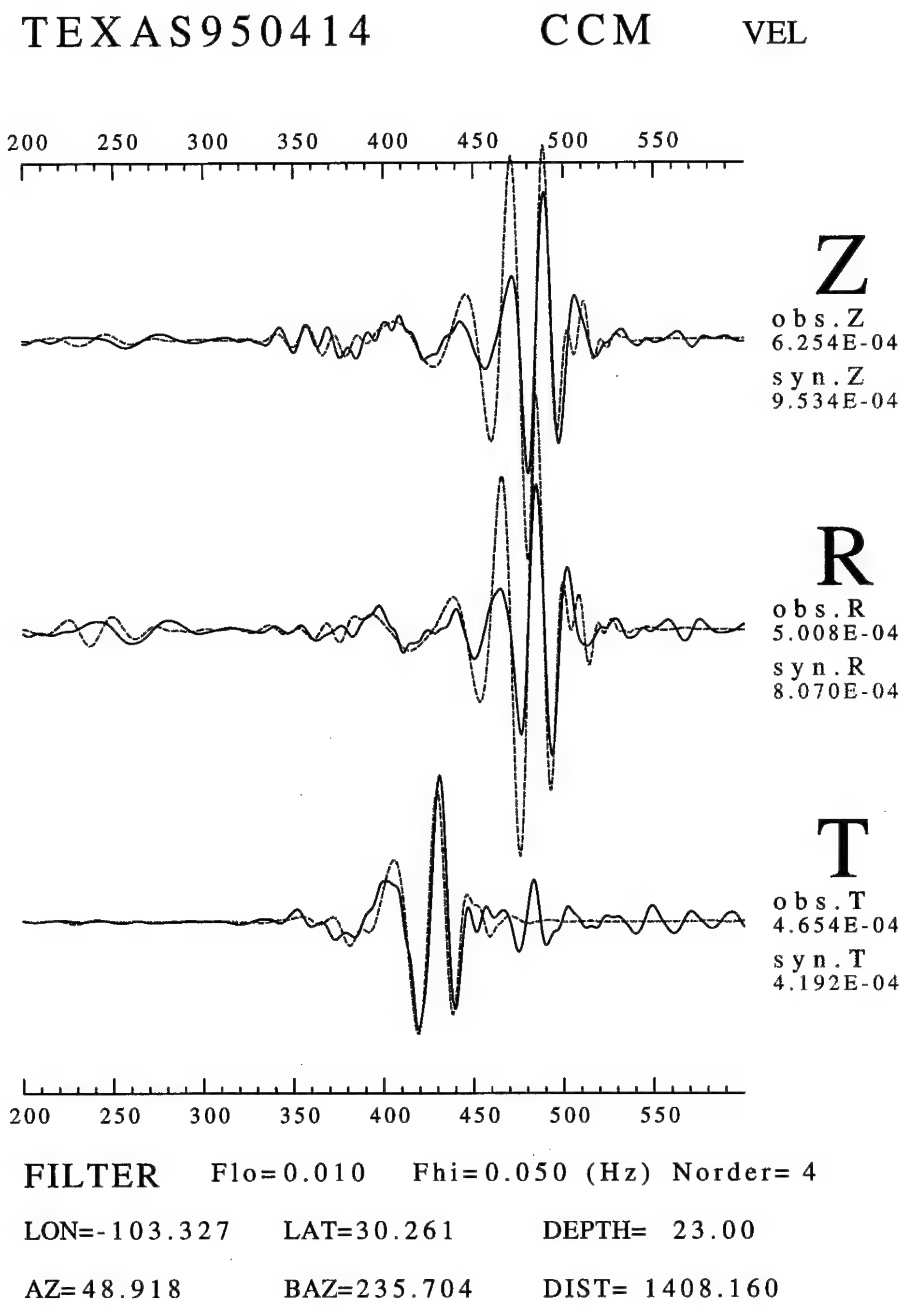

Fig. 3.6. The result of inversion using the second procedure. This inversion procedure inverts S wave velocity from Love wave and after that inverts P wave velocity from Rayleigh wave by assuming no anisotropy effect. This shows a acceptable waveform match in phase, but not in envelope.

study, we set the Poisson's ratio as 0.25 for crust, 0.28 for the layers

between 40 km and 220 km, and adopt the values from PREM model for those layers deeper than 220 km.

When we invert for shear-wave velocity structures, the attenuation factors can be determined simultaneous either by joint inversion of V_β and Q or by another separated Q inversion. The Q determination is not definitive, since we have a lot uncertainties in our source and velocity structures in our inversion, so the only objective criteria for determining Q is the envelope shape of the surface wave wavetrain. As shown on Figure 3.8, the Rayleigh wave signal at large distance is well dispersed with a strong Airy phase. This Airy phase corresponding is affected by crustal wave propagation, therefore, the envelope amplitude of the Airy phase is controlled by the crustal attenuation factors. So the Q structure determined is sensitive to the crust and uppermost mantle.

3.8 Inversion results

Data from 43 of 89 broadband stations were inverted. In this report, three stations were selected to present the inversion results and the waveform fitting success will be shown on several different frequency bands.

Station ALE, which located in Arctic region is the farthest station used in this study. There are some interesting features for the inverted results. Looking at the waveform fit in the low frequency range (0.005-0.03 Hz bandpass; shown as Figure 3.8a), it is clear to see that the synthetic seismograms successfully match the observed surface wave. Two velocity models, PSV and SH are inverted respectively from Rayleigh wave and Love wave.

For ALE, the attenuation factor was fixed during inversion. A high Q structure ($Q_S = 1000$) is used for crust, a low Q ($Q_S = 100$) was adopted for structure between 40 km and 500 km, and using $Q_S = 143$

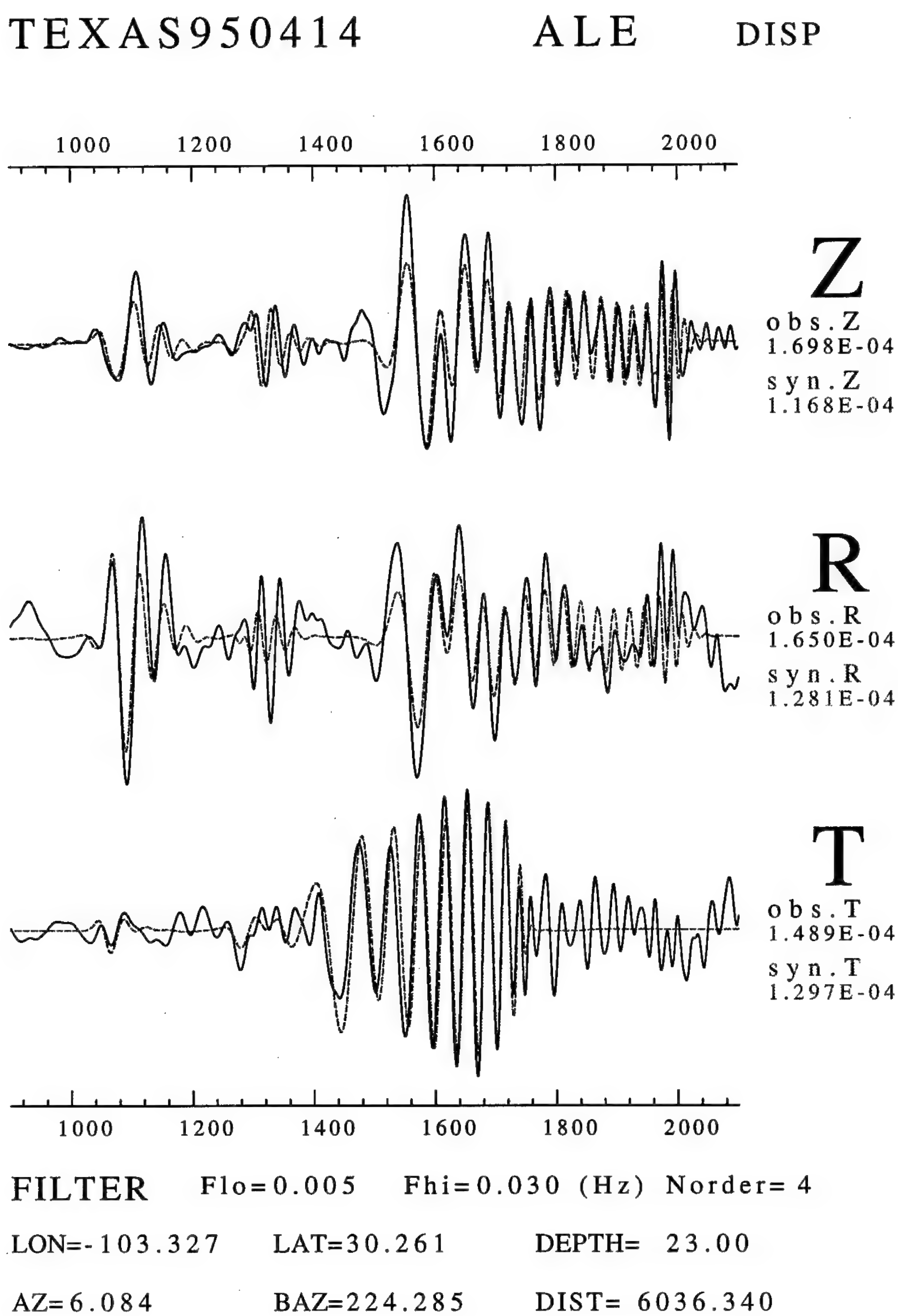

Fig. 3.8a. Waveform fit of the final inverted model for ALE in the frequency band of 0.005-0.03 Hz. The signal which arrives at 1020 seconds and around 1300 seconds are S and SS phase, respectively. From the S phase waveform, we can say that the source time function used in this inversion is a little short but is close enough.

for those deeper than 500 km. And from Figures 3.8a,b, the synthetic

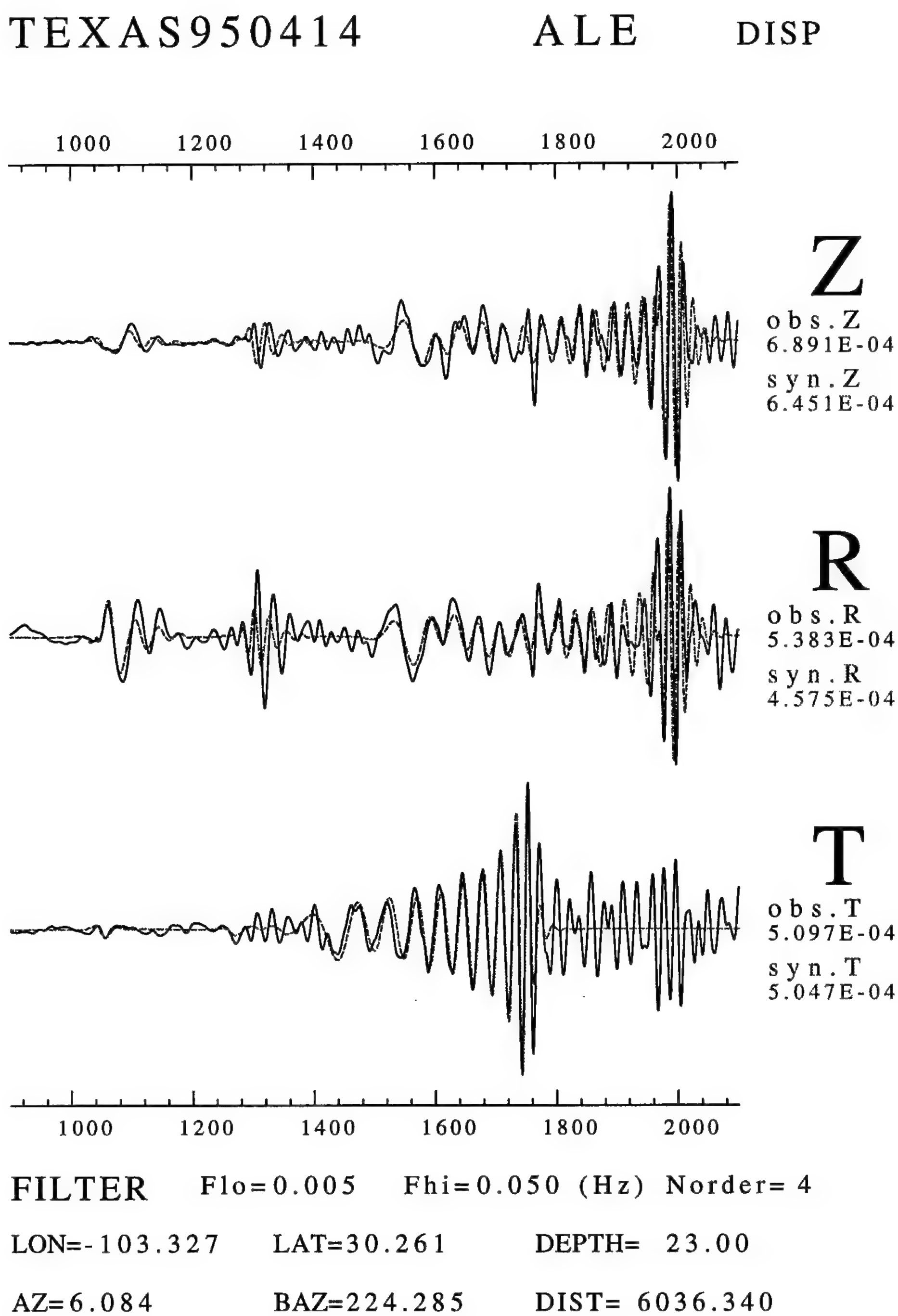

Fig. 3.8b. (Cont'd). Waveform fit in the 0.005-0.05 Hz frequency band.

Rayleigh wave and Love wave amplitudes only show small deviation from observed seismogram, therefore the Q model is considered adequate. We also notice this sharp Q contrast between crust and mantle

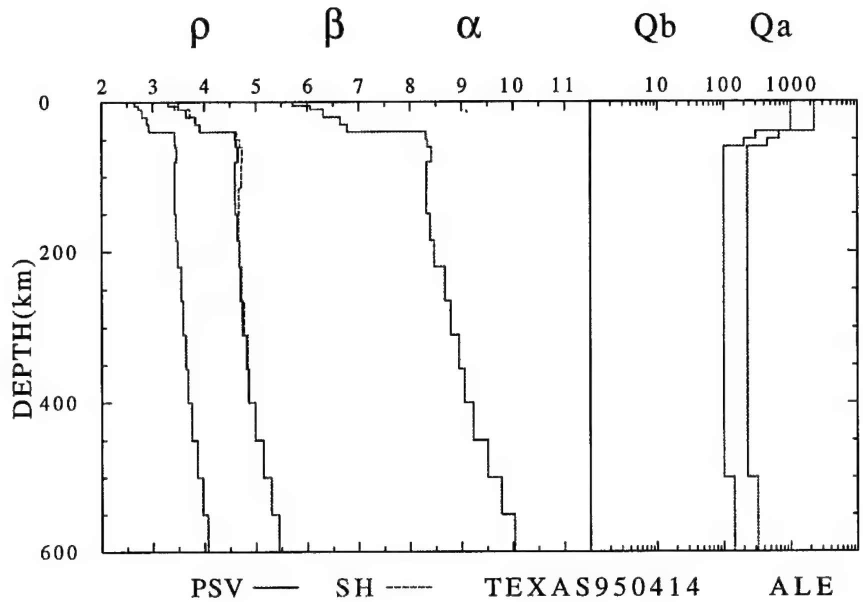

Fig. 3.9. The inverted models for ALE. Two models (PSV and SH) were inverted for Love wave and Rayleigh Wave. From these two models, there is one slight anisotropic zone above 200 km.

is a common character for those stations located inside the North America craton region.

The second station is FCC which located on the west shoreline of Hudson Bay and is in the center of the North America craton. The inverted models (Figure 3.10) show high shear velocity for upper mantle but not as high as SNA model (Grand and Helmberger, 1984). The current inversion result shows 4.5% anisotropy between 70 km and 140 km. The synthetics fit data well at low frequency (Figure 3.11a) and can fit the fundamental mode as high as 0.1 Hz (Figure 3.11), but have difficulty to produce some higher mode arrivals at 800 and 940. the time range.

The final station is PAS. The wave propagates through the southern Rocky Mountains. The inverted model (Figure 3.12) does not require anisotropy and the shear velocity model is very close to the TNA model (Grand and Helmberger, 1984). The synthetics fit the S phase which arrives around 350 seconds and surface wave very well

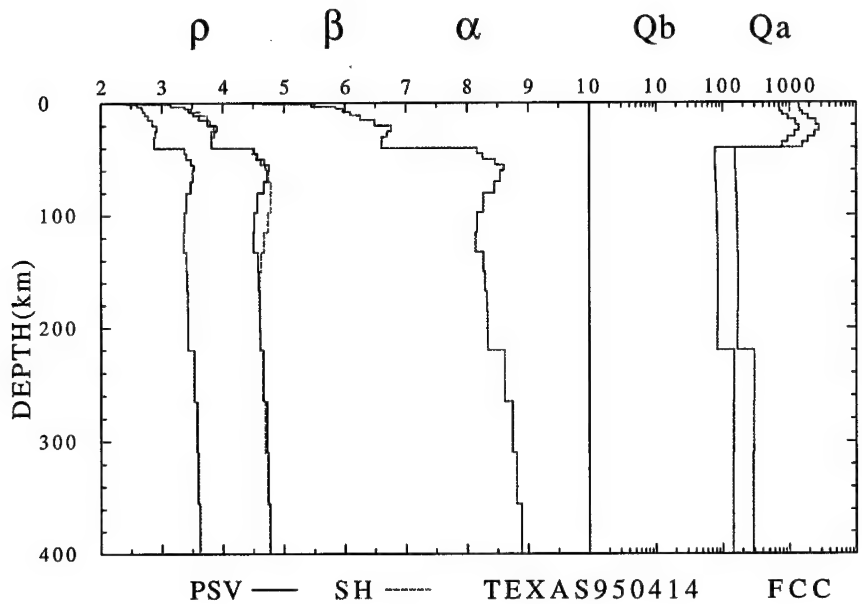

Fig. 3.10. The final inverted model for FCC. There is 4.5% anisotropy effect exists between 70 and 140 km.

(Figures 3.13abc) and this suggests that there is a velocity discontinuity at 220 km which can not be seen in the TNA model. The Q is very low, with the average Q for crust of lower than 200. However we found one interesting feature about the Q behavior. The Q values between 40 and 220 km are slightly higher than PREM model, i.e., a low Q crust underlain a slightly high Q upper mantle with respect to the reference model.

3.9 Conclusion

We implemented the Generalized Seismological Data Functionals technique of Gee and Jordan (1992) in a surface-wave waveform inversion algorithm. A simple synthetic test shows its robust inversion ability. After a successful synthetic test, we useed this inversion algorithm on real data to further test its ability. The Texas earthquake (30.26 °N 103.33°W, 00:32:55UT, April 14, 1995) is a very good

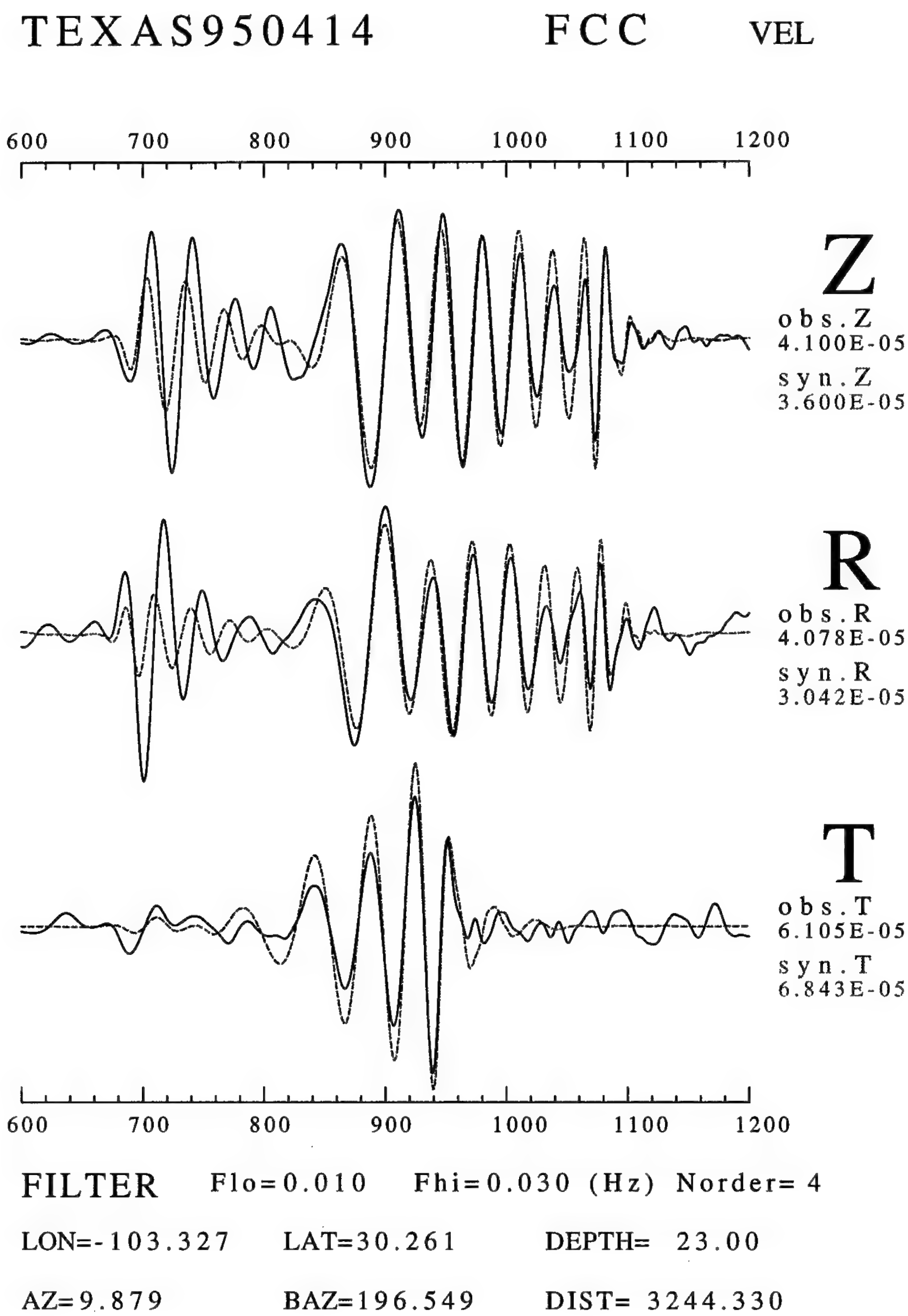

Fig. 3.11a. The waveform fitting for final model in FCC are shown at three frequency bands : (a) 0.01-0.03 (b) 0.01-0.05 (c) 0.01-0.1 Hz. The SS phase arrives at 660 seconds. The inverted model can fit fundamental mode Love wave and Rayleigh wave waveforms as high as 0.1 Hz, but it lacks the ability to simulate the higher modes.

earthquake for this purpose because it was well recorded, its source

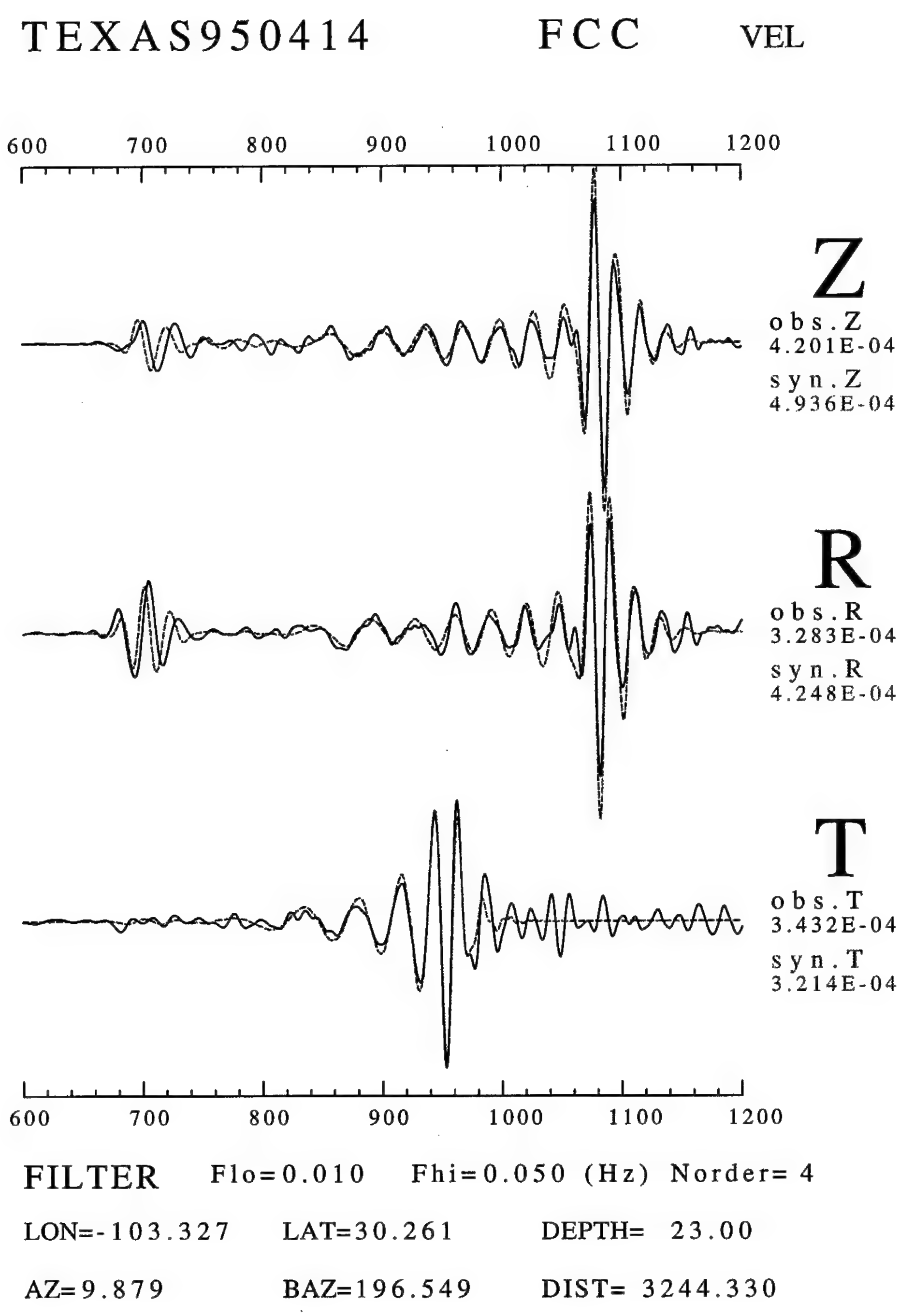

Fig. 3.11b. (Cont'd). (b) 0.01-0.05 Hz.

depth is well constrained, the focal mechanism is fairly determined, and the seismic moment is constrained by long period surface waves. The inversion results are excellent and show some interesting

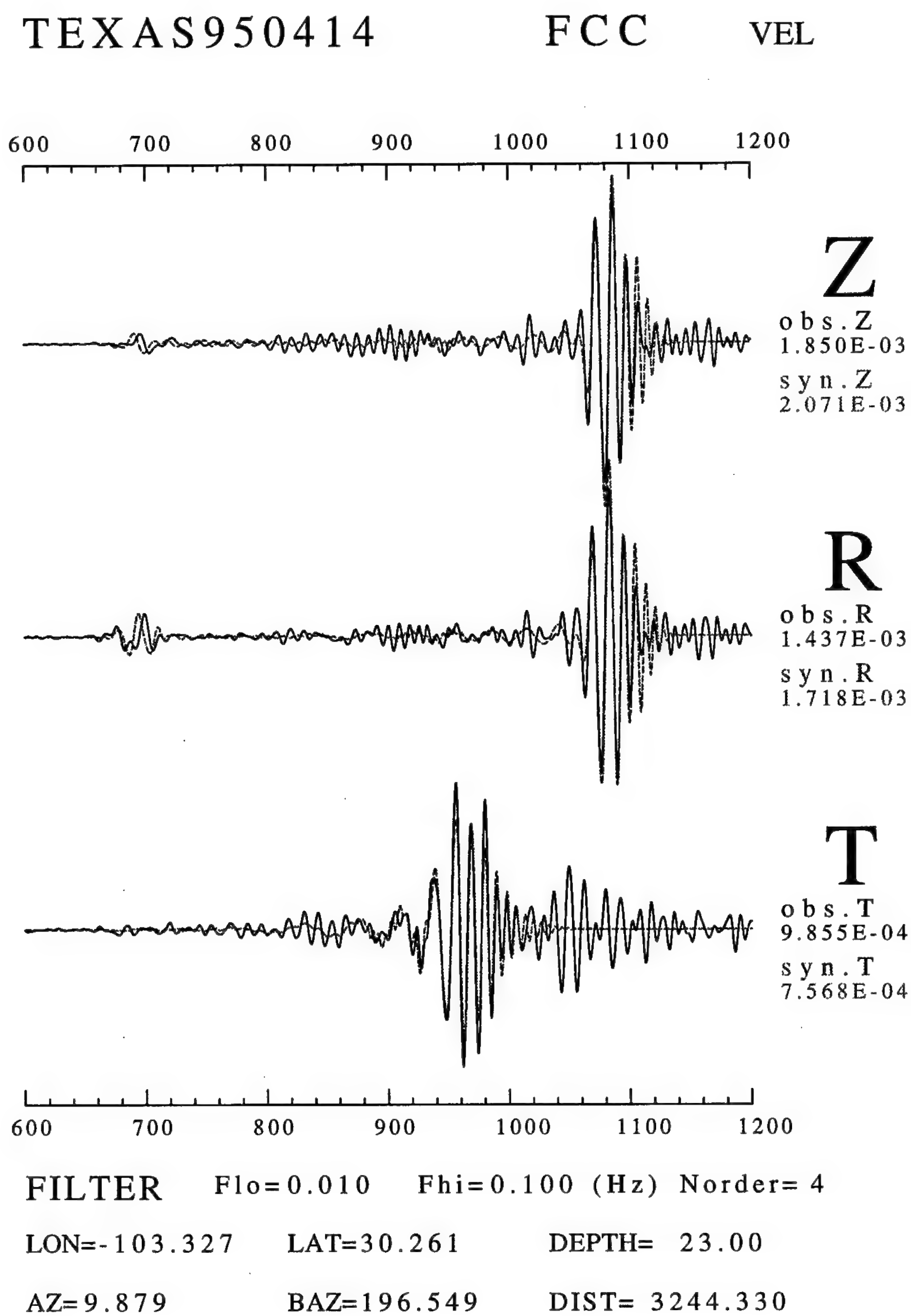

Fig. 3.11c. (Cont'd). (c) 0.01-0.1 Hz. The SS phase arrives at 660 seconds. The inverted model can fit fundamental mode Love wave and Rayleigh wave waveforms as high as 0.1 Hz, but it lacks the ability to simulate the higher modes.

features. For the craton there is some evidence for anisotropy and crustal Q is high. For the mountain region, although the inverted

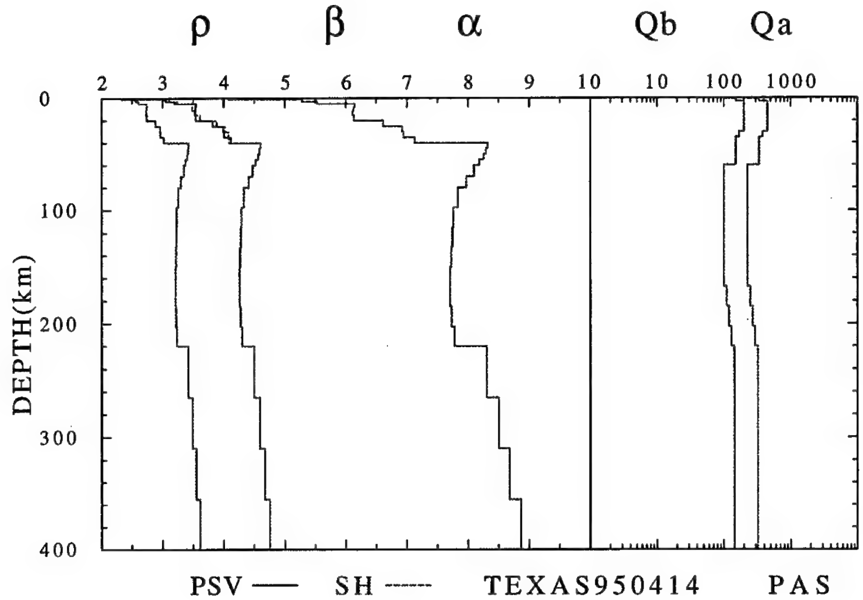

Fig. 3.12. The inverted models for PAS. There is no clear anisotropy effects. The crustal Q is very low.

model show very similar shear velocity structure like TNA model, but from the S-wave waveform the model prefers a velocity discontinuity at 220 km. These features worth more effect on them.

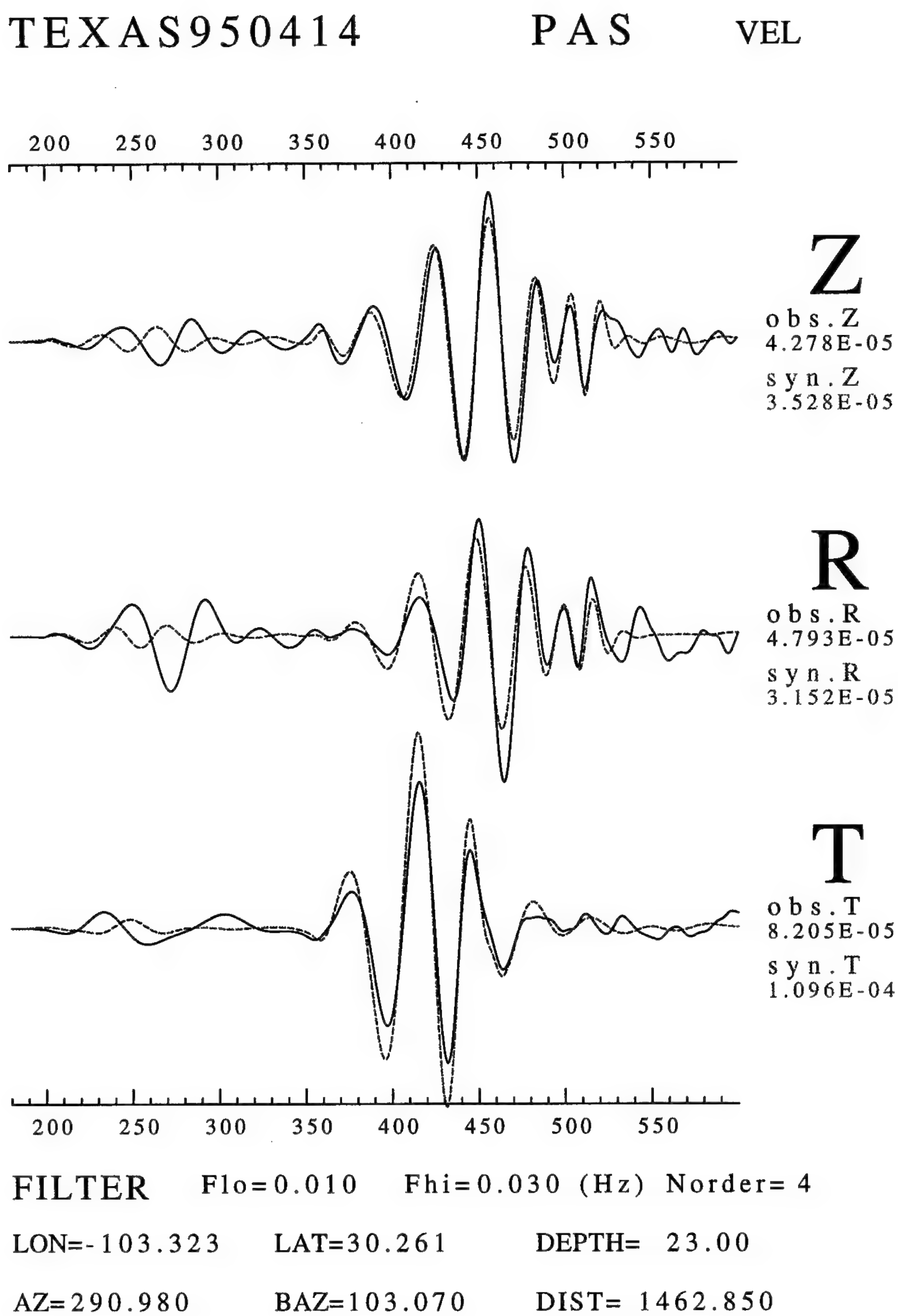

Fig. 3.13a. Waveform fitting are shown on three frequency bands : (a) 0.01-0.03 (b) 0.01-0.05 and (c) 0.01-0.1 Hz. The S wave signal arrives at 350 seconds.

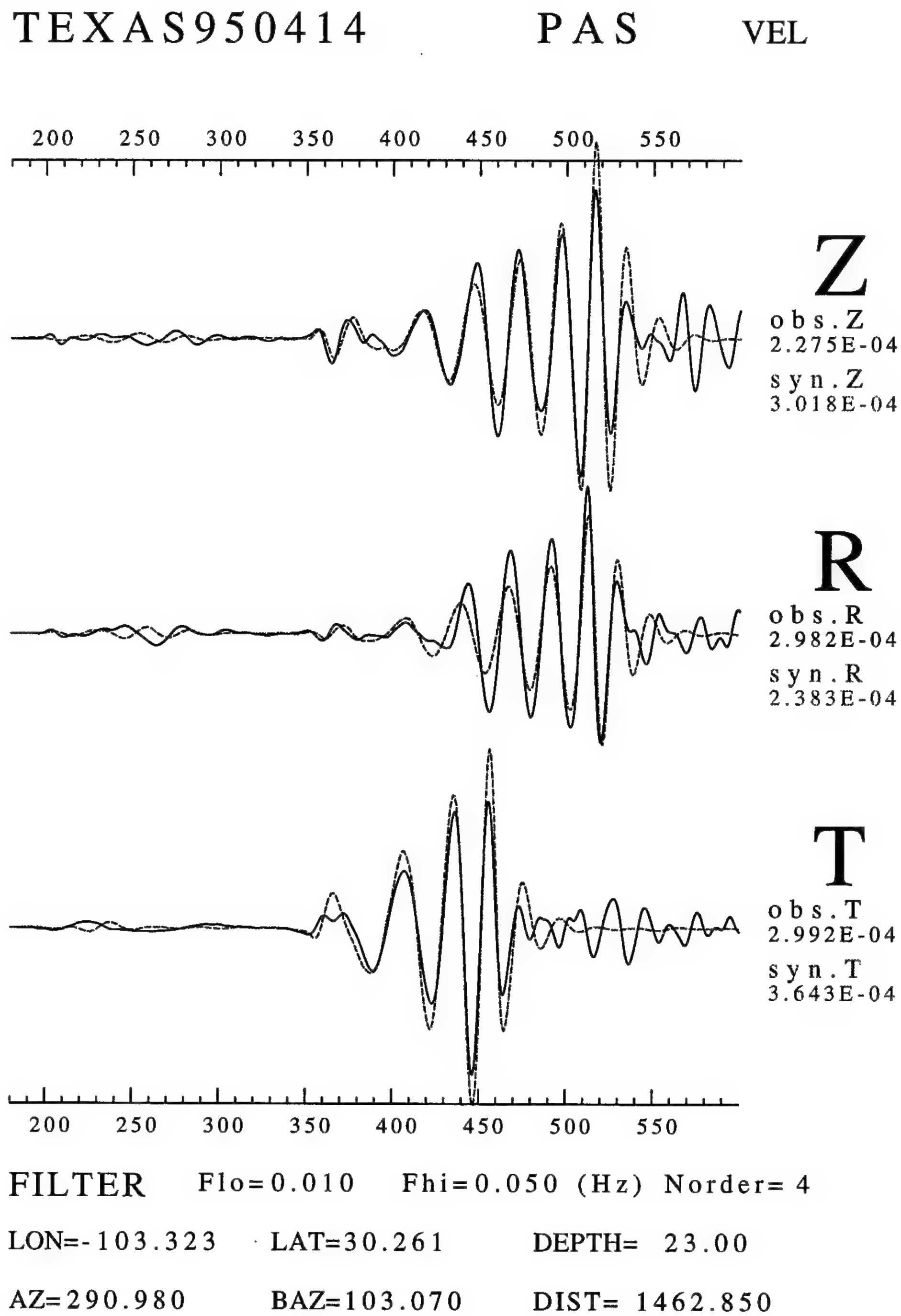

Fig. 3.13b. (Cont'd). (b) 0.01-0.05 Hz.

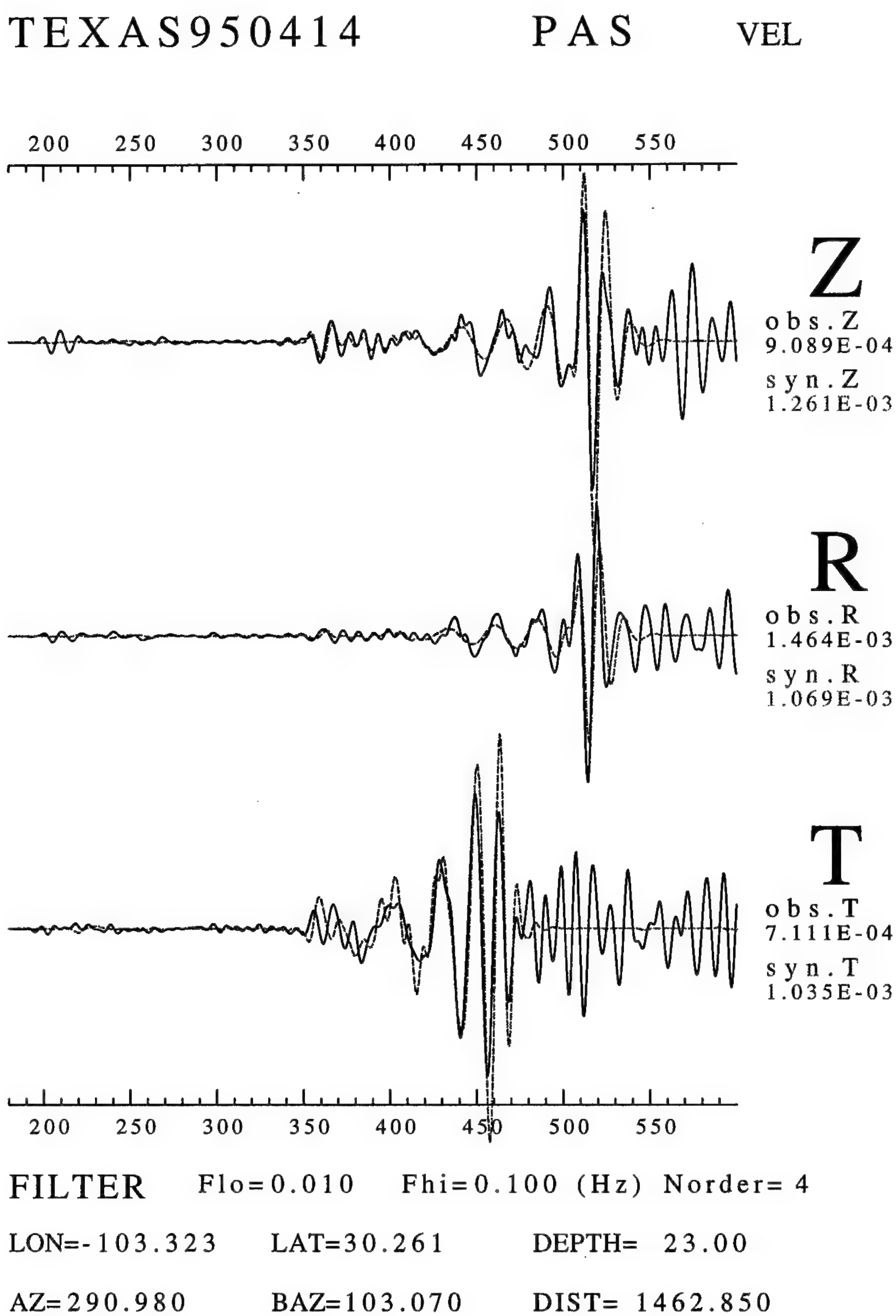

Fig. 3.13c. (Cont'd). (c) 0.01-0.1 Hz.

CHAPTER 4
GENETIC ALGORITHMS

Most of seismological inverse problems are nonlinear. The techniques used to solve such nonlinear problems can be concluded as two groups. The strategy of first group is to linearize nonlinear problems, then use iterative processes to seek a better solution by using the gradient information of misfit function. The strategy of second group is to directly search the model space, and find the acceptable models.

The methods such as least squares method, steepest descent, and conjugate gradients belong to the first group. Although these methods are widely used in seismology, there is a well-known disadvantage that is the requirement of a good starting model. For studying large scale low-frequency structures or deep features which beneath the lithosphere, this would not be a real problem because the researches of the past half century already provide some good starting models such as PREM, IASPEI91 (Kennett and Engdahl, 1991). In the other hand, for studying the crustal or lithospheric structures, a good starting model may not be available because the crust or lithosphere is the most structural heterogeneous region in the Earth. However, to study the lithosphere is very important because the evolution history of lithosphere is hidden in its structure. We have to investigate the structure of the crust and lithosphere all over the world to know the evolution history, to understand the tectonic processes, to make better prediction of seismic activities, and to lower the damage of hazards.

Base on such a situation, we need to find a way to investigate many possible models, i.e. to search the whole model space and find out the possible models of structure and their variations. The methods

like Monte Carlo method, simulated annealing (SA), and genetic algorithms (GA) are belong to this group. The Monte Carlo method is a random search method which has been used in seismology for a long time (e.g. Press, 1968; Keilis-Borok and Yanovskaja, 1967). Press (1968) showed a successful experiment which use Monte Carlo method to search the model that can produce correct body-wave travel-times, surface-wave dispersion, the earth's free oscillation periods, mass, and moment of inertia. Six models were found from about five million randomly generated models. As pointed out by Press (1968), the reason that using Monte Carlo method is because it offers the advantage of exploring the range of possible solutions and indicate the degree of uniqueness achievable with currently available geophysical data. Examine these six models, we can find that the structure for the lower mantle are pretty consistent, but large variation in the upper mantle. However, Monte Carlo method has its own disadvantage. As pointed out by Keilis-Borok and Yanovskaja (1967), Monte Carlo method does not use information obtaining from previous trials in the next trial.

For recent years, simulated annealing and genetic algorithms methods are very popular in seismological society. The simulated annealing method is stimulated from the crystalizing process observed in chemistry. The genetic algorithm is inspired from the evolution process observed in biological science. These two algorithms are better search methods than Monte Carlo method because they use the information obtained in previous trials. The seismological applications such as estimation of residual statics (Rothman, 1985 and 1986), waveform inversion of reflection data (Sen and Stoffa, 1992; Stoffa and Sen, 1991; Sambridge and Drijkoningen, 1992), earthquake hypocenter location determination (Sambridge and Gallagher, 1993), and receiver function inversion (Shibutani, Sambridge, and Kennett, 1996). There is one comon thing for all these applications, that is they all deal with nonlinear problems, and particularly in some cases which due to complexity of structure.

For example, in the receiver function inversion, Ammon *et al.* (1990) showed that the final models were dependent on the initial models. Shibutani *et al.* (1996) showed that using genetic algorithm can estimate an average model which is more stable and less dependent on the starting assumptions.

We can see that both simulated annealing and genetic algorithms are good ways to perform the uncertainty assessment in a complicated nonlinear problem. As stated by Sambridge and Drijkoningen (1992) on SA and GA methods: "any problem feasible by one could also be tackled by the other". To select which methods (GA or SA) is better on surface-waveform modeling problem, we need to know both algorithms and the purpose of our application. As is well known, generating multi-mode surface wave synthetics is computationally intensive. So the computation time will be a crucial factor for selection.

4.1 Workflow of Simulated Annealing method

The computation procedures of simulated annealing is like following.

- start from an arbitrary model
- temperature-loop : at temperature $T = T_0 - k \cdot \delta T$
    - □ parameter-loop : for model parameter $S_i, i = 1, \cdots, m$

      fix all other parameter value except S_i

      for the parameter S_i, there is n possible values.
        - o possible-value-loop : $S_{ij}, j = 1, \cdots, n$

          calculate the energy function $E(S_{ij})$ which is the normalized cross-correlation of observed and synthetic seismogram.
        - o end of possible-value-loop
    - □ end of parameter-loop

  compute the probability distribution

$$P(S_{ij}) = \frac{\exp[\frac{-E(S_{ij})}{T}]}{\sum_{j=1}^{m} \exp[\frac{-E(S_{ij})}{T}]}$$

- end of temperature-loop

We can see that for each temperature, it is necessary to perform $(m \cdot n)$ forward computation of synthetics. If there is k step in lowering temperature to reach the global minimum, the total forward computation will be $(k \cdot m \cdot n)$. The problem is that there is no rule in choosing the starting temperature T_0 and increment of temperature difference δT. Basu and Frazer (1990) designed a sequence test runs to find the critical temperature. Even though, it is still too time consuming for surface-waveform modeling.

4.2 Workflow of genetic algorithm

For a m member society evolving through n generation, the computation sequence of genetic algorithm is as following.

- Randomly generate m individuals as first generation.
- Generation-loop : for $generation = 1, \cdots, n$

  Compute m synthetic seismograms (individuals)

  Evaluate each individual's performance; i.e. calculate the goodness-of-fit.

  □ population-loop : for $child = 1, \cdots, m$

    Base on the individuals' performance (probability)
    to select them as parents;
    to change parents' DNA; and
    to apply possible mutation on their children.

  □ end of population-loop

- end of generation-loop

We can see it is possible to perform GA on a small population society. This will be more computational efficient than SA in the surface-waveform modeling problem. However, perform GA on a small population society has its own risk, as pointed out by Sambridge and Drijkoningen (1992). That is when society's members are not close to global solution, the relatively good individual in the society will multiple itself and dominate the population (i.e. trapped in local minimum). This problem can be solved by increase the population size. However, our purpose for using GA in surface-waveform modeling is not relying on GA to reach the global minimum. Instead, we prefer to have several runs to see the possible uncertainty, get the rough idea about the structure, and find some good initial models for other inversion techniques. In our test, a GA run will take 1 to 3 hours of CPU time in SUN ULTRA 1 (167MHz) workstation. It is affordable to have several reruns if we find it trapped in such situation. So we choose the genetic algorithm for modeling surface-waveform. In the following sections, we will address several technical issues in appling GA in surface-waveform modeling.

4.3 Smoothing mechanism

Since GA is one type of random search method, there is no strong constraint between parameters (layer S-velocity in this case). Usually, there will be a strong zig-zag pattern in the velocity model; this is undesirable for the purpose in seismology if the emphasis is on determining the simplest acceptable model. To reduce this pattern in velocity model, we smooth the layer velocity by considering the adjacent velocity contrast without change the vertical travel times. As shown on Figure 4.1, the original model (solid line) has a strong zig-zag pattern but the smoothing mechanism reduces the contrast between layer shear velocities (dashed line represents the after smoothed model). We are thus attempting to find the smoothest model consistent with data.

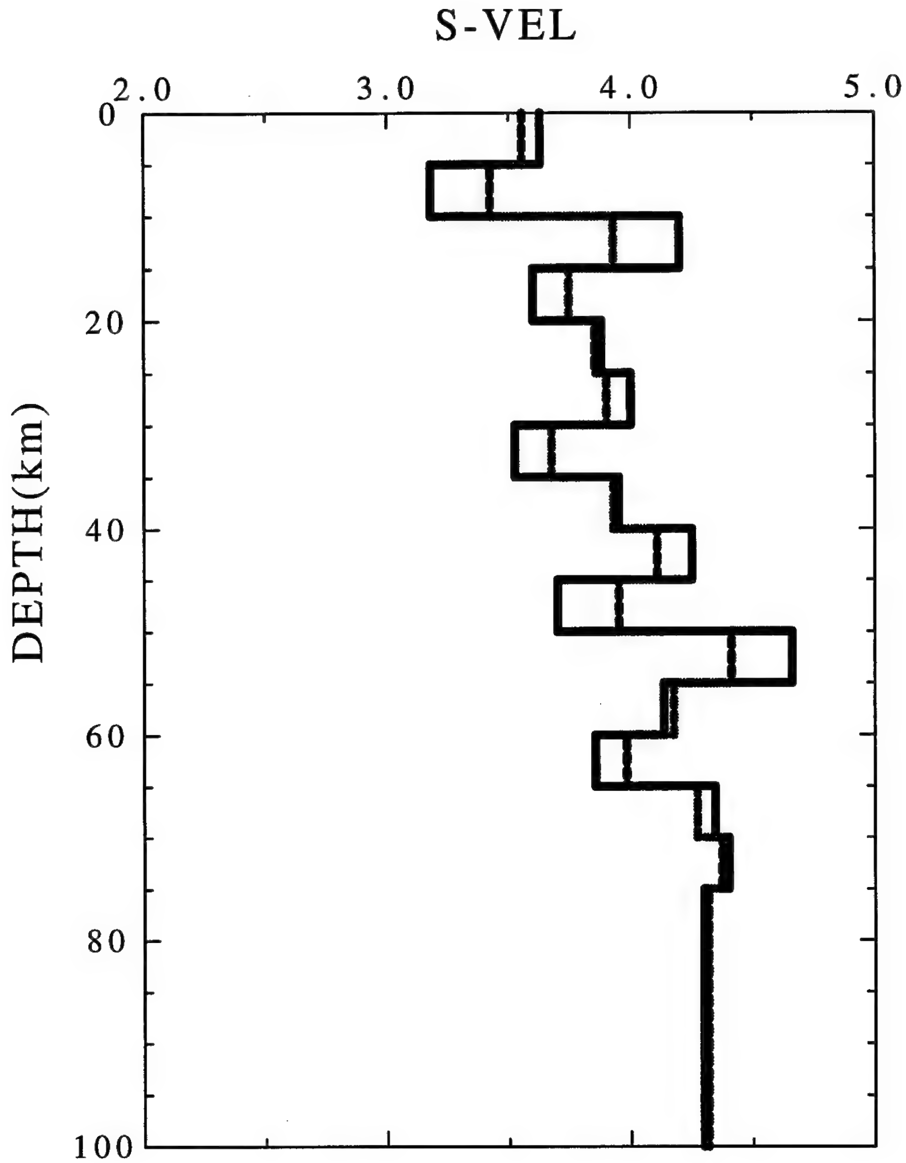

Fig. 4.1. In GA, models are randomly generated, so there always have some 'ZIG-ZAG' patterns. For obtaining a smooth background velocity model, a smoothing mechanism is introduced. Without changing the vertical shear wave travel time, the smoothed model (dashed line) has less 'ZIG-ZAG' pattern than the original model (solid line).

The introducing of this smoothing mechanism can be viewed as a heavy mutation case in GA. Of course, the best model may not survive under such mutation through final. But, we can find it from the record

of models of each generation. This may help to escape from some local minimum in some cases and provide driving force for evolution.

4.4 Generation number and population size

Although GA is a global search method which can potentially find the global minimum, we did not set that as our goal in this study. Due to the intensive computation load of generating multi-mode surface-wave synthetics, we limited our computations to a small population size and only perform it through finite generations. We hoped, via using GA search method, to get some good models to use as starting models for other inversion algorithms. To understand what generation number is sufficient for our purpose, we have tested the consequences of a large generation number. In this test, shown as in Figure 4.2, we performed 500 generations and find that after 50 generations model improvement proceeds less rapidly, indicating a degree of convergence. Therefore, in the subsequent tests, we will only perform 50 generations for a small population (i.e. 20), and this will only consume 1 to 3 hours of CPU time in SUN ULTRA 1 workstation.

In some cases, we do find the GA trapped in a local minimum. Usually this situation is associated with other difficulties like cycle-skipping problem for teleseismic waveforms. This will be discussed later.

4.5 Criteria of goodness-of-fit

A surface-wave signal has a longer duration and a more complicated waveform behavior than any single, pulse-like body-wave phase. To model such long-duration complicated waveforms, there is a cycle-skipping problem which may produce an unreasonably low or high velocity model. In addition when processing surface-wave data, we

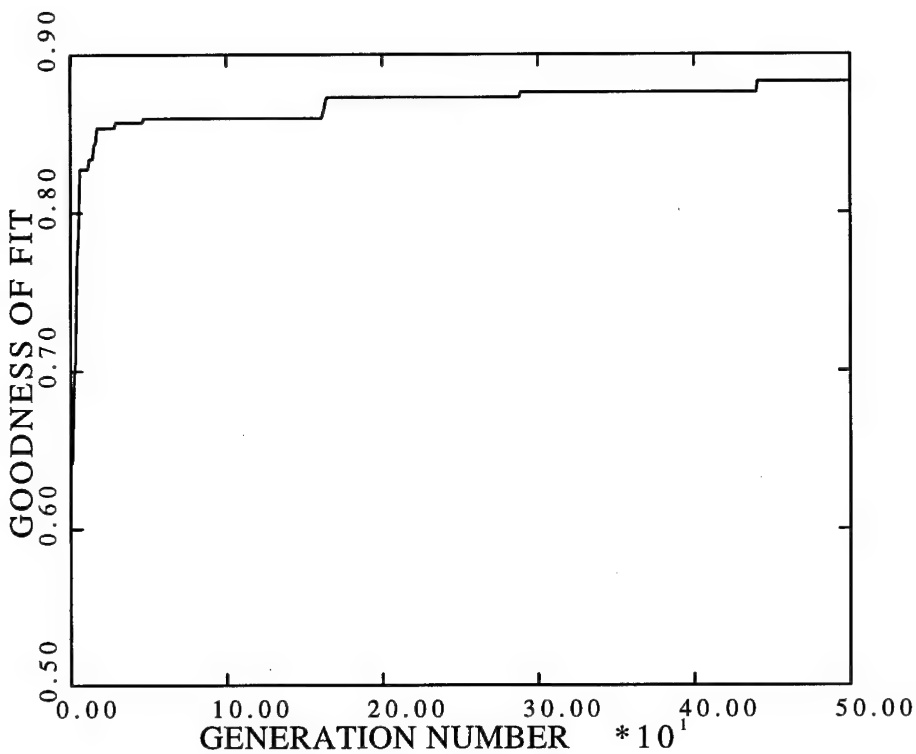

Fig. 4.2. To know how many generations is necessary for surface-waveform modeling, an experiment with large generation number (500) is tested. The result shows that GA can find a fairly good model within 50 generations. After that, the model improvement proceeds less rapidly.

cannot shift the synthetic seismogram to match the observed arrival time, a well adapted technique in processing body wave data such as receiver function inversion. Due to this effect, an L2 norm, such as used by Gomberg and Masters (1988), may not be suitable for quantifying surface-waveform goodness-of-fit. Instead we choose a cross-correlation as our criteria of goodness-of-fit to circumvent the oscillatory signal character, and to focus on agreement of waveform shapes.

Surface-waves usually have a broad frequency content, which means a single cross-correlation measurement only represents the fit of the largest amplitudes, which are typically high-frequency for crustal earthquakes. This will only resolve the very shallow part of

structure but leave the deeper structure uncertain with high variation. To overcome this problem, we divide the frequency range of interest into several subranges and evaluate the cross-correlation of narrow band-filtered observed and synthetic seismograms for each subrange. An averaged cross-correlation value of these subrange cross-correlations is used as our goodness-of-fit. For example, for ANMO, we divided the period range (10-50 sec) into 4 intervals : (10-20 sec), (20-30 sec), (30-40 sec), (40-50 sec). Using these period intervals as the ranges for bandpass filtering observed and synthetic seismograms, a cross-correlation value is computed for each interval and an average cross-correlation is used as our goodness-of-fit.

4.6 Test on the western Texas earthquake

We apply this GA search method to the April 14, 1995 Texas earthquake (30.26 °N 103.33°W, 00:32:55UT). The source depth of the Texas event is 23 km, with strike, dip, rake angles of 114°, 64°, -101°, respectively with $\mathbf{M}_w = 5.6$.

Three stations (ANMO, TUC, WMOK) are selected to show the ability of the GA search method. For each station, three plots of final good models, waveform fitting, and cross-correlation of different period ranges of the best result are shown. The first plot shows the search bounds (thickest dashed line), the good models (thin dashed line) which have goodness-of-fit greater than a certain value, and the best model (black solid line). The second plot shows the waveform fit of the best model. The observed seismogram is drawn as a black line and the synthetics as a thin dashed line. The third plot shows the cross-correlation measurements of the best searched model in the different period ranges which gives us the idea how good can this model fits the data. We also can see the reason why using averaged cross-correlation as our criteria of goodness-of-fit because the broadband (e.g. 10-50 sec) waveform at top row is dominated by high frequency signal such as

waveform on the second row (e.g. 10-20 sec).

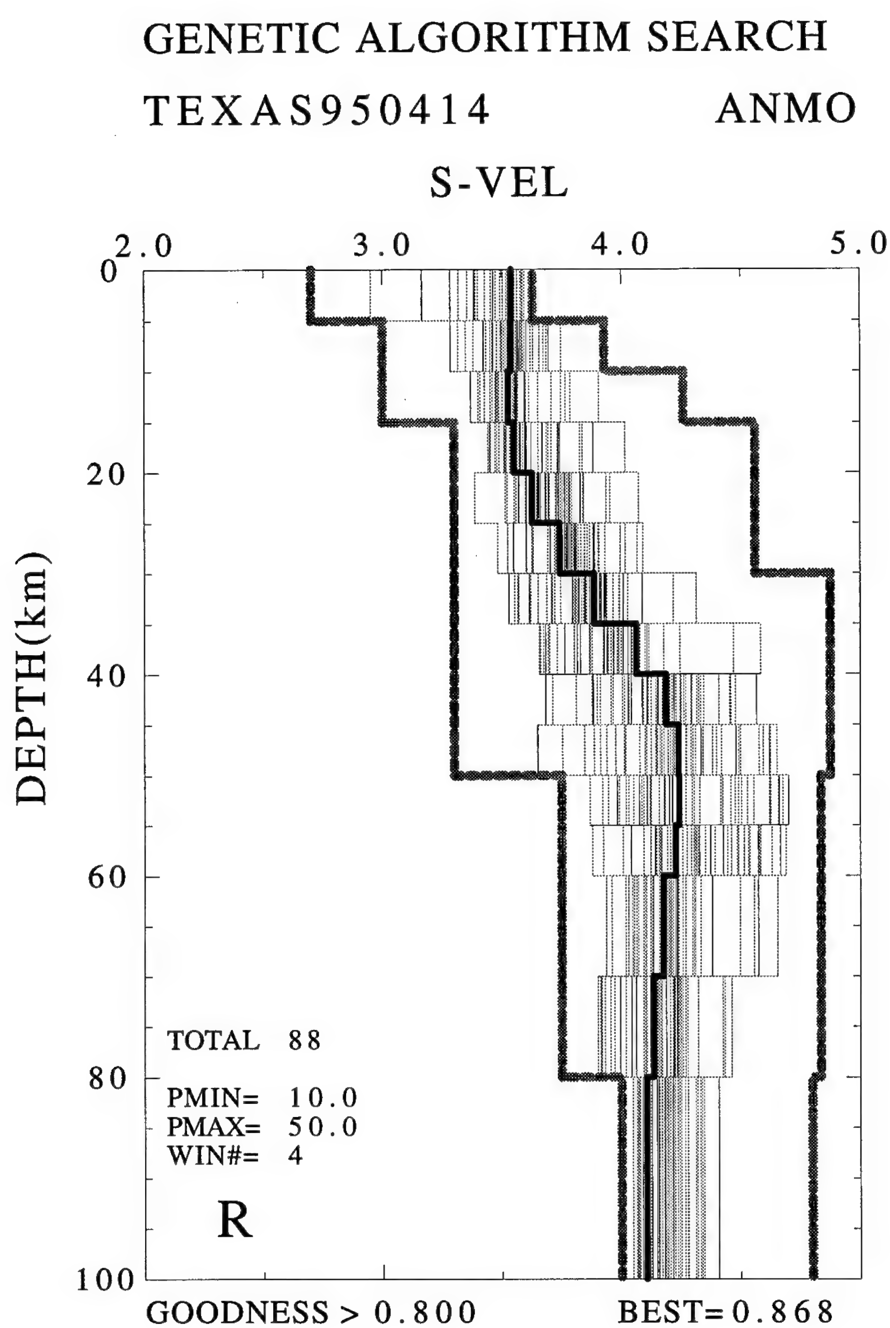

Fig. 4.3b. (cont'd). (b) Searched models for Rayleigh wave.

Examining the results for ANMO (Figures 4.3, 4.4, 4.5), we found that our best final model for Rayleigh wave has a unreasonably low

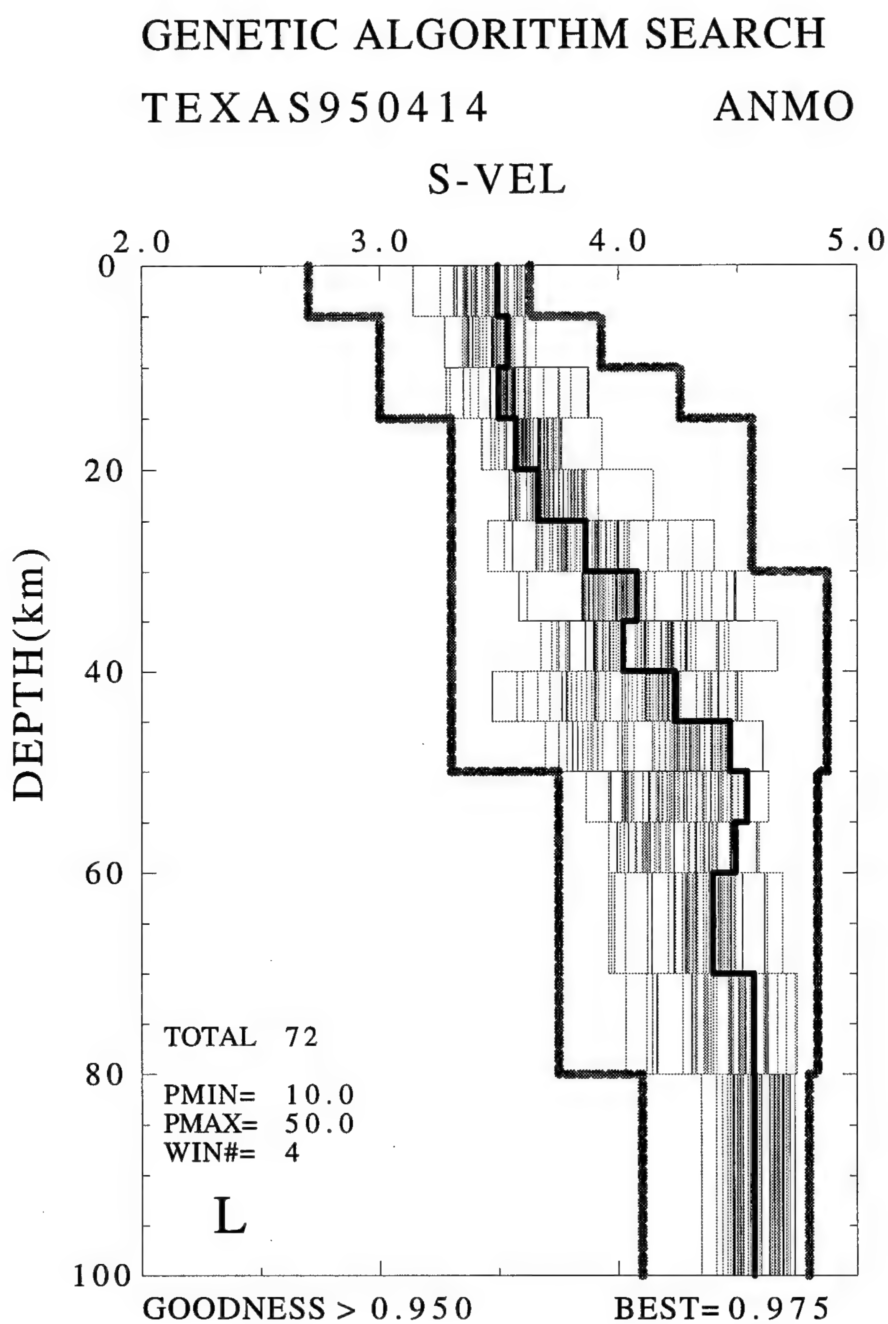

Fig. 4.3a. Using GA to model the surface-waveform of station ANMO. In this test, two GA runs were conducted for Love and Rayleigh wave respectively. The searched models are shown in these figures, the heavy lines are the search bounds, the thin lines are searched model which have their goodness-of-fit greater than a certain value shown at the left bottom, and the best model is plotted as thick black line. (a) Searched models for Love wave.

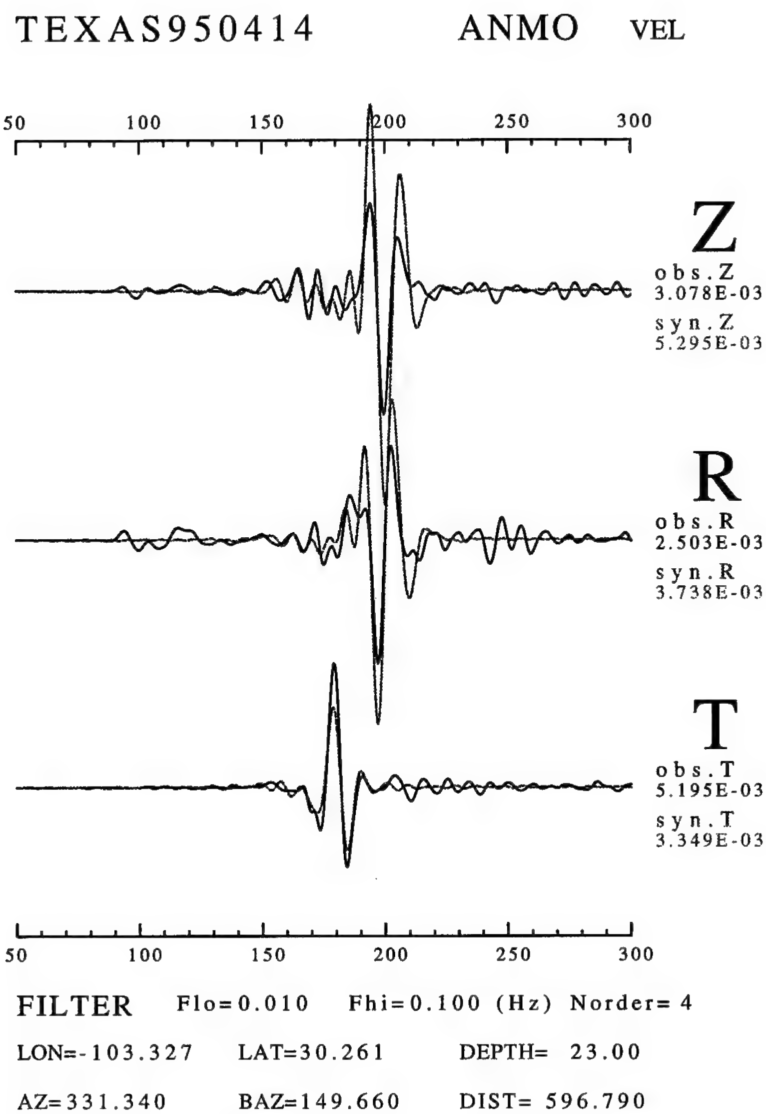

Fig. 4.4. For ANMO, the observed waveforms (solid line) and predicted waveforms (dashed line) which generated for the best searched models for Love and Rayleigh wave at frequency range 0.01 to 0.1 Hz.

velocities for layers deeper than 50 km. Also on the cross-correlation diagram, we can see that at the 40-50 second period, the envelope's maximum of the Z component is off central position. This is the flaw of currently used criteria which can not overcome the cycle-skipping problem. Combining the correlation coefficient at zero lag with the lag shift of the maximum correlation may be another goodness of fit

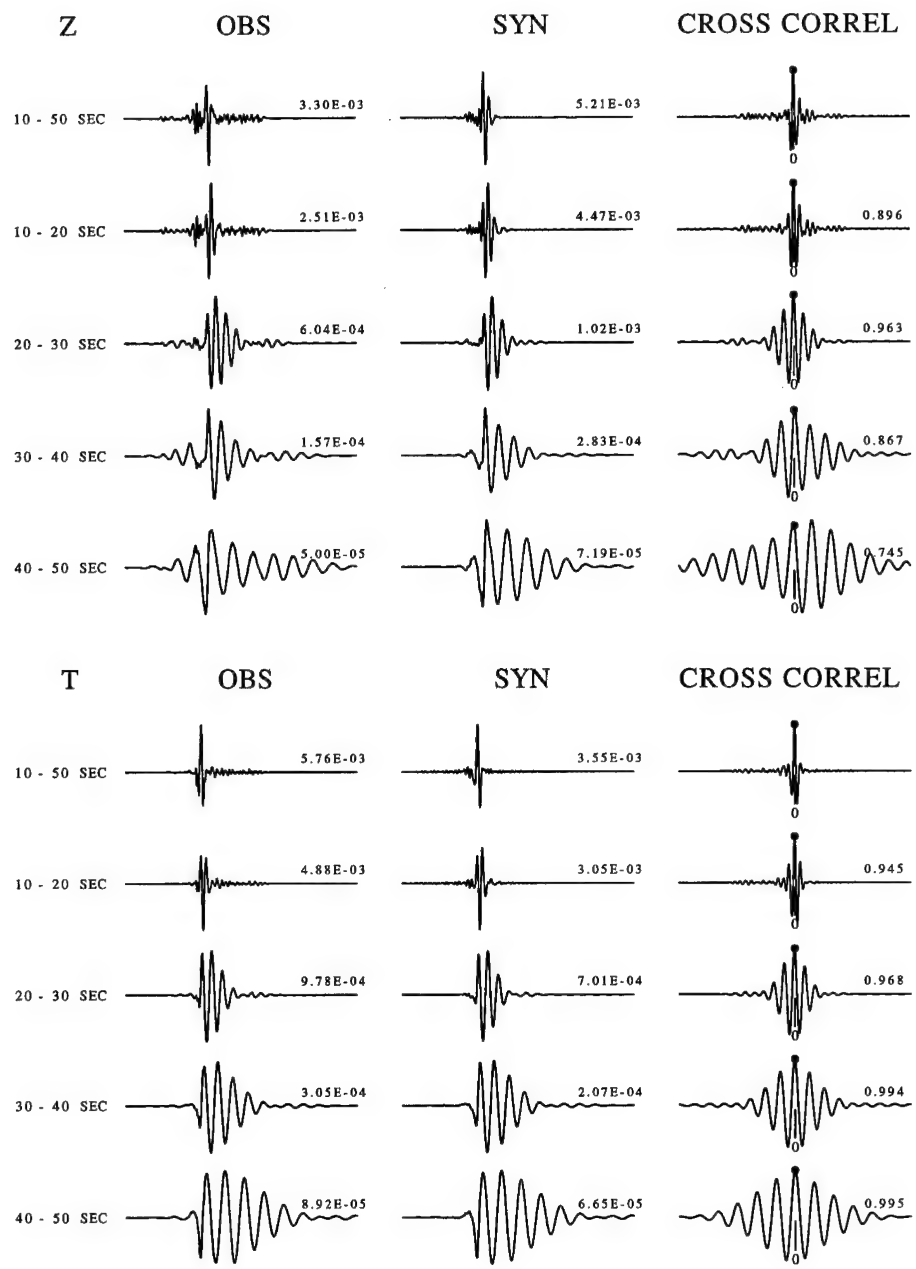

Fig. 4.5. For ANMO, the filtered cross-correlations of observed and synthetic waveforms at different frequency bands. The number at the right of cross-correlation traces is the cross-correlation value at zero-lag which is used to construct the value of goodness-of-fit.

criterion to use in the future. However, compare two best models obtaining from separated GA searchs for Love and Rayleigh wave, we can find these two models show a very similar model for upper 50 km.

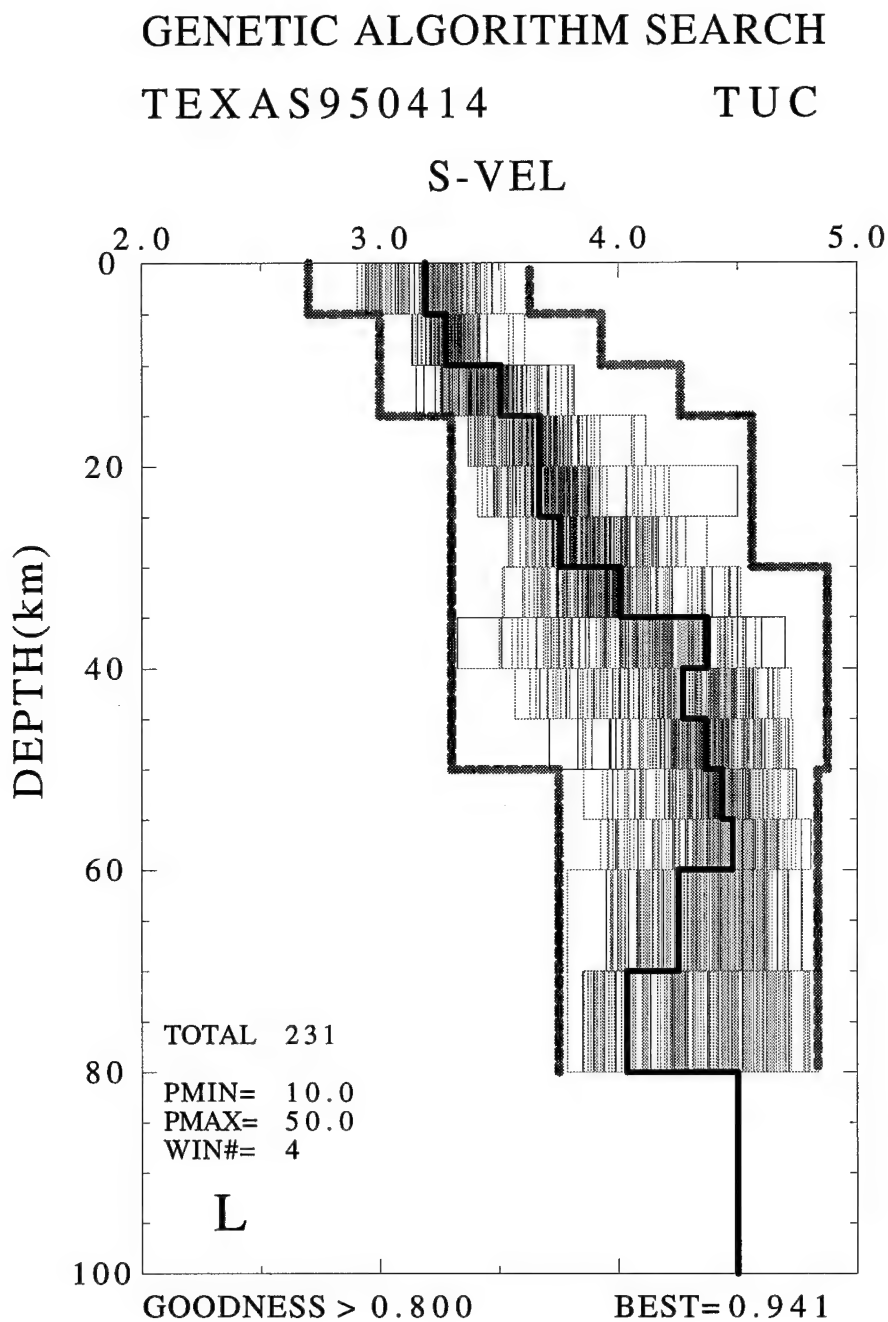

Fig. 4.6a. Separated GA searchs for Love and Rayleigh wave recorded at TUC. (a) Searched models for Love wave.

At TUC (Figures 4.6, 4.7, 4.8, and 4.9), we tested this search scheme on three cases: using Rayleigh wave only, using Love wave only, and using both Rayleigh and Love wave. The final results show

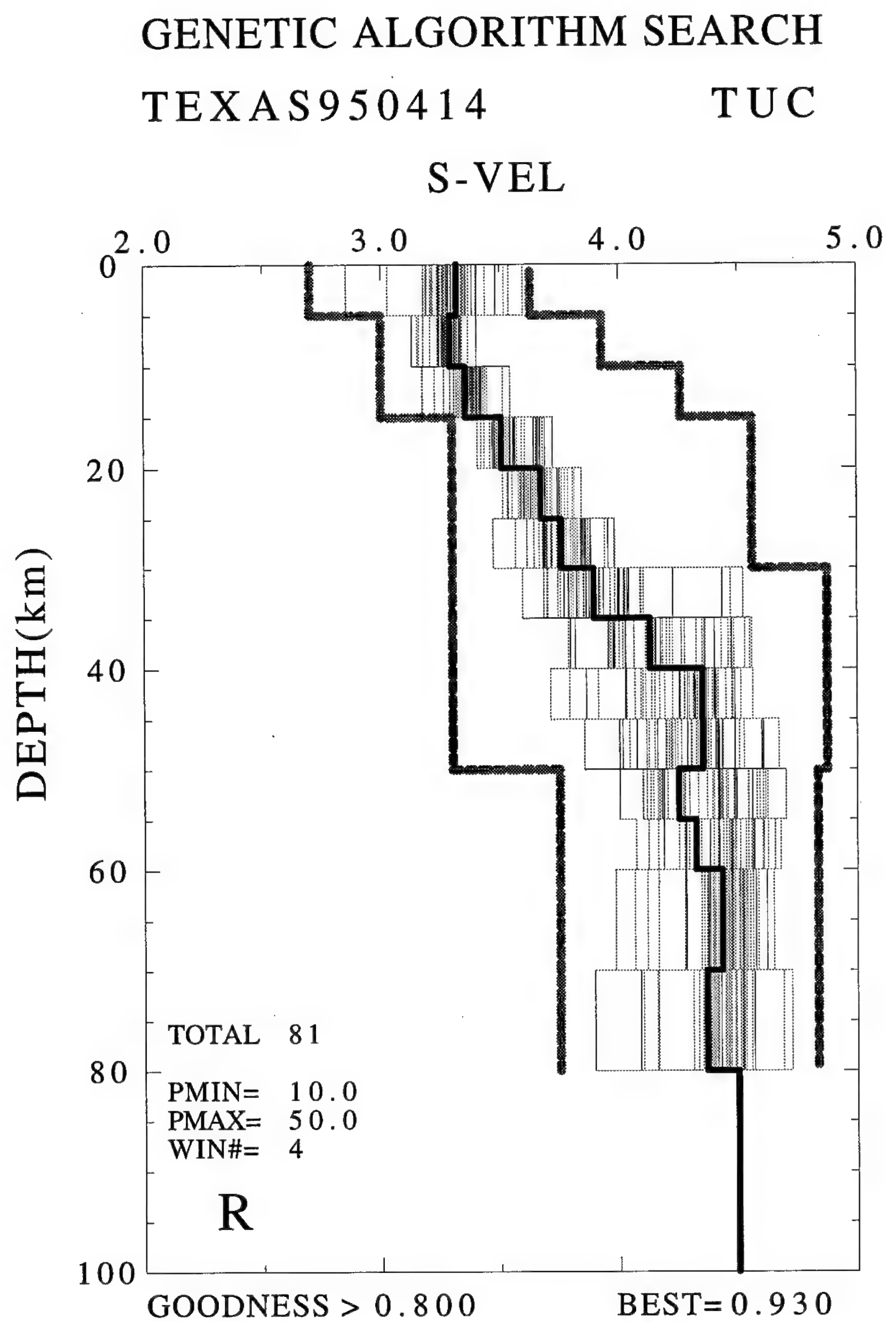

Fig. 4.6b. (cont'd). (b) Searched models for Rayleigh wave.

that waveform fitting from the separated search are better than those from the joint search. But in the macroscopic view, they all have a very similar velocity gradient in the crust. This may illustrate that the crustal structure is well resolved. In the uppermost mantle,

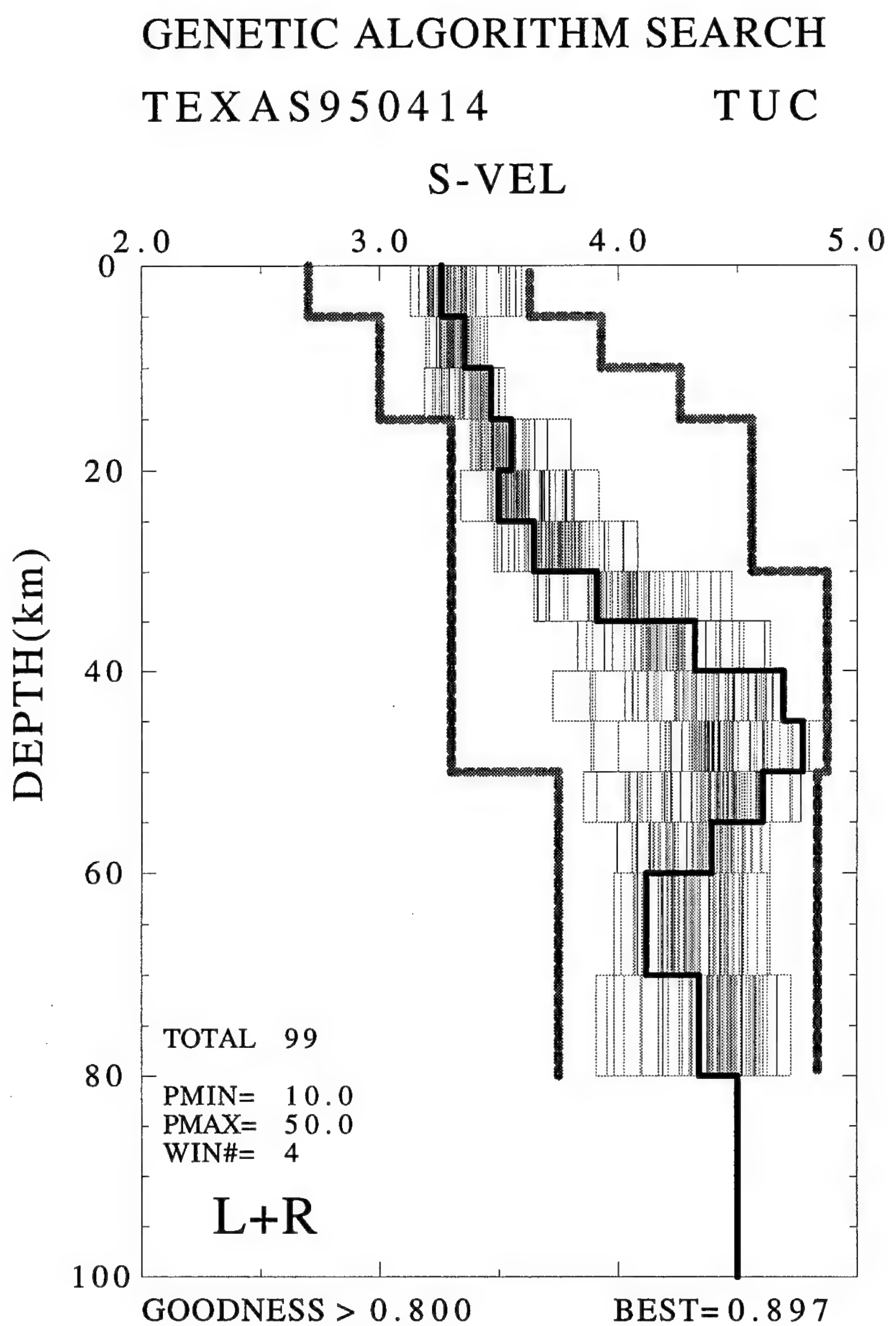

Fig. 4.7. A joint GA search using both Love and Rayleigh waveforms at TUC.

Figure 4.6(a) shows that a fixed half-space beneath 80 km may not be appropriate and cause the model which between 60 to 80 km to lower their values to compensate this high velocity half-space. However, from Figure 4.6(b), the Rayleigh wave seems prefer this high velocity

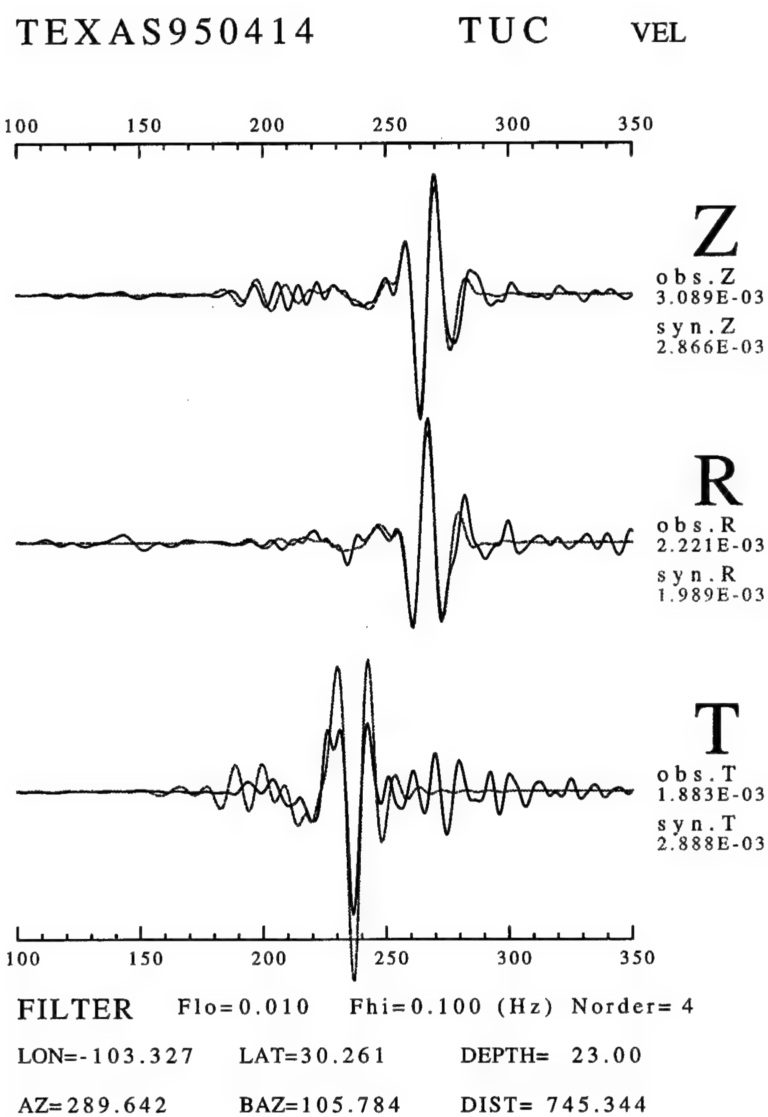

Fig. 4.8a. For TUC, filtered waveforms at frequency range 0.01 to 0.1 Hz for observed and predicted seismograms. (a) The predicted seismograms were generated using the best models from separated searched for Love and Rayleigh wave (Figures 4.6ab).

half-space. So we need to conduct more tests to see if there exists an anisotropy zone beneath the propagation path.

At WMOK (Figures 4.10, 4.11, and 4.12), the waveform of the best model fits the observed seismogram very well, not only for the fundamental mode but also for the first higher mode Rayleigh wave. The

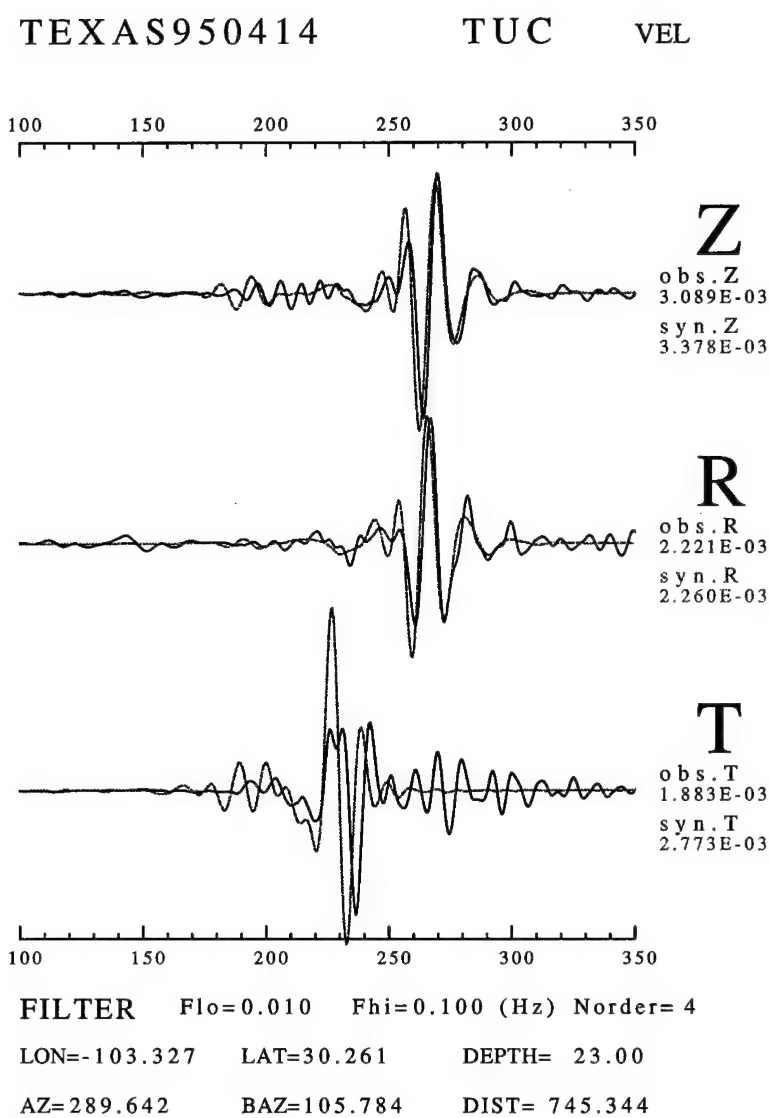

Fig. 4.8b. (cont'd). (b) The predicted seismograms were generated using the best model from a joint searched for both Love and Rayleigh wave (Figure 4.7).

propagation path through the west Texas region is only 655 km. This region under the propagation path is a uniform platform between Rocky mountain and Ouachita orogenic belt. From the final model, we can see the existence of a transitional crust-mantle-boundary between 35 and 50 km.

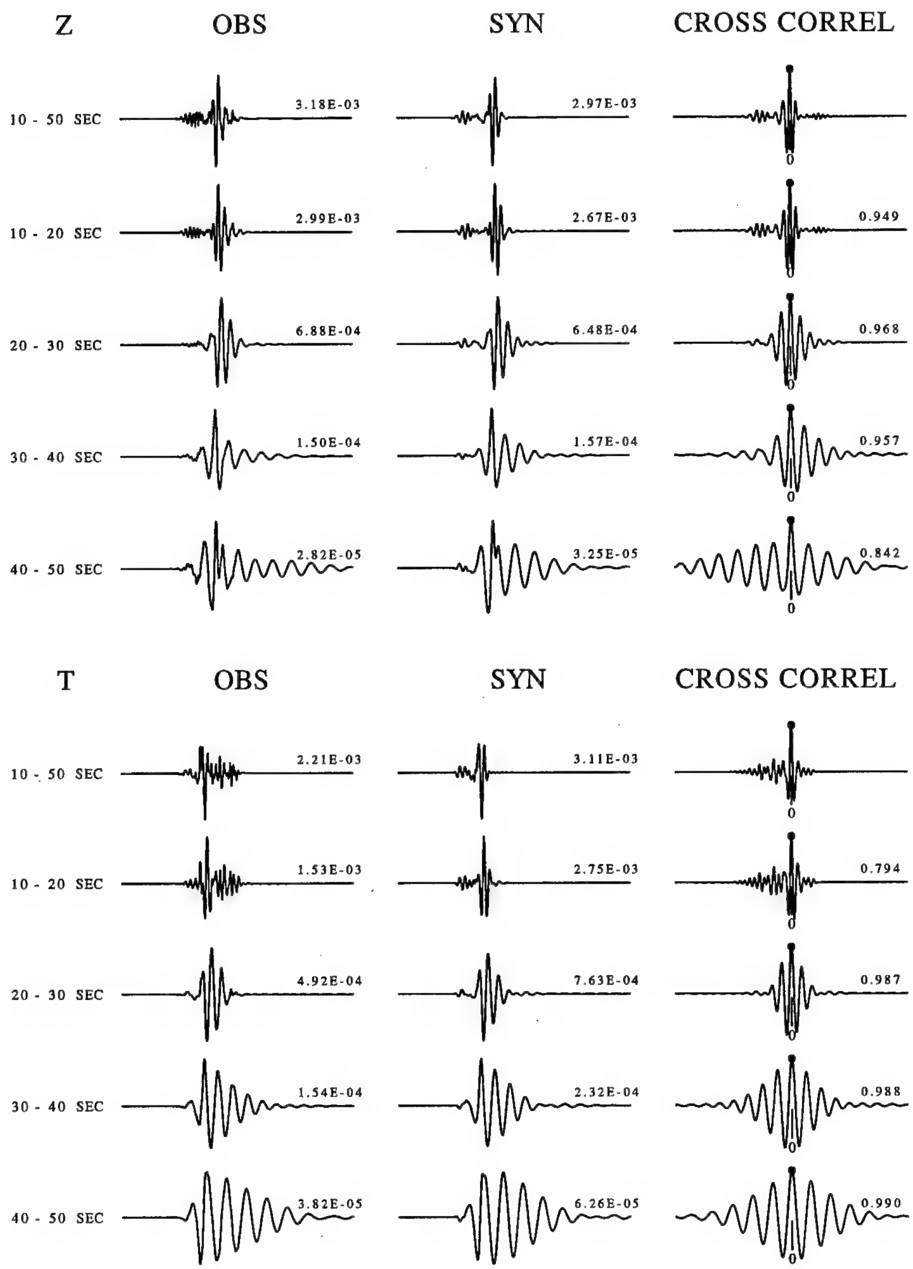

Fig. 4.9a. For TUC, the cross-correlations for the observed and synthetic seismograms which were generated using GA searched models. (a) The synthetics were computed using the best models from separated searched models for Love and Rayleigh wave (Figures 4.6ab).

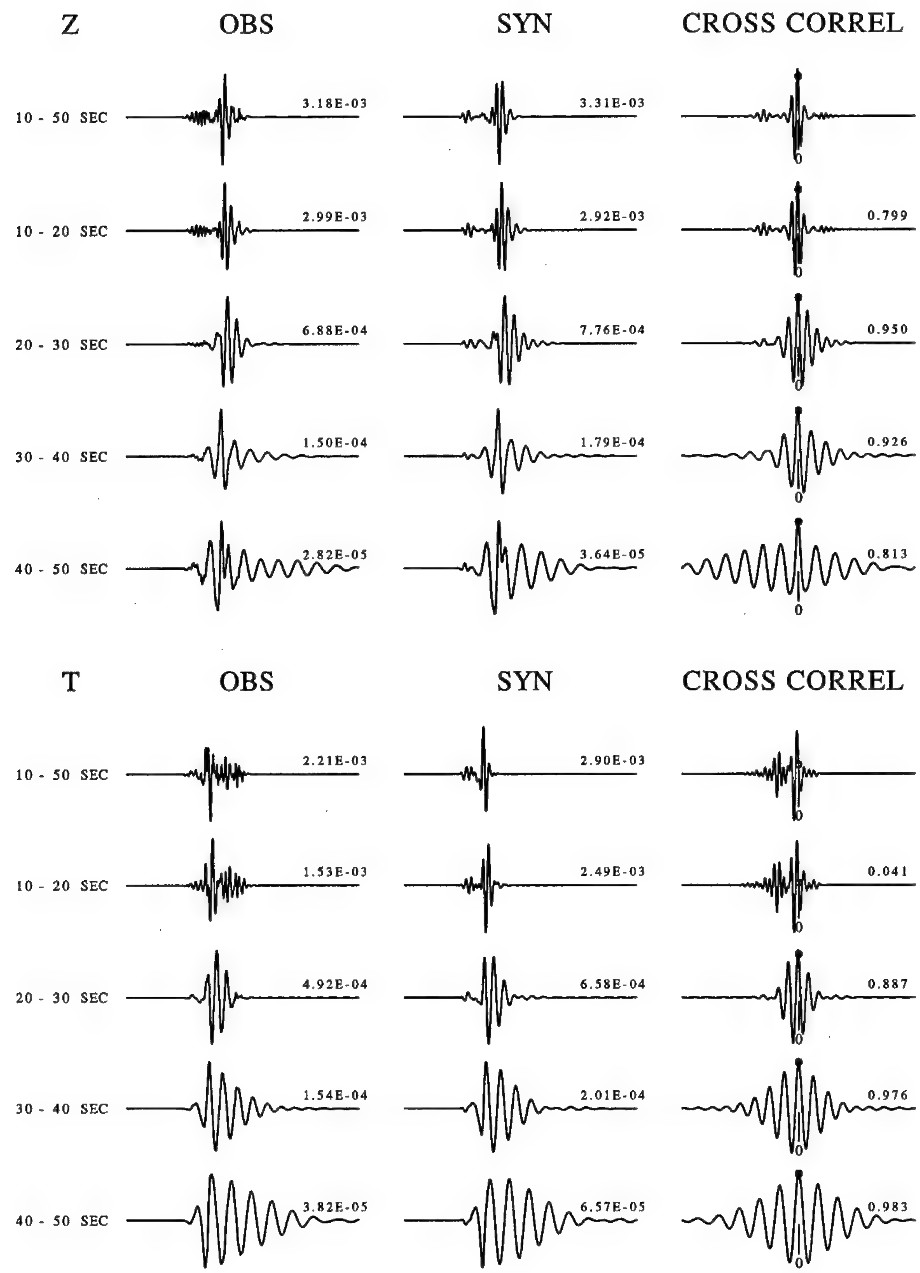

Fig. 4.9b. (cont'd). (b) The synthetics were computed using the best model from a joint search for both Love and Rayleigh wave (Figure 4.7).

4.7 Test for teleseismic traces

In our test, we found that our implement of GA described above is only work for short epicenter distance records. For the teleseismic

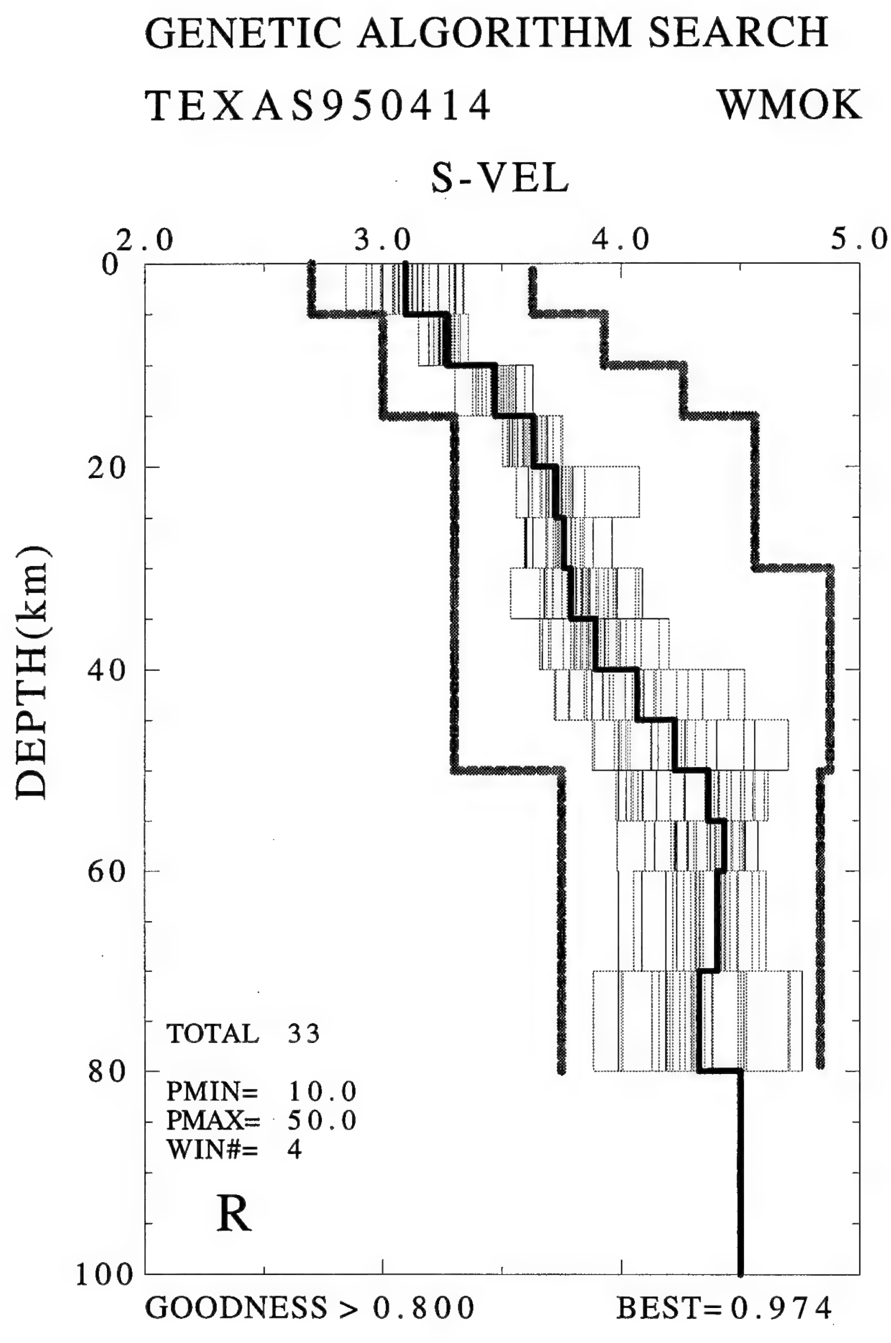

Fig. 4.10. The models from GA search for Rayleigh wave recorded at WMOK.

records, this algorithm doesn't work simply because the cycle-skipping problem. However the surface wave at teleseismic distance samples the upper mantle, and is very important to provide information and constraints on the upper mantle. We need to find a way to apply GA

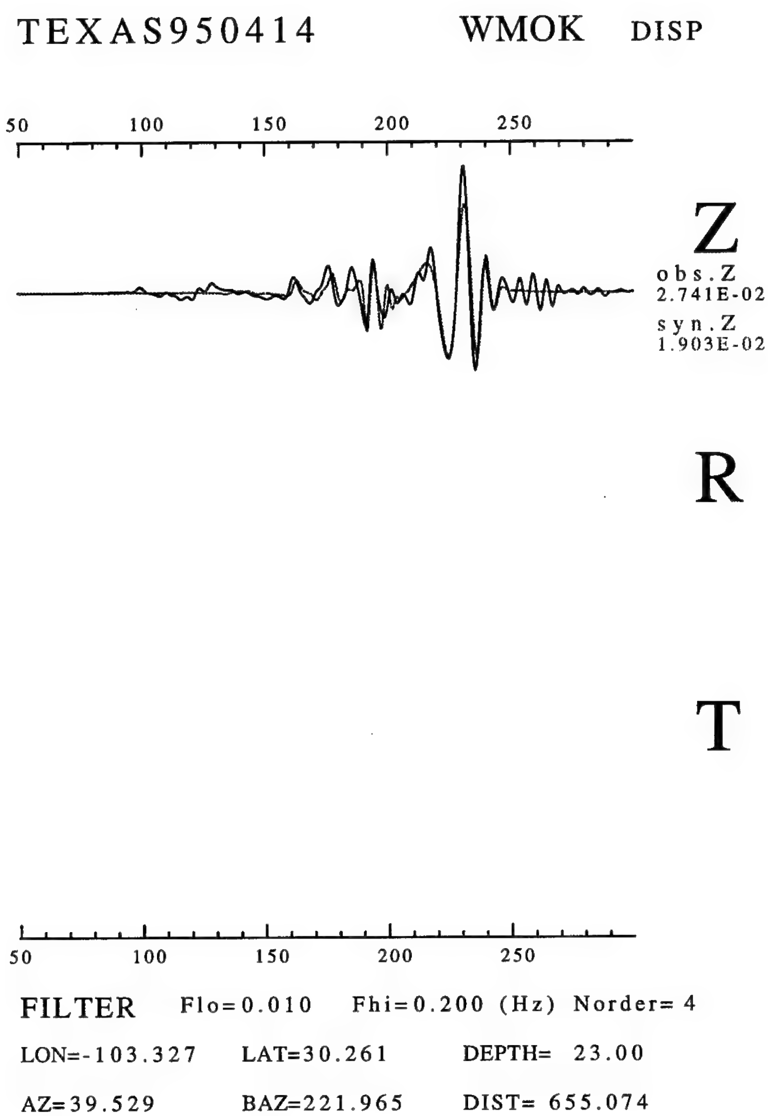

Fig. 4.11. The waveform comparison of observed and synthetic seismograms for WMOK (Figure 4.10).

search technique to teleseismic records.

To apply GA search technique to teleseismic seismograms, we change the way of parameterization. We use three 20 km thick layers over a half-space, which corresponding to the upper crust, lower crust, uppermost mantle, and the upper mantle. From the reports on the structure of lithosphere, we notice that the average velocity for the

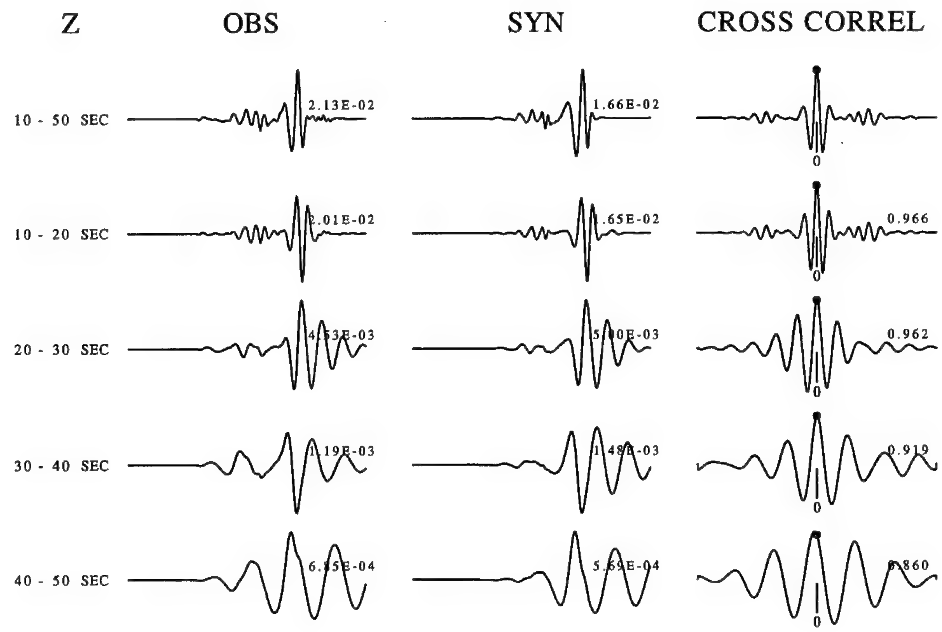

Fig. 4.12. The cross-correlation of the best GA searched model for WMOK (Figure 4.10).

uppermost mantle (40-60 km) is greater than the lower crust (20-40 km), and the lower crust velocity is higher than upper crust (0-20 km). In the upper mantle (half-space in this parameterization), the average velocity should not deviate too much from the uppermost mantle. So we place these physical constraints on our GA searched models, i.e. the velocities of the first three layer should be monotonic increasing and the difference between the uppermost mantle and upper mantle should not greater than 0.2 km/sec.

The test results show a good improvement in searched model, it overcomes the cycle-skipping problem. Three results (HRV, FRB, LMN) are shown here to show the successful GA searched results. However, this strategy has its own weakness. We will use the GA searched results for INK to illustrate the problem.

In HRV (Figures 4.13, 4.14), the best GA searched model can predict the waveform very well at the frequency range 0.01 to 0.05 Hz. The models show a fairly small uncertainty and the best model is

consistent with the velocity structure of stable continents. In FRB (Figures 4.15, 4.16), the GA search show its ability to find the models to predict the well dispersed waveform. We also notice the envelope of synthetics is small than observed seismograms which may reflect that the model is not good enough to produce correct amplitude. From Figure 4.16, we can see that lower crust velocity may be too low and uppermost mantle velocity may be a little high. In LMN (Figures 4.17, 4.18), the waveform fit is all right and its model looks reasonable, but we can see the synthetics does not match the observed Airy phase. This may be caused by the criteria of goodness-of-fit. In applying GA search technique to teleseismic seismograms, we divided the period range 10-70 seconds into 6 subranges. The period content of wave traveling through crust is mainly shorter than 30 seconds, therefore the criteria of goodness-of-fit has more weighting for low-frequency signals and may not properly represent the crust wave. The problem is more clear in INK (Figures 4.19, 4.20). Wen can see that due to the lack of proper representation of crustal signals, GA search technique fail in searching good model for the noisy traces like INK which suffer from multipathing problem.

4.8 DISCUSSION

From this experiment, we found that GA search method works well for regional seismograms ($\Delta < 1000$ km) but not good for teleseismic traces ($\Delta > 2500$ km). The reasons for this are as follow:

- First, the regional seismograms have a more concentrated energy envelope instead of a well-dispersed wavetrain seen in teleseismic surface waves. Therefore, the cycle-skipping problem is less severe in this case.
- Second, the goodness-of-fit criteria may be too simple. The criteria only utilize the amplitude information of the cross-correlation but ignore the time-shift information.

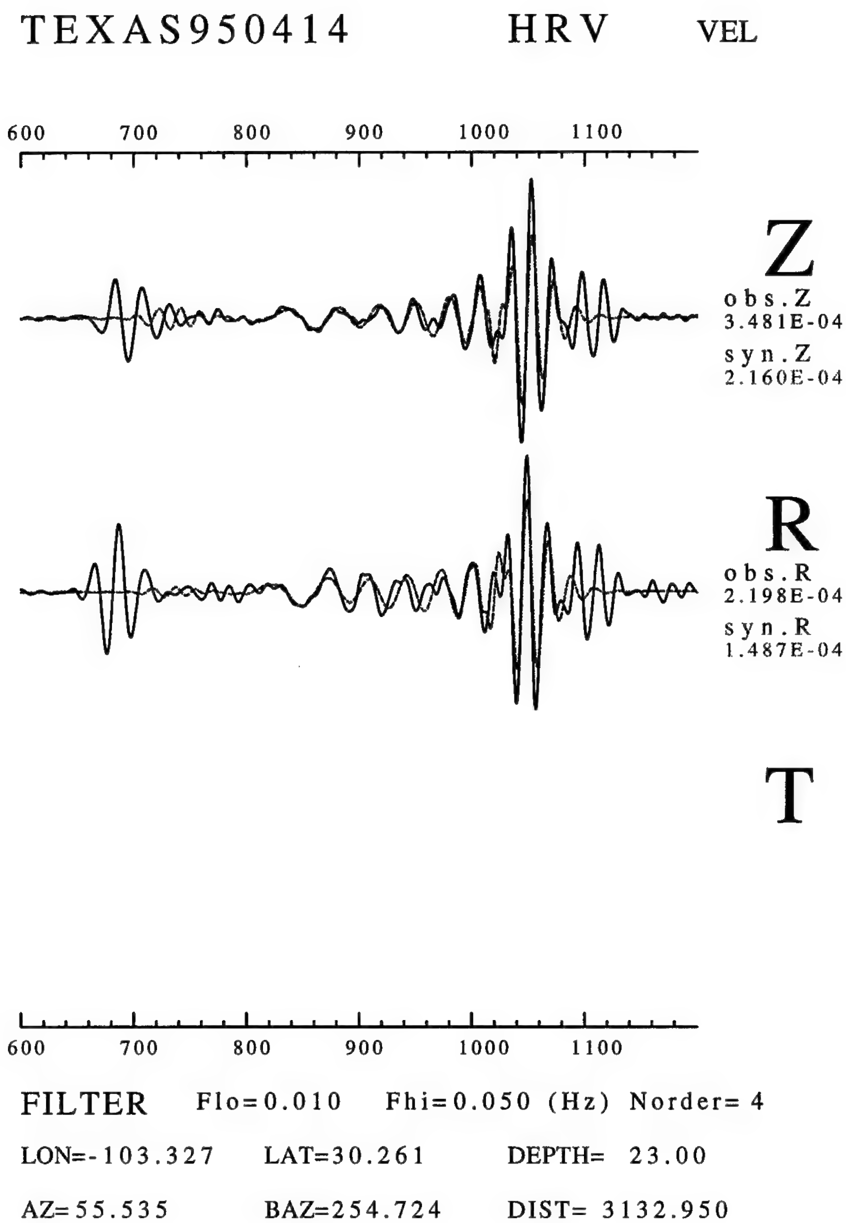

Fig. 4.13. The waveform fit of the best GA searched model for HRV.

A different parameterization which designed for teleseismic seismograms is working well for some high S/N ratio with strong Airy phase traces.

Another important result of genetic algorithms is that they provide a suite of possible models. The distribution of possible solutions

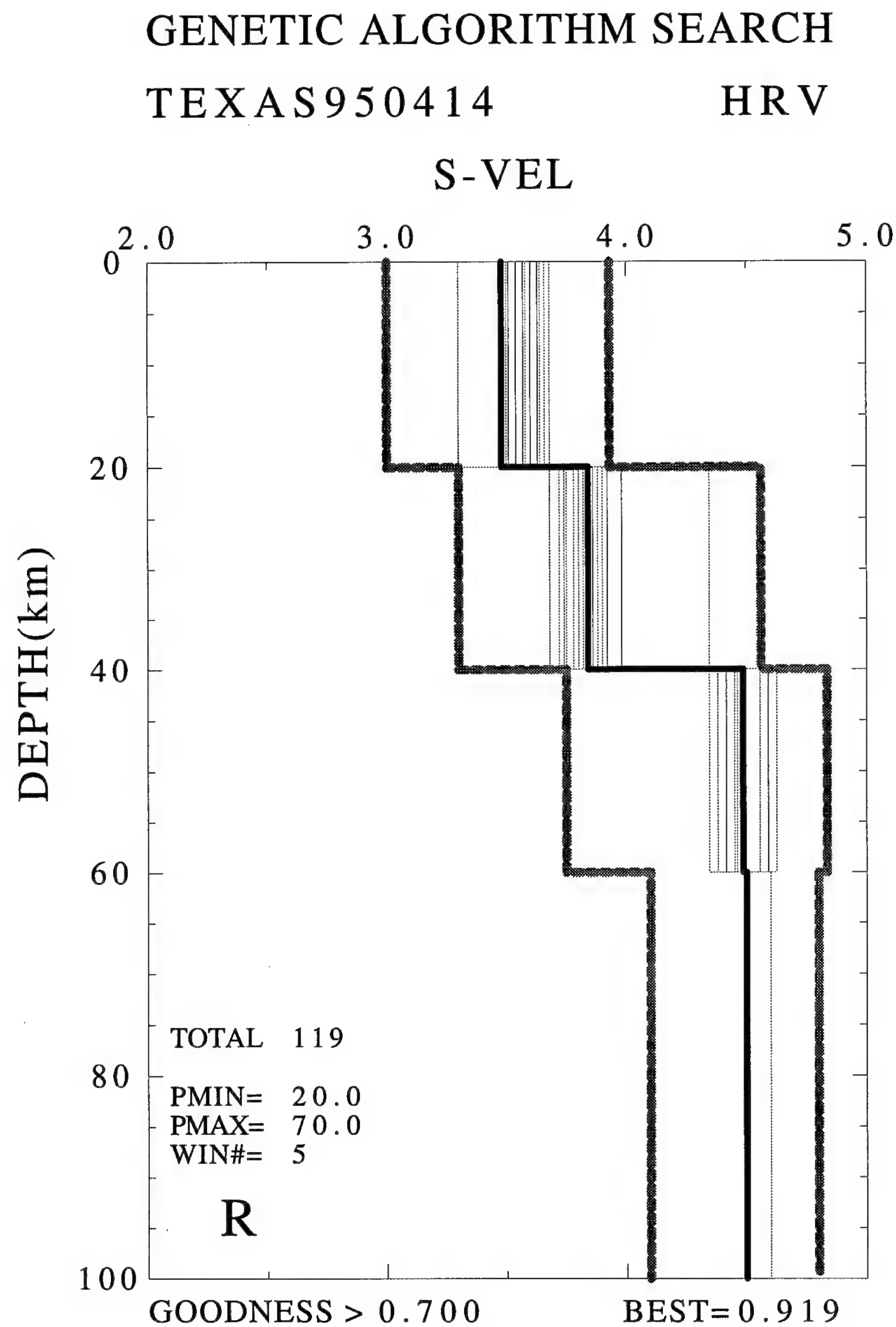

Fig. 4.14. The GA searched models for HRV.

at a given depth qualitatively indicates the sensitivity of the velocity to

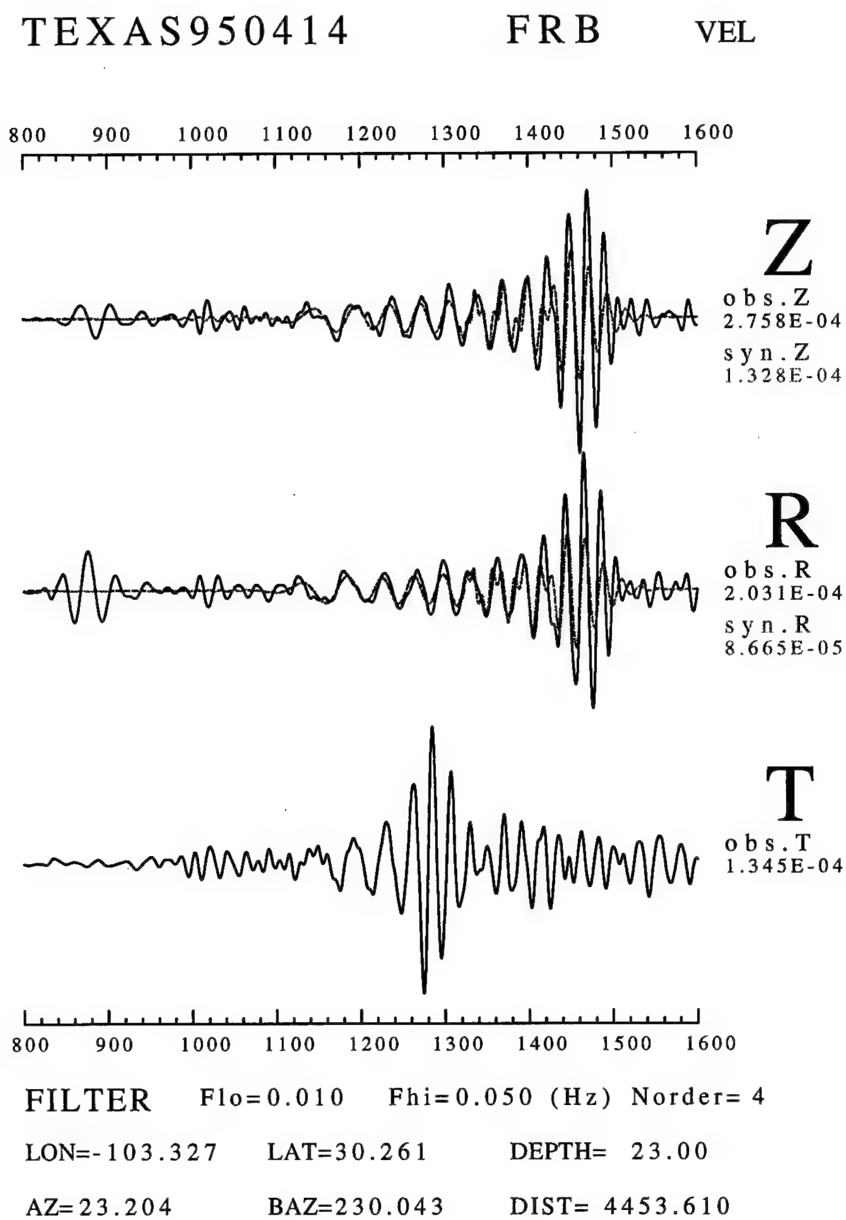

Fig. 4.15. The waveform fit of the best GA searched model for FRB.

the data. For example, for the ANMO transverse component, the crustal velocities are better defined than upper mantle velocities, which is as expected for a signal recorded only 600 km away from a crustal event.

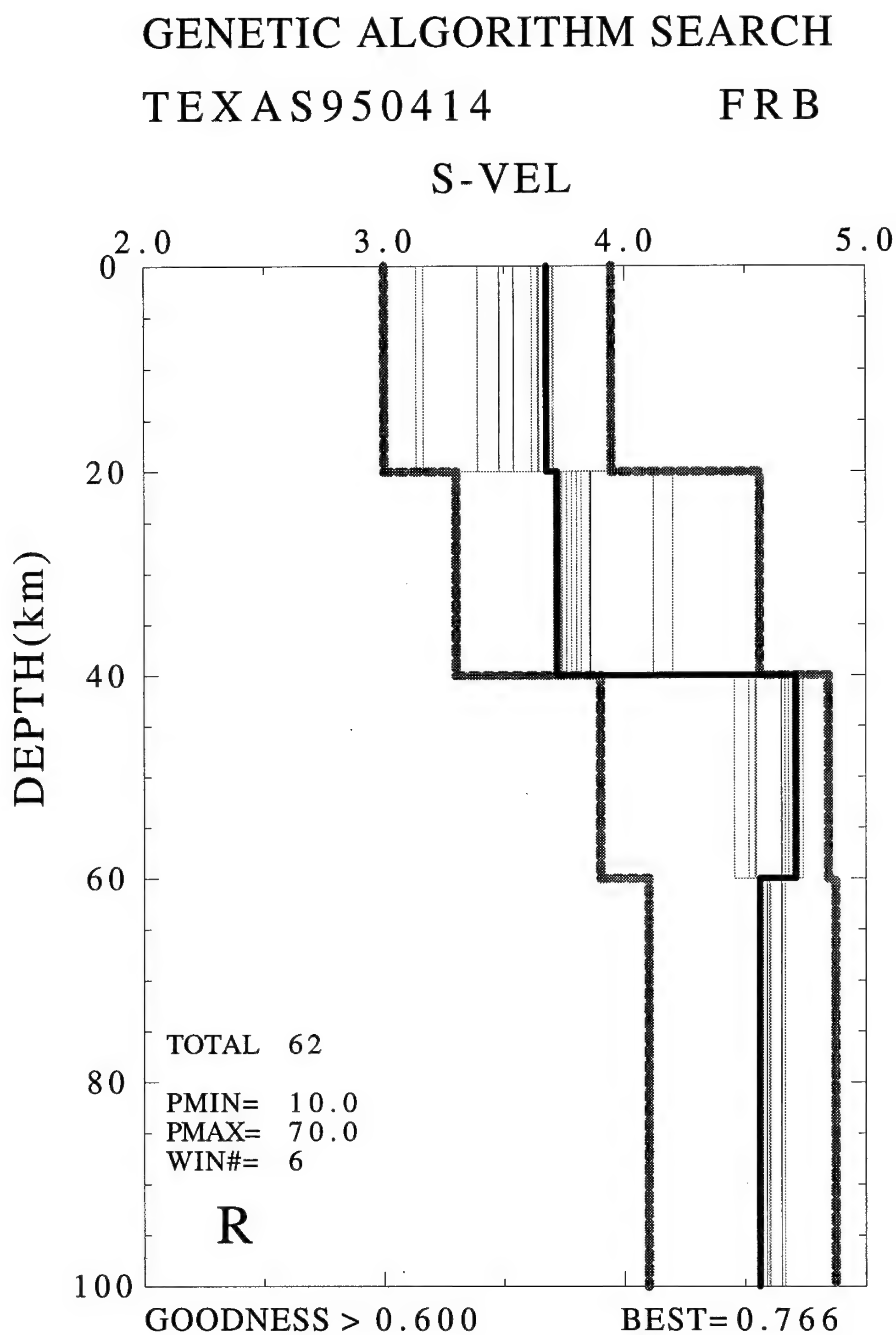

Fig. 4.16. The GA searched models for FRB.

The experience we learned here can be used to build a more

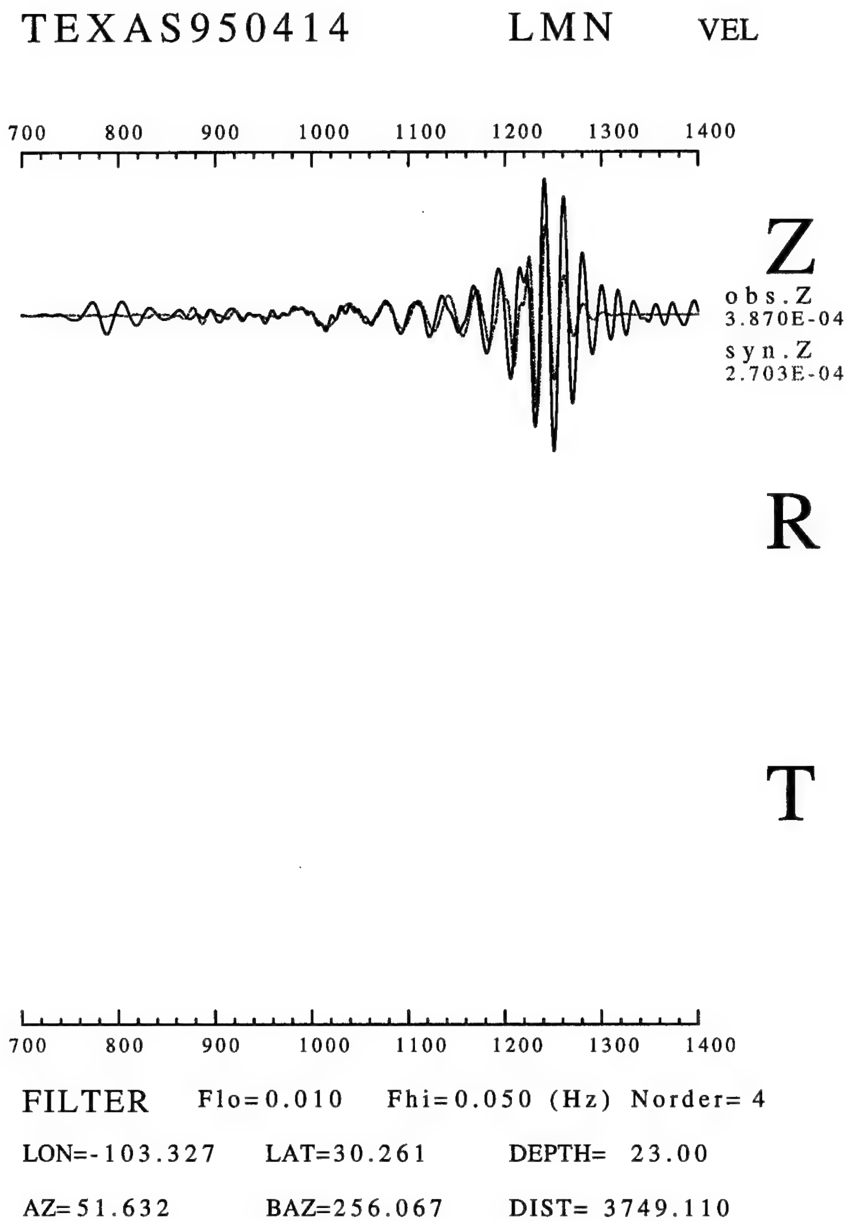

Fig. 4.17. The waveform fit of the best GA searched model for LMN.

intelligent algorithm for modeling surface-wave waveform in the future. This future algorithm should use both amplitude and time-shift information as its criteria of goodness-of-fit. Also, the better way of parameterization will further improve GA search technique's applicability.

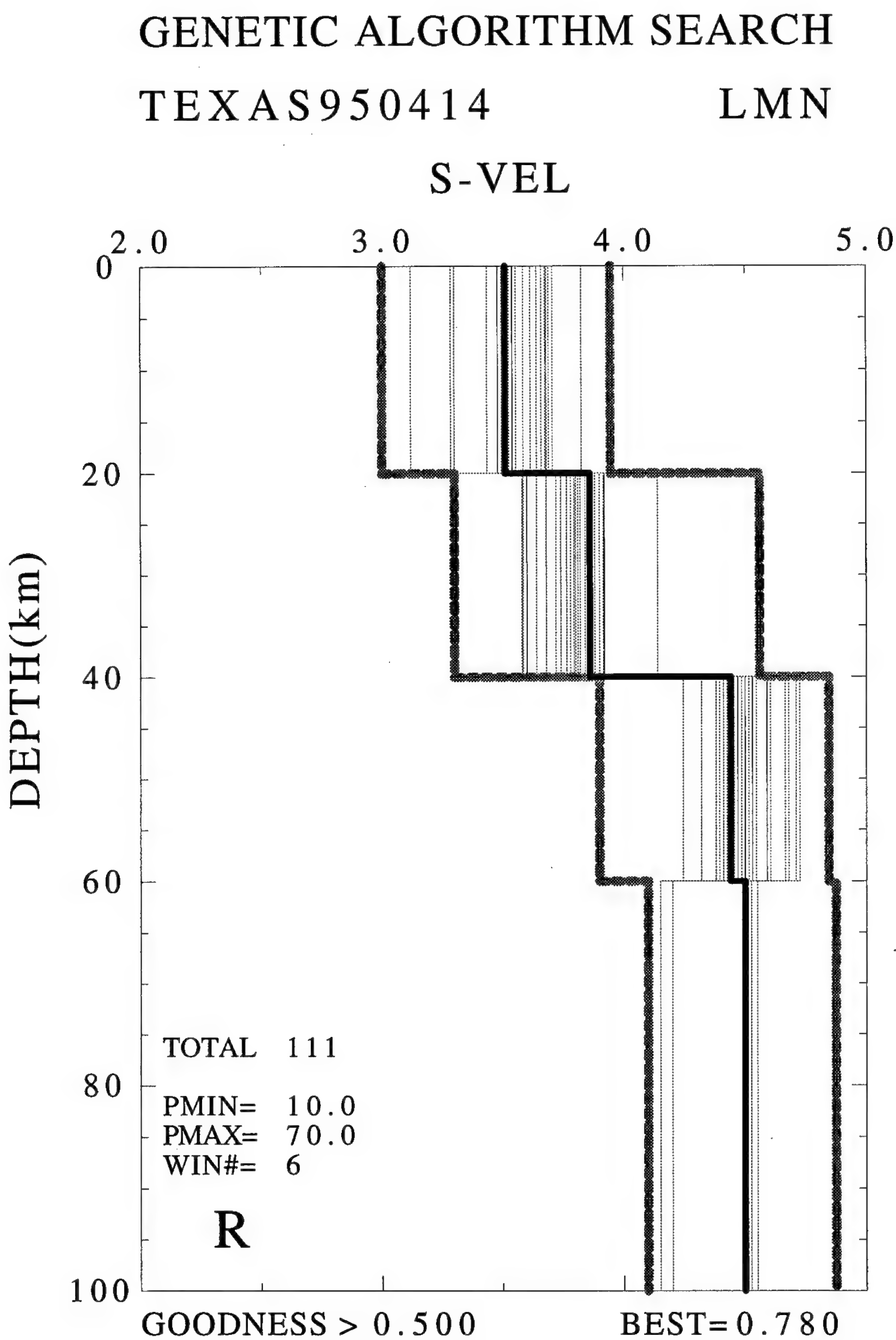

Fig. 4.18. The GA searched model for LMN.

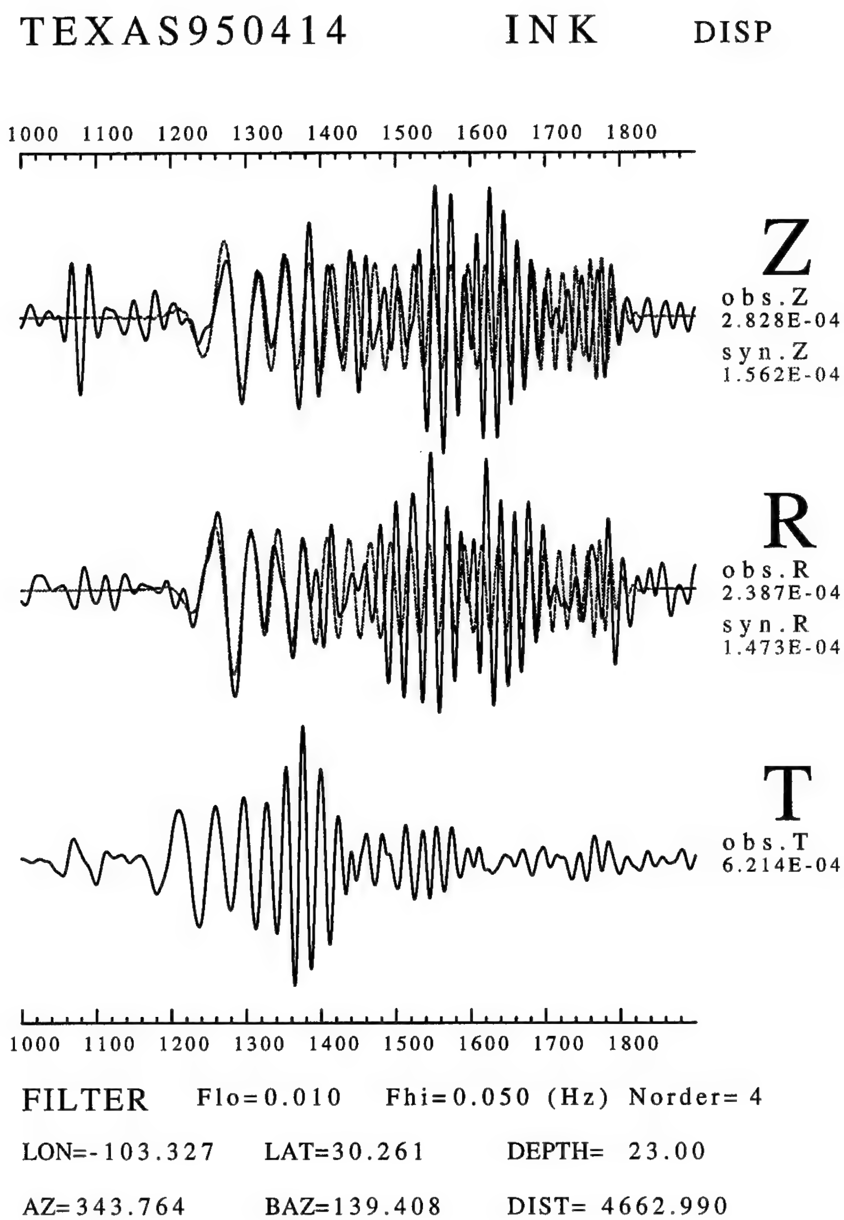

Fig. 4.19. The waveform fit for INK. INK is located in the most northwest of Canada. From the Rayleigh wave trace, we can see the wavetrain due to the multipathing effect come in after the 1600 seconds. The current used criteria of goodness-of-fit can not properly represent the crust wave and cause the wrong long lasting synthetic wave.

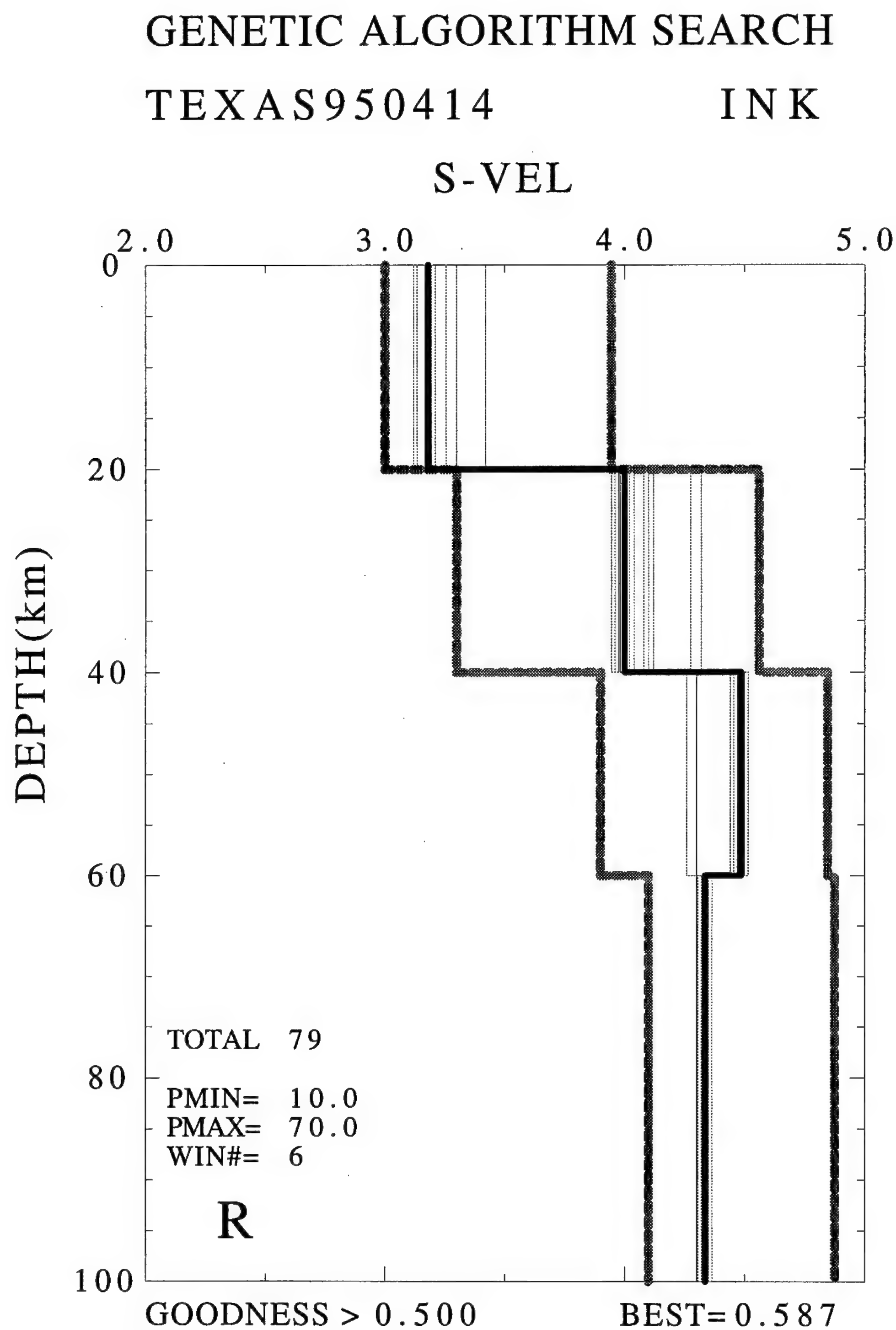

Fig. 4.20. The GA searched models for INK. The unreasonable low crust velocity value is causing by the criteria of goodness-of-fit which can not properly represent the crust wave.

CHAPTER 5
COMPARISON OF TECHNIQUES

In this chapter, four different techniques will be used to modeling the surface-waveform which recorded at CCM (Cathedral Cave, Missouri). These techniques are Genetic Algorithm, traditional surface inversion of dispersion data, linear waveform inversion (Gomberg and Masters, 1988), and GSDF inversion. The comparison of different results will illustrate the strength and weakness of each method. A discussion will address on what new knowledge can we learn through the waveform modeling and what is the good way to judge the reliability of inversion results.

The reason to use CCM data in this test is that we found CCM waveform is very difficult to model. It can not be fit by any simple model. Through all these waveform modeling tests, we believe that some new knowledge can be learned. All these experiences can be used to improve the algorithms of waveform modeling.

5.1 Genetic Algorithms

In applying GA search method to CCM, two steps search were performed. As mentioned in chapter 4, there is a cycle-skipping problem in applying many layers GA search to long distance stations. Base on this reason, the first step search were performed using 4-layers GA search. The best result from this first step search is used to reconstruct the searching bounds for the second step GA search.

Figure 5.1 shown the first step 4-layers GA searched results and searching bounds. The best model from first step search can match

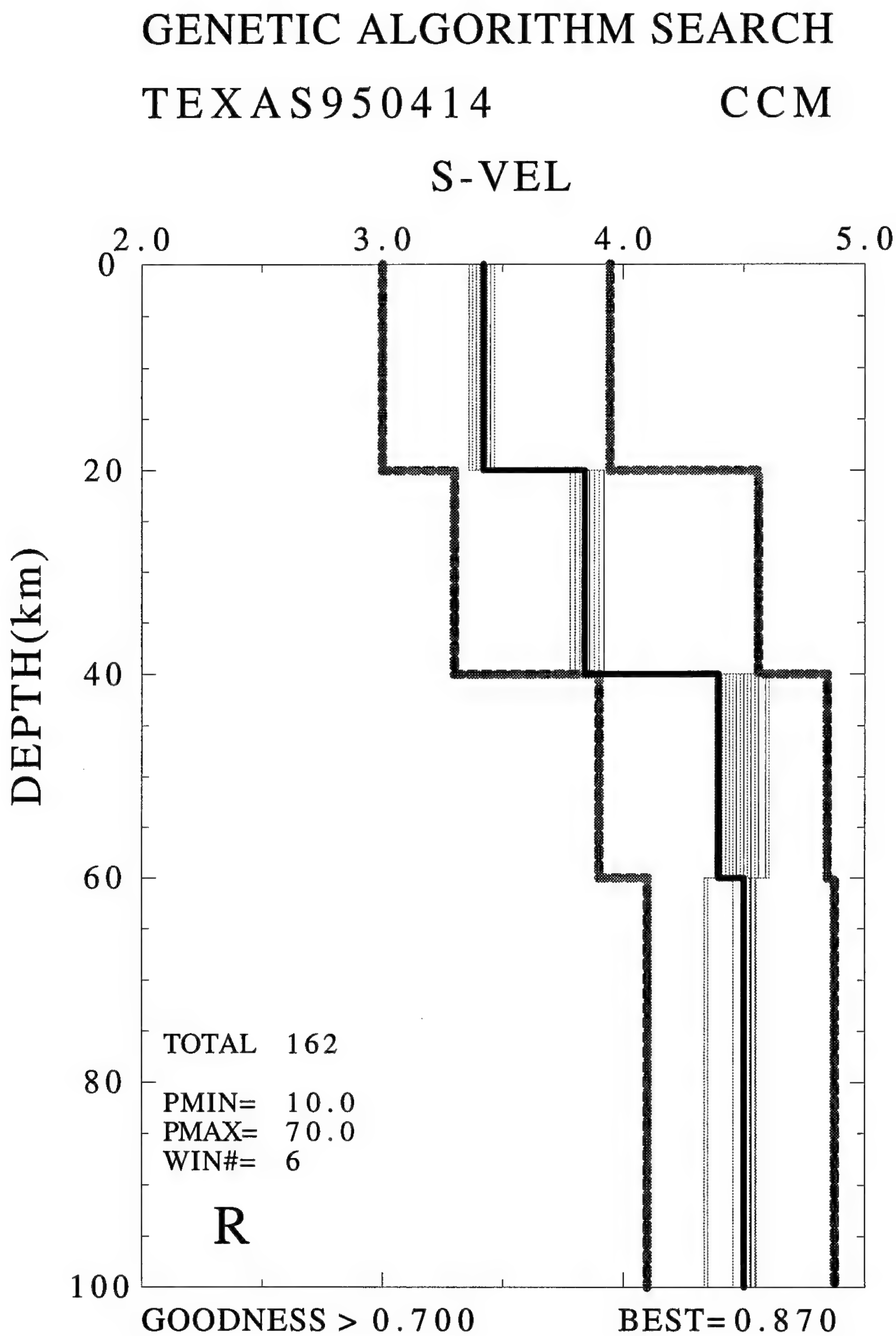

Fig. 5.1. First step 4-layers GA searched result.

the low frequency waveform (Figure 5.2). According the first step

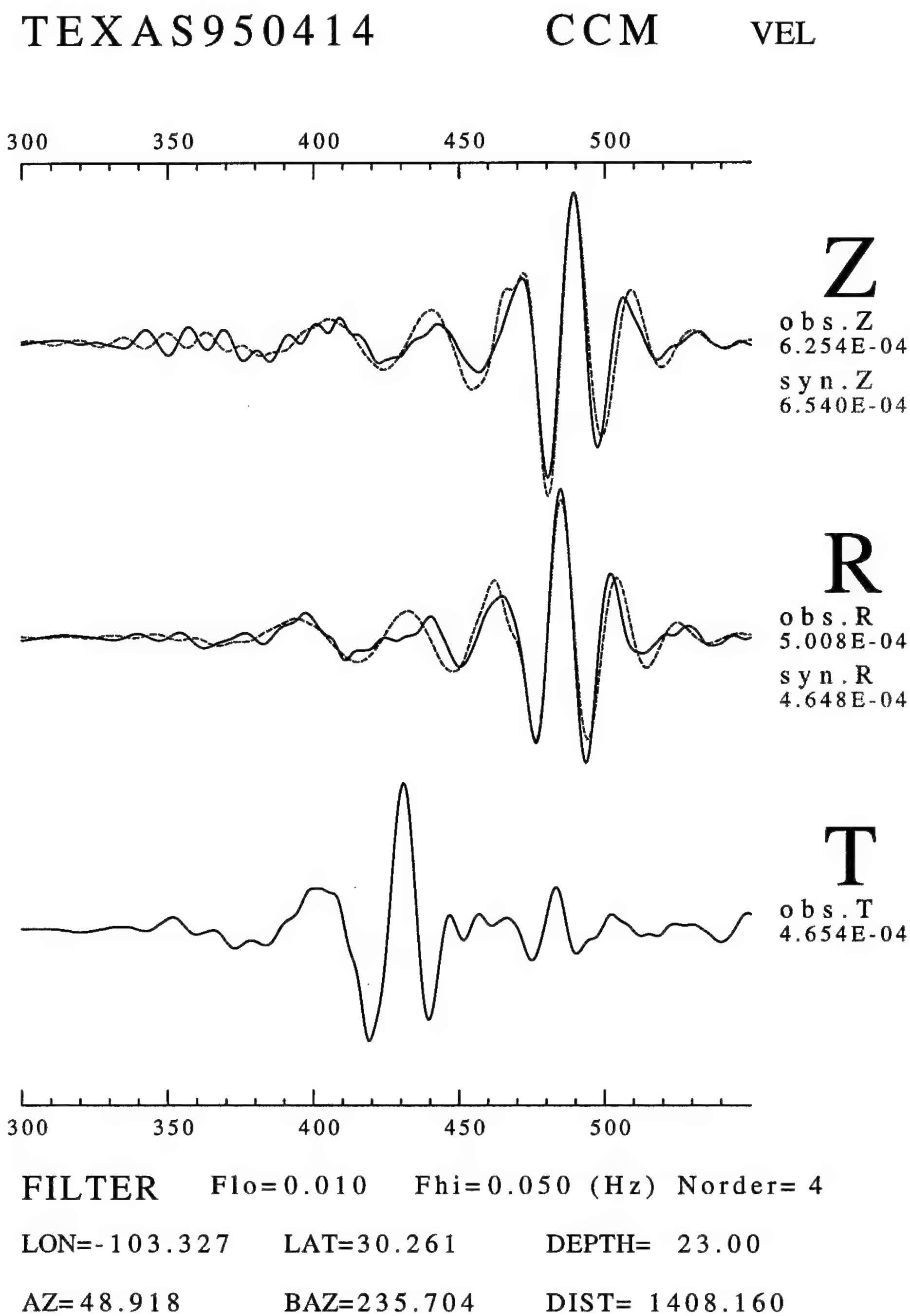

Fig. 5.2. The waveform fit for the best model in first step GA search.

search result, the second step GA searching bounds were designed. The second step GA search result are shown as Figure 5.3. The waveform predicted from the best model can fit the fundamental mode as

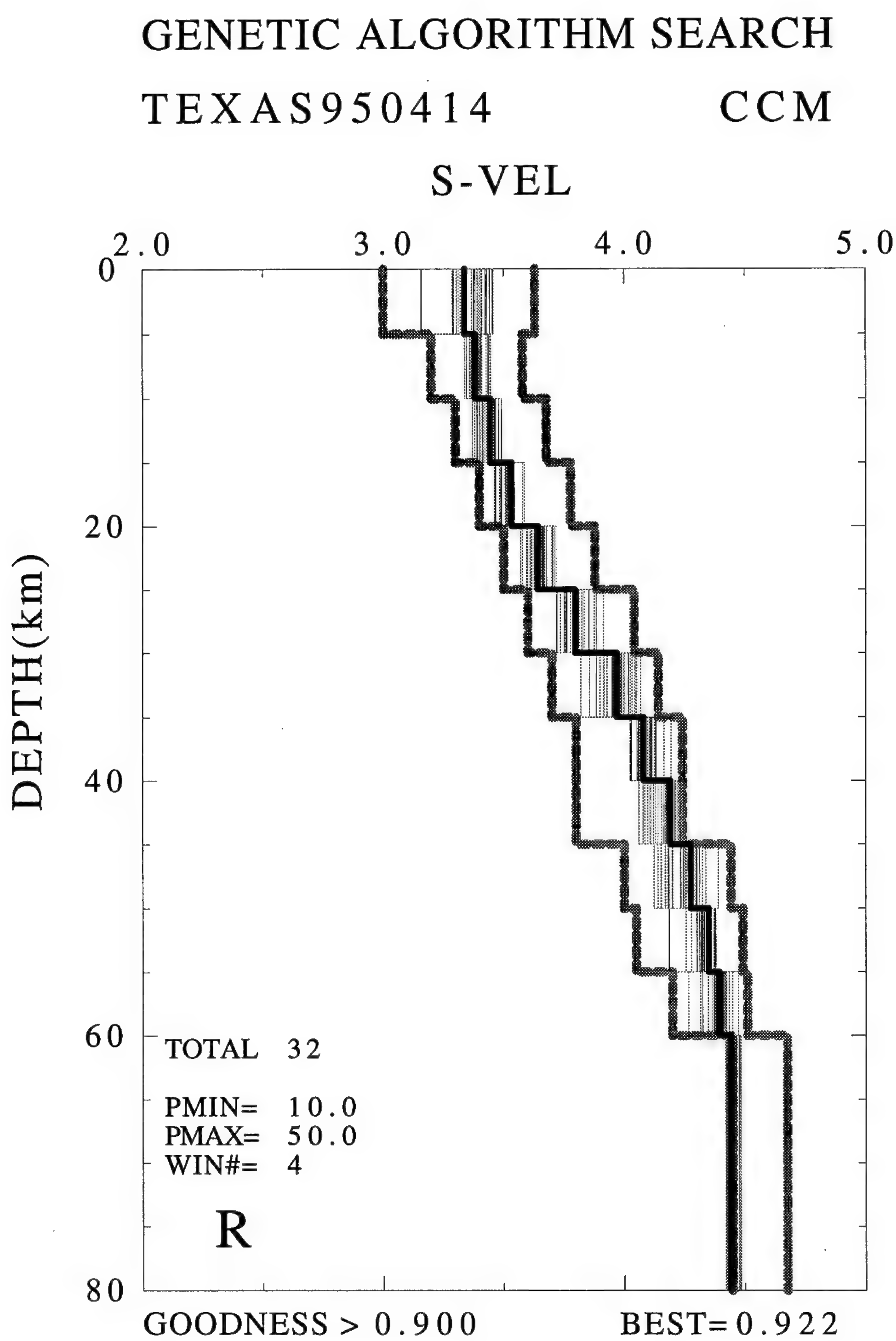

Fig. 5.3. Second GA searched results.

high as 0.1 Hz, but the higher mode is out of phase..

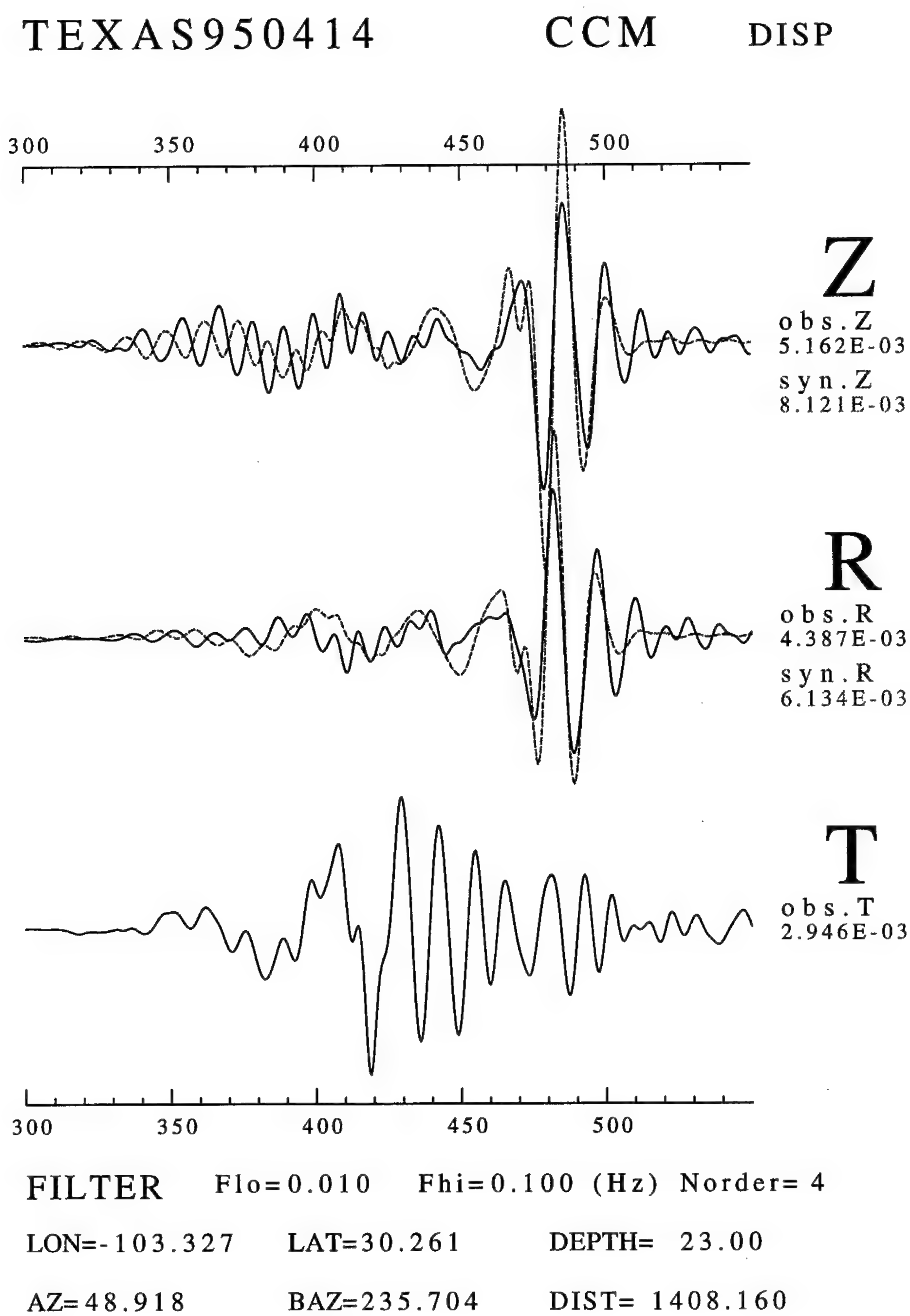

Fig. 5.4. The waveform fit of the best model in second step GA search.

The GA search method provides a very good starting model which has the fundamental mode matched in phase. The higher mode may be out of phase, but the model is a good starting model for final tuning.

The most important advantage for GA search method is that requires no human judgement during the search. The consumed time is the least among all methods tested in this study.

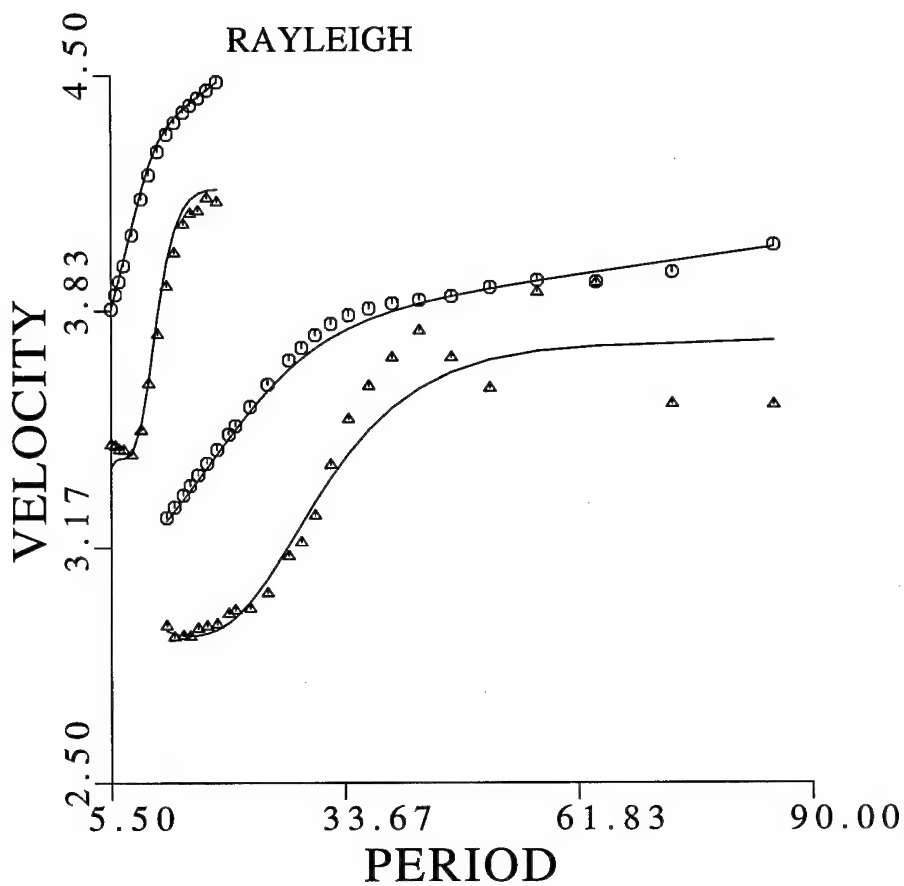

Fig. 5.7. The comparison of observed (circle) and predicted (line) phase velocity of inversion.

5.2 Inversion of Dispersion Data

The traditional surface wave inversion method to get seismic structure is using the dispersion data (e.g. Russell, 1987). This method requires first to evaluate surface wave dispersion data. The Multiple Filter Technique (Dziewonski et. al., 1969; Herrmann, 1973) is often used in extracting surface wave group velocity dispersion

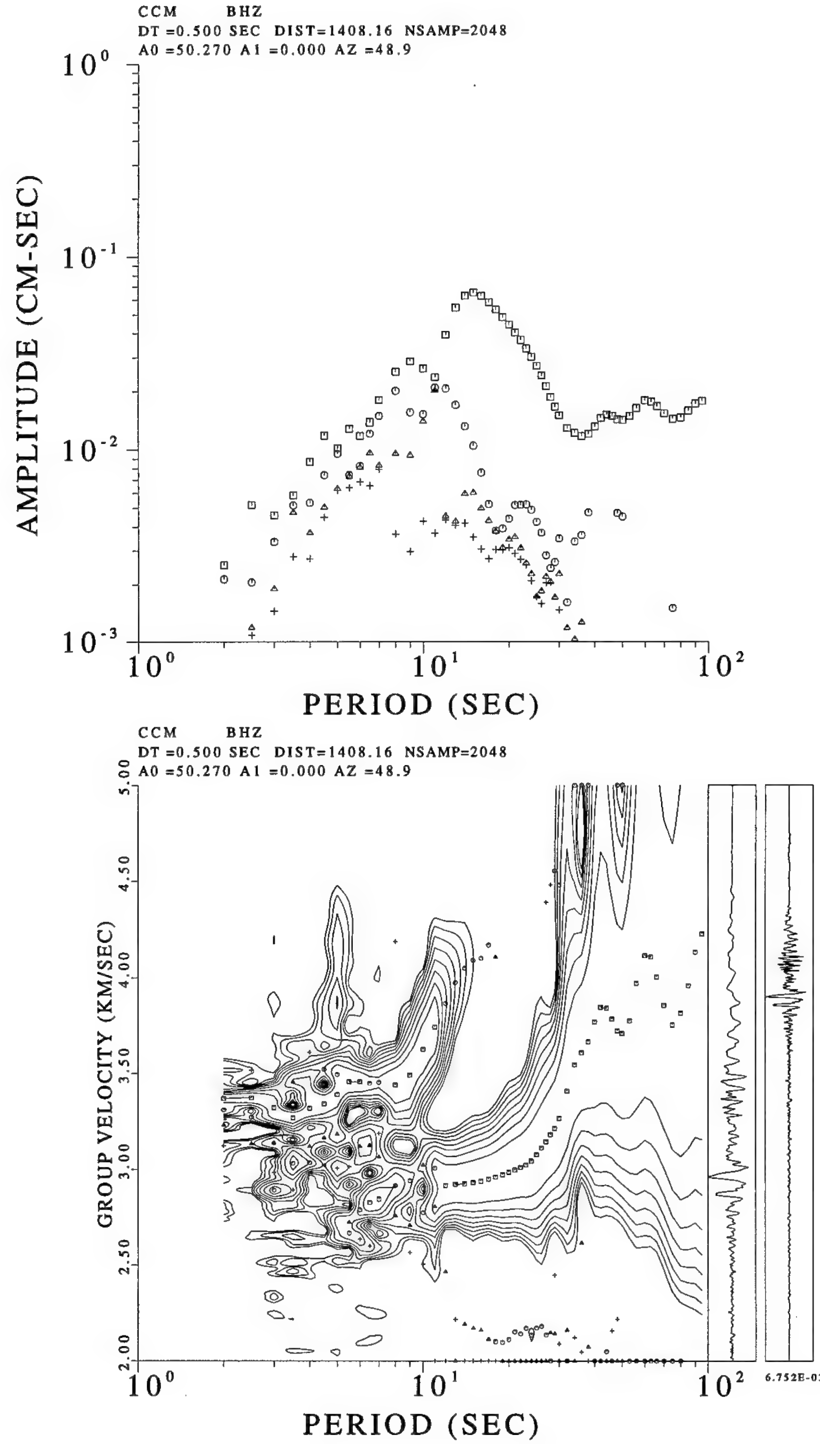

Fig. 5.5. The extracted surface wave dispersion data using multiple filtering techniques. The top plot shows the spectrum amplitudes at different periods. The bottom plot shows the group velocity dispersion curve.

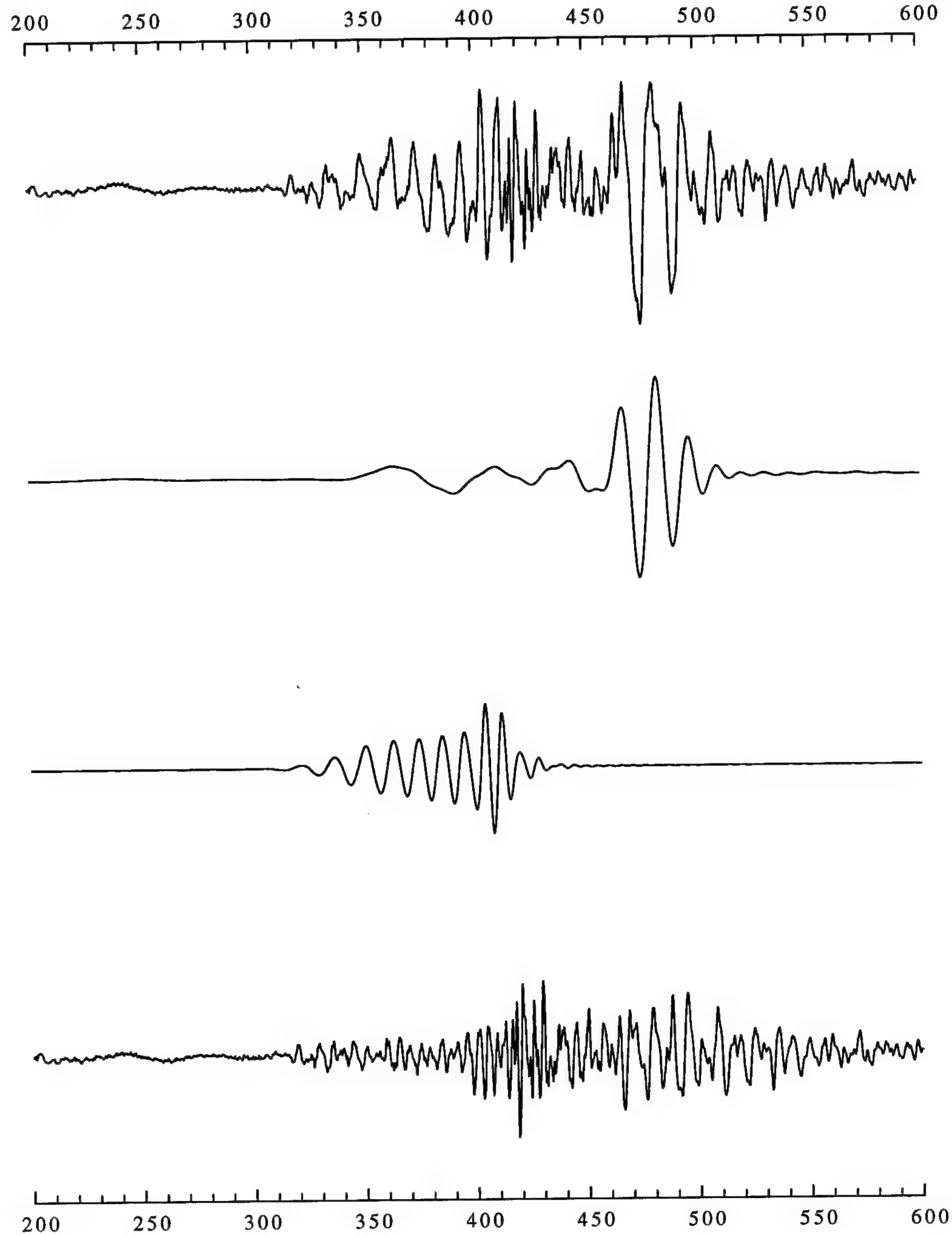

Fig. 5.6. This figure shows the extracted traces using phase match filter technique. The top trace is the vertical component displacement type seismogram of CCM. The second trace is extracted fundamental mode. The third trace is the extracted first higher mode. The bottom trace is the residual.

curves. However, inversion using only group velocity dispersion data usually suffer nonuniqueness and unstability. The better way is using

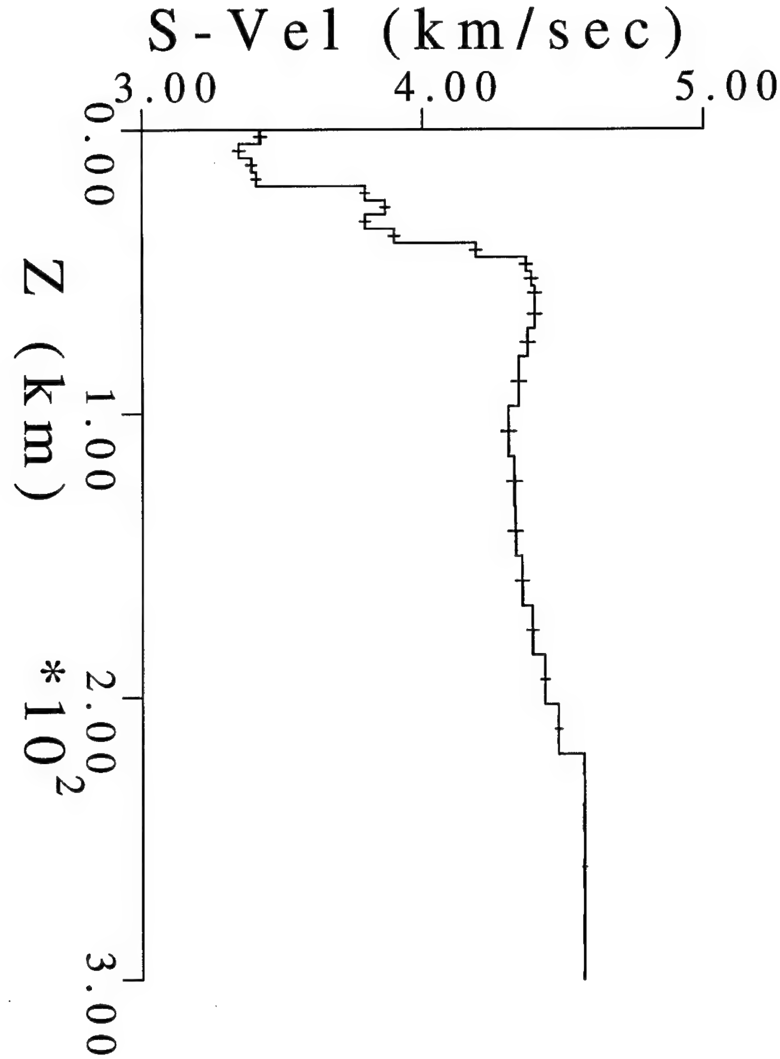

Fig. 5.8. The inversion model.

both group and phase velocity dispersion in inversion. This require another procedure to extracting surface wave phase velocity dispersion data. Herrin and Goforth (1977) introduce the Phase-Matched Filter method to estimate the phase velocity. After these two procedures, we can perform the traditional surface wave dispersion curve inversion.

In figure 5.5, we show the multiple filtering result. The bottom figure shows the group velocity dispersion curve. In CCM, the vertical component of displacement type record shows a very clear

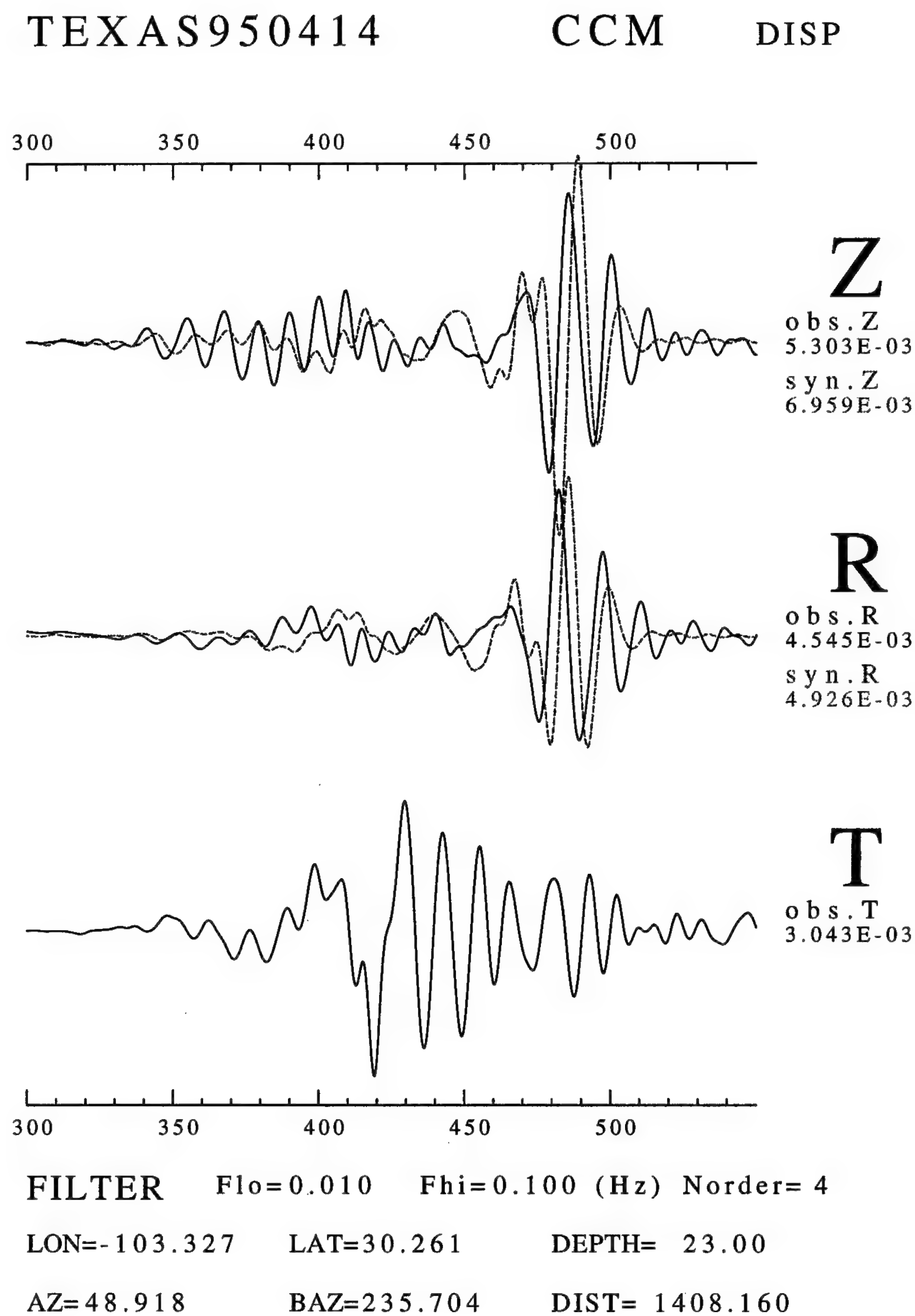

Fig. 5.9a. The waveform fit of observed and predicted seismograms. The model is shown as figure 5.8. (a) Displayed at frequency range 0.01-0.1 Hz.

fundamental mode and first higher mode Rayleigh wave. For period longer than 40 seconds, the fundamental mode curve is not smooth as

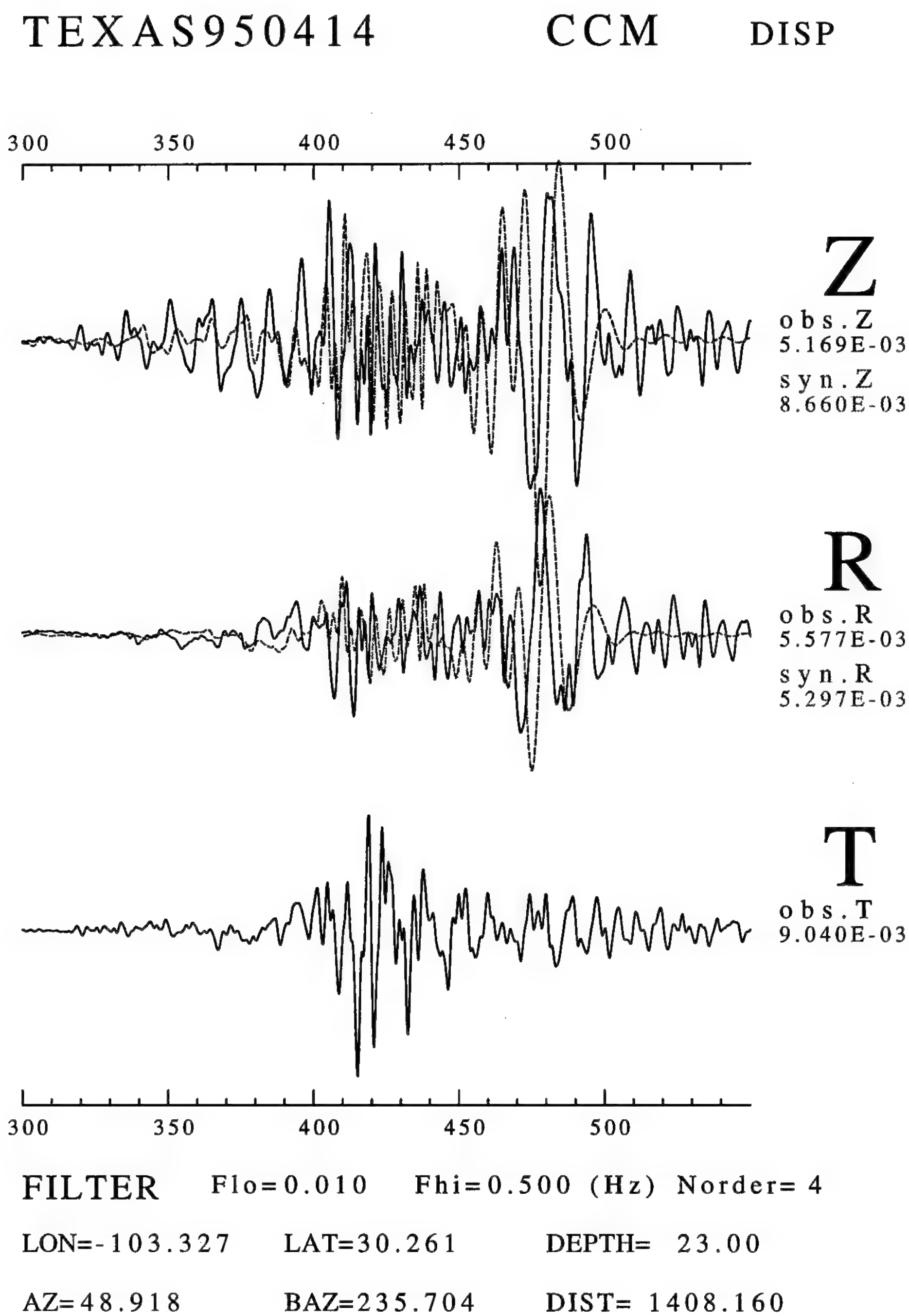

Fig. 5.9b. (Cont'd) (b) The waveform fit for the frequency range 0.01-0.5 Hz.

shorter periods. This character, which is observable for stations in similar geological region such as CBKS (shown on figure 5.24), may caused by some structure in deep. The first higher mode is clearly

identified between 6 and 18 seconds. But for periods shorter than 5 seconds, the possible second higher mode is coming in and form a strong Lg phase at 3.4 km/sec. We would like to see whether all these features can be modeled through waveform modeling. Figure 5.6 shows the extracted fundamental and first higher mode using phase-matched filter technique. The top trace is the observed data and the bottom trace is the residual seismogram after subtracting the extracted fundamental and first higher mode Rayleigh wave. In the residual seismogram, we can see a possible second higher mode signal in the time window 320 to 430 seconds. But there still remain one question about what kind signal is that which arrives between 440-540 seconds with strong energy.

Using group and phase velocities in inversion, the results are shown on figure 5.7 and 5.8. Figure 5.7 shows the used data and predicted curve by inverted model. Figure 5.8 shows the model of inversion. The starting model is the best model obtained in first-step GA search shown on figure 5.1. Figure 5.9 shows the waveform fit using the inverted model at two different frequency bands 0.01-0.1 and 0.01-0.5 Hz. There is *a priori* information used in generated synthetics which is not available from this inversion. That is the frequency dependent Q which will be described later in this chapter. From the dispersion curve fit, it is not surprising to see that synthetic fundamental mode is slightly slow than observed for the crustal wave and the mantle wave is not matched (figure 5.9a). Also, the first higher mode (figure 5.9b) should be fitted much better than fundamental mode.

This exercise shows that traditional surface wave inversion can provide a fairly good model from the point of view of waveform modeling. However this method also has its limitations such as the inversion has been dominated by short period data which has more data point than long period data and has no ability to change model to fit the data around 30 seconds in this case. However, this technique is

very fast comparing to waveform inversion techniques.

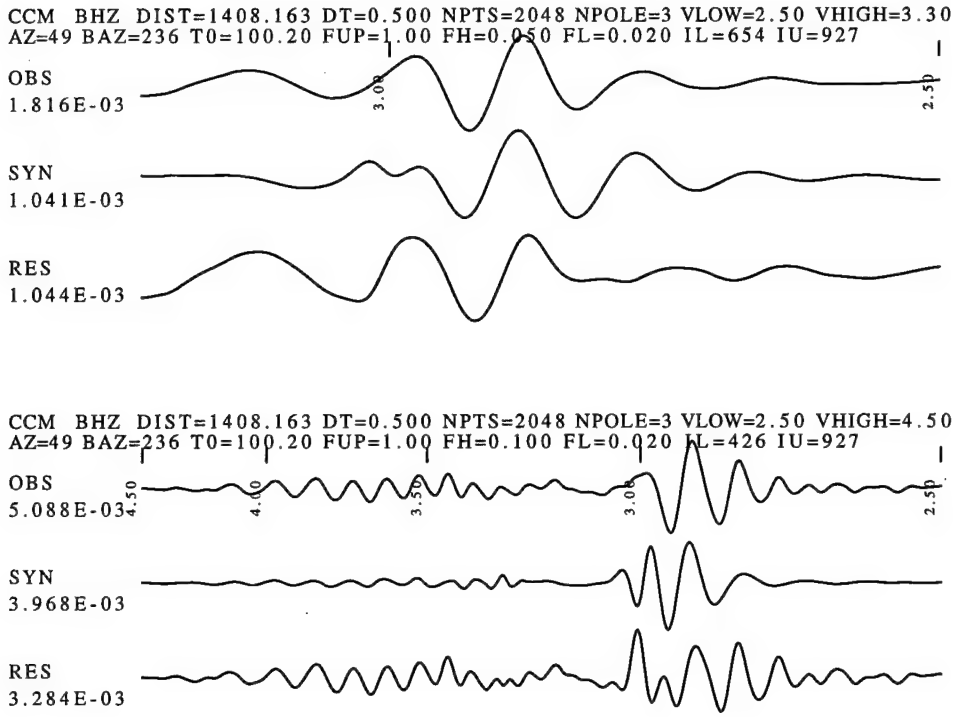

Fig. 5.10. The waveform comparison of observed, synthetic, and the residual seismograms at two different frequency bands. The top panel which corresponding to apparent velocity 3.3-2.5 km/sec is plotted at 0.02-0.05 Hz. The bottom panel for 4.5-2.5 km/sec at 0.02-0.1 Hz.

5.3 Linear Waveform Inversion

Gomberg and Masters (1988) introduce the linear waveform inversion technique. This technique formulates the residual seismogram of observed and synthetic seismograms in terms of model parameter perturbations. In this section, we will show the inversion result obtained by applying the method to CCM data. The programs used here is coded by professor Robert Herrmann, Saint Louis University.

In the original paper (Gomberg and Masters, 1988), the inversions were performed directly using whole frequency range interested.

However, it is found by professor Herrmann, that a better way to using this tool in inversion is performing the inversions in different frequency bands. This improved procedure can utilize different information for low frequency and high frequency to constrain the model in a more stable and robust way. The similar idea was reported by Bunks *et al.* (1995) for studying the reflection data.

Using the best model obtained from first-step GA search, and perform the linear waveform inversion. In figure 5.10, it shows the waveform fit at two frequency ranges. We can see that the phase and amplitude of fundamental mode is matching the observed. The first higher mode does not match the observed data because the *a priori* information of frequency dependent Q is not used in this test. The inverted model is not shown because it is used to do fine adjustment by trial and error and a better waveform fit is obtained which will be presented later.

Although all reported applications of linear waveform inversion were for the short distance records, we believe it is possible to apply this technique to longer distance records. The strength for this method is the inversion will force on the large residual between observed and predicted data. However, the weakness of this method is associated with its strength, i.e. it needs a sophisticated controlling method to avoid the effects that caused by improper knowledge of source.

5.4 GSDF Inversion

In this section, we are applying the GSDF inversion method to CCM data. As the model obtained from linear waveform inversion, the inverted model is not shown here, and an improved waveform fit, by trial and error adjustment, based on this model will be shown later in this chapter. Figure 5.11 shows the waveform fit of the GSDF inversion result.

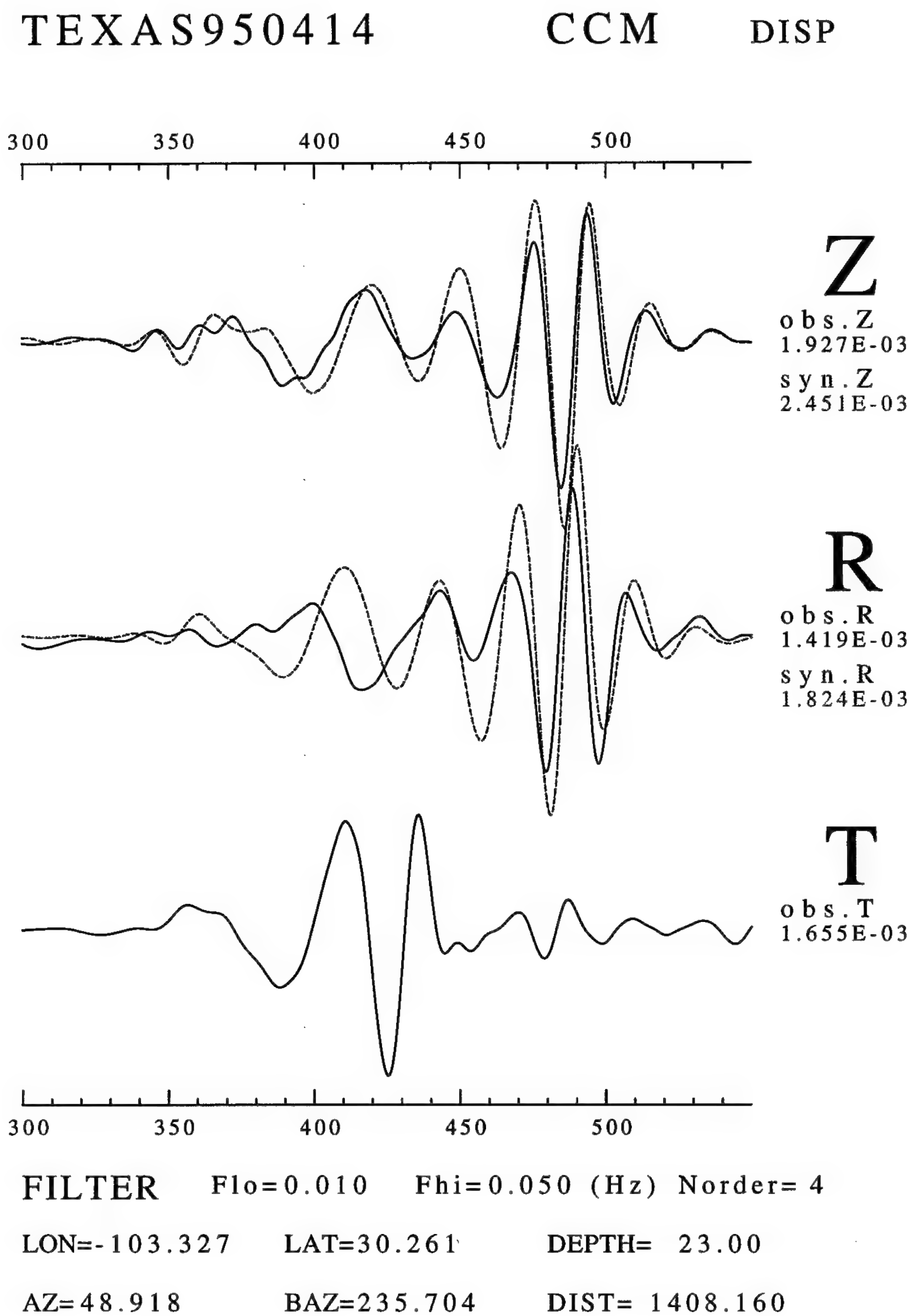

Fig. 5.11a. The waveform fit for the model obtained from GSDF inversion. Three different frequency ranges are shown: (a) for 0.01-0.05 Hz.

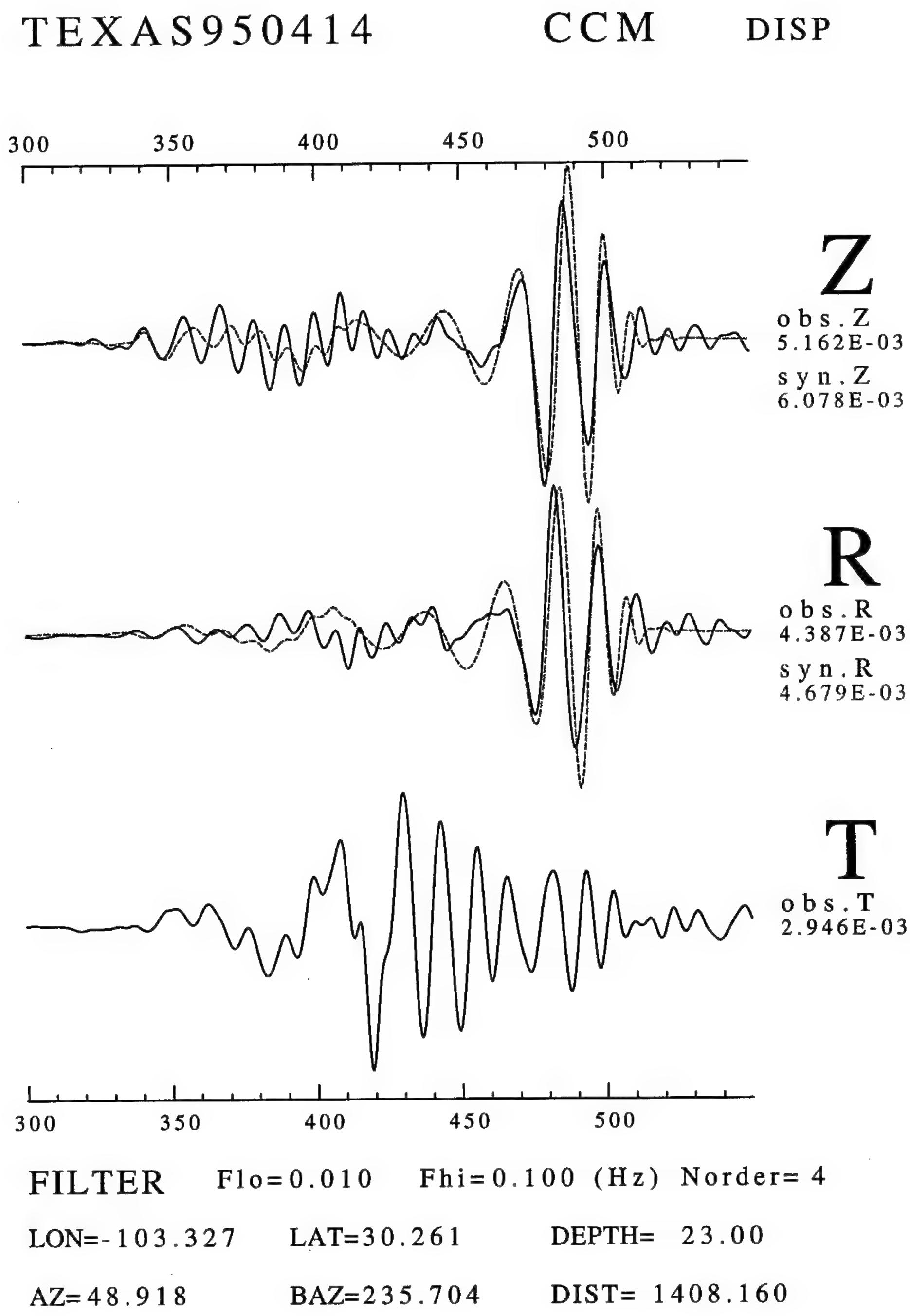

Fig. 5.11b. (Cont'd) (b) for 0.01-0.1 Hz.

5.5 How To Judge the Waveform Fit

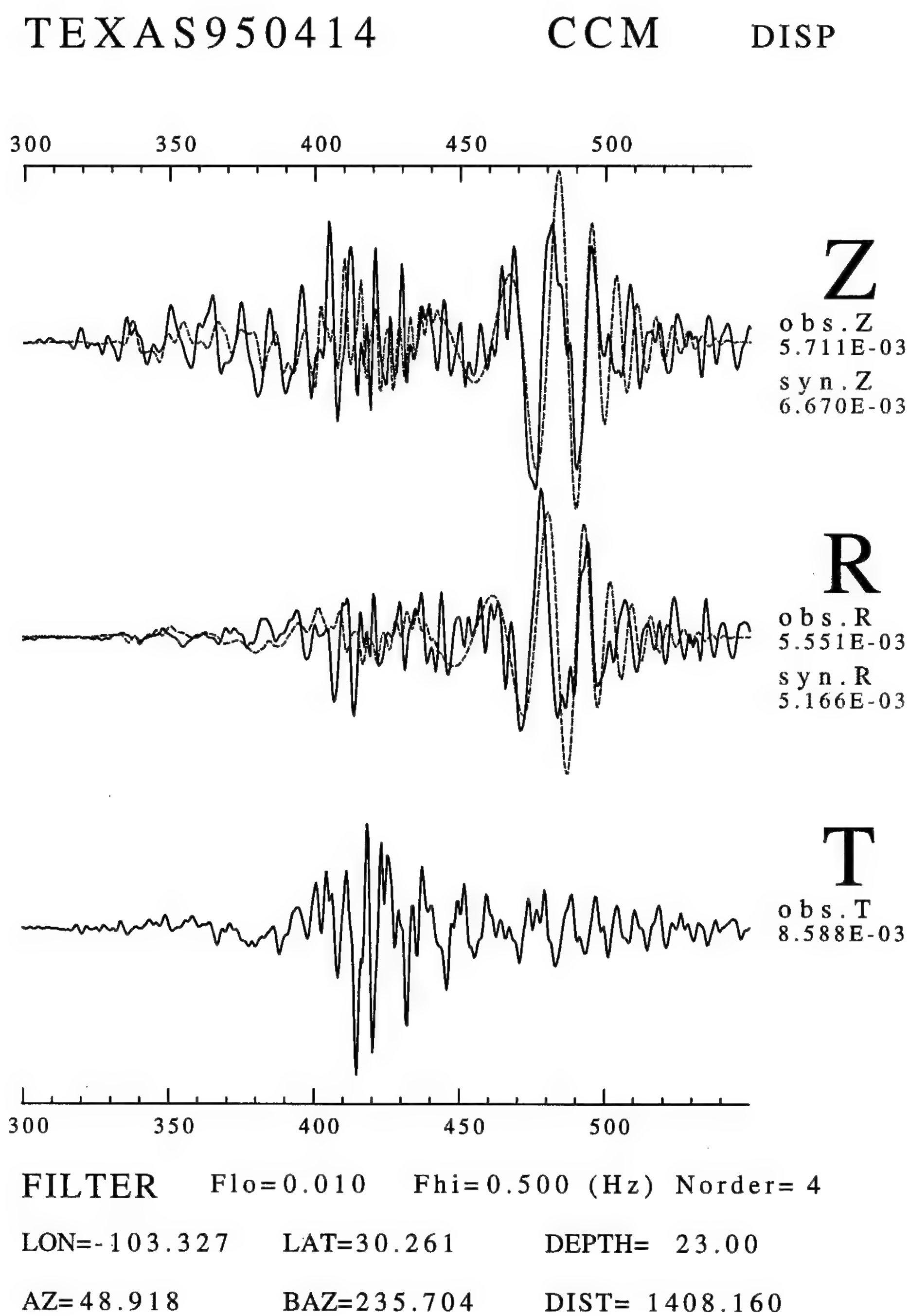

Fig. 5.11c. (Cont'd) (c) for 0.01-0.5 Hz.

What is the criteria to assess the goodness of waveform fit? From the viewpoint of waveform modeling, the synthetics should be able to match the observed data in both phase and amplitude for different

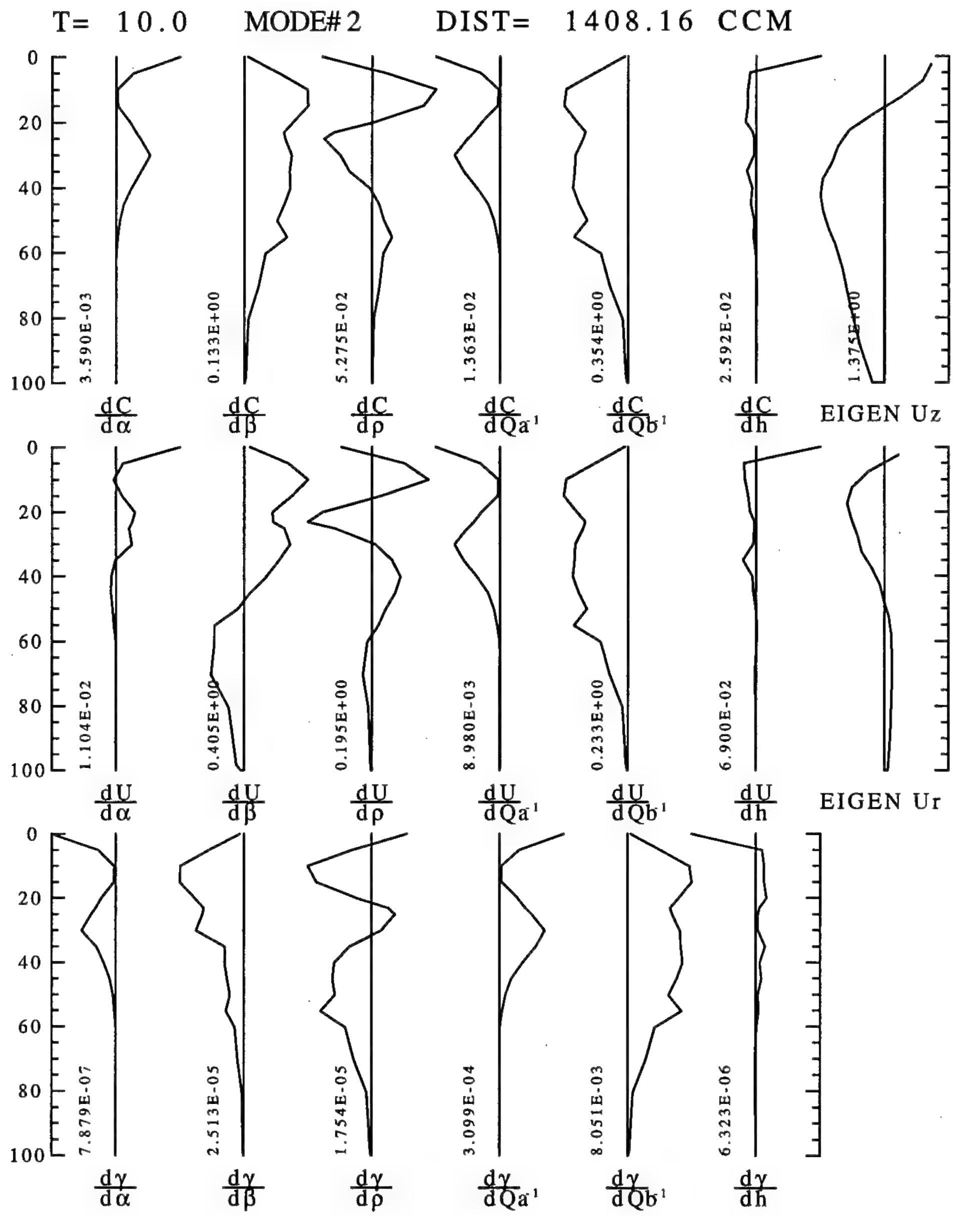

Fig. 5.12. The partial derivatives of first higher mode at 10 seconds which computed for GSDF inversion.

frequency bands. In this case, first let's see what are observable from recorded seismograms of station CCM. In CCM, we can see fundamental mode and first higher mode with large amplitude, so the first requirement should be matching both fundamental and higher modes signal. If we can find such a model which can predict observed surface

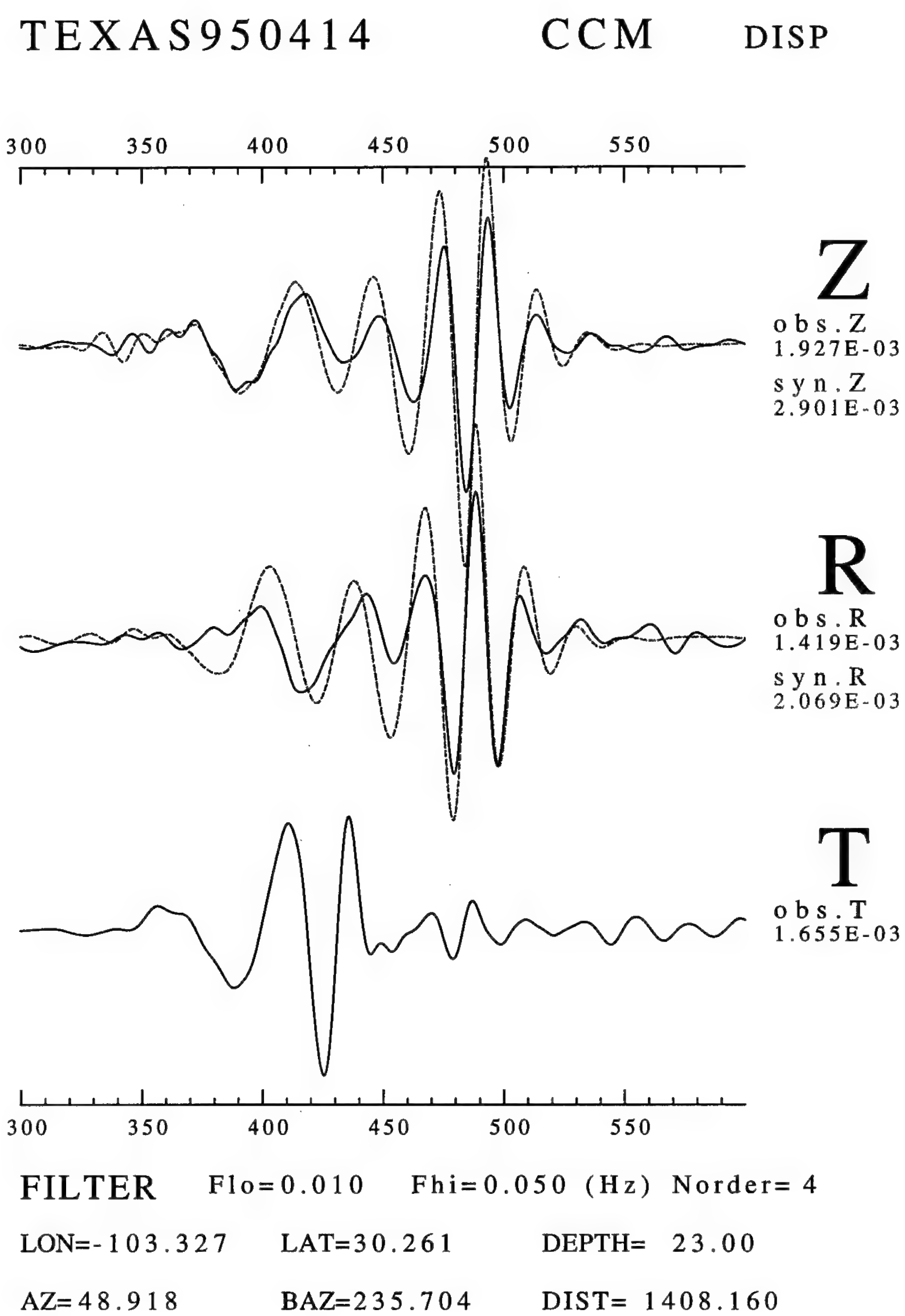

Fig. 5.13a. Waveform fit for the model which increasing the upper mantle Q. Three different frequency ranges are displayed: (a) 0.01-0.05 Hz.

waveform, we would like to know whether this model is good enough to match the body wave, P_{nl} and S in this case. After that, we would like

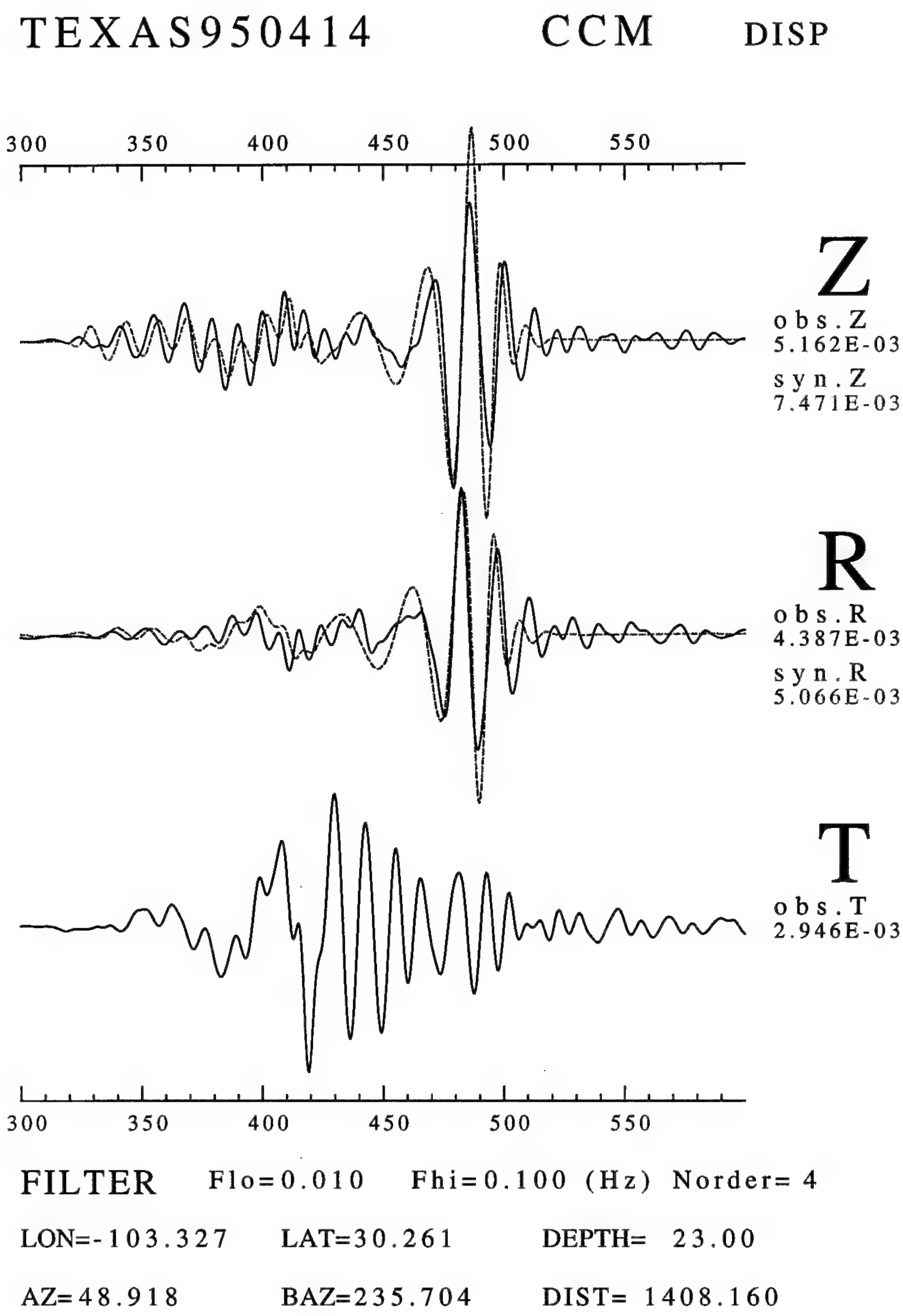

Fig. 5.13b. (Cont'd) (b) 0.01-0.1 Hz.

to know if a model can generally meet the first two requirement, is there a way to tell us how confident this model can be or any improvement can be expected in the future modeling.

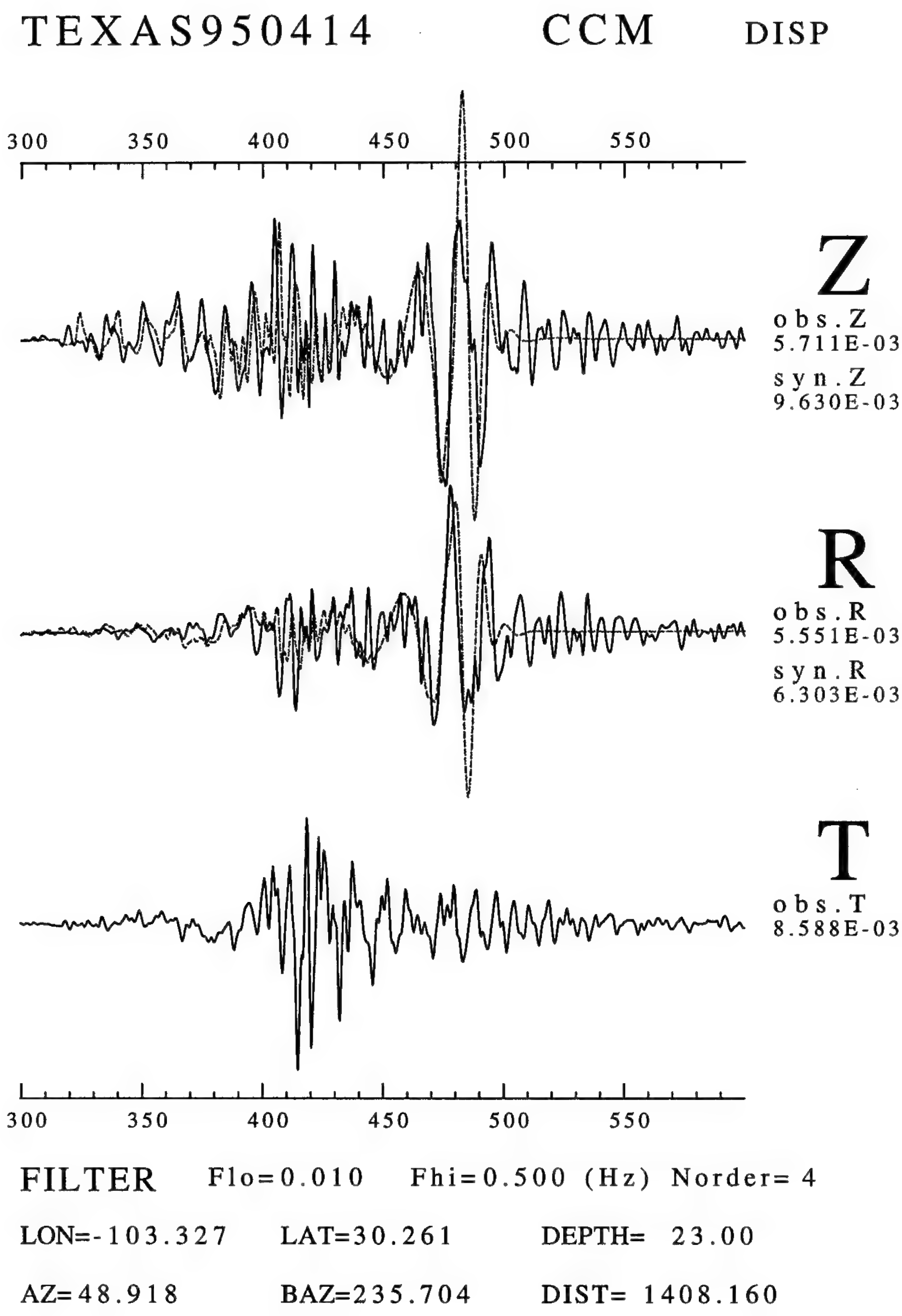

Fig. 5.13c. (Cont'd) (c) 0.01-0.5 Hz.

From above, we can say that all four algorithms can provide fairly good models that can match fundamental mode up to 0.1 Hz. However, those model can not fit the higher mode, therefore the question is

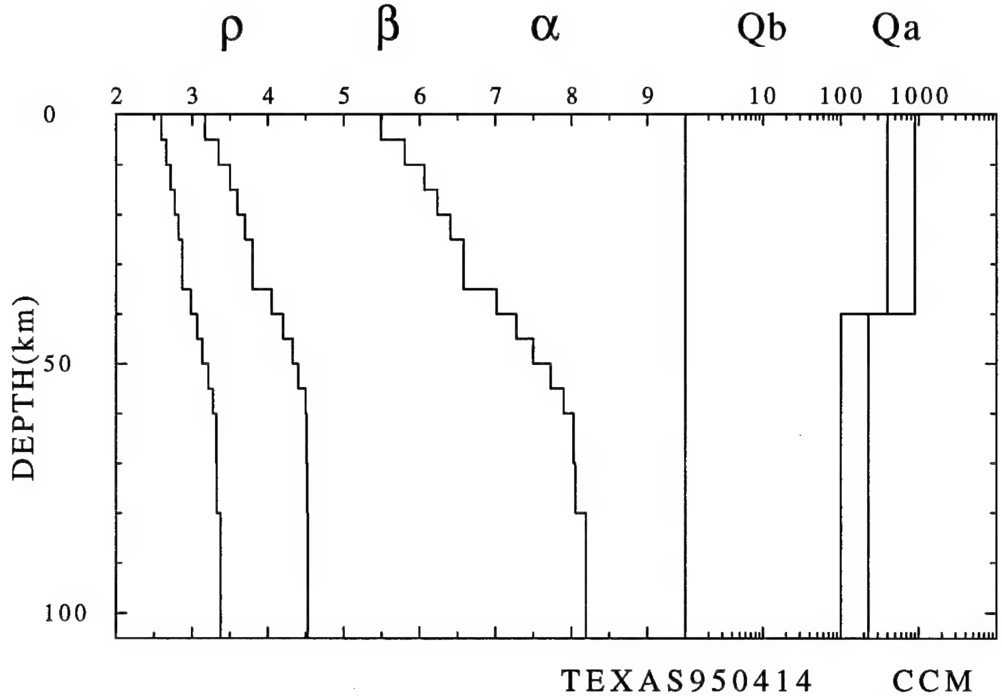

Fig. 5.14. This figure shows a better model which based on GSDF inversion result, and using trial and error to do the fine tuning.

how to match the higher mode. Especially looking at the GSDF inversion result (figure 5.11b), we can see predicted higher mode amplitude is about factor two smaller than observed data.

There are two possible ways to increase the higher mode amplitude. Let's check all the partial derivatives created for the GSDF inversion. As shown on figure 5.12, we can find that if we increase the upper mantle Q value, it is possible to increase the higher mode amplitude. Of course, the crustal Q value should decrease to compensate the change and to maintain the fundamental mode amplitude. The result is shown as figure 5.13. Indeed, the higher mode amplitude is increasing, but compare to figure 5.11 we can find not only higher mode but also fundamental mode amplitude are increasing. Especially the low frequency part of fundamental mode which corresponding to the wave traveling through the upper mantle. Another problem is

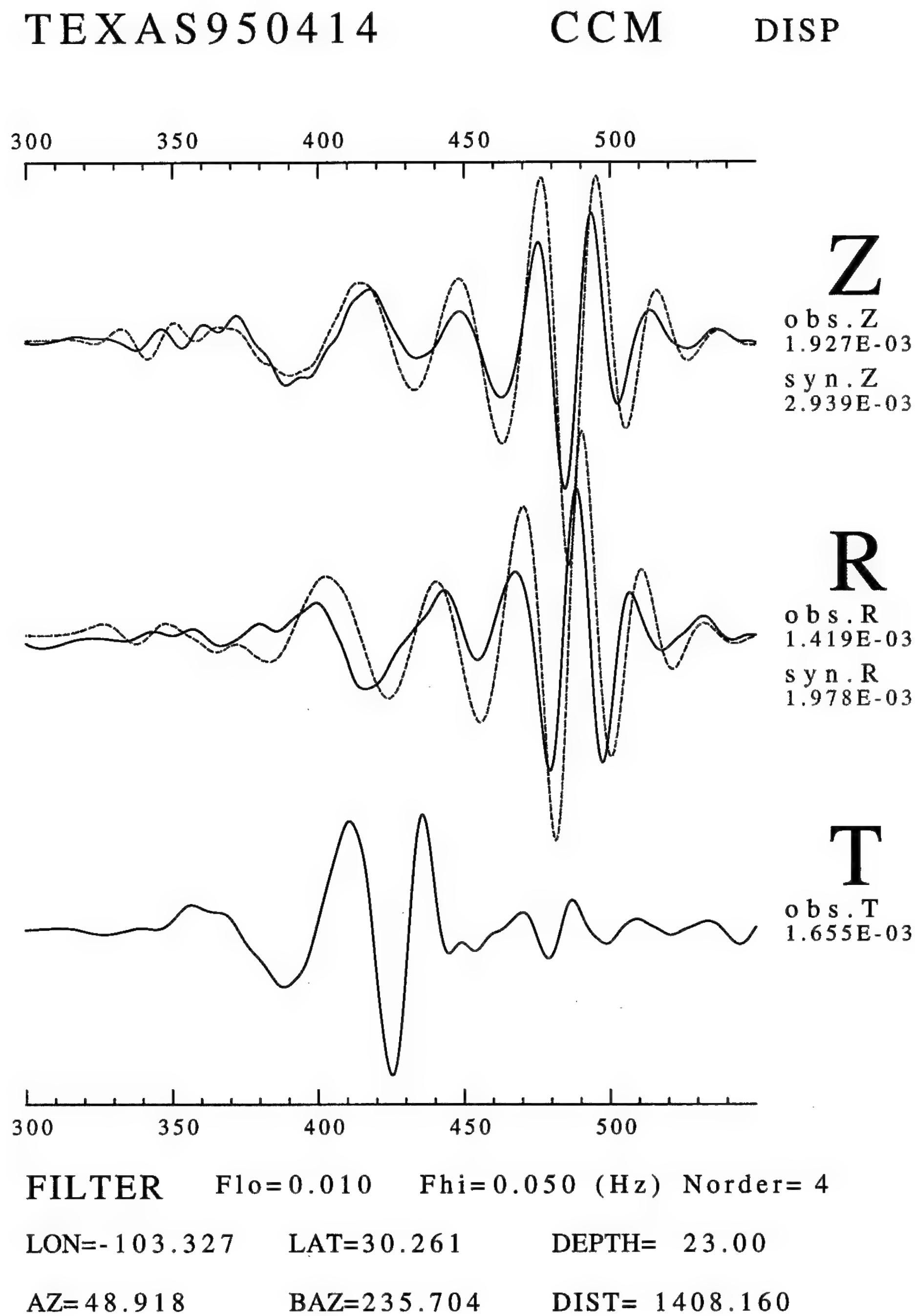

Fig. 5.15a. The waveform fit of the model shown as figure 5.14. Three frequency ranges are displayed: (a) 0.01-0.05 Hz.

from this model, we can not explain what signal are those in the time window 420-440 seconds.

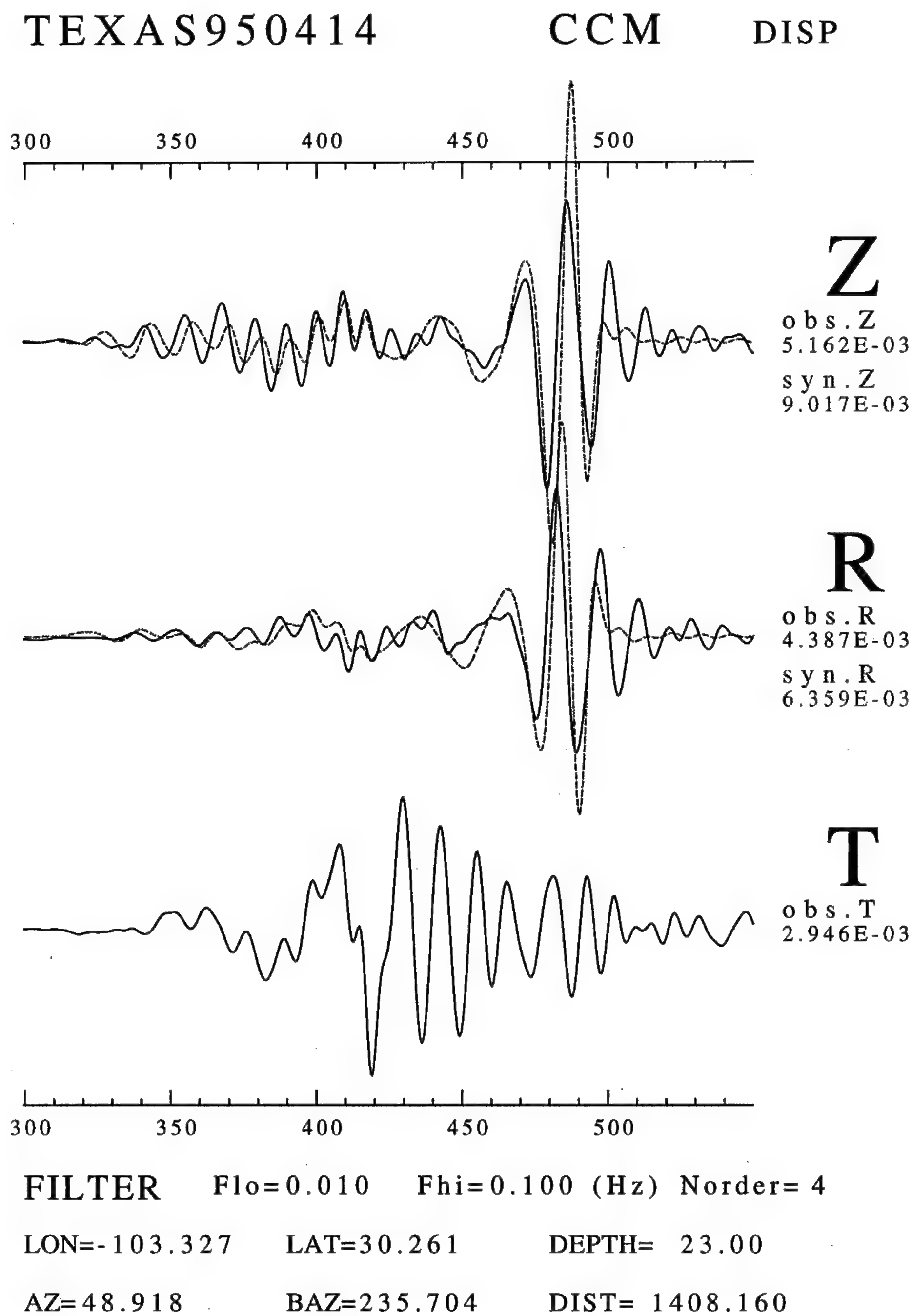

Fig. 5.15b. (Cont'd) (b) 0.01-0.1 Hz.

The second way to increase the higher mode amplitude is to consider frequency dependent Q for high frequency signal. To preserve the low frequency fundamental mode amplitude, the frequency

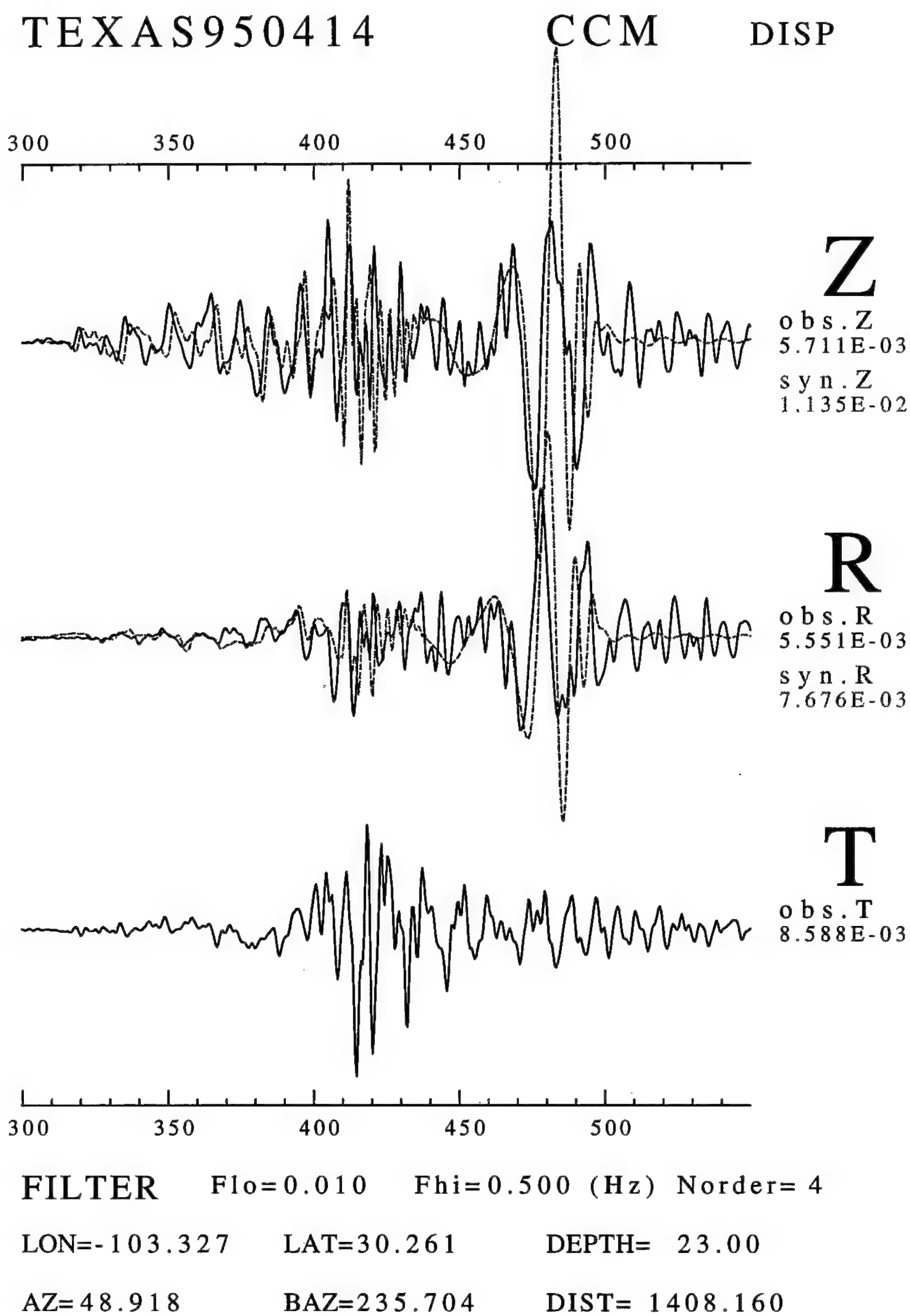

Fig. 5.15c. (Cont'd) (c) 0.01-0.5 Hz.

dependent Q only apply to signal whose frequency content is greater than 0.1 Hz. To avoid the abrupt change in spectrum shape when applying frequency dependent Q, a transition zone is used for 0.1-0.2

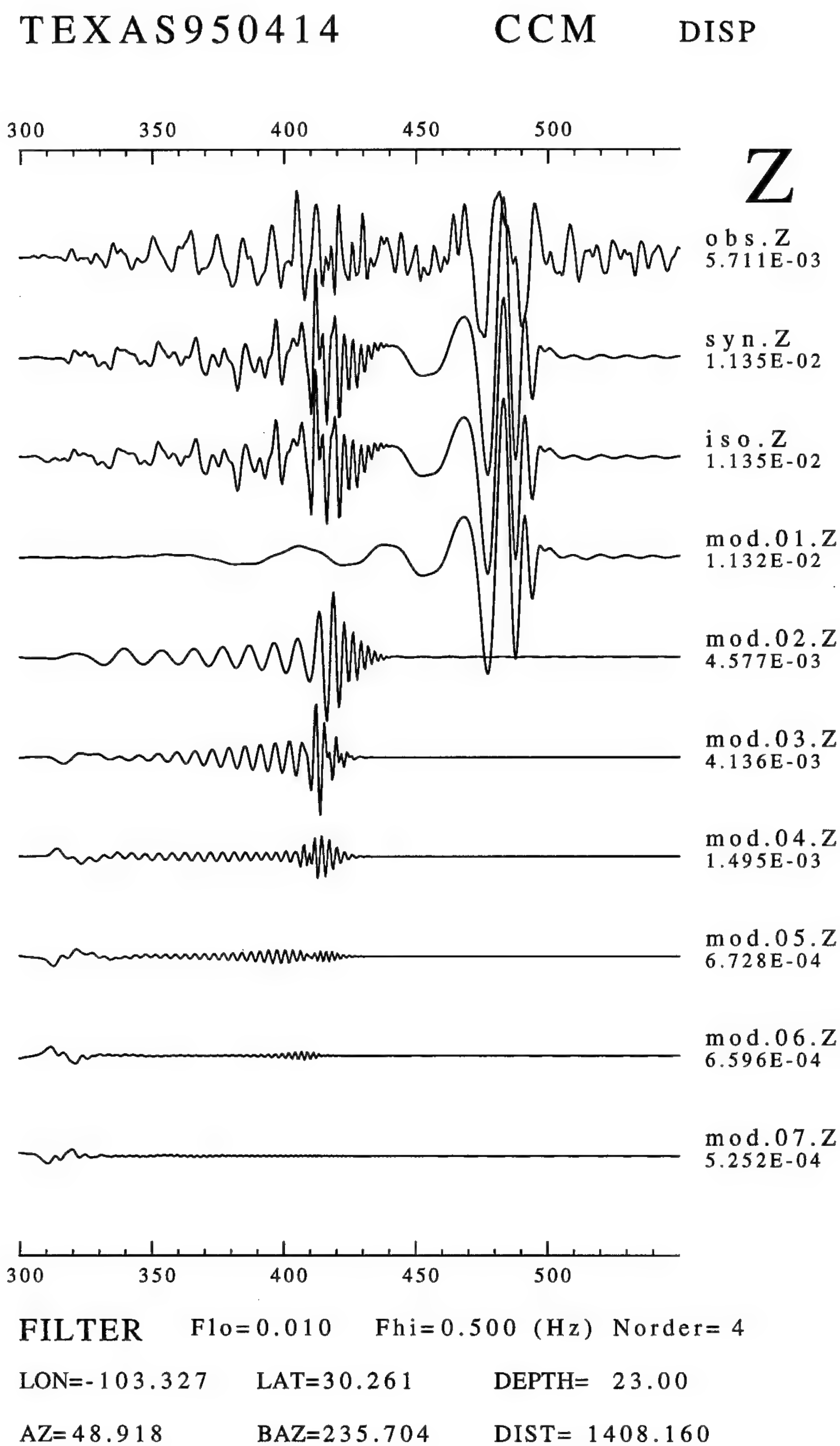

Fig. 5.16. The observed, synthetic, and seven single-mode seismograms were shown here.

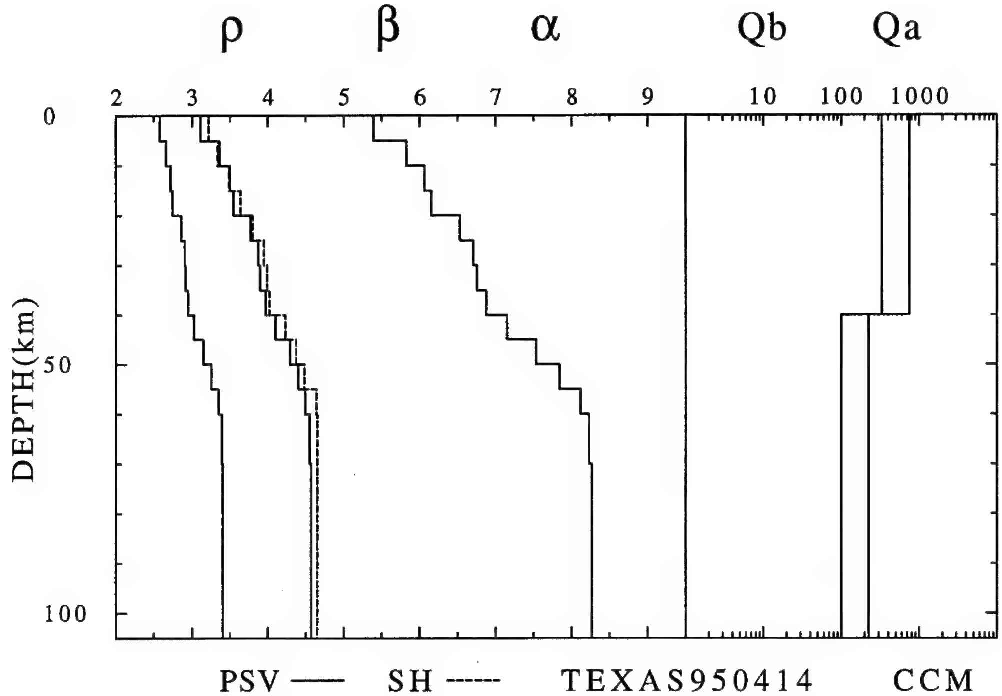

Fig. 5.17. This figure shows a better model which based on linear waveform inversion result, and using trial and error to do the fine tuning.

Hz. The following two examples are based on trial and error adjustment for two models from GSDF inversion and linear waveform inversion. The reference period of Q is 0.1 Hz and $\eta = 0.5$. During the trial and error adjustment, the fundamental mode phase may shift and out of phase. But the purpose is to see how to fit the higher mode phase and amplitude, and what process creates such strong Lg wave.

The first example is a fine tuning result for the GSDF inversion result. The model is shown as figure 5.14 and using frequency dependent Q. The waveform fit is displayed as figure 5.15. From the waveform, we can see that low frequency fundamental mode amplitude does not change much. Through the trial and error adjusting, the higher mode phase and amplitude are generally matched. However, the Airy phase amplitude is increased during such adjustment. The waveform, again, can not match the signals in the time window 420-440 seconds;

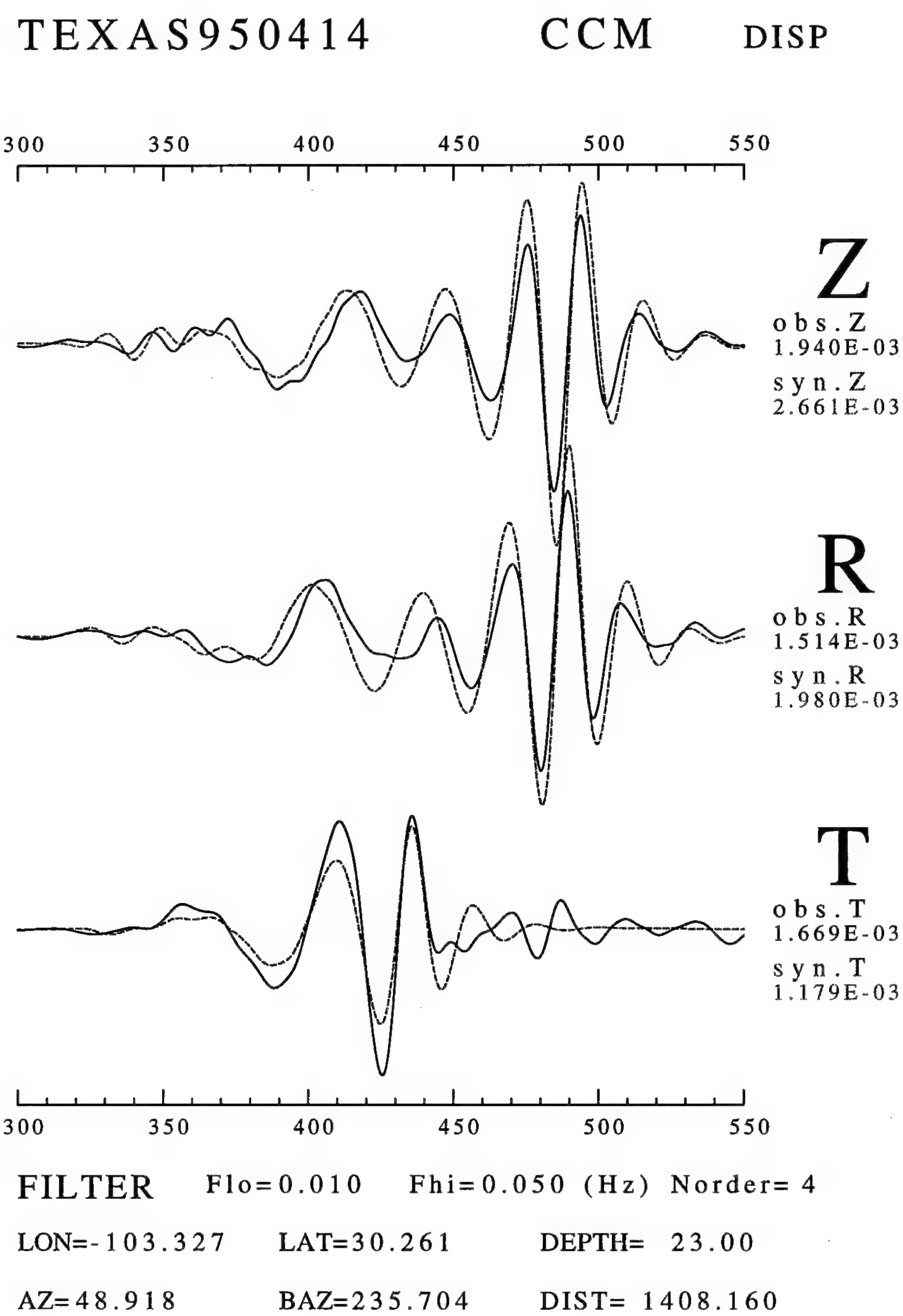

Fig. 5.18a. The waveform fit of the fine-tuning model shown at figure 5.17. Three different frequency ranges are shown: (a) 0.01-0.05 Hz.

also it can not explain what high frequency signals are those between 440 and 470 seconds. Looking at the single modes display (figure

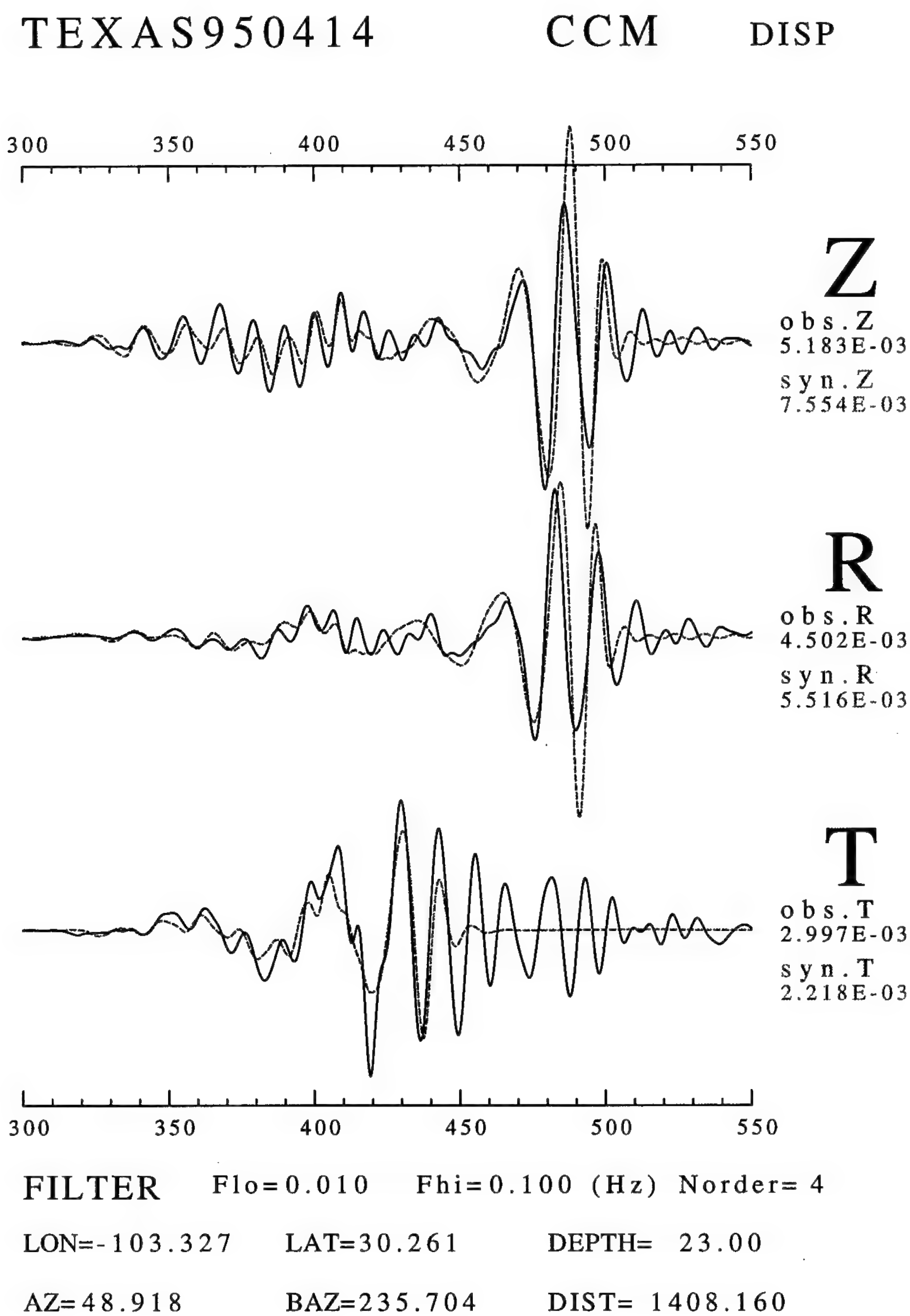

Fig. 5.18b. (Cont'd) (b) 0.01-0.1 Hz.

5.16), it shows that the higher mode signal are mainly constituted by first two higher modes.

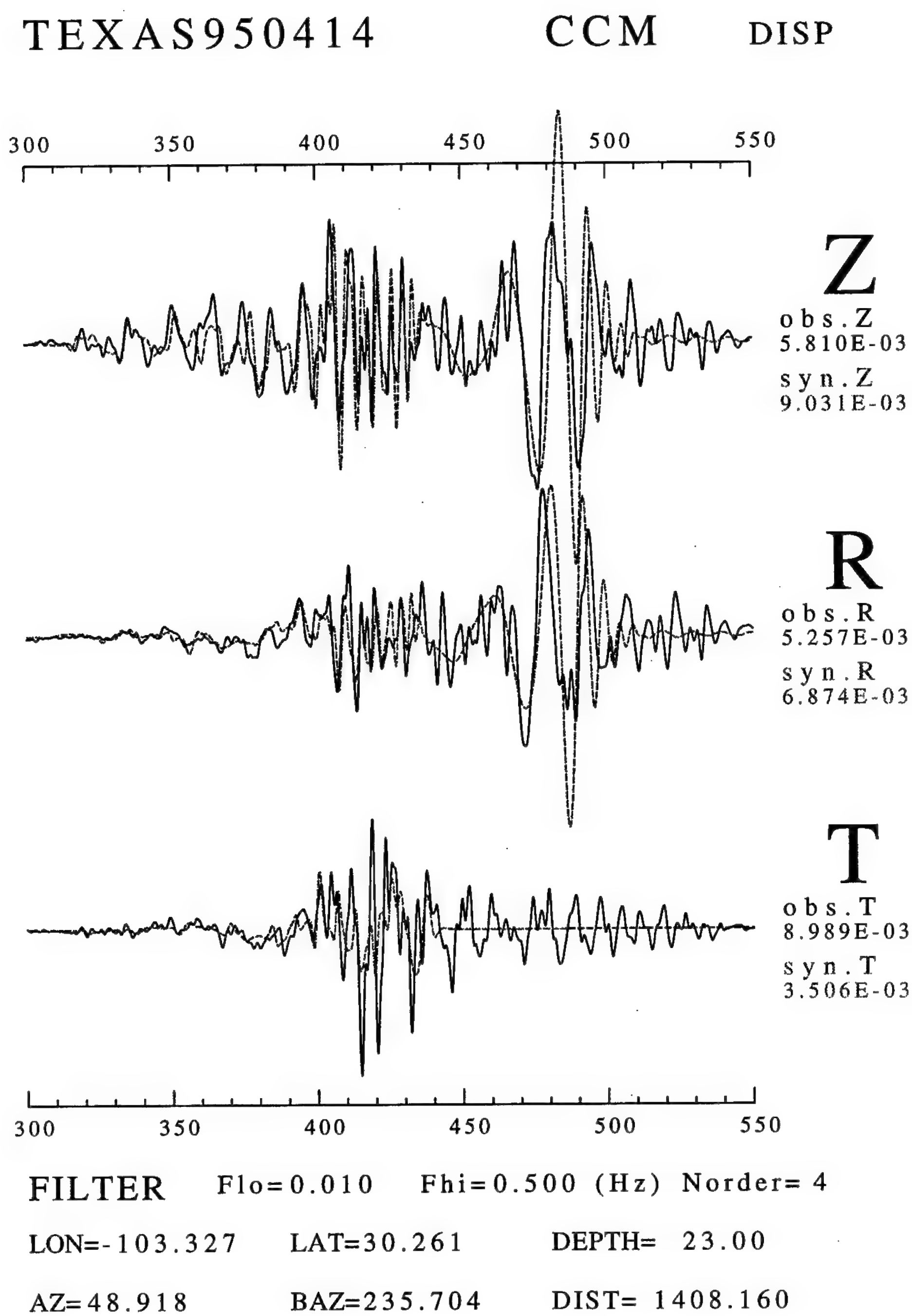

Fig. 5.18c. (Cont'd) (c) 0.01-0.5 Hz.

The second example is based on the inversion result of linear waveform inversion. This adjusted model shows good agreement with observed data, so we will use this model as an example to illustrate

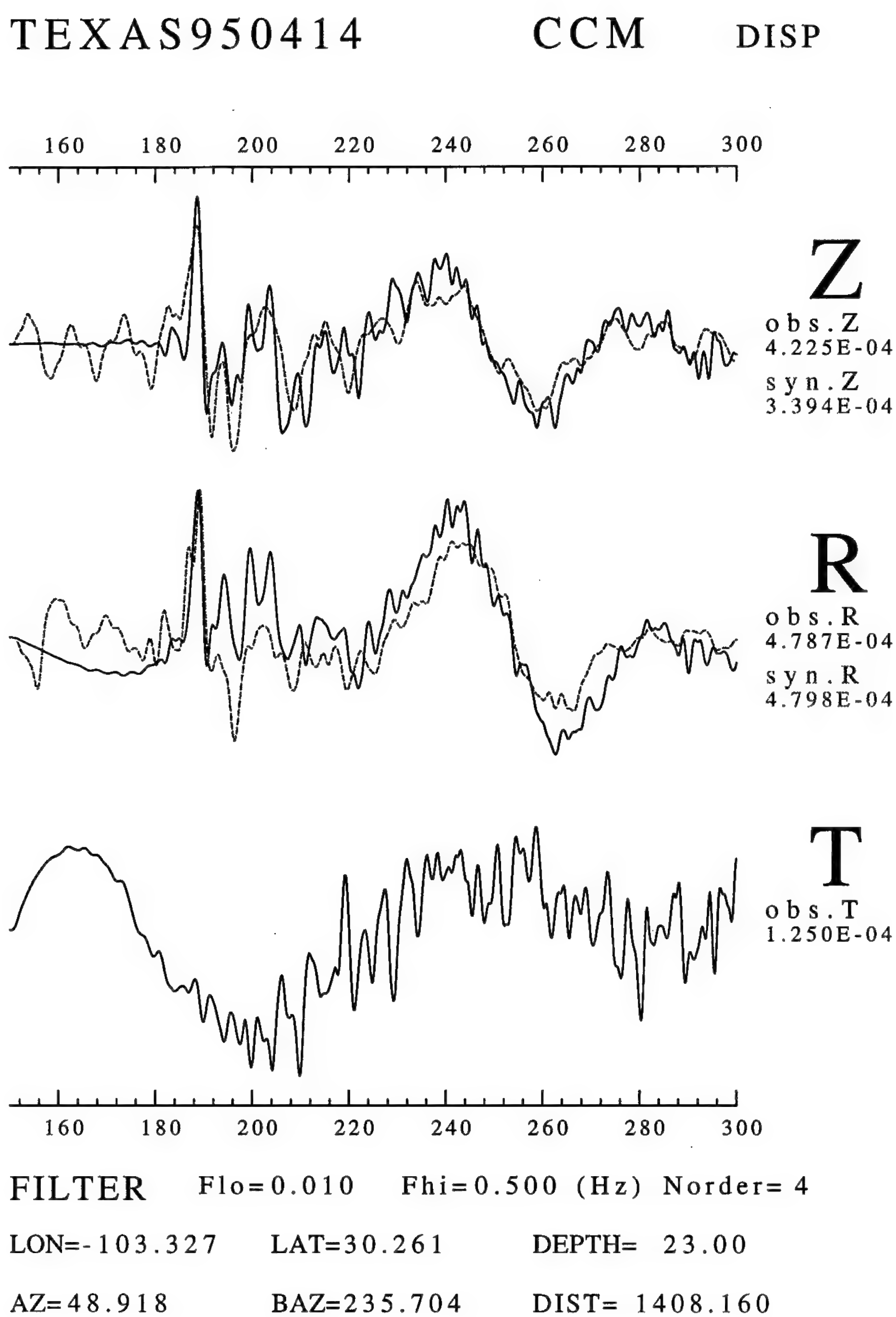

Fig. 5.19. The P_{nl} waveform fit which computed using locked mode approximation for the fine-tuning model shown at figure 5.17.

what is the reliability of model. In this model, not only the Rayleigh wave but also the Love wave are modeled. Figure 5.17 shows the

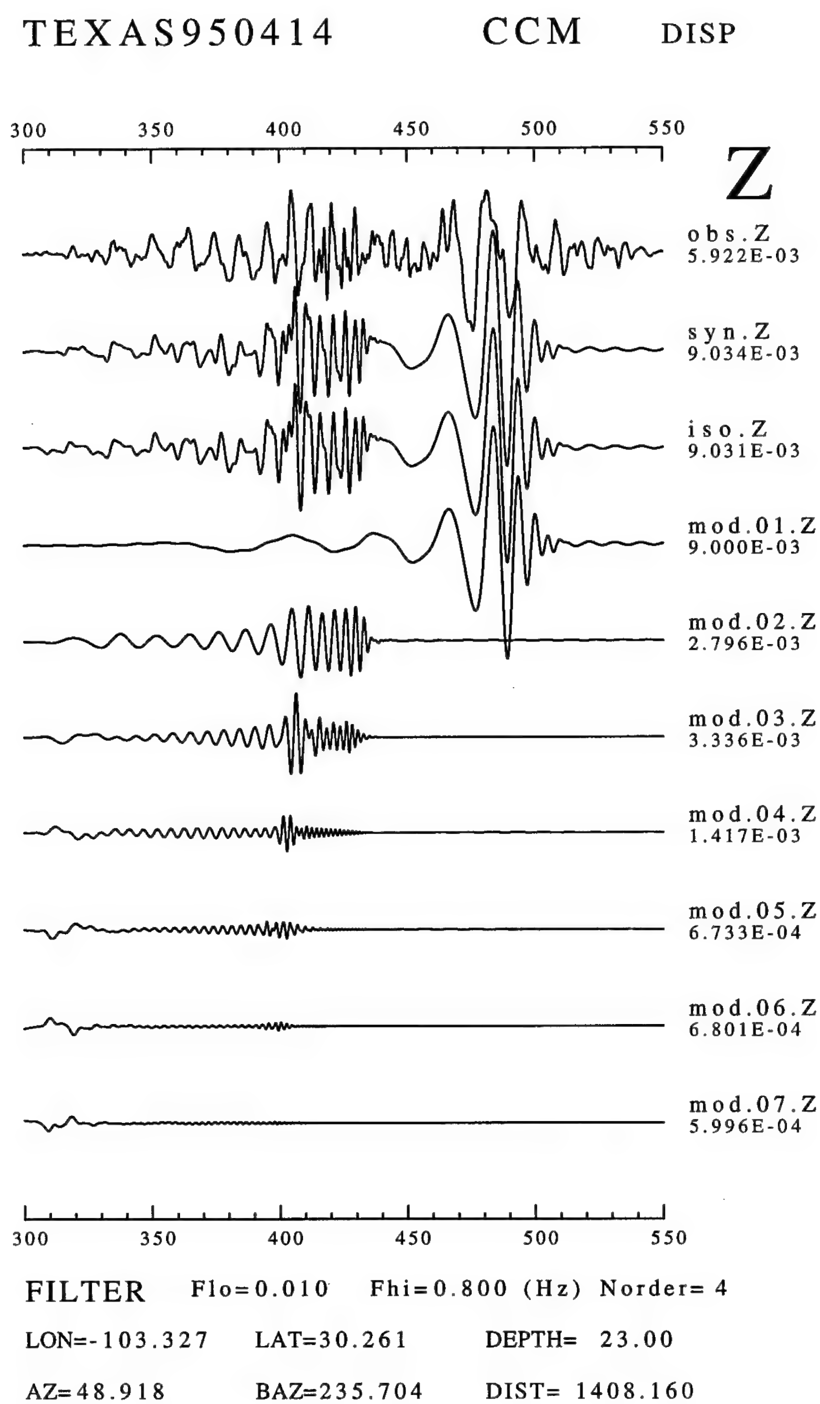

Fig. 5.20. The observed, synthetic, and seven single-mode seismograms were shown here.

models for the Rayleigh and Love waves. There are several characters

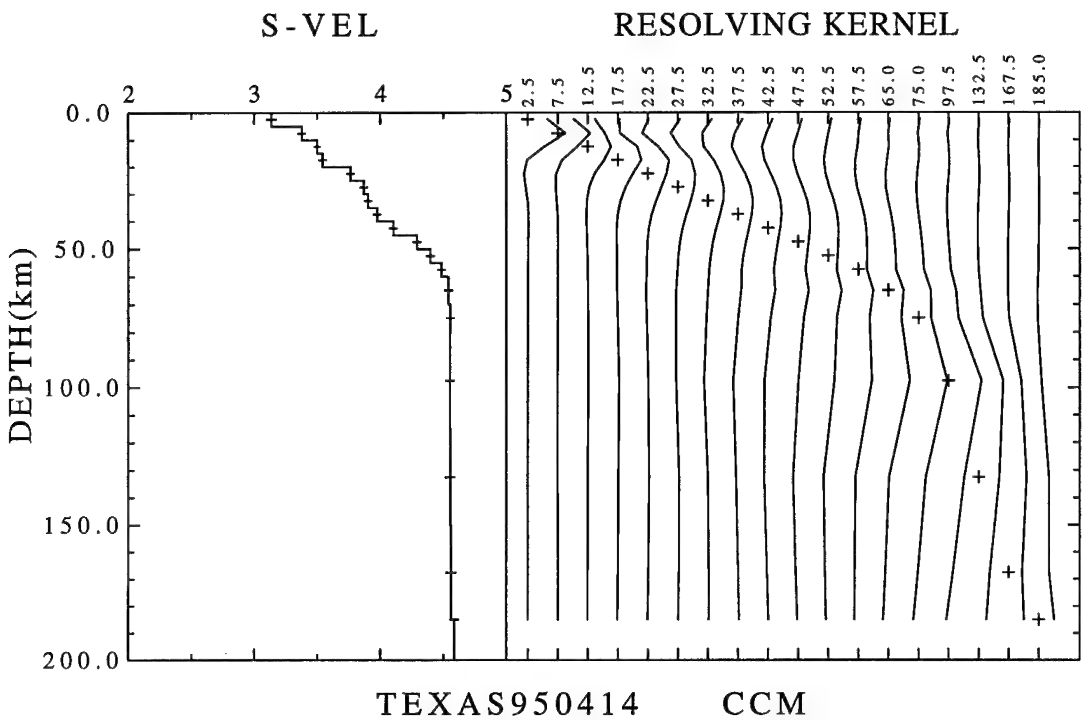

Fig. 5.21. The resolving kernel for the model shown on figure 5.18.

worth to mention. First of all, during the adjusting process, no low velocity zone is allow to exist in the crust. Second of all, there is no need to introduce a funny low velocity zone in the uppermost mantle (40-220 km) which is usually seen in other reported surface wave inversion results. Third of all, the model shows a gradient zone between 40 and 60 km instead of a sharp crust-mantle boundary. Final, the lower crust (20-40 km) is a steep velocity zone. Figure 5.18 shows the waveform fit at three different frequency ranges. From these plots, we can find that the higher mode waveform fit the observed data very well. Especially the signals in the 400-440 time window which is not well modeled by the other models. From figure 5.20, the single modes display shows a very good first higher model envelop with a nice tail after 410 seconds. This is consistent with the observed data. It also show that the amplitude variation is possibly caused by construction and destruction of higher modes. Figure 5.19

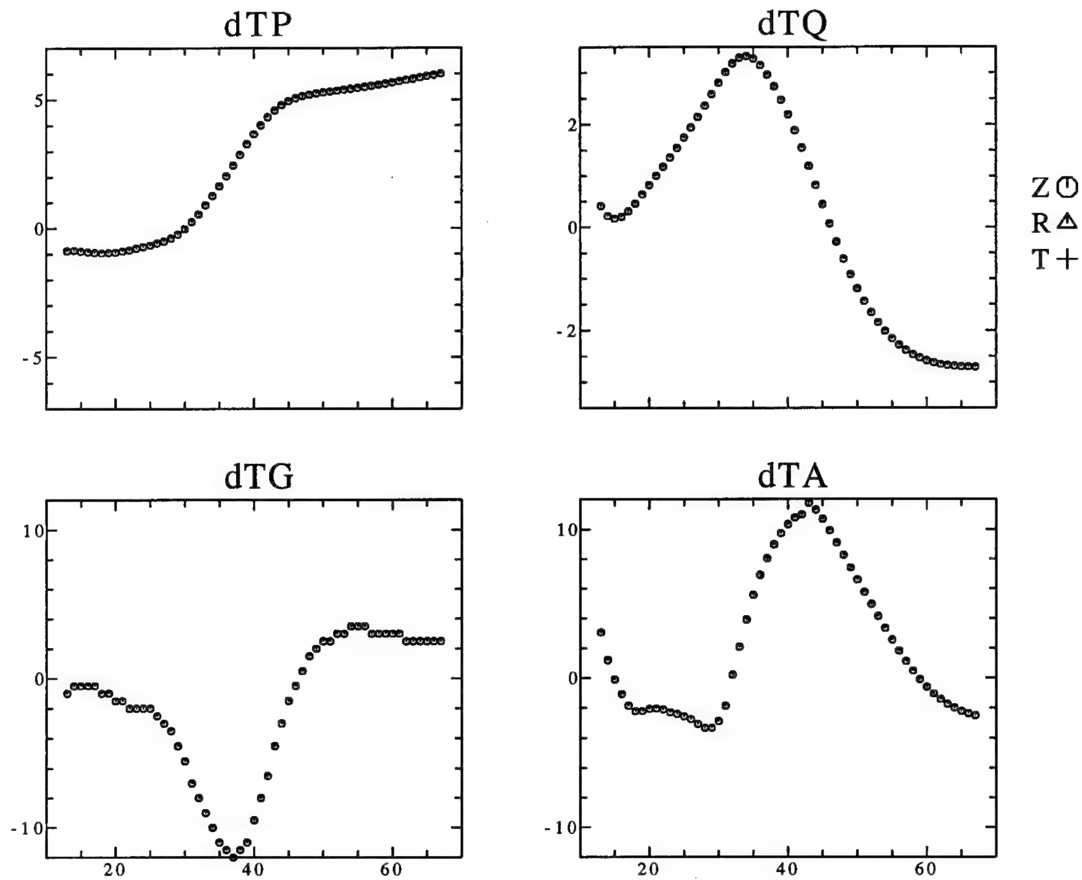

Fig. 5.22. The measurements of four GSDF functionals for the model shown on figure 5.18.

shows the synthetic seismograms which generated by locked mode approximation can match the P_{nl} phase. One of the importances of waveform modeling shown here is that it demonstrates a single 1-D model can match both body wave and surface wave waveforms in a regional stable area.

How confident can this model tell? In this study, the inversions were performed using damped least square method (Marquardt, 1963). The calculation of resolving kernels are straightforward. Figure 5.21 shows the resolving kernels and standard deviation of model parameters. However, the standard deviation bar is depend on the damping value used, it really can not show any information. On the other hand,

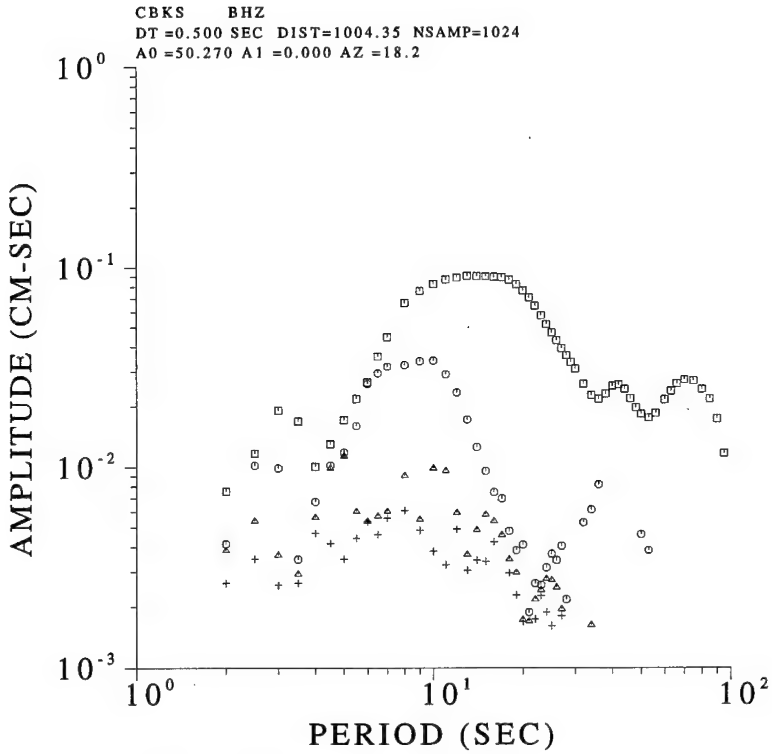

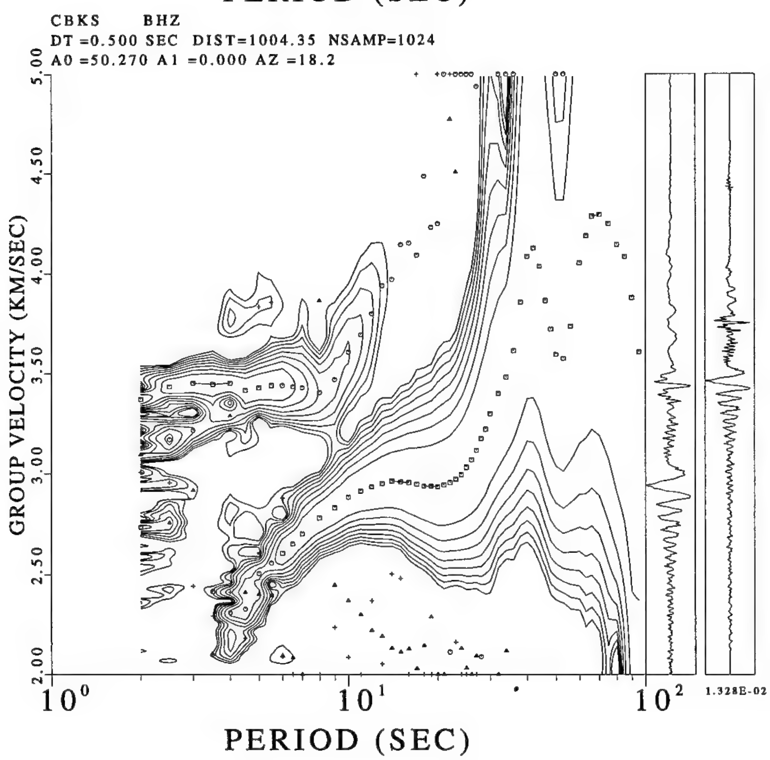

Fig. 5.23. The group velocity dispersion curve and spectrum amplitudes for station CBKS.

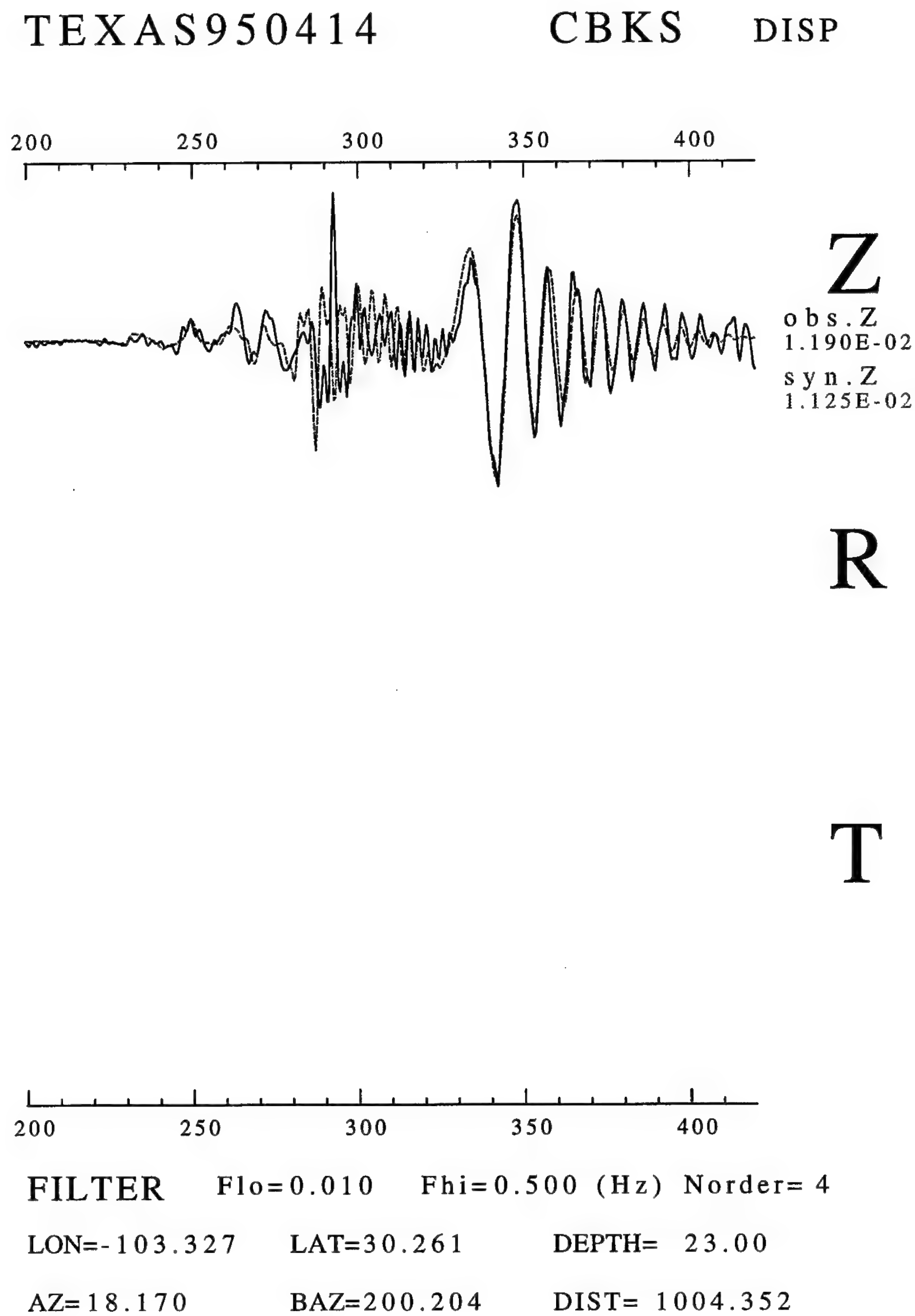

Fig. 5.24. The waveform fit for station CBKS at frequency band 0.01-0.5 Hz.

the measurements of four GSDFs may provide extra information to indicate the goodness of waveform fit. Figure 5.22 show the four GSDF measurements of vertical component Rayleigh wave. From the

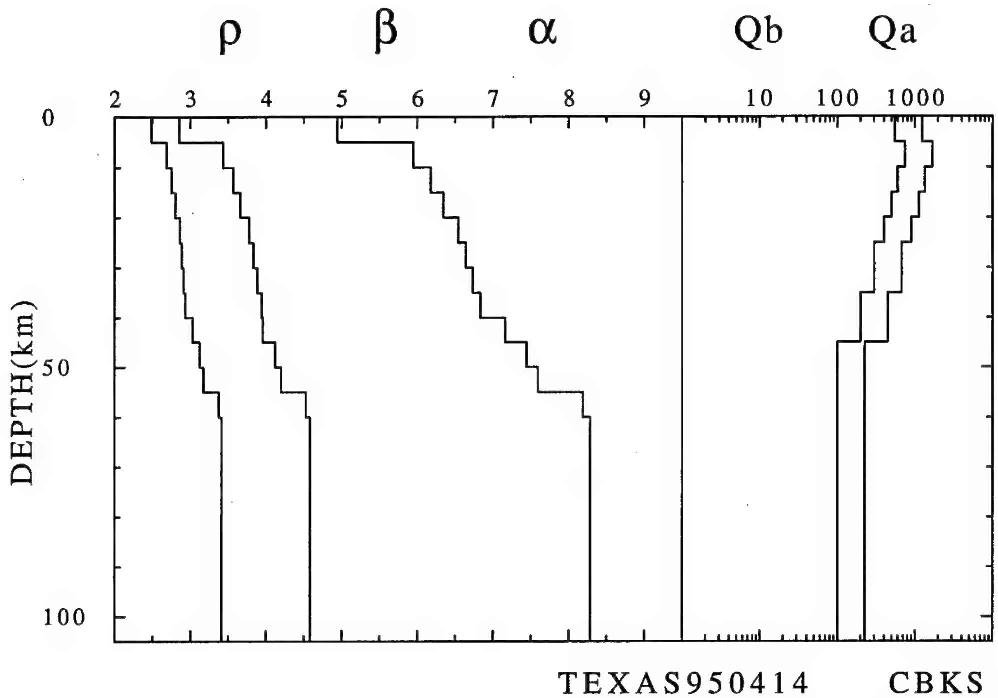

Fig. 5.25. The fine-tuning model for station CBKS which based on the GSDF inversion result.

group velocity differential time dTG, it indicate that around 37 seconds which represents the predicted Airy phase envelop is 15 seconds slow than observed. From dTP, it is clear to see that this model may doing well in high frequency but the low frequency part is systematically 5 seconds faster than data. From dTQ, we can see that for the period around 35 seconds, the synthetic seismogram's amplitude is too large. The GSDF measurements are better indicator of waveform fit than resolving kernels.

So far, there are two new hypotheses proposed. The first hypothesis is that a gradient velocity transition zone exist at the uppermost mantle instead of a sharp crust-mantle boundary. The second hypothesis is that whether the frequency dependent Q is real or not. We will use another two stations in the same region to test these two hypotheses.

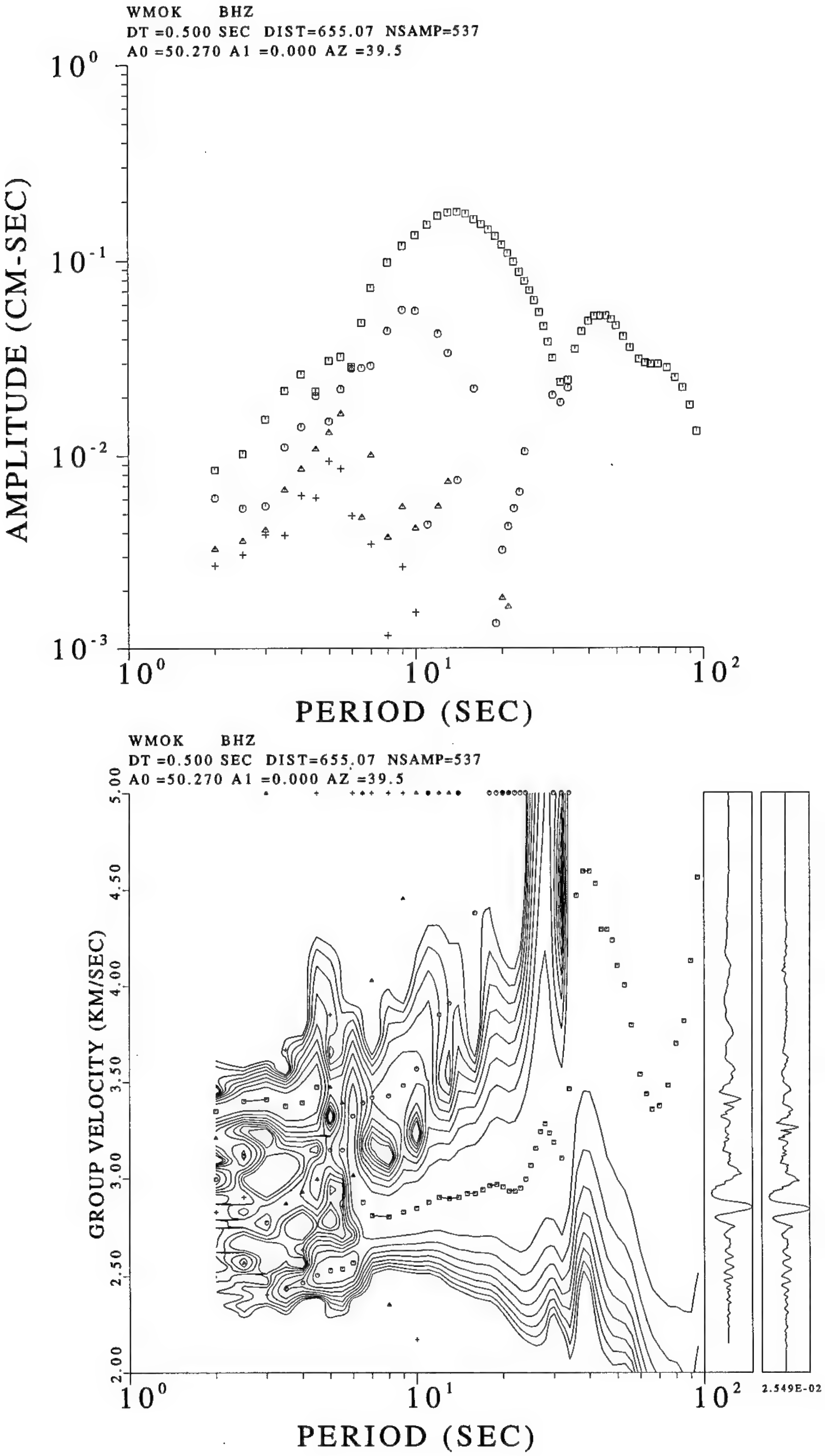

Fig. 5.26. The group velocity dispersion curve and spectrum amplitudes for station WMOK.

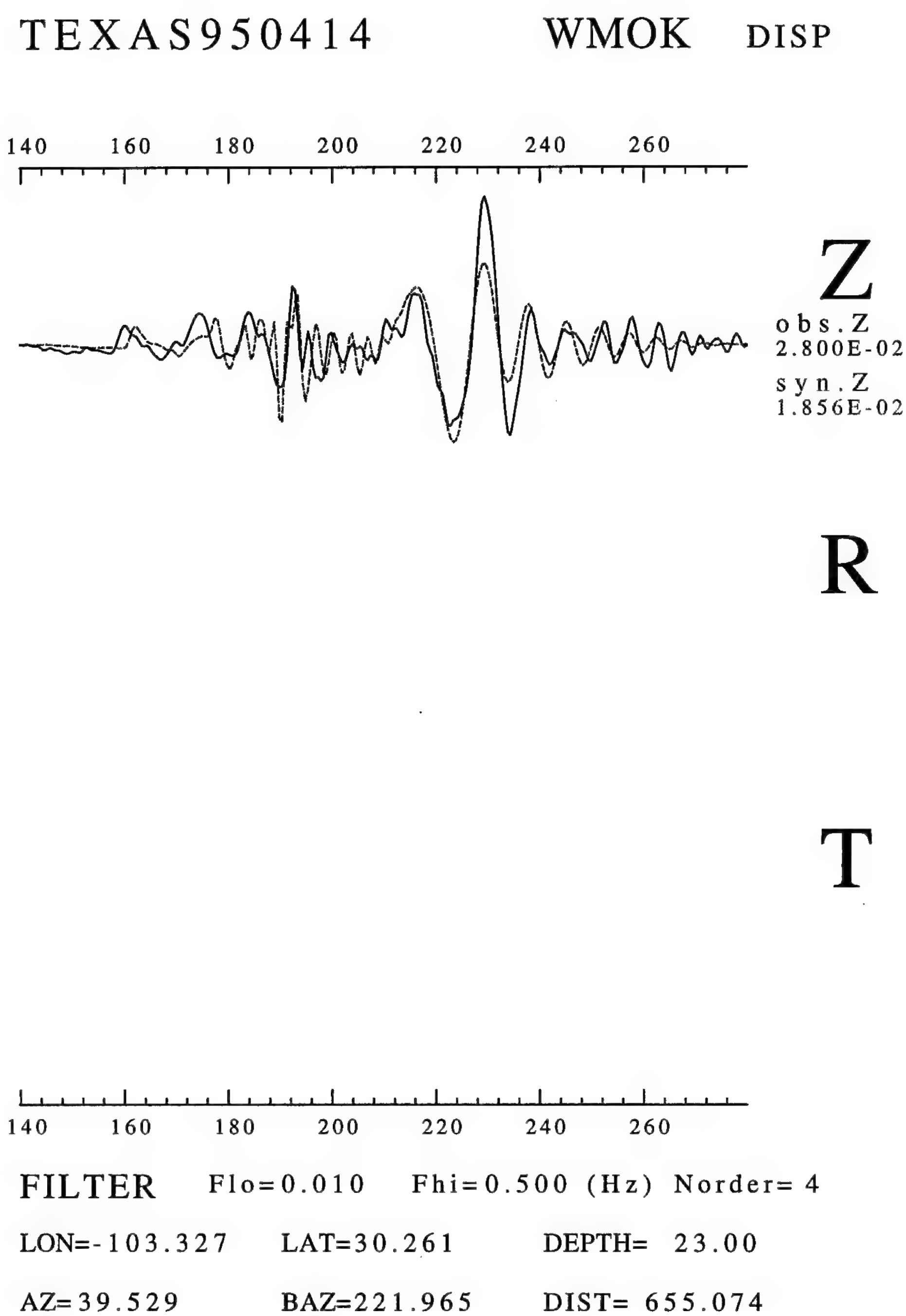

Fig. 5.27. The waveform fit at 0.01-0.5 Hz of station WMOK for the model shown on figure 5.28.

The first station is CBKS. From its group velocity dispersion curve (figure 5.23), it shows almost no interference from noise. The

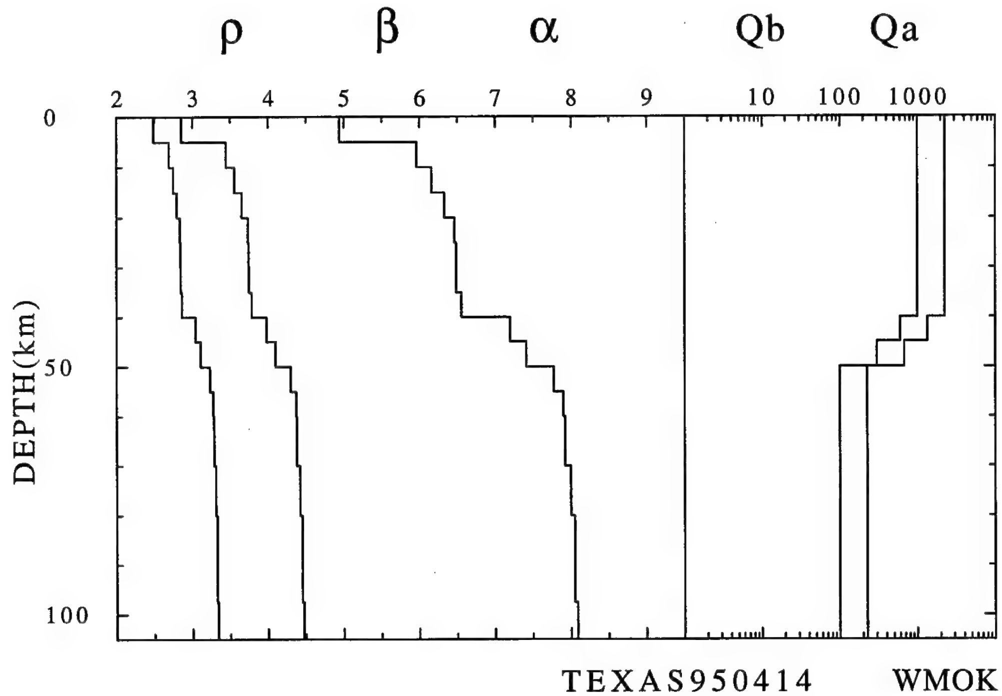

Fig. 5.28. The fine-tuning model for WMOK which based on GSDF inversion result.

GSDF inversion result shown as figure 5.25 and its associated waveform fit is shown as figure 5.24. The second station used to test those hypothesis is WMOK. The hypocentral distance is very short, only about 650 km. The dispersion curve is not as clean as CBKS, only the 8-30 seconds fundamental mode can be identified. The waveform fit is shown as figure 5.27 and the model is shown as figure 5.28. Although the waveform fit for both CBKS and WMOK are not perfect for higher mode, but they have correct amplitudes. From the models, they do not require frequency dependent Q to fit the amplitudes of both fundamental and higher modes. But comparing to CCM, these two models all have a high crustal Q values. However, there are two possibilities for this:

(1). The frequency dependent Q behavior is not observable for short distance stations.

(2). The observed frequency dependent Q at CCM is an artifact due to improper source radiation pattern which create large amplitude synthetics and force the crustal Q decreasing to compensate this effect and frequency dependent Q behavior is then required to match the higher mode amplitude.

Although, there is no conclusive answer for this question, but this question which related to the fundamental behavior of earth structure is noticed through modeling waveforms.

By comparing models of CCM, CBKS, and WMOK, it is found that all three models have a velocity transition zone at the uppermost mantle. Durrheim and Mooney (1994) use seismic and geochemical data to constrain the evolution of Precambrian lithosphere evolution. Their conclusion is that underplating is only happen at the Proterozonic instead Archean crust-mantle boundary. The seismic signature of underplating is a basal layer with high P-velocity (7.0-7.6 km/sec). In our study, the source is located between the Proterozonic platform and Rocky mountains, and the station CCM, CBKS, and WMOK lay inside the Proterozonic platform, therefore the propagation paths are sampling the relatively uniform platform. With fixed Poisson's ratio in inversion, the transitional velocity zone between 40 and 60 km shown in each model should be the evidence of underplating process. It would be interesting to study the Archean region using waveform modeling techniques to see whether a basal layer exists or not.

There is one question remain unanswered. That is what are those signals arrives between 430 and 470 seconds in vertical component CCM data. We have no answer for this. But from figure 5.9(b), the dispersion curve inversion result, we see a clue.

From results of reflection and refraction studies of continental lithosphere, it has been observed that there exists a reflective lower crust (e.g. Mooney and Brocher, 1987). Such seismic reflectors can be related to geological interpretations such as thrust stack, duplex, and so on (Hatcher, 1986). Braile and Chiang (1986) conduct numerical

experiments to study what kind structure can produce the reflective Moho. Their tests show that a Moho transition zone with many fine layers which have small velocity variations (ZIG-ZAG pattern) can be the possible model.

During the trial and error modeling process, we manually keep the velocity model as smooth as possible and remove the low velocity zones. The layer thickness of the model is 5 km for top 60 km. For such layer thickness and smooth velocity curve, it will only generate a smooth fundamental mode. Therefore, a fine-layer velocity model with small perturbations is a possible origin for those signals.

5.6 Discussion

In this chapter, we test four different algorithms to model the surface waveform. The results turn out each algorithm can provide different waveform fit result which emphasize different part of waveform due to their different criteria and formulations. For example, the GA search algorithm can find models that match the most energetic phase, fundamental mode in this case, but it lacks the ability to match the other less energetic phases such as higher modes. The reason is simple because of the criteria used. In a similar fashion, the linear waveform inversion is also controlled by the large residuals which might be artifacts caused by improper source. Using different windows and filters to force the inversion to focus on different part of waveform is a possible solution, but the controlling mechanism will strongly depend on user's expertise. The traditional dispersion curve inversion also has its own problems such as the accuracy in phase velocity measurements and the data density used in inversion. Like the traditional dispersion curve inversion, GSDF inversion also suffer from data density problem because both of them utilize the different remeasurements from waveform.

All four algorithms can provide reasonable model with waveform fit as good as up to 0.1 Hz. However, more structural information are revealed in higher frequency contents, the design of a model refining algorithm will be the task for seismologists. From this study, we believe that a multi-isolation-filters GSDF inversion algorithm can be a possible solution.

What is a good criteria for waveform modeling? So far, there is no answer for this question. But we know what is not a good criteria. To measure a simple pulse, several widely used criteria like cross-correlation and norm-2 can serve the purpose. However to judge the similarity of a complicated waveform, all these criteria will not give a satisfactory answer. The cross-correlation can only tell the similarity of the most energetic phase. The 2-norm will behave as a oscillatory wavelet, like cross-correlation, when the cycle-skipping problem involved. Therefore, we believe that the success of waveform inversion algorithms will depend on how the criteria have been designed.

When a good model obtained, without tectonic interpretation it is just a model. We would like outline the possible contributions from interpreting waveform modeling results. First we would ask what is the physical process happen in continental lithosphere? So far, the evidences from all branchs of geoscience are too few to give us a conclusive picture about what happen down there. So we will ask what kind seismic evidences can we provide to this topic?

Jordan (1975) proposed the continental tectosphere hypothesis. The continental tectosphere will have a cool thick root (up to 400 km). Using numerical modeling, the influence of such thick tectosphere on the geodynamic process of mantle and on the plate motion has been modeled (e.g. Stoddard and Abbott, 1996). Therefore, the first question is how to determine the thickness of continental lithosphere?

As described previously, the evolution model of Precambrian lithosphere proposed by Durrheim and Mooney (1994) suggest that the Archean lithosphere is thicker than Proterozonic lithosphere. Some

mantle process are different such as underplating only happen in Proterozonic crust-mantle boundary. Therefore, the second question will be: Can we find the fundamental difference of these two regions from seismological studies?

Sato *et al.* (1989) suggest that seismic velocity and Q model can be used to estimate the temperature gradient and partial melt fraction in the upper mantle. The temperature gradient can be inferred from the waveform modeling results. This could be another indirect constraint besides the heat flow measurements for continental lithosphere evolution.

Anisotropy is a common observed phenomenon from waveform modeling result. From observing the SKS and SKKS splitting, Silver and Chan (1991) suggest that the anisotropy is caused by the subcontinental upper mantle deformations during the different tectonic episodes. Therefore, anisotropy can be another indicator to the evolution history of continental lithosphere.

CHAPTER 6
DISCUSSION AND CONCLUSION

In this study, several algorithms have been used to model surface waveform.. Each algorithm has different advantages and weaknesses. One of the most important conclusion is that, through carefully waveform modeling, both body wave and surface wave can be modeled using 1-D model. Waveform modeling can also provide more detail structure information which is not obtainable by fitting gross data sets such as surface wave dispersion data.

The difference of tested algorithms are mainly in the "data" preparation for inversion. The linear inversion scheme used is working for inversion with no *a priori* information (Lawson and Hanson, 1974). Some issues that involving the different inversion schemes such as incorporating *a priori* information (Tarantola and Valette, 1982), and constrained inversion (Carrion, 1989) has not been tested in this study.

Another issue that related to inversion schemes is the weighting functions. For linear inversion, each parameter is acting as a free parameter, usually the inversion will become unstable due to the parameterization and data density used in inversion. Russell (1987) introduced "differential" weighting function to limit the parameters movement. However, when dealing with teleseismic records or many thin layers parameterization, this weighting function will not be able to avoid producing some funny low-velocity zones in model. Therefore, a Nolet style weighting function (Nolet, 1990; Snoke *et al.*, 1997) could be tested in the future to see can it stablize the inversion result.

what can be done in future? In the aspect of technique improvement: First of all, from this study, we notice that the envelope of

surface wave is a good indicator for Q structure. We believe that to formulate an algorithm to invert Q structure from different band-passed surface wave envelop will be a better tool to study upper mantle Q structure. The similar idea has already been reported by Cara *et al.* (1987) and Nolet (1990). Second of all, a fine tune-up algorithm is needed to match the less energetic higher mode waveforms without destroy the matched fundamental mode. We believe it can be implemented by constructing a multiple isolation filters GSDF inversion scheme which will utilize information from different wavegroups simultaneously. Another alternative will be multi windowed linear waveform inversion. Third of all, to implement the anisotropy inversion for surface waveform. Finally, to invent a inversion using both both surface and body waves.

In the aspect of application: We strongly feel that waveform inversion techniques can be very powerful tools to study regional events. First of all, regional events have their energy concentrate in a short time window which may have less influence by multi-pathing effects. The GA search results shown in chapter 4 can support this argument. Second of all, the propagation path is more likely travel through the same geological region. Although such modeling may only provide information of average crustal structure, but it can apply to many regions. It would be interesting to apply waveform inversion methods in a more small region.

In the aspect of global search technique: The major thing need to be done is to find a better criteria of waveform fit. This criteria is directly concern the success of global search technique for waveform modeling. The second work is to find a way to combine GA search and gradient information to speed the process. This will increase the application of global search technique. The other thing is to test other parameterization for GA search.

BIBLIOGRAPHY

Ammon, C. J., G. E. Randall, and G. Zandt (1990). On the nonuniqueness of receiver function inversions, *J. Geophys. Res.,* **95,** 15303-15318.

Basu, A., and L. N. Frazer (1990). Rapid determination of the critical temperature in simulated annealing inversion, *Science,* **249,** 1409-1412.

Braile, L. W. (1973). Inversion of crustal seismic refraction and reflection data, *J. Geophys. Res.,* **78,** 7738-7744.

Braile, L. W., and C. S. Chiang (1986). The continental Mohorovicic discontinuity: results from near-vertical and wide-angle seismic reflection studies, in Reflection Seismology: A Global Perspective, (eds. M. Barazangi and L. Brown), Geodynamics Series V. 13, Am. Geophys. Union.

Bunks, C., F. M. Saleck, S. Zaleski, and G. Chavent (1995). Multiscale seismic waveform inversion, *Geophysics,* **60,** 1457-1473.

Carrion, P. M. (1989). Generalized non-linear elastic inversion with constraints in model and data spaces, *Geophys. J.,* **96,** 151-162.

Cara, M., and J. J. Leveque (1987). Waveform inversion using secondary observables, *Geophys. Res. Lett.,* **14,** 1046-1049.

Crase, E., A. Pica, M. McDonald, and A. Tarantola (1990). Robust elastic nonlinear waveform inversion: application to real data, *Geophysics,* **55,** 527-538.

Dreger, D. S., and D. V. Helmberger (1993). Determination of source parameters at regional distances with three-component sparse network data, *J. Geophys. Res.,* **98,** 8107-8125.

Durrheim, R. J., and W. D. Mooney (1994). Evolution of the Precambrian lithosphere: seismological and geochemical constraints, *J. Geophy. Res.,* **99,** 15359-15374.

Dziewonski, A. M., S. Bloch, and M. Landisman (1969). A technique for the analysis of transient seismic signals, *Bull. Seis. Soc. Am.,* **59,** 427-444.

Dziewonski, A. M., and D. L. Anderson (1981). Preliminary reference earth model, *Phys. Earth Planet. Int.,* **25** 297-356.

Dziewonski, A. M., T-A. Chou, and J. H. Woodhouse (1981). Determination of earthquake source parameters from waveform data for studies of global and regional seismicity, *J. Geophys. Res.,* **86,** 2825-2852.

Dziewonski, A. M., and J. H. Woodhouse (1983). An experiment in systematic study of global seismicity: centroid-moment tensor solutions for 201 moderate and large earthquakes of 1981, *J. Geophys. Res.,* **88,** 3247-3271.

Dziewonski, A. (1984). Mapping the lower mantle: determination of lateral heterogeneity in P velocity up to degree and order 6, *J. Geophys. Res.,* **89,** 5929-5952.

Ekstrom, G (1996). Studying global seismicity, *EOS,* Trans. Am. Geophys. Union, **77,** F47.

Fan, G. and T. Wallace (1991). The determination of source parameters for small earthquakes from a single, very broadband seismic station, *Geophys. Res. Lett.,* **18,** 1385-1388.

Gaherty, J. B., and T. H. Jordan (1995). Lehmann discontinuity as the base of an anisotropic mechanical boundary layer beneath continents, *Science,* **268,** 1468-1471.

Gaherty, J. B., T. H. Jordan, and L. S. Gee (1996). Seismic structure of the upper mantle in a central Pacific corridor, *J. Geophys. Res.,* **101,** 22291-22309.

Gee, L. S., and Jordan, T. H. (1988). Polarization anisotropy and fine-scale structure of the Eurasian upper mantle, *Geophys. Res. Lett.,* **15,** 824-827.

Gee, L. S., and Jordan, T. H. (1992). Generalized seismological data functionals, *Geophys. J. Int.,* **111,** 363-390.

Gomberg, J. S., and T. G. Masters (1988). Waveform modeling using locked-mode synthetic and differential seismograms: application to determination of the structure of Mexico, *Geophys. J.,* **94,** 193-218.

Grand, S. P., and D. V. Helmberger (1984). Upper mantle shear structure of north America, *Geophys. J. R. astr. Soc.,* **76,** 399-438.

Hacher, R. D. (1986). Interpretation of seismic reflection data in complexly deformed terranes: a geologist's perspective, in Reflection Seismology: The Continental Crust, (ed. M. Barazangi and L. Brown), Geodynamics Series, V. 14, Am. Geophys. Union.

Herrin, E., and T. Goforth (1977). Phase-matched filters: application to the study of Rayleigh waves, *Bull. Seis. Soc. Am.,* **67,** 1259-1275.

Herrmann, R. B. (1973). Some aspects of band-pass filtering of surface waves, *Bull. Seis. Soc. Am.,* **63,** 663-671.

Herrmann, R. B. (1974). Surface wave generation by central United States earthquakes, Ph.D. Dissertation, Saint Louis University.

Huang, H., C. Spencer, and A. Green (1986). A method for the inversion of refraction and reflection travel times for laterally varying velocity structures, *Bull. Seis. Soc. Am.,* **76,** 837-846.

Jordan, T. H. (1975). The continental tectosphere, *Rev. Geophys. Space Phys.,* **13,** 1-12.

Keilis-Borok, V. I., and T. B. Yanovskaja (1967). Inverse problem of seismology (structural review), *Geophys. J. R. astr. Soc.,* **13,** 223-234.

Kennett, B. L. N., and E. R. Engdahl (1991). Traveltimes for global earthquake location and phase identification, *Geophys. J. Int.,* **105,** 429-465.

Koren, Z., K. Mosegaard, E. Landa, P. Thore, and A. Tarantola (1991). Monte Carlo estimation and resolution analysis of seismic background velocities, *J. Geophys. Res.,* **96,** 20289-20299.

Lawson, C. L. and R. J. Hanson (1974). Solving least squares problems, Prentice-Hall Inc., New Jersey.

Lerner-Lam, A. L. and T. H. Jordan (1983). Earth structure from fundamental and higher-mode waveform analysis, *Geophys. J. R. astr. Soc.,* **75,** 759-797.

Lerner-Lam, A. L., and T. H. Jordan (1987). How thick are the continents?, *J. Geophys. Res.,* **92,** 14007-14026.

Mao, W. J., G. F. Panza, and P. Suhadolc (1994). Linearized waveform inversion of local and near-regional events for source mechanism and rupturing processes, *Geophys. J. Int.,* **116,** 784-798.

Marquardt, D. W. (1963). An algorithm for least-squares estimation of nonlinear parameters, *J. Soc. Indust. Appl. Math.,* **11,** 431-441.

Masters G., T. H. Jordan, P. G. Silver, and F. Gilbert (1982). Aspherical earth structure from fundamental spheroidal-mode data, *Nature,* **298,** 609-613.

Mooney, W. D. and T. M. Brocher (1987). Coincident seismic reflection/refraction studies of the continental lithosphere: a global review, *Rev. Geophys.,* **25,** 723-742.

Mooney, W. D., G. Laske, and G. Masters (1996). Crust 5.1 : a revised global crustal model at 5°×5°, *EOS,* Trans. Am. Geophys. Union, **77,** F483.

Mora, P. (1987). Nonlinear two-dimensional elastic inversion of multi-offset seismic data, *Geophysics,* **52,** 1211-1228.

Nakanishi, I., and D. Anderson (1983). Measurements of mantle wave velocities and inversion for lateral heterogeneity and anisotropy-I. analysis of great circle phase velocities, *J. Geophys. Res.,* **88,** 10267-10283.

Nakanishi, I., and D. Anderson (1984). Measurements of mantle wave velocities and inversion for lateral heterogeneity and anisotropy-II. analysis by the single-station method, *Geophys. J. R. astro. Soc.,* **78,** 573-617.

Nataf, H.-C., I. Nakanishi, and D. Anderson (1986). Measurements of mantle wave velocities and inversion for lateral heterogeneities and anisotropy-III. inversion, *J. Geophys. Res.,* **91,** 7261-7307.

Nolet, G. (1990). Partitioned waveform inversion and two-dimensional structure under the network of autonomously recording seismographs, *J. Geophys. Res.,* **95,** 8499-8512.

Nowack, R. L., and L. W. Braile (1993). Refraction and wide-angle reflection tomography: theory and results, in *Seismic Tomography: Theory and Practice.,* (eds H. M. Iyer and K. Hirahara),Chapman & Hall, London.

Pan, G. S., and R. A. Phinney (1989). Full-waveform inversion of plane-wave seismograms in stratified acoustic media: applicability and limitations, *Geophysics,* **54,** 368-380.

Press, F. (1968). Earth models obtained by Monte Carlo inversion, *J. Geophys. Res.,* **73,** 5223-5234.

Rodi, W. L., Glover, P., Li, T. M. C. & Alexander, S. S., 1975. A fast, accurate method for computing group-velocity partial derivatives

for Rayleigh and Love modes. *Bull. seis. Soc. Am.,* **65,** 1105-1114.

Rothman, D. H. (1985). Nonlinear inversion, statistical mechanics, and residual statics estimation, *Geophysics,* **50,** 2784-2796.

Rothman, D. H. (1986). Automatic estimation of large residual statics corrections, *Geophysics,* **51,** 332-346.

Russell, D. R. (1987). Multi-channel processing of dispersed surface waves, Ph.D. Dissertation, Saint Louis University.

Sambridge, M. and G. Drijkoningen (1992). Genetic algorithms in seismic waveform inversion, *Geophys. J. Int.,* **109,** 323-324.

Sambridge, M., and K. Gallagher (1993). Earthquake hypocenter location using genetic algorithms, *Bull. Seis. Soc. Am.,* **83,** 1467-1491.

Sato, H., I. S. Sacks, and T. Murase (1989). The use of laboratory velocity data for estimating temperature and partial melt fraction in low-velocity zone: comparison with heat flow and electrical conductivity studies, *J. Geophys. Res.,* **94,** 5689-5704.

Sen, M. K. and P. L. Stoffa (1992). Rapid sampling of model space using genetic algorithms: examples from seismic waveform inversion, *Geophys. J. Int.,* **108,** 281-292.

Shibutani, T., M. Sambridge, and B. Kennett (1996). Genetic algorithm inversion for receiver functions with application to crust and uppermost mantle structure beneath eastern Australia, *Geophys. Res. Lett.,* **23,** 1829-1832.

Silver, P. G., and W. W. Chan (1991). Shear wave splitting and subcontinental mantle deformation, *J. Geophys. Res.,* **96,** 16429-16454.

Sipkin, S. A. (1986). Interpretation of non-double-couple earthquake mechanisms derived from moment tensor inversion, *J. Geophys. Res.,* **91,** 531-547.

Snoke, J. A. and D. E. James (1997). Lithospheric structure of the Chaco and Parana basins of south America from surface-wave inversion, *J. Geophys. Res.,* **102,** 2939-2951.

Stein, R. S., G. C. P. King, and J. Lin (1992). Change in failure stress on the southern San Andreas fault system caused by the 1992 magnitude=7.4 Landers earthquake, *Nature,* **258,** 1328-1332.

Stoddard, P. R., and D. Abbott (1996). Influence of the tectosphere upon plate motion, *J. Geophys. Res.,* **101,** 5425-5433.

Stoffa, P. L. and M. K. Sen (1991). Nonlinear multiparameter optimization using genetic algorithms: inversion of plane-wave seismograms, *Geophysics,* **56,** 1794-1810.

Su, W.-J. and A. M. Dziewonski (1992). On the scale of mantle heterogeneity, *Phys. Earth and Planet. Int.,* **74,** 29-54.

Tarantola, A., and B. Valette (1982). Generalized non-linear inversion problems solved using the least-squares criteria, *Rev. Geophys. Space Phys.,* **20,** 219-232.

Thio, H. K., and H. Kanamori (1995). Moment-tensor inversions for local earthquakes using surface waves recorded at TERRAscope, *Bull. Seis. Soc. Am.,* **85,** 1021-1038.

Vidale, J. E., and D. V. Helmberger (1992). Elastic finite-difference modeling of the 1971 San Fernando, California earthquake, *Bull.*

Seis. Soc. Am., **78,** 122-141.

Wang, C. Y. (1981). Wave theory for seismogram synthesis, Ph.D. Dissertation, Saint Louis University.

Wessel, P., and W. H. F. Smith (1991). Free software help map and display data, *EOS Trans. AGU,* **72,** 445-446.

Woodhouse, J., and A. Dziewonski (1984). Mapping the upper mantle: three-dimensional modeling of earth structure by inversion of seismic waveforms, *J. Geophys. Res.,* **89,** 5953-5986.

Woodward, R. L., and G. Masters (1991). Global upper mantle structure from long-period differential travel times, *J. Geophys. Res.,* **96,** 6351-6377.

Zelt, C. A. and R. B. Smith (1992). Seismic traveltime inversion for 2-D crustal velocity structure, *Geophys. J. Int.,* **108,** 16-34.

Zhang, Y. S. and T. Tanimoto (1992). Ridges, hotspots and their interaction as observed in seismic velocity maps, *Nature,* **355,** 45-49.

Zhou, L-S., and D. V. Helmberger (1991). Broadband modeling along a regional shield path, Harvard recording of Saguenay earthquake, *Geophys. J. Int.,* **105,** 301-312.

Zhou, L-S., and D. V. Helmberger (1994). Source estimation from broadband regional seismograms, *Bull. Seis. Soc. Am.,* **84,** 91-104.

Zhu, L., and D. V. Helmberger (1996). Advancement in source estimation techniques using broadband regional seismograms, *Bull. Seis. Soc. Am.,* **86,** 1634-1641.